University of Texas at El Paso
DigitalCommons@UTEP

Open Access Theses & Dissertations

2016-01-01

An Integrated Geophysical Survey Of Kilbourne Hole, Southern New Mexico: Implications For Near Surface Exploration Of Mars And The Moon

Nisa Maksim
University of Texas at El Paso, nrhodes@miners.utep.edu

Follow this and additional works at: https://digitalcommons.utep.edu/open_etd

 Part of the Geology Commons, and the Geophysics and Seismology Commons

Recommended Citation
Maksim, Nisa, "An Integrated Geophysical Survey Of Kilbourne Hole, Southern New Mexico: Implications For Near Surface Exploration Of Mars And The Moon" (2016). *Open Access Theses & Dissertations*. 886.
https://digitalcommons.utep.edu/open_etd/886

This is brought to you for free and open access by DigitalCommons@UTEP. It has been accepted for inclusion in Open Access Theses & Dissertations by an authorized administrator of DigitalCommons@UTEP. For more information, please contact lweber@utep.edu.

AN INTEGRATED GEOPHYSICAL SURVEY OF KILBOURNE HOLE, SOUTHERN NEW MEXICO: IMPLICATIONS FOR NEAR SURFACE EXPLORATION OF MARS AND THE MOON

NISA MAKSIM

Doctoral Program in Geological Sciences

APPROVED:

José Miguel Hurtado, Jr., PhD., Chair

Diane I. Doser, PhD.

Laura Serpa, PhD.

Terry Pavlis PhD.

Efrain Ferrer, PhD.

Charles Ambler, Ph.D.
Dean of the Graduate School

Copyright©

By

Nisa Maksim

2016

Dedication

To my late father, you told me to go see the world for you, here you go.

AN INTEGRATED GEOPHYSICAL SURVEY OF KILBOURNE HOLE, SOUTHERN NEW MEXICO: IMPLICATIONS FOR NEAR SURFACE EXPLORATION OF MARS AND THE MOON

by

NISA MAKSIM, M.S.

Department of Geological Sciences

DOCTORAL DISSERTATION

Presented to the Faculty of the Graduate School of

The University of Texas at El Paso

in Partial Fulfillment

of the Requirements

for the Degree of

DOCTOR OF PHILOSOPHY

Department of Geological Sciences

THE UNIVERSITY OF TEXAS AT EL PASO

August 2016

Acknowledgements

I am so grateful to be a part of UTEP geology family. From the first day I started my research here, I have received tremendous amount of help and intellectual input and all the love in the world that make the impossible, possible. This dissertation is the result of hard labor from so many individuals inside and outside the Department of Geological Science. I would like to take this space mention their names, as their hard work should not go anonymous. I would like to give a special thanks to my academic advisor Dr. Jose Hurtado, who never got tired of giving his time to all of his students. My gratitude to all of my committee, Dr. Diane Doser, Dr. Laura Serpa, Dr. Terry Pavlis, and Dr. Efrain Ferrer, for that I have learned so much from them. I give a big bow to my field crews for their assistant and companionship: Victor Avila, Niti Mankhemthong, Ezer Patlan, Ibrahim Cerda, Felix Ziwu, Jose Navarro, Arturo Ramirez, Francisco Torres, Doug Standart, Humberto Garcia, Jackie Clark, Tobgay Tobgay, Jackie Cordova, Matthew Cannon, Perry Houser, Julian Biddle, Anna Mwangi, Alina Valdez, William Seelig, Jenny Gonzalez, Joey Castro, Alexander Traver, Elisa Carrillo, Marc Lucero, and astronaut Reid Wiseman. I also would like to thank you UTEP-Geology staff members: Pamela Hart, Galen Kaip, Carlos Montana, Adriana Perez, and Joel Gilbert whom had dealt a great tedious tasks that makes my fieldwork and academic work goes smoothly. Lastly I am very thankful for my family in Thailand, my mother and sister and for my loving husband for standing by me during these hard years, without them I am nothing.

Abstract

Features such as the Home Plate plateau on Mars, a suspected remnant of an ancient phreatomagmatic eruption, can reveal important information about paleohydrologic conditions. The eruption intensity of a phreatomagmatic volcano is controlled mainly by the quantity of water and magma, the internal geometry of the volcano, and the depth of the interaction zone between magma and water. In order to understand the paleohydrologic conditions at the time of eruption, we must understand all the factors that influenced the phreatomagmatic event. I conducted an integrated geophysical survey, which are magnetic and gravity surveys, and a ground-penetrating radar (GPR) surveys at Kilbourne Hole, a phreatomagmatic crater in southern New Mexico. These investigations serve an analog paleo-hydrogeological study that could be conducted on Mars and the Moon with an implication for planetary exploration. These geophysical surveys are designed to delineate the internal structure of a phreatomagmatic volcano and to define the volumes and masses of volcanic dikes and excavation unit, the depth of feeder dikes, and impacted velocity of the volcanic blocks. For the gravity and magnetic surveys at Kilbourne Hole, I collected data at a total of 171 gravity survey stations and 166 magnetics survey stations. A 2D gravity and magnetic inverse model was developed jointly to map the body of the magma intrusions and the internal structure of Kilbourne Hole. A total of 6 GPR surveys lines were also completed at Kilbourne Hole to image and to define locations of pyroclastic deposits, volcanic sags and blocks, the sizes distribution of volcanic blocks, and the impact velocity of the volcanic blocks. Using the size distribution and impact velocity of volcanic blocks from our GPR data, I derived the initial gas expansion velocity and the time duration of the gas expansion phase of the Kilbourne Hole eruption.

These obtained parameters (volumes, masses, and depths of the feeder dikes and the excavation zone, and the initial gas expansion velocity) are used to quantitatively calculate the mass, volume and condition of groundwater involved in the magma-water interaction process that caused Kilbourne Hole eruption. The joint gravity and magnetic 2D inversion reveals two main bodies of basaltic intrusion dike underneath Kilbourne Hole. The depth to the top of the dike is varied between 0.91 and 3.58 km from the ground surface. The models are able to delineate several complex areas of slumping blocks and collapsed crater, the area of the diatreme and the area of the original crater's excavation. The estimated depth of the diatreme is ~13.6-15.8 km. The model shows that the tuff ring deposits extend 600 m to 1 km away from the crater rim and vary in thickness (50-150 m). Based on our 2D gravity and magnetic inverse models of Kilbourne Hole, we were able to calculate the mass of the magma and the final product of this research, which is the mass of water that fed the Kilbourne Hole eruption. The total mass of the magma (M_m) is 1.38 ± 0.15 x 10^{13} kg and the mass of water (M_w) is (1.09 ± 0.31) x 10^{13} kg. The water to rock mass ratio of the Kilbourne Hole eruption was 0.01-0-02. With the GPR surveys results, we estimate that the initial gas expansion velocity (V_0) of the Kilbourne Hole eruption was 123 ± 9 m/s and the time duration of the gas expansion phase was 92 ± 11 s. The obtained initial gas expansion velocity and the depth of the dikes suggest that the eruption occurred at an initial pressure of 163 ± 9 bar.

I also utilized the lunar gravity field measured by the Gravity Recovery and Interior Laboratory (GRAIL) mission to reconstruct the history of lunar mascon basin formation and magmatic activity. We hypothesize that a combination of uplifted lunar Moho, impact melt sheets, and brecciated crust creates the gravity signature of lunar mascon basins. To test this hypothesis, We performed low-pass and preferential filtering on the free-air anomaly map

derived from GRAIL lunar gravity model GL0660A. Using the preferential filtering method, we isolated the gravity anomalies associated with structures at 16 km and 30 km depth where we can avoid high-frequency gravity signal from the highly impacted subsurface topography and mare basalt. We construct four 2D inversion models from the filtered gravity data to visualize the internal structure of lunar mascon basins. We conclude from our 2D inversion models that the parameters that determine the gravity signatures of mascon basins are: (1) the extent of the impact-melt sheet; (2) the depth to the mantle; and (3) the thickness and density of the surrounding crust.

Keywords: phreatomagmatic volcano, Ground Penetrating Radar, pyroclastic deposits, volcanic sags, volcanic blocks, gravity survey, magnetic survey, Kilbourne Hole, planetary geophysics, groundwater, paleohydrology, Home Plate, GRAIL, mascon, preferentially filtering, gravity anomaly separation, window filtering, power spectrum, impact melt sheets, impact basin, 2D joint inversion, Mesilla basin.

Tables of Contents

Page

List of Tables

List of Figures

Chapter 2

Chapter 3

Chapter 1: Introduction and Dissertation Overview

The recent discoveries of abundant water on the Moon and Mars (e.g., Cohen and Coker, 2000; Saal et al. 2008; Hauri et al. 2015; Robinson and Taylor, 2014; Anand et al., 2014; Boyce et al., 2014; Furukawa et al., 2014; Robinson and Taylor, 2014; Pendleton, 2015) will have very significant implications for human space exploration. Exploration of the lunar and Martian subsurface would provide critical information about the early history of the Solar System and a critical knowledge of Earth's geological formation. Martian crust probably contains a hydrosphere due to impact fragmentation and processes. Theoretical groundwater models suggested ancient groundwater activity. What does the groundwater system of an early Mars look like? We are not yet certain. The evidence of phreatomagmatic eruptions found on Mars Home Plate indicates the timing when the groundwater and tectonic activity were still active and were actually interacted. We hypothesized that the understanding of the phreatomagmatic volcano's morphology and structure could lead us to the understanding of the groundwater system that fed this particular phreatomagmatic eruption. We have a well-known phreatomagmatic volcanic site locally that could serve well as an analog site. With an implication for planetary exploration in mind, we aim to design a ground-based integrated geophysical survey that could efficiently and perhaps remotely map the internal structure of the phreatomagmatic volcano. We also aim to develop strategies to help us quantitatively interpret paleohydrological condition using a phreatomagmatic volcano as a climate proxy. On the Moon, however, we already have a series of high-resolution gravity and magnetic data from the Gravity Recovery and Interior Laboratory (GRAIL) that were opened for public usage. Instead of purposing a survey designs and approaches, we suggested a methodology to utilize the said data to understand the Moon's internal structure. We found that it is very difficult to interpret the

Moon's high-resolution gravity data, as currently we do not have enough surficial information of the Moon to constrain the gravity model. Without sufficient constraints, geophysical modeling approaches should not be the sole method for resolving unknown geological features. Alternative approaches for resolving the internal structure of phreatomagmatic volcano or mascon basins should also be considered. Currently, the information about the shallow and deep interiors of Mars and the Moon are only derived from low-resolution gravity, magnetospheric, and seismic studies on the Moon. Previous research provided some knowledge about the lunar interior, such as the existence of a liquid core (Williams et al., 2001; Weber et al., 2011) and estimates for crustal thickness (Wieczorek et al., 2006), but most geophysical studies still depend on modeling for interpretation (Williams et al., 2001; Wieczorek et al., 2006; Weber et al., 2011; Zuber et al., 2014). All three of our researches provided an improvement to the traditional modeling approach. For example, we integrated our GPR surveys result and our 2D Gravity and Magnetic jointed inverse model and, we applied the power spectrum depth analysis to constraint the depth of our lunar crustal gravity model.

The primary objective of this dissertation is to design an integrated geophysical method for paleohydrogeological study with an implication for planetary exploration. The product of the primary objectives is the estimated quantity of the groundwater reservoir that fed the Kilbourne Hole eruption. The second objective of this research is to develop a procedure to utilize the high-resolution lunar gravity data GRAIL. The obtained product of the secondary objectives were two detail crustal models of the Moon that reveal the internal structure of type I and type II mascons. We also aim to provide a design of integrated geophysical approaches to geophysical modeling that are easy to conduct and process, while gaining the most information about a planet. We considered several ground-based geophysical survey methods, which are GPR, gravity, and

magnetic that can be performed by a rover and do not rely solely on modeling to investigate internal structures on either Mars or the Moon. This dissertation comprises four chapters. The main focus of Chapters 2 and 3 is Kilbourne Hole, New Mexico, a maar volcano that is a planetary analog to phreatomagnatic eruptioins that may have occurred on Mars and elsewhere. In those chapters, I aim to understand: (1) the geomorphic and internal features of phreatomagmatic volcanoes and how they form in response to hydrologic and volcanic processes; (2) the feasibility of performing ground-based geophysical surveys that include magnetics, gravity, and, GPR to image those geomorphic and stratigraphic features; (3) how shallow subsurface geophysical surveys of a phreatomagmatic volcano can be used to quantitatively estimate paleohydrogeologic conditions at the time of the eruption; and (4) how geophysical methods might be employed on other planets, such as Mars and the Moon. In Chapter 4, I: (1) develop a power spectrum analysis and preferential filtering method that can be used to isolate the gravity signal of a specific depth for 2D modeling; and (2) provide a quantitative interpretation of lunar crustal structure and mascon basins using a 2D gravity inversion method.

The products of this dissertation are three manuscripts intended for publication, first of which is centered on magnetic and gravity methods (Chapter 2), second of which is centered on the GPR method (Chapter 3), and the third will focus on the preferential filtering and inverse modeling of the Moon's free air gravity anomaly (Chapter 4). Chapter 2 describes the design of magnetic and gravity surveys at Kilbourne Hole, the data collection scheme, and the construction of a joint 2-D inverse model that is used to delineate the internal structure, thicknesses, and volumes of the eruptive units around Kilbourne Hole as well as the depth of the buried feeder dikes below Kilboune Hole. The inversion process is constrained by the thicknesses and types of

pre-eruptive lithologies, the topography of the area, magnetic susceptibility, and density. Several best-fit joint inversion models for Kilbourne Hole were used to estimate the parameters needed for paleohydrological study. These parameters include the volume of ejected pyroclastic material and the volume and the depth of the feeder dikes. These parameters are used to calculate the changes in internal heat energy, potential energy, and kinetic energy needed to solve for the gas-to-magma mass ratio and the amount of groundwater at the time of eruption. In Chapter 3, I present the results of a GPR campaign at Kilbourne Hole. Six GPR profiles oriented radially with respect to the center of the crater were performed. The goal of the GPR campaign was to map the size distribution of volcanic blocks as a function of distance from the crater in order to derive the maximum gas expansion velocity of the eruption (V_0). This velocity is used to calculate the kinetic energy of the eruption, a quantity that is related the amount of water involved in the eruption. Knowing this velocity is essential to constraining the amount of water in the eruptive system. Chapter 4 describes the application of modeling of GRAIL mission data to determine lunar crustal structures and the formation of mascon basins. Prior to inversion modeling of the free-air gravity anomaly, we also first applied a low-pass filter and the preferential-filtering method (Spector and Grant, 1970; Guo et al., 2013) to remove the high frequency gravity signal from the free air gravity data and selectively filter the gravity signal from the depths of 16 km and 30 km. We also applied a power spectrum depth analysis method (Spector and Grant, 1970; Guo et al., 2013) to constrain the depth result of our inversion model. Our 2D inversion models provided the quantitative interpretation of lunar crustal structure and mascon basins which are: (1) the extent of the impact-melt sheet; (2) the depth to the mantle; and (3) the thickness and the density of the crust surrounding mascons.

References

Anand, M., Tartèse, R., and Barnes, J. J., 2014, Understanding the origin and evolution of water in the Moon through lunar sample studies: *Philosophical Transactions of the Royal Society A: Mathematical, Physical and Engineering Sciences*, vol. 372, no. 2,024, p. 2,013-2,054.

Baker, V. R., Hamilton, C. W., Burr, D. M., Gulick, V., Komatsu, G., Luo, W., Rice, J. W. and Rodriguez, J. A. P., 2015, Fluvial geomorphology on Earth-like planetary surfaces: A review: *Geomorphology*, vol. 245, p. 149-182.

Boyce, J. W., Tomlinson, S. M., McCubbin, F. M., Greenwood, J. P., and Treiman, A. H., 2014, The lunar apatite paradox: *Science*, vol. 344, no. 6,182, p. 400-402.

Cohen, B.A. and Coker, R.F., 2000, Modeling of liquid water on CM meteorite parent bodies and implications for amino acid racemization: *Icarus*, vol. 145(2), p.369-381.

Furukawa, Y., Samejima, T., Nakazawa, H., and Kakegawa, T., 2014, Experimental investigation of reduced volatile formation by high-temperature interactions among meteorite constituent materials, water, and nitrogen: *Icarus*, vol. 231, p. 77-82.

Hauri, E. H., Saal, A. E., Rutherford, M. J., and Van Orman, J. A., 2015, Water in the Moon's interior: Truth and consequences. *Earth and Planetary Science Letters*, vol. 409, p. 252-264.

Pendleton, Y., 2015. Water on the Moon: *IAU General Assembly*, vol. 22, p. 54,184.

Rampe, E. B., Morris, R. V., Bish, D. L., Vaniman, D. T., Bristow, T., Chipera, S., Blake, D. F., Ming, D. W., Farmer, J., Morrison, S. M. and Treiman, A. H., 2014, Mineralogy of

Fluvio-Lacustrine Sediments Investigated by Curiosity during the Prime Mission: Implications for Diagenesis: *AGU Fall Meeting Abstracts*, vol. 1, p. 4.

Robinson, K. L. and Taylor, G. J., 2014, Heterogeneous distribution of water in the Moon: *Nature Geoscience*, vol. 7, p. 401-408.

Saal, A. E., Hauri, E. H., Cascio, M. L., Van Orman, J. A., Rutherford, M. C., and Cooper, R. F., 2008, Volatile content of lunar volcanic glasses and the presence of water in the Moon's interior. *Nature*, vol. 454(7201), p. 192-195.

Spector, A. and Grant, F. S., 1970, Statistical models for interpreting aeromagnetic data: *Geophysics*, vol. 35, no .2, p. 293-302.

Squyres, S. W., Aharonson, O., Clark, B. C., Cohen, B. A., Crumpler, L., De Souza, P. A., Farrand, W. H., Gellert, R., Grant, J., Grotzinger, J. P., Haldemann, A. F. C., Johnson, J. R., Klingelhofer, G., Lewis, K. W., Li, R., McCoy, T., McEwen, A. S., McSween, H. Y., Ming, D. W., Moore, J. M., Morris, R. V., Parker, T. J., Rice, J. W., Ruff, S., Schmidt, M., Schroder, C.,Soderblom, L. A., and Yen, A., 2007, Pyroclastic activity at Home Plate in Gusev Crater, Mars: *Science*, vol. 316, no. 5,825, p. 738-742.

Weber, R. C., Lin, P. Y., Garnero, E. J., Williams, Q., and Lognonné, P., 2011, Seismic detection of the lunar core: *Science*, vol. 331, p.309-312.

Williams, J. G., Boggs, D. H., Yoder, C. F., Ratcliff, J. T. and Dickey, J. O., 2001, Lunar rotational dissipation in solid body and molten core: *Journal of Geophysical Research*, vol. 106 (E11), p.27933-27968.

Wieczorek, M. A., Jolliff, B. L., Khan, A., Pritchard, M. E., Weiss, B. P., Williams, J. G., Hood, L. L., Righter, K., Neal, C. R., Shearer, C. K., and McCallum, I. S., 2006, The

constitution and structure of the lunar interior: *Reviews in mineralogy and geochemistry*, vol. 60, no. 1, p.221-364.

Zuber, M. T., Smith, D. E., Watkins, M. M., Asmar, S. W., Konopliv, A. S., Lemoine, F. G., Melosh, H.J., Neumann, G.A., Phillips, R.J., Solomon, S.C., Wieczorek, M.A., Williams, J.G., Goossens S. J., Kruizinga, G., Mazarico, E., Park, R. S., and Yuan, D. N., 2013, Gravity field of the Moon from the Gravity Recovery and Interior Laboratory (GRAIL) mission: *Science*, vol. 339, no. 6,120, p. 668-671.

Chapter 2: Gravity and Magnetic Surveys at Kilbourne Hole, Southern New Mexico: Implications for Near Surface Geophysical Exploration of Home Plate on Mars

[1] Nisa Maksim, [2] José M. Hurtado, Jr, and [3] Diane I. Doser

The University of Texas at El Paso, 500 West University Avenue, El Paso, TX 79662

[1] nrhodes@miners.utep,edu, [2] jhurtado@utep.edu, [3] doser@utep.edu

Abstract

Features such as the Home Plate plateau on Mars, a suspected remnant of an ancient phreatomagmatic eruption, can reveal important information about paleohydrologic conditions. The eruption intensity of a phreatomagmatic volcano is controlled mainly by the quantity of water and magma, the internal geometry of the volcano, and the depth of the interaction zone between magma and water. In order to understand the paleohydrologic conditions at the time of eruption, we must understand all the factors that influenced the phreatomagmatic event. We mapped the internal structure of a well-known phreatomagmatic volcano, Kilbourne Hole in southern New Mexico, in order to quantify the mass of the dike (m_m) and volume of the diatreme (V_{dia}), the depth of the magma source (h), the mass of pyroclastic material (m_f), and the volume of excavated crater (V_{exc}) of the Kilbourne Hole structure. We then calculated the amount of groundwater that fed the volcanic system using these quantities (h, m_m, m_f, V_{exc}, V_{dia}). A phreatomagmatic volcano produces very explosive eruptions and a very deep volcanic structure rooted into the pre-eruptive rock formation. The juxtaposition between volcanic structures and the pre-eruptive rock formation make gravity and magnetic surveys an appropriate method for this purpose. To quantitatively estimate the masses and volumes of Kilbourne Hole phreatomagmatic deposits, we must quantitatively define the geometry of all the units of

Kilbourne Hole phreatomagmatic deposits; we performed a 2D inversion modeling from both of our gravity and magnetic surveys at Kilbourne Hole. Inverse modeling of the gravity and magnetic data reveals three basaltic dikes beneath Kilbourne Hole. The depth below the pre-eruption ground surface to the top of the dikes varies: dike 1, on the eastern rim of the crater, is 1.75-2.25 km deep; dike 2, beneath the center of the crater, is 0.91-3.58 km deep; and dike 3, beneath the western rim of the crater, is 0.14-2.50 km deep. The inverse models are also able to delineate several complex areas of slump and rotated blocks associated with crater collapse, the diatreme, and post-eruption fill units within the crater. The estimated total depth to the bottom of the diatreme is 13.6-15.8 km from the pre-eruption surface. The tuff ring deposit around the crater extends 600 m to 1 km away from the crater rim and our inverse model shows that it varies in thickness between 50 and 150 m. Based on the geophysical models we have developed for Kilbourne Hole, we estimate the mass of the magma (m_m) related to the Kilbourne Hole eruption to be (1.38 ± 0.15) x 10^{13} kg and the mass of water (m_w) to be (1.09 ± 0.31) x 10^{13} kg, for a water-to-magma mass ratio of 0.79 ± 0.23.

Keywords: phreatomagmatic volcano, gravity, magnetics, Kilbourne Hole, planetary geophysics, groundwater, paleohydrology, tilt angle derivative, 2D inversion, Mesilla basin, Rio Grande rift

1. Introduction

Phreatomagmatic eruptions occur when groundwater comes in contact with magma in the subsurface. The heated water will flash into steam, which, if confined, will build up pressure, potentially to the point of explosive release. The resulting explosion will excavate a crater and eject pyroclastic material (Wohletz and Sherridan, 1981). The efficiency of resulting explosion is determined by the ratio between the mass of water to the mass of magma that fed the eruption system (Wohletz, 1986). The size and volume of pyroclastic deposits from a phreatomagmatic eruption is a function of the amount of groundwater in proportion to the amount magma. The study of the internal structure of a phreatomagmatic volcano can lead us to an understanding of the amount of groundwater present prior to the eruption. By quantifying the volume of the pyroclastic deposit from a phreatomagmatic eruption, we can also quantifying the amount of groundwater interacted with the magma source at the time of eruption. This chapter focuses on the results of our ground-based gravity and magnetic study at a well-known phreatomagmatic volcano – Kilbourne Hole in New Mexico – designed specifically to decipher the paleohydrogeological conditions at the time of eruption. The present geological setting of Kilbourne Hole is similar to Martian volcanic terrain. The surface of Kilbourne Hole is covered with 50 -150 m thick of tuff ring and pyroclastic deposit. Underlain the pyroclastic deposit is the Aden and Afton basalt flow layer. The techniques used in this research can serve as an analog for ground based gravity and magnetic surveys that can be applied to paleohydrologic exploration of other planets such as Mars. The main implications of this combined application for the exploration of Mars are: (1) our field survey methods; (2) the methodology used to process the gravity and magnetic data to reveal the internal structure of Kilbourne Hole, specifically to allow us to map the extent and volume of ejected pyroclastic material and the size and shape of the

magma body that triggered the eruption; and (3) an estimate for the amount of groundwater present at the time of the Kilbourne Hole explosion.

Both magnetic and gravity surveys are non-invasive, portable and easy to process. They are also passive methods that do not need probe, electrode or any energy to be inserted into the ground in order to acquire data; this makes the magnetic and gravity method operable by a rover and is suitable for a remote setting such as Mars or the Moon. Here we provided a design of gravity and magnetic surveys that were used specifically to delineate all shapes and sizes of the internal features of a phreatomagmatic volcano. We also provided an adaptation of an integrated 2D modeling of gravity and magnetic data to quantitatively interpret and map the internal features of a phreatomagmatic volcano. The internal structures of phreatomagmatic volcanoes are very complex. The eruptions of phreatomagmatic volcanoes are catastrophic and chaotic; following the mass removal process is the caldera-like collapsing of the crater, resulting in several fault zones and rotated fault blocks that overlap and superimpose upon one another with no extinctive bedding. This makes it very difficult to extract and delineate geo-anomaly signals of this kind of landform. The gravitational anomaly from this complex feature of the phreatomagmatic crater may not be differentiated under the traditional assumption and interpretation. Therefor in addition to traditional gravity anomaly interpretations and 2D modeling, we apply a nonlinear method called a tilt-derivative method to our gravity and magnetic data (Miller and Singh, 1994) to define edges and geometry of the buried pyroclastic formation. The result of integrated 2D modeling of gravity and magnetic data can successfully resolves complex structures of a phreatomagmatic eruption at Kilbourne Hole including: 1) excavation zone due to the mass removal process of eruption, 2) rotated blocks of pre-eruptive rocks buried inside the vent due to is the collapsing of the crater, 3) several fault zones created

by the collapsing of the crater, 4) dikes, 5) diatreme or the brecciated rocks that filled in the volcanic vent, and 6) surrounding tiff ring. We demonstrated in this chapter the conduction of our field surveys and the steps we used to extract gravity and magnetic anomalies that reveal the internal structures of Kilbourne Hole. Lastly, we then demonstrate how we determine the eruption efficiency and the relationship between the mass of magma and the mass of water that fed the eruption and how to quantifiably interpret the related groundwater that caused the phreatomagmatic eruption of Kilbourne Hole. While GPR (Chapter 3) will be used to map the shallow subsurface structures of volcanic blocks and sags, gravity and magnetic surveys (Chapter 2) provided diagnostic information about the deeper subsurface lithology, shape, and structures of the diatreme, deep intrusion zones, and its regional geology.

2. Study Location

Kilbourne Hole is a well-known phreatomagmatic volcanic crater located in Southern Doña Ana County, New Mexico, in the Mesilla basin at the southwest margin of the Rio Grande rift (Figure 1). This maar crater is a 2-km wide, 200-m deep depression (Reiche, 1940). The Kilbourne Hole eruption occurred during the mid-Pleistocene (0.02-0.1 Ma; Seager, 1984). Seager (1984) and Lorenz (1973) suggested that the excavation of Kilbourne Hole was caused by catastrophic subsidence, similar to caldera collapse, following phreatomagmatic explosive activity.

The Rio Grande rift and the series of basins related to it are major tectonic features of the North American continent that extends from Colorado, through New Mexico, and into northern Chihuahua, Mexico, covering a distance of about 950 km (Ramberg et al., 1978; Keller et al., 1990). The extension that formed the Rio Grande rift, and the associated volcanism, began about 30 million years ago (Ingersoll, 2001) and still continues today (Keller et al., 1990). Volcanic activity has occurred throughout the Rio Grande rift (Lipman, 1969). During the Pliocene to Quaternary, volcanic activity in the Rio Grande Rift mostly erupted alkali-olivine basalt and, in some localities, tholeiitic basalts (Keller et al., 1990). This variation in composition indicates that magmas have been derived from various depths, with tholeiitic basalts originating at shallower depths than alkalic basalts (Lipman, 1969).

The Mesilla Basin is bound on the east by the Organ, Franklin, and Sierra de Juarez mountains, and on the west by fault-block and volcanic uplands that extend northward from the East Potrillo Mountains and West Potrillo basalt field to the Aden and Sleeping Lady Hills (Figure 2). Prior to the Kilbourne Hole eruption, there were already series of volcanic flows in the vicinity of Kilbourne Hole (Seager, 1984). This volcanic flow series is called the Potrillo

volcanic field. The central area of the Potrillo volcanic field is covered by a series of three to five lava flows that erupted from Aden and Afton craters (Hoffer, 1972). Below the Afton-Aden basalt flows is the Late Quaternary (2-3 Ma) Santa Fe group (Figure 2). The Santa Fe group is a 1.5-2-km thick package of fluvial sediments deposited by the ancestral Rio Grande River (Seager, 1984). There are two parts of the Santa Fe group. The younger unit is the Camp Rice Formation, which contains fluvial and piedmont sediments (Lorenz, 1986). The older unit is the Fort Hancock formation, which contains alluvial sediments (Hawley, 1975).

The Kilbourne Hole explosion excavated through both the Santa Fe group and the overlying Afton-Aden basalt flows. Both pre-eruptive units can be seen exposed inside Kilbourne Hole. The Kilbourne Hole explosion deposited 50-150 m of air-fall and pyroclastic surge deposits around the crater rim (Lorenz, 1986). Pieces of alkali olivine can be found within the pyroclastic deposits, indicating that there was a basaltic intrusion located underneath Kilbourne Hole (Hoffer, 1972; Hawley, 1975). The pyroclastic deposits can be traced 800-1000 m radially away from the modern crater rim (Seager, 1987). There are two sets of pyroclastic layers: one that was deposited as a tuff ring around the crater rim, and one that has collapsed into the crater (Figure 3). The dips of both sets of pyroclastic strata range from 8° to 35° (Seager, 1987). After the Kilbourne Hole eruption, aeolian and fluvial sediments were deposited throughout the area, including the interior of Kilboune hole, and these deposits mantle all of the older units (Figure 3).

3. Background

3.1 Hydrology and Physics of Phreatomagmatic Eruptions

A phreatomagmatic eruption is a kind of volcanic eruption caused by the explosive interaction between rising magmas and external sources of water, such as an aquifer or surface water (Wilson and Head III, 2003). The resulting eruptive phenomena include pyroclastic flows, debris flows, air fall tephra, and the ejection of volcanic blocks (Barberi et al., 1989). Landforms produced by phreatomagmatic eruptions include an excavated crater, called a maar, and the surrounding tuff ring or cone (White and Ross, 2011).

The relationship between the amount of water and the resulting explosive eruption was established by Wohletz and Sheridan (1981) based on a comparative study of the geomorphology and stratigraphy of eleven basaltic phreatomagmatic volcanoes. A tuff ring (pyroclastic deposit with 0°-10° dips) is formed from an explosion at a shallower depth than a tuff cone (pyroclastic deposit with 10°-25° dips). Wetter eruptions can result in larger diameter tuff rings and tuff cones (Wohletz and Sheridan, 1981). Based on their observations, Wohletz and Sheridan (1981) suggested that fluid-dynamic interactions between groundwater and the melt could affect the strength of the resulting explosion. The existence of fluid in the eruption process forms a large crater and creates a remarkably high-volume of ejecta, including pumice, ash flows, and airfall (Wilson and Head, 1994).

Most of the empirical research to quantify water-magma interactions has been done by Wohletz and Sheridan (1981; 1982; 1983; 1989) using a water tank and thermite to simulate the groundwater reservoir and magma, respectively. These experiments have investigated the

parameters that describe the characteristics of phreatomagmatic eruptions. We highlighted which parameters we could obtain using gravity and magnetic methods.

When magma contacts groundwater, a large amount of heat is exchanged between the magma and the water. Water's high specific heat index effectively converts thermal energy into mechanical energy (Self and Sparks, 1978). In a phreatomagmatic explosion, typically only a small percentage (<10%) of the magmatic heat is converted to explosive energy, most likely because the magma and water do not mix well (Wohletz, 1986).

The process of magmatic heat exchange of a phreatomagmatic eruption can be explained using thermodynamics of an open system (Wohletz, 1986). An open system in thermodynamic is when there is an exchange of energy (heat and work) between the system and their environment. A boundary allowing energy exchange between the system and their environment must be permeable. To explain the eruption process of Kilbourne Hole using thermodynamics, we make these following assumption: (1) the system of a phreatomagmatic eruption is where the crater were excavated. The volume of the system (V_{sys}) is equivalent to the volume of fragments and water vapor that were ejected from the crater (V_{exc}), (2) the permeable environment that allows heat to transfer to the system is the crater vent filling sediment that lies between the magma (dikes) and the system. The volume of the permeable environment is equivalent to the volume of Kilbourne Hole's vent excluding the volume of the dike or the volume of the diatreme (V_{dia}).

Another parameter used in thermodynamics to explain the phreatomagmatic eruption is thermal efficiency. The thermal efficiency of an eruption indicates how much heat is converted to energy output. The efficiency of the eruption can be quantified by the conversion rate (CR) between the change in thermal energy (ΔU) and the change in work done to the system (ΔW_{sys}) (Wohletz, 1986).

$$CR = \frac{\Delta W_{sys}}{\Delta U} = \frac{\Delta W_{exc}}{\Delta U} \quad (1),$$

where ΔU is the change in magmatic thermal energy and ΔW_{sys} is the change in work done to the system. ΔW_{exc} is the change in work done to the excavation zone of the volcano.

The change in thermal energy is result of heat exchange between the magma and pore water. The amount of change depends on the mass of magma, heat capacity of magma, and the associated temperatures. A mass of basaltic magma, m_m, at an absolute temperature (T_m) of 1493 K (Wohletz, 1986) comes in contact with a mass of external water, m_w, at an absolute temperature (T_w) of 298 K. The amount of change in thermal energy from the magma intrusion at Kilbourne Hole is (Wohletz, 1986):

$$\Delta U = m_m C_{vm}(T_m - T_e) \quad (2).$$

where m_m is the mass of magma, C_{vm} is the specific heat of the magma at constant volume (C_{vm} = 1 kJ kg^{-1} K^{-1}; Wohletz, 1986); and T_e *is* the ideal equilibrium temperature (298 K; average Earth surface temperature).

In the first stage of the eruption, magmatic thermal energy is converted into the change in work done to the system. The total energy in the system is partitioned between the change in kinetic energy of the excavated fragments and released water vapor (ΔKE), the potential energy of the excavated fragments and released water vapor ($p_0 V_{exc}$), and the change in potential energy inside the diatreme (ΔPE_{dia}) (Wohletz, 1986).

The total energy in the eruption system (Δ_{excs}) is:

$$\Delta Wsys = \Delta \mathrm{KE} + \Delta PE_{dia} + p_o \Delta V_{exc} \quad (3),$$

where ΔKE is the change in kinetic energy of the excavated fragments and released water vapor, ΔPE_{dia} the change in potential energy inside the diatreme, and $p_0 V_{exc}$ is the potential energy of the excavated fragments and released water vapor.

In the second stage of the eruption, the system expands isentropically into atmosphere (Wohletz, 1986). The change in kinetic energy of the excavated volcanic fragments and released water vapor is equal to:

$$\Delta KE = \frac{1}{2}(m_f + m_w)\, v_{max}^2 \qquad (4),$$

where v_{max} is the maximum velocity of the excavated fragments and released water vapor, and m_w and m_f are the masses of water and volcanic fragments, respectively, that are released from the eruption. The mass of water is unknown, and it is the goal of this research to estimate it. The mass of the volcanic fragments can be estimated using gravity and magnetic data as we show in this paper. Similarly, v_{max} can be derived from geophysical data, specifically by measuring the clast size distribution of ejected volcanic blocks using ground-penetrating radar (GPR) (Rhodes and Hurtado, 2014; v_{max} = 113.46-132.21 m/s; see Chapter 3).

Prior to the expansion of volcanic gas, the diatreme were under a litho-static pressure that is equal to the weight of the material above the interaction zone between water vapor and magma source. The confined pore water inside the diatreme was heated by magma intrusions. Explosive eruptions are thought to initiate when: (1) magma comes in contact with external water; and 2) pore fluid pressure overcomes the tensile strength of the rock above the dikes (Spieler et al., 2004; Mueller et al., 2008). The pore fluids can develop super-pressured condition when permeability inside the diatreme increases rapidly (Rubey and Hubbert, 1959a). The increasing of permeability inside the diatreme can be a result from hydrofracturing or explosive brecciation

of the rocks, or fault ruptures (Rubey and Hubbert, 1959a). We are not certain whether the eruption of Kilbourne Hole ever developed a super-pressured condition or not. From our mode, there are several faults found at the location of Kilbourne Hole. Although with the extension mechanism along the edge of Rio Grande Basin those faults zone is the pre-existing rifting and faulting, not involving with super-pressured condition.

Day (1996) confirmed that the reduction in strength of volcanic materials is due to the effect of high pore pressure relative to confining pressure. This can be expressed as the ratio, λ, of the pore pressure to the confining pressure. In a phreatic eruption, pore fluid pressure is equal to litho-static pressure (λ = 1). If the eruption occurs in super-pressured conditions, in which fluid pressure is sufficient to cause tensile failure of rock, then λ >1. Pore pressure as a fraction of litho-static load in super-pressured condition is:

$$\lambda = 1 + \frac{\tau_o}{p_1} \qquad (5),$$

where p_1 is the litho-static load pressure at the depth of rupture, and τ_o is the cohesive strength of rock or the cohesive strength of a pre-existing fracture (generally very small or zero). We can calculate the litho-static load pressure at the depth of rupture using the information derived from our model which are the density of rocks that are the litho-static load, the cross-sectional area of the excavation. Our model is able to reveal the location and the depth where magma interacted with the litho-static load. The eruption of Kilbourne Hole occurred when the pore pressure inside the diatreme became equal to the litho-static load pressure. We can calculate the litho-static load pressure (p_1) inside the diatreme of Kilbourne Hole as follows (Athy, 1930):

$$p_1 = \rho g h \qquad (6),$$

assuming that gravitational acceleration (g) is a constant with depth (h) and where ρ is the density of the overlying rock at depth h. Our integrated gravity and magnetic models of Kilbourne Hole can be used to reveal the depth of the litho-static load. The density of the litho-static load should be a weighted average density of all geological material included in the litho-static load. The litho-static load at Kilbourne Hole: (1) Camp Rice formation with a density of ~2560 kg/m^3; and (2) Aden basalt with a density of ~3100 kg/m^3.

Immediately before the eruption, prior the brecciating of the diatreme and the rupture of the volcanic system, the potential energy was being stored inside the diatreme in the form of increasing pore pressure. The change in potential energy, ΔPE_{dia}, of the Kilbourne Hole's diatreme, the releasing of potential energy initiate and sustain the fragmentation process, is provided by the expansion of the pressurized gas trapped in the pore space of the diatreme material. ΔPE_{dia} can be written as:

$$\Delta PE_{dia} = p_1 V_{dia} \qquad (7),$$

where V_{dia} is the volume of the diatreme (Wohletz, 1986). Because this pressure increases with depth, the depth at which the magma and groundwater interact is an important control on the litho-static pressure and on the resulting power of the eruption.

The third term of Equation (2) ($p_o \Delta V_{exc}$) is the result of the change in the volume of the system after rock fragments and water vapors were excavated at the time of the eruption, where p_o is the pressure of the system at the final stage of eruption and V_{exc} is the change of the volume in the volcanic system. To estimate the final-stage pressure of the eruption, we assume that towards the latter stages of eruption the pressure of the system was close to atmospheric pressure at the time prior the eruption. The atmospheric pressure is 0.89 bars at 1.22 km elevation above

the sea level, the estimated elevation of the pre-eruption surface (the top of the Aden basalt) (NOAA, 1976). We use 0.89 bars as the final stage pressure (p_o) for the Kilbourne Hole eruption. The results of our gravity and magnetic models of Kilbourne Hole can be used to determine V_{exc}. We define V_{exc} to be the sum of: (1) the volume of the unfilled crater; and (2) the volume of the alluvium inside the crater.

By substituting Equations (2)-(7) into Equation (1) we obtain:

$$CR = \frac{\frac{1}{2}(m_f + m_w)v_{max}^2 + p_1 V_{dia} + p_0 V_{exc}}{(M_m C_{vm}(T_e - T_m)} \quad (8).$$

This can be rearranged to solve for the mass of groundwater (m_w):

$$m_w = \frac{2\,(CR.m_m C_{vm}(T_m - T_e) - p_1 V_{dia} - p_0 V_{exc})}{v_{max}^2} - m_f \quad (9).$$

In order to determine the mass of groundwater using Equation (9), we must define the mass of the melt (m_m), the volume of excavated fragments (V_{exc}), the total volume of the diatreme (V_{dia}), and the maximum ejection velocity of volcanic blocks (v_{max}). In this paper, we describe how to determine the masses and volumes using magnetic and gravity surveys. In Chapter 4, we describe how to determine v_{max} using ground-penetrating radar (GPR).

3.2 Eruptions Efficiency and Gas to Magma Mass Ratio

The explosive energy of an eruption can be expressed in terms of eruption efficiency, which is quantified as the ratio of thermal energy to mechanical energy (Wohletz, 1983). The mechanical energy results from the flash vaporization of water due to rapid superheating (Wohletz, 1983). The mechanical energy is then partitioned among fragmentation energy,

kinetic energy, seismic energy, and acoustic energy. The efficiency of this eruption process is dominantly a function of the mass of the melt, the mass of the water, and the confining pressure in the zone where the melt and water interact (Wohletz, 1983). Thermal energy results from the heat transfer between magma and liquid water. The thermal energy is proportional to the heat capacity of liquid water, mass of water that was in contact to the magma body, and the temperature difference between liquid water and magma (Wohletz, 1983).

Sheridan and Wohletz (1981) outlined the factors that control the energy of phreatomagmatic eruptions using the results of prior observation (Fuller, 1931; Jaggar (1949; Wohletz, 1983) of the 1924 eruption of Kilauea Volcano on several individual fall and surge and sand wave beds. Figure 2 plots eruption efficiency versus water-to-melt mass ratio as determined from experimental and field studies (i.e., Wohletz and McQueen, 1981; Wohletz and Sheridan, 1982). The curve in Figure 2 can be subdivided into regions: Strombolian activity (mass ratio of 0 to 0.1); Surtseyan activity (mass ratio of 0.1 to 1.00); and submarine extrusion of pillow basalts (mass ratio >3.00). Phreatomagmatic water vapor explosions occur at mass ratios near 0.1 and reach a maximum mass ratio near 0.3 (Wohletz and Sheridan, 1982). A mass ratio of 1.0 produces pyroclastic surges of dry, superheated steam that deposit dune or sandwave beds (Wohletz and Sheridan, 1982). Ratios above 1.0 result in wet, condensed steam eruptions that deposit massive pyroclastic surge and flow beds (Wohletz and Sheridan, 1982). Such deposits commonly are associated with accretionary lapilli, lahars, and soft-sediment deformation (Wohletz and Sheridan, 1982).

The kinetic energy of an eruption is in the form of pyroclastic material moving away from the vent. At the moment of eruption, the potential energy associated with the accumulated gas pressure is converted to kinetic energy (E_k) (Zimanowski et al., 1995):

$$E_k = \frac{1}{2}(M_f + M_w)V_0^2 \qquad (5),$$

where M_f is the mass of pyroclastic fragments and M_w is the mass of water. By knowing the kinetic energy, the maximum velocity of the gas (water vapor) and the pyroclastic fragments, and the mass of pyroclastic fragments, we can solve for the mass of water in the system.

4. Methodology

4.1 Magnetic and Gravity Surveys

A magnetic survey was performed during March 2011 and May 2011 to map the subsurface magnetic anomalies within and around Kilbourne Hole. A single-sensor G858 cesium-vapor magnetometer was used to make measurements at a total of 166 stations arranged in a grid with a 200-m grid spacing that covers the entire crater (Figure 4). All the measurements were tied to three base stations that were set up along the three corners of the crater (Figure 4). The magnetic base stations were reoccupied every 2-3 hours during the survey and at the beginning and at the end of each survey day.

A gravity survey was performed at Kilbourne Hole during June 2013 and November 2014. A Lacoste and Romberg G30 gravimeter was used to make a total of 172 gravity measurements at the same stations where the magnetic measurements were made, along with an additional 6 measurements. Precise elevations for each gravity station were measured using a Topcon GB-1000 real-time kinematic (RTK) differential GPS unit. The RTK surveys provided a horizontal accuracy of ±10 mm and a vertical accuracy of ±15 mm. All the gravity measurements were tied to same three base station locations used for the magnetic survey (Figure 4) and to the absolute gravity geospatial base station located at John W. Kidd Memorial Seismological Observatory at The University of Texas at El Paso (http://www.gis.utep.edu/subpages/states/documents/Texas/DESC.EL_PASO_A.pdf). The gravity base stations were reoccupied every 2-3 hours during the survey and at the beginning and at the end of each survey day.

4.2 Gravity and Magnetic Data Corrections

Prior to modeling, magnetic data must be processed and corrected for diurnal geomagnetic field fluctuations, the magnetic field background at the latitude of the survey, the polarization of rock formations in the area, and noise sources such as thunderstorms or electrical wires. Kilbourne Hole is far away from cultural noise, and Kilbourne Hole is relatively young to have been effected by magnetic field reversal or polarization of the magnetic field in the rock. Therefore we only corrected our magnetic data for the diurnal geomagnetic field fluctuations and the magnetic background at the latitude of Kilbourne Hole. The diurnal correction is done by comparing the location and time of each magnetic measurement to measurements taken at a base station. To correct for magnetic background, we use the total magnetic field intensity from the International Geomagnetic Reference Field as adopted by the International Association of Geomagnetism and Aeronomy (Finlay et al., 2010). In addition to these corrections, we also performed a reduction-to-pole operation to recalculate the total magnetic intensity data as if the inducing magnetic field had a 90^{o} inclination (Bankey et al., 2002). This transforms dipole magnetic anomalies to monopole anomalies centered over their causative bodies, which can simplify the interpretation of the data. Our reduction-to-pole magnetic data and its coordinates are included in Appendix A.

For the raw gravity data collected from Kilbourne Hole, we followed the correction process described in Briesacher at el. (2002) to make our field data compatible with the regional southwestern North American gravity data in the GEONET database (Hildrenbrand et al. (2002); Appendix B). Terrain corrections were calculated using a digital elevation model and a technique implemented in *Geosoft 7.0* (Nagy, 1966). We used the digital elevation model Kilbourne Hole 32106a6 with a resolution of 1/3 arc second (~10 m). Latitude and longitude

values are referenced to NAD27 (North American Datum 27) and elevation values are referenced to the NGVD88 geodetic vertical datum (USGS, 2009). The weight of the atmosphere can affect the gravity measurements, and, because of this, we also performed an atmospheric correction to our gravity data. The correction varies from 0.87 mGal at the ellipsoid to 0 mGal at about 34 km above the ellipsoid (Moritz, 1980).

After we performed the terrain and atmospheric corrections to our gravity data, we performed the free-air and Bouguer corrections. To correct for the decrease in gravity with height above the ellipsoid, we employed a free-air correction with a second order height correction (Heiskanen and Moritz, 1969; Li and Gotze, 2001). To correct for the gravitational attraction of the mass between each station, we performed the Bouguer correction. Because of the small size of our survey area (~10 km^2) we employed a horizontal infinite slab Bouguer correction instead of a spherical cap correction. Our Bouguer correction uses the following constants (Mohr and Taylor, 2001): spherical Earth radius of 6371 km; crustal density of 2,670 kg/m^3; and Newtonian gravitational constant of $(6.673 \pm 0.01) \times 10^{-11} m^3\ kg^{-1}\ s^{-2}$. Our corrected gravity data and its coordinates are included in Appendix B

4.3 Tilt Angle Derivatives and Edge Detection

After the correction of gravity and magnetic data, we can then plot gravity and magnetic anomaly maps (Figure 4). Based on the gravity and magnetic anomaly maps of Kilbourne Hole, we can make qualitative interpretations about subsurface features that may being contributing to the high and low value anomalies present in the maps. To acquire quantitative interpretation of both gravity and magnetic anomalies using the inverse modeling method, it would be beneficial

to have had *a priori* knowledge about the dimension of a source that contributed to the anomaly (Paterson and Reeves, 1985). In this research we used the inverse modeling method to quantitatively interpret our gravity and magnetic anomaly maps of Kilbourne Hole.

Euler deconvolution is a computational process used in the inversion method. It was first presented by Thompson (1982) and is widely used to interpret magnetic and gravity data. The main advantage of Euler deconvolution in inversion modeling is that it can provide an estimated location and shape for source bodies. The disadvantage of the Euler deconvolution for inverse modeling is that it requires an assumption to be made about the geological properties of the model bodies. Another disadvantage is that the result of Euler deconvolution can be non-unique and must be constrained with *a priori* data. We can constrain our inverse models using known ranges of rock density and magnetic susceptibility, and the size, depth, or geometry of the geological features. However, even with a well-constrained model, non-uniqueness is still a problem.

In addition to inverse modeling using Euler deconvolution, we also use the tilt-angle derivative technique to define the shape and edges of the gravity or magnetic anomaly (Miller and Singh, 1994; Verduzco et al., 2004). The tilt angle derivative of a magnetic or gravity source can define the edge of the anomaly in a way that is relatively insensitive to the depth of the source and, as a result, it can resolve shallow and deep sources equally well (Miller and Singh, 1994). Our gravity and magnetic anomaly map of Kilbourne Hole contains sources from both shallow and deep sources. To resolve for both shallow and deep sources and to constrain our model with known geometry, we use the tilt angle method (Miller and Singh, 1994).

This tilt-angle derivative method yields an estimated location of the anomaly and geometry of the source without any *a priori* data. The example given here is for the case of a

magnetic field anomaly, the tilt angle derivative in the vertical direction is (Miller and Singh, 1994):

$$\theta = \tan^{-1}\left[\frac{\frac{\partial M}{\partial z}}{\frac{\partial M}{\partial h}}\right] \qquad (10),$$

where:

$$\partial M/\partial h = \sqrt{\left(\frac{\partial M}{\partial x}\right)^2 + \left(\frac{\partial M}{\partial y}\right)^2} \qquad (11),$$

And $\partial M/\partial x$ and $\partial M/\partial y$ and $\partial M/\partial z$ are the first-order derivatives of the magnetic field *M* in the *x*, *y* (x and y are map coordinates expressed in terms of horizontal distance) and *z* (z is the depth of the signal expressed in terms of wave number). Equation (10) expresses a tilt angle derivative in term of radians and the value of the tilt angle derivative always will be between $-\pi/2$ and $\pi/2$. To implement tilt angle derivative method and compute the tilt derivative from our gravity and magnetic data, we used the tilt-angle derivative function (`tiltdrv.gx`) implemented in *Geosoft Oasis Montaj 6.2*. The tilt angle derivative equation for the gravity field is similar to the tilt angle derivative equation for the magnetic field; only the main variable would be ∂G (gravity field) instead on of ∂M (magnetic field).

The tilt angle method can also enhance deep anomalies by adjusting the anomalies with the ratio of the vertical derivative of gravity or magnetic anomaly to the horizontal derivative of gravity or magnetic anomaly (Miller and Singh, 1994). If the gravity or magnetic source is deep, the vertical derivative will be positive, resulting in a positive tilt angle (Miller and Singh, 1994). If the gravity or magnetic source is shallow, the vertical derivative will be negative, resulting in a negative tilt angle (Miller and Singh, 1994). At the edge of a gravity or magnetic anomaly, there is no change in the horizontal derivative, resulting in a tilt angle of zero. With the tilt angle

derivative method in Figure 5, we can then enhance the area of the gravity and magnetic anomaly from the deeper layers, and we can also identify the edge of the anomaly. Knowing the edge of the anomaly can provide us geometry of the geological features that can constrain our inversion model.

4.4 Two-Dimensional Joint Inverse Model of Gravity and Magnetic data from Kilbourne Hole

The traditional geophysical inverse model was formulated for one single data set by Goltsman (1982) and Tarantola (1987). Most geophysical inverse problems have to deal with uncertain information in the observed data and *a priori* knowledge. By jointly making interpretation from two sets of data, we can limit those uncertainties. The joint inverse model uses integrated multimethod geophysical data to yield the solution of geophysical inverse problems. The traditional way of performing joint interpretation of magnetic and gravity data is based on a laboratory empirical correlation between rock density and rock magnetic susceptibility (Hrouda, 1982; Bosch and McGaughey, 2001). In order to determine the internal structure of Kilbourne Hole, a joint inversion of the magnetic and gravity survey data was done using *Geosoft Oasis Montaj-GM-SYS* software. *Oasis Montaj* provides an automated workflow for determining the position (distance and depth), dip, density, and magnetic susceptibility of geological bodies for given magnetic and gravity profiles. To obtain the result, the software implemented with three mathematical approaches: Werner deconvolution; analytic signal deconvolution; and extended Euler deconvolution (Mushayandebvu el al., 2001). To perform joint gravity and magnetic inverse model, we imported together both data components into the same conceptual model. We then build several model bodies representing geological units in the

field and assign to them initial widths, thicknesses, densities, and magnetic susceptibilities. The software algorithms iteratively calculated the shape of the model body that could yield similar anomaly to the observed anomaly. The quantitative result from the joint inversion method still however carried the uncertainty. Additional geological knowledge is required to reduce this ambiguity and to provide the uniqueness of the model solution. The additional geological information we used to constrain our model includes:

1) Topography. We used the SDTS digital elevation model with 1/3 arcsecond (~10 m/pixel) resolution (USGS, 2009) to constrain the surface topography;
2) Surface Geology. Geologic mapping of Kilbourne Hole was completed in November 2014 (Figure 3). All our field measurements (e.g., rock formation thickness, strike and dip angle) are included in our model. There are a total of 8 units included in our model (see Table 1).
3) Magnetic susceptibility. We assigned magnetic susceptibilities to each rock unit using values derived from the empirical work of other researchers (Gubbins and Herrero-Bervera, 2007; Shearer, 2005; Hunt et al., 1995; Gidley and Stuart,1980) and our own *in situ* magnetic susceptibility measurements made using a SM-30 magnetic susceptibility field meter (see Table 1.).
4) Density. The densities used in the model are based on Dorren and Seijmonspergen (2003) and Tenzer et al. (2011) (see Table 1).
5) The spatial distribution of the geological bodies. We developed a Tilt angle derivative (TDV) map of the gravity data and a TDV map of the magnetic data from Kilbourne hole. The TDV map defines the edges of the anomaly providing their estimated locations and horizontal dimensions.

4.5 Volumes and Mass Estimation

The joint inversion model provides us the spatial location of geologic bodies inside Kilbourne Hole such as pyroclastic units, crater, the diatreme and the dike. We developed a MATLAB code (Appendix C) to calculate the volume of subsurface geologic bodies and the total volume of excavation.

Our joint inversion model yields two-dimensional, cross-sectional views of the internal structure of Kilbourne Hole. The volumes of the various geologic bodies can be estimated from these cross-sectional views. To do this, the cross-sectional shapes of the bodies of interest are exported in `.csv` format from *Geosoft Oasis Montaj-GM-SYS* to MAT LAB. We then plot these data using the `scatter` command in MATLAB and use the `alphashapes` command to determine the best-fit polygons to the cross-sectional shapes. The `alphavol` command is then used to compute the area inside the polygons using Delaunay triangulation (Jonas Lundgren, 2010).

To convert the cross-sectional areas to volumes, assumptions about the geometry of the bodies need to be made. It is not certain if the geological bodies are cylindrical or cone shaped. For our purposes, we assume that all the geologic bodies are in rectangular prisms. The width of the geological bodies are derived from the magnetic TDV map where the edge of the bodies are detectable (see Figure 16). The magnetic TDV map provided better edge detection than the gravity TDV map. We speculated because the magnetic susceptibility contrast between magma and pre-eruptive units are greater than the gravity contrast between magma and pre-eruptive units. Multiplying the surface area of a body by its length yields the volume of the body as if it is in rectangular prism.

4.6 Statistical Analysis and Error Propagation

The experimental data measured and observed from our gravity and magnetic model is not perfect. We directly measure dimensions of geological bodies of interest on our developed 2D joint inverse model of Gravity and Magnetic data from Kilbourne Hole, but the measurements contain errors. The variation inherit in the errors can be from numerous factors that interfere with the measurement. Even though we made every effort to reduce systematic errors, it is impossible to totally eliminate all measurement error. For the measurements to be truly representative of the underlying phenomenon and the process we are observing (in our case, the phenomenon are e.g. the dimensions of Kilbourne Hole internal structures, the thickness of pyroclastic flow layers, the volumes of the dike, and the mass of excavation), we report the error of our result and provide confidence limits to describe the region of the true value of the variable in term of uncertainty (δ). Here we also used the measurements from our models to infer to the value of other quantities indirectly, for example, if we want to know the volume of the pyroclastic flow unit, we measured the thickness of a unit from our model cross-section and measured the surface area of the unit from our gravity anomaly map. The volume of the unit is then calculated as the thickness and the surface area multiplied. The errors in the measurements of the thickness and the surface area were translated and propagated into the achieved volume result following the Gaussian equation for normally distributed errors method (Taylor, 1997; Bevington and Robinson, 2002). Taylor (1997) and Bevington and Robinson (2002) summarized some rules for error propagation; If we have quantities a, b, c with uncertainties δa, δb, δc, the Gaussian equation for normally distributed errors are used slightly different based on the relationship and function between a, b, and c. Assuming the uncertainty are relatively small and

there is no covariance between them, then we are be able to derive the propagated uncertainty using the Gaussian equation for normally-distributed errors method.

5. Results

5.1 Gravity and Magnetic Anomaly Maps of Kilbourne Hole

The magnetic anomaly map (Figure 5a) of Kilbourne Hole reveals three magnetic anomalies associated with: (1) buried basaltic flows and dikes; (2) the Camp Rice formation and older units that pre-date the eruption, as well as reworked material that post-dates the eruption; and (3) pyroclastic deposits associated with the Kilbourne Hole eruption. The contrast in total magnetic anomaly between (1) and (2) is ~600-800 nT, whereas the contrast between (1) and (3) is ~100-300 nT. Our magnetic maps can be used to locate buried basalt lava flows, dikes, and faults that are not evident at the surface.

The gravity anomaly map (Figure 5b) of Kilbourne Hole reveals three anomalies associated with: (1) the diatreme and dikes; (2) the Camp Rice formation and older units that pre-date the eruption; and (3) buried basalt lava flows. The contrast in total gravity anomaly between (1) and (2) is ~40mGal, whereas the contrast between (1) and (3) is ~20 mGal. Unlike the magnetic anomaly map, the gravity anomaly map does not show significant detail. It is very difficult to identify and locate buried basalt lava flows, dikes, and faults that are not evident in surface exposure from the gravity anomaly map of Kilbourne Hole.

The Kilbourne Hole intrusive dikes appear on both the gravity and magnetic models. This confirms the volcanic origin of Kilbourne Hole and spatial distribution of the buried volcanic vent. Although it is not obvious on the gravity anomaly map, evidence of crater collapse is very obvious in the magnetic anomaly map (Figure 5 a and b). There are several magnetic anomaly bodies inside the crater that showed similar magnetic susceptibility to the pyroclastic deposit. We interpret that magnetic anomalies belonging to the rotated block of pyroclastic deposit can be found inside the crater.

5.2 Magnetic Tilt Derivative Map and Gravity Tilt Derivative map of Kilbourne Hole

The tilt derivative map (TDV) of the magnetic anomaly shows the edges of the dikes more precisely (Figure 6a) than the magnetic anomaly map itself. The tilt derivative map of the Bouguer gravity anomaly map of Kilbourne Hole reveals more distinctive features of mafic intrusion than the gravity map itself (Figure 6b). As seen on the TDV map of the gravity anomaly, the anomaly of the intrusions appeared to be narrower and stronger that the anomaly of the intrusions on the gravity anomaly map. Our magnetic and gravity tilt derivative maps show areas of positive tilt angle derivative (approximately 1.4 radian) and areas of negative tilt angle derivative (approximately -1.4 radians). The areas where there are no changes in tilt angle derivative (tilt angle derivative ~ 0 radain) (white ovals in Figures 6a and 6b) are considered to be the edges of intrusions (Miller and Singh, 1994). Small changes (close to 0 radians) in the vertical derivative indicate that the buried bodies must be located at great depth.

5.3 Two-Dimensional Gravity and Magnetic Joint Inversion Model of Kilbourne Hole

Figures 7-9 show the results of the gravity-magnetic joint inversion along three transects (A1-A1', A2-A2', and A3-A3') across the Kilbourne Hole (Figure 5). The RMS misfits between predicted magnetic anomalies to the observed magnetic anomaly are 64.628 nT (16.57%), 187.268 nT (5.59%), and 33.633 nT (5.69%). The RMS misfits between our predicted gravity anomaly to the observed gravity anomaly are 5.968 mGal (9.94%), 5.647 mGal (17.11%), and 5.254 mGal (15.01%). Our models reveal three dikes underneath Kilbourne Hole. The depth below the pre-eruption ground surface to the top of the dikes varies: dike 1, on the eastern rim of

the crater, is 1.75-2.25 km deep; dike 2, beneath the center of the crater, is 0.91-3.58 km deep; and dike 3, beneath the western rim of the crater, is 0.14-2.50 km deep. The depth to the bottom of the diatreme is 13.6-15.8 km and the width of the diatreme features is ~4-km wide. The models show that the tuff ring deposits extend 600 m to 1 km away from the crater rim and vary in thickness (50-150 m). On the west rim of Kilbourne Hole, the tuff ring is generally thinner, but it extends further out, compare to the tuff ring formation seen on the east rim of the crater where the pyroclastic deposits are the thickest (Figures 7). The model also suggests the presence of a series of normal faults within Kilbourne Hole that may be the result of post-eruption crater collapse (Figures 7-9).

All three inversion models of Kilbourne Hole are able to delineate several complex fault blocks of pyroclastic deposits that collapsed and rotated into crater, the area of the diatreme, the area of the original crater excavation, and the area that was later filled with alluvium. The diatreme has a cone shape with steep sides, and includes rotated blocks of pyroclastic deposits and pre-eruptive units. To confirm that all three inversion models are geologically and geometrically consistent, we visualized them with fence diagrams (Figures 10-12). The fence diagrams show the connectivity of three dikes among transects A1-A1', A2-A2', and A3-A3'. The diatreme extends down from the post-eruptive crater floor to the feeder dikes below. The thickness and the extent of the diatreme obtained from the three transects are 13.6 -15.8 km deep and is about 4 km wide.

5.4 Volumes, Mass, and Litho-Static Pressure Estimation

Figures 13-15 show the cross-sectional area and the volume estimations of the three dikes underneath Kilbourne Hole. We inspected the cross-sections along transects A1-A1', A2-A2', and A3-A3' (Figures 7-9) to determine the most representative cross-sectional areas for each dike for the purpose of calculating volumes. For example, dike 2 can be seen in both transect A1-A1'and A2-A2', and its cross-sectional area in transect A2-A2' is larger than what it is on transect A1-A1'. Therefore we choose the area of dike 2 along transect A2-A2' to best represent cross-sectional area of dike 2. The uncertainty of the cross-sectional area is propagated from the uncertainty of the width of the body in y direction and the uncertainty of the depth the body in z direction. We made an assumption that the dikes are elongate along the fault and are in rectangular prism. We measured the diameter of the dikes and other volcanic structure of Kilbourne Hole on TDV magnetic map of Kilbourne Hole (Figure 16). The length of dike 1 is ~0.98 ± 0.1 km. The uncertainty is based on the spatial resolution of our magnetic anomaly map and magnetic TDV map. The map was interpolated from our 200 m resolution data. Therefore the certainty of model result should only be half the resolution, which is 100 m or ±0.1 km. Similarly, the length of dike 2 is ~0.55 ± 0.1 km, and length of dike 3 is ~0.51 ± 0.1 km. By multiplying the cross-sectional area of each intrusion by its length, we obtained the volumes of dike1, dike2, and dike 3: 1.98 ± 0.29 km^3, 1.47 ± 0.29 km^3, 1.02 ± 0.23 km^3, respectively. The uncertainties of the cross-sectional area are propagated from the uncertainty of the diameter of the cross-sectional area, which is ±0.1 km, and the uncertainty of the depth or the thickness of the cross-sectional area, which is ~ ±0.12 km. This uncertainty is based on the sensitivity our model. By trial-and-error, we found that the thickness and the depth of the buried dikes can be varied up to ±0.12 km and still yield an acceptable model misfit. By combining the total volume

of the dikes, including their uncertainties, we estimate that the total volume of the basaltic magma that caused the Kilbourne Hole eruption was 4.46 ± 0.0.48 km^3. Using the density of basalt (3100 kg/m^3), we estimate the total mass of the melt (m_m) to be (1.38 ± 0.15) x 10^{13} kg. Similarly, we calculate the total volume of the volcanic fragments excavated during the Kilbourne Hole eruption to be 1.55 ± 0.23 km^3 and the total mass that was excavated to be (2.53 ± 0.38) x 10^{12} kg. The total volume of the Kilbourne Hole diatreme was 14.2 ± 0.17 km^3 (we do not need to know the mass of the diatreme to solve for equation (8), so we left with the mass of the diatreme uncalculated). All calculations, including error propagation, are shown in detail in Appendix D. Errors from all measurements were propagated when the measurements are used to obtain other indirect results using the procedure provided by Taylor (1997) (see section 4.6).

Because all three sections of our integrated gravity and magnetic models of Kilbourne Hole reveal intrusions at depths between 0.14 km and 3.5 km, we assume that the depth of 3.5km is where the maximum pressure from litho-static load occurred. The Kilbourne Hole vent material from the surface to the depth of 3.5 km includes: (1) ~3.47 km thick diatreme filled material with a density of ~2,560 kg/m^3; and (2) 0.03 km of basalt with a density of ~3,100 kg/m^3. Therefore the thickness-weighted density of the Kilbourne Hole litho-static load is 2,507 kg/m^3. Using Equation (6) we calculated that the litho-static load pressure (p_1) inside the vent of the Kilbourne Hole was 8.81 x 10^2 bar.

5.5 Mass of Water in the Groundwater Reservoir

We calculated the mass of groundwater in the groundwater reservoir at the time of eruption by substituting these following variables into Equation (8):

1) A maximum ejection velocity of 122.8 ± 9.3 m/s (113.5-132.2 m/s; Rhodes and Hurtado, 2014),
2) The total volume of the diatreme, 14.2 ± 0.17 km^3 (we do not need to know the mass of the diatreme to solve for equation (8), so we left the mass of the diatreme uncalculated).
3) The total volume of the excavated volcanic fragments, 1.55 ± 0.23 km^3
4) The total mass that was excavated, ~ (2.53 ± 0.38) x 10^{12} kg.
5) The total mass of all three dike (section 5.4), ~ (1.46 ± 0.33) x 10^{13} kg

From the calculation of equation (8), we calculated the mass of water (m_w) involving in Kilbourne Hole eruption to be (1.09 ± 0.31) x 10^{13} kg. The ratio of mass of water to mass of magma and the known mass of the magma (m_w/m_m) is 0.79 ± 0.23 (Figure 17).

6. Discussion

6.1 Geologic interpretation of Gravity-Magnetic Joint Inversion Model of Kilbourne Hole

Unlike most regional gravity and magnetic models of a typical volcano, our gravity and magnetic survey of a phreatomagmatic volcano such as what we did at Kilbourne Hole provided ~ 200 m resolution gravity and magnetic anomaly map. The 2D joint gravity-magnetic inversion from our ~ 200 m resolution gravity and magnetic anomaly map allowed us to model the internal structure of Kilbourne Hole in great detail. The geometrical results of our joint gravity and magnetic model of Kilbourne Hole shows great similarity between the internal structure of Kilbourne Hole and the internal structure of other phreatomagmatic volcano described by White and Ross (2011). Both our model of Kilbourne Hole and White and Ross (2011) models of phreatomagmatic volcano are consistent with a zone of chaotic breccia that is cut by multiple dikes at various depths (Figure 10-12). Beyond that, our model of Kilbourne Hole revealed the structure of rotated blocks of pre-eruptive units, and rotated blocks of collapsed crater rim material. However. Our models are also able to show the transition from the diatreme to the intrusion in the root zone of the phreatomagmatic volcano and the spatial distribution of the buried rotated blocks and the post –eruptive crater filled material (Figure 10-12). The depths of the diatreme roots (at ~ 13.6-15.8 km) and the depth of the basement rocks (~1.5 – 4.6 km) in the vicinity beneath Kilbourne Hole crater provided on all 3 cross-sectional models are correlated to other workers estimation of the Potrillo Volcanic Field (PVF) and the Mesilla basin. Averill (2007) and Gillespie (2002) suggested the basement rock of both western and eastern flank of the Mesilla basin are at the shallower depth than the rest of the Rio Grande basin. Their seismic and regional gravity models suggested the Mesilla basin is an asymmetric basin adjoining on the eastern side to the PVF and on the western side to the base of the Franklin mountain uplifts.

Averill (2007)'s seismic velocity models indicate that the Mesilla basin upper crustal basement rock is ~3-5 km deep and is defined by velocities of 5.96-6.09 km/s. The seismic velocity profile of the PVF also shows a distinctive thickening layer of mid-crust with a velocity contrast of 6.2 - 6.35 km/s at depths of 11-12 km. This distinctive layer is not the layer of the lower crust with velocity of 6.15-6.62 km/s at ~20 km, neither upper mantle with velocities of ~7.8 km/s at 30-31 km depth (Averill, 2007). Previously Averill (2007) was not certain of his interpretation of this thickening mid crust at the depth of ~11-12 km. It was noted that this middle-crust's interface is located abruptly at approximately 20 to 12 km depth just to the west of the PVF. This interface also shows a crustal thickening trend beneath the PVF. The velocities range from 6.28 to 6.4 km/s and the densities range from 2.75-2.88 g/cm^3 of these mid-crust is not high enough to be interpreted as the magma chamber or lower curst and is not low enough to be interpreted as the limestone type upper crustal basement rock. Averill (2007) interpret this mid-crust anomaly may be an extensional faulting that may relate to volcanism in the PVF region. Our gravity and magnetic models of Kilbourne Hole was performed with 200 m spacing in the PVF region and contain sufficient detail to resolve this feature. Our interpretation of the geological bodies at the depth of 13.6-15.8 km with the density of 2.58-2.64 g/cm^3 is that this feature is a diatreme of Kilbourne Hole, is supported by the previous interpretation of Averill (2007).

A minimum of three dikes were found at various depths inside Kilbourne Hole. Each dike may be a record of changes in the location of individual explosions during the eruption. Because in a phreatomagmatic eruption, the dike that came to interact to groundwater sources tend to lose its heat and became frozen dike buried at the location where its last interact with groundwater. Another observation made based on our model of Kilbourne Hole are that the spatial location of

the dike not at the center of Kilbourne Hole. The spatial distribution of the dikes may also be an explanation of the irregular shape of Kilbourne Hole (see Figures 10-12).

Our inverse models of Kilbourne Hole indicate that the magnetic signal is more sensitive to the geometry of the subsurface bodies at Kilbourne Hole than the gravity signal. This may be because the magnetic susceptibility contrast between the mafic intrusions underneath Kilbourne Hole and the Camp Rice formation is very high, so that even slight adjustment could result in great change in magnetic anomaly.

With the vertical tilt derivative method applied to the magnetic data, we are able to better locate the edge of the dikes and the diatreme. The dike when buried deep inside the diatreme, instead of providing a sharp narrow anomaly on the map, it only shows broad and wide anomaly on the map with no distinction to the anomaly of the surrounded alluvium. Without the help of tilt derivative method, we may not be able to model the edge of the dikes.

6.2 Paleohydrological Conditions of Kilbourne Hole at the Time of Eruption

With reliable constraints for the internal structure of Kilboune Hole, we estimate that the groundwater reservoir at the time of the eruption supplied $(1.09 \pm 0.31) \times 10^{13}$ kg of water. The volume of this amount of groundwater was approximately 10.87 ± 3.12 km^3. To provide a perspective to how much water was in the groundwater reservoir, we made an assumption that Kilbourne Hole's aquifer has an approximate volume of ~ 64 km^3 (4 x 4 x 4 km), considering that the Mesilla basin were filled with ~4km thick sediment and the size of Kilbourne Hole was about 4 x4 km. This volume of groundwater in comparison to the volume of Kilbourne Hole's reservoir suggested that it is ~16.9 ± 4.8% of groundwater. The water to magma mass ratio,

therefore, was 0.79 ± 0.23. Wohletz (1986), Wohletz and Sheridan (1982; 1983), and Wohletz and McQueen (1984) suggested (Figure 17) that the Kilbourne Hole's phreatomagmatic eruption produces thinly-bedded, dry base surge, and vapor-expanded tuff ring. Our results are supported by the observation of thinly bedded dry base surge, and extended tuff ring deposit along the rim of Kilbourne Hole (Figure 18). The evidence of boulder sized volcanic blocks and associated sags also confirm that the eruption event that formed Kilbourne Hole was highly explosive.

This percent of groundwater is also supported by the paleohydrologic conditions in the Mesilla basin during the Plio-Pleistocene. With ~16.9 ± 4.8% of groundwater, the climate condition of the Mesilla basin may have been wetter than the present day Chihuahua desert climate (Mack et al., 2014). For example, Mack et al. (2014) observed carbon isotopes of pedogenic carbonates from the Camp Rice formation and suggested that the climate of the lower Rio Grande basin in Late Pleistocene time showed a steady trend toward higher temperatures than today's and summer-dominated rainfall. Kilbourne Hole is located on the southwestern edge of the Rio Grande basin; therefore, it should have experienced the same climate trends as the rest of the Rio Grande basin. The Santa Fe group (including Camp Rice and Fort Stockton formation) is the main aquifer of all groundwater sources within the Rio Grande basin. Today it is estimated that the Santa Fe group aquifer is about 1-5 km thick (Keller et al., 1990) and the depth the groundwater level is 1.5-4.8 km (Robson and Banta, 1995). Our model suggests that the mafic intrusions that triggered the Kilbourne Hole explosion interacted with groundwater at about 0.17-3.58 km depth. This suggests that the groundwater level in the Rio Grande basin at the time of Kilbourne Hole eruption was higher than it is today.

6.3 The application of gravity and magnetic surveys on Mars Home Plate

Our gravity and magnetic survey at Kilbourne Hole had demonstrated that we could quantify the amount of groundwater involving in a phreatomagmatic eruption using the result of our 2D-gravitya and magnetic joint inversion model results. The gravity and magnetic surveys we did at Kilbourne Hole can be used as a guideline to design similar surveys of phreatomagmatic craters and other volcanic activities on a planet such as Mars or the Moon to understand their paleo-hydrological conditions. Because the geological and geophysical setting of Kilbourne Hole is very similar to what we observe at Home Plate on Mars (e.g., cross-bedded pyroclastic flow deposit, basalt flow deposit, volcanic blocks and sags features, size of volcanic blocks and thicknesses of their ash bed) (Figure 18), it is possible that internal structures similar to Kilboune Hole could also be well preserved underneath Mars Home Plate. Even with the highest resolution of the most recent GRAIL and MGS (Mars Global Surveyor) gravity data from the Moon and Mars, its resolution of ~7.6 km is still not sufficient to detect an anomaly from a volcano the scale to Kilbourne Hole eruption, we suggested a high resolution ground-based gravity and magnetic data are needed on Mars and the Moon. All of ground based gravity and magnetic survey may be completed by a rover but it may also require the geophysicist to provide a survey that it was carried out accurately, and to interpret the results using *a priori* geological information. To do a gravity and magnetic survey on Mars, there are several factors to consider:

1) Rocks formed after the core dynamo ceased may yield an opposite anomaly of the same geological feature as on Earth (Cisowskil and Fuller, 1978; Isac et al., 2015);

2) Magnetic susceptibilities many not have been the only attribute to remnant magnetization and magnetic signal anomalies. Large impacts can de-magnetize or re-magnetize rocks and altered rock density; and
3) To date, there has been little work to systematically determine the magnetic susceptibility of rock types on Mars (Cisowskil and Fuller, 1978; Isac et al., 2015).

A ground-based magnetic and gravity survey using 200 m spacing similar to what we did at Kilbourne Hole should be sufficient to map the volcanic activity on Mars Home Plate. However, the traditional data processing and interpretation on the magnetic data retrieved from Earth is not completely adaptable on Mars. Firstly, because any volcanic rock that formed after the core dynamo on Mars ceased (Isac et al., 2015; Langlais et al., 2010) would not yield any magnetic anomaly and therefor is not appropriate for modeling method (Cisowskil and Fuller, 1978; Isac et al., 2015). Secondly, de-magnetized or re-magnetized rocks due to large impact event would complicate magnetic data correction. On Earth, our dipole magnetic field are in N-S direction and we can perform reduce to pole correction so that all the anomalies are aligned in the same direction prior the model inversion. On Mars remanents magnetic field are not in N-S direction but in fact are depend on the zone of de-magnetize or re-magnetize. Without a detail map of Mars remanents magnetic field, the surveyor would not be able to perform sufficient magnetic data correction to achieve a reliable magnetic model. Lastly, because there are no rock samples from Mars; the information about Mars' rocks is very limited. Only some magnetic information obtained from ALH84001 Martian meteorites can provide us constrain for magnetic modeling on Mars surfaces (Weiss et al., 2002).

To do a ground-based gravity survey on Mars is slightly less complicated than to do a magnetic survey because, both Mars and Earth are terrestrial planets of almost similar size and gravitational acceleration. The only concern in bringing ground-based gravity surveys to Mars is similar to the concern with using GRAIL data from the Moon. Both Mars and the Moon are highly bombarded by large impact events thought-out is formation history and the gravity signal retrieved from Mars surface is not a reflection of its internal structure but instead a reflection of its impacted subsurface. Similar to the Moon, the large impact events on Mars also created an abnormally high positive gravity anomaly zone called mascon (Zuber et al., 2013; Isac et al., 2015; Langlais et al., 2010). To quantitatively interpret the gravity data from Mars, we might need to consider filtering out the gravity signal from the highly impacted Mars subsurface. However, quantitatively interpreting the magnetic data from Mars is not quite possible yet for the reasons stated earlier.

Our gravity and magnetic study at Kilbourne Hole is only a pilot study on a phreatomagmatic volcano on Earth. Our result successfully yields quantitative interpretation of the internal structure of Kilbourne Hole and quantitatively estimation of the amount of groundwater involved in Kilbourne Hole eruption. In this study, we present a conceptual methodology for modeling gravity and magnetic data and solution to evaluate and to quantify the amount of groundwater (see section 4) on a terrestrial phreatomagmatic volcano site on Earth. Here we reported the strategies and the adaptation of our gravity and magnetic survey's design, gravity and magnetic data collection, and gravity and magnetic data correction on the analog site on Earth. However to carry out our study on Mars, we must first obtain more information about the physical

rock properties, particularly magnetic susceptibility and bulk density, before we can provide an adaptation of our method to be used on Mars.

7. Conclusions

In conclusion, we are able to design ground-based surveys using gravity and magnetic methods at an Earth analog site (Kilbourne Hole, NM). We concluded that our designed geophysical method could also be performed on a phreatomagmatic or volcanic outcrop on Mars and the Moon. We are also able to provide gravity and magnetic interpretation methods that do not rely solely on just the modeling method. By integrating the results of my joint gravity and magnetic model and the GPR surveys of Kilbourne Hole, we are able to provide quantitative results of the paleo-hydrogeological conditions at the time of eruption, which are mass and volume of the Kilbourne Hole groundwater reservoir. Our models allow us to interpret the internal structure of Kilbourne Hole within the geological context of the Rio Grande rift basin and the Mesilla basin. The application of the tilt derivative method also allows us to constrain the model and to retrieve precise edges and locations of the buried geological bodies. We found that the magnetic method responds very well to the bodies of high iron content basaltic intrusions as opposed to the gravity method, which cannot distinguish between the diatreme and the intrusions because they have the same density. However, our combined use of gravity and magnetic data is very helpful in: (1) delineating subsurface volcanic and sedimentary materials and (2) identifying mafic intrusions and diatreme.

The results from my study at Kilbourne Hole not only confirm the ability of our method in planetary exploration, but it also reveals important information about the internal structure of Kilbourne Hole itself. From our study, we are able to understand Kilbourne Hole's eruption history and the paleo-hydrologic conditions of the Rio Grande rift basin in much more detail than any surface geological study. Kilbourne Hole eruption was active during the Plio-Plesitocence time; where the climate amplitude and magnitude were fluctuating highly. Our quantitative result

of groundwater conditions at Kilbourne Hole aligns with the regional paleo-climate trend at the time. The ~16.9 ± 4.8% of groundwater in the reservoir shows that water activity was very high during the time Kilbourne Hole last erupted, even though the present environment is semi-arid.

The adaptation of our method on Mars is likely possible. The current climate of Mars is arid with some evidence of water presence. The modern observable cryosphere contains an equivalent global layer of water ~35 m thick (Michalski et al., 2013). It is also suggested by Burt et al. (2003) that the largest fraction of Martian water is in the subsurface in the form of briny groundwater. Mars groundwater contains greater subsurface porosity than Earth (Burt et al., 2003). It is believed that after Mars tectonic activity stopped in Noachian, Martian groundwater was no longer altered by volcanic outgas process and ultimately had become sequestered into the subsurface, and/or froze into the cryosphere, and/or lost to space (Michalski et al., 2013). Our method was specifically designed to not only provided information about the phreatomagmatic volcano's preserved internal structure but also was intent to reveal the condition of the groundwater reservoir at the time of eruption. Conducting integrated geophysical survey procedures similar to those that we performed at Kilbourne Hole on Mars would reveal further understanding to early Mars climate conditions.

However, it must be noted that our results from the gravity and magnetic surveys are not a stand-alone result. To obtain the final product of this research, which is the amount of groundwater in the reservoir at the time of Kilbourne Hole eruption, we must know the initial velocity of the gas expansion at the time of eruption which can only be retrieved from our GPR results (Chapter 3). The reliability and detail provided by our two dimensional joint gravity and magnetic model are very much dependant on the quality of *a priori* information. In other words, the more limited background geological knowledge exist of the planet, the less reliable our

model results. Therefor to practically adapt our method for Martian ground based surveys, numbers of other key observations must also be made. For example, we were unable to perform gravity and magnetic inversion modeling unless we first know what densities and magnetic susceptibility of the rock units on Mars are. In addition to present exploration of Mars that is focused on evaluating the habitability of surface environments, we argue that we may also need to look back further in time as the Martian surface had become extremely cold, oxidizing and arid long before. With further observations, great information can be learned about the climate history of the terrestrial planets through this type of research.

References

Andrews-Hanna, J. C., Asmar, S. W., Head, J. W., Kiefer, W. S., Konopliv, A. S., Lemoine, F. G., and Zuber, M. T., 2013, Ancient igneous intrusions and early expansion of the Moon revealed by GRAIL gravity gradiometry: *Science*, vol. 339, no. 6, 120, p. 675-678.

Athy, L. F., 1930, Density, porosity, and compaction of sedimentary rocks. *AAPG Bulletin*, vol. 14, no. 1, p. 1-24.

Averill, M.G., Miller, K. C., Keller, G. R., Kreinovich, V., Araiza, R., and Starks, S. A., 2007, Using expert knowledge in solving the seismic inverse problem: *International Journal of Approximate Reasoning*, vol. 45, p. 564-587.

Bankey, V., A. Cuevas, D.D., Finn, C. A., Hernandez, I., Hill, P., Kucks, R., Miles, W., Pilkington, M. , Roberts, C., Roest, W., Rystrom, V., Shearer, S., Snyder, S., Sweeney, R., Velez, J., Phillips, J. D., and Ravat D., 2002, Digital data grids for the magnetic anomaly map of North America: U.S geological Survey Open-File Report 02-414, 2 p.

Barberi, F., Navarro, J. M., Rosi, M., Santacroce, R., and Sbrana, A., 1988, Explosive interaction of magma with ground water: Insights from xenoliths and geothermal drillings: *Rendiconti della Societa Itaiana di Mineralogia e Petrologia*, vol. 43, no. 4, p. 901-926.

Briesacher, A., Flanagan, G., Hinze, W.J., Hittelman, A.M., Keller, G.R., Kucks, R.P., Plouff, D., Roest, W., Seeley, J. and Smith, D.A., 2002, Rationale and operational plan to upgrade the US gravity database: U.S geological Survey Open-File Report 02-463, 14 p.

Bosch, M. and McGaughey, J., 2001, Joint inversion of gravity and magnetic data under lithologic constraints. *The Leading Edg*e, vol. 20(8), p.877-881.

Bevington, P. R. and Robinson, K.D., 2002, *Data Reduction and Error Analysis for the Physical Sciences (3rd ed.)*: McGraw-Hill Education (New York), 336 p.

Burt, D. M., and Knauth, L. P., 2003, Electrically conducting, Ca-rich brines, rather than water, expected in the Martian subsurface: *Journal of Geophysical Research: Planets*, vol. 108, no. E4, p. 8026-8032.

Day, S.J., 1996, Hydrothermal pore fluid pressure and the stability of porous, permeable volcanoes, *in* McGuire, W.J., Jones, A.P. and Neuberg, J., (eds.), 1997, *Volcano Instability on the Earth and Other Planets*: Geological Society (London) Special Publication, vol. 110, p. 77-93

Comer, R. P., Solomon, S. C., and Head, J. W., 1985, Mars: Thickness of the lithosphere from the tectonic response to volcanic loads: *Reviews of Geophysics*, vol. 23, no. 1, p. 61-92.

Dorren, L. and Seijmonsbergen, A.C., 2003, Comparison of three GIS-based models for predicting rockfall runout zones at a regional scale: *Geomorphology*, vol. 56, p. 49-64.

Ebinger, C. J., J. van Wijk, D. Keir, 2013, The time scales of continental rifting: Implications for global processes, *in* M. Bickford (ed.), *Tectonics: 50 years after the revolution*: Geological Society of America Special Paper vol. 500, p. 371-396.

Finlay, C. C., Maus, S., Beggan, C. D., Hamoudi, M., Lowes, F. J., Olsen, N., and Thébault, E., 2010, Evaluation of candidate geomagnetic field models for IGRF-11: *Earth Planets Space*, vol. 62, no. 10, p. 787-804.

Gidley, P. R. and Stuart, D. C., 1980, Magnetic property studies and magnetic surveys of the Elura prospect, Cobar, NSW: *Exploration Geophysics*, vol. 11, no. 4, p. 25.

Gubbins, D. and Herrero-Bervera, E. (eds.), 2007, *Encyclopedia of Geomagnetism and Paleomagnetism*: Springer Science & Business Media (Dordretch, The Netherlands), 1054 p.

Guo, L., Meng, X., Chen, Z., Li, S., and Zheng, Y., 2013, Preferential filtering for gravity anomaly separation: *Computers & Geosciences*, vol. 51, p. 247-254.

Hawley, J. W., 1975, Quaternary history of Dona Ana country region, south-central New Mexico, *in* Seager, W. R., Clemons, R. E., Callender, J. F. (eds.), *New Mexico Geological Society 26th Annual Fall Field Conference Guidebook*: New Mexico Geological Survey (Soccoro, NM), p. 68.

Heiskanen, W. A. and Moritz, H., 1967, Physical geodesy: *Bulletin Géodésique*, vol. 86, no. 1, p. 491-492.

Hildenbrand, T. G., Briesacher, Allen, Hinze, W. J., Hittelman, A. M., Keller, G.R., Kucks, R. P., Roest, W. R., and Smith, D. A., 2002a, Web-based U.S. Gravity Data System Planned: *EOS*, vol. 83, no. 52, p. 613-618.

Hildenbrand, T. G., Briesacher, A., Flanagan, G., Hinze, W. J., Hittelman, A. M., Keller, G. R., Kucks, R. P., Plouff, D., Roest, W., Seeley, J., Smith, D. A., and Webring, M., 2002b, Rationale and operational plan to upgrade the U.S. gravity database: *U.S. Geological Survey Open-file Report 02-463*, 12 p., http://geopubs.wr.usgs.gov/open-file/of02-463.

Hoffer, J. M., 1971, Mineralogy and petrology of the Santo Tomas-Black Mountain basalt field, Potrillo volcanics, south-central New Mexico: *Geological Society of America Bulletin*, vol. 82, no. 3, p. 603-612.

Hamblock, J. M., Andronicos, C. L., Miller, K. C., Barnes, C. G., Ren, M. H., Averill, M. G., and Anthony, E. Y., 2007, A composite geologic and seismic profile beneath the southern Rio Grande rift, New Mexico, based on xenolith mineralogy, temperature, and pressure: *Tectonophysics*, vol. 442, no. 1, p. 14-48.

Hrouda, F., 1982, Magnetic anisotropy of rocks and its application in geology and geophysics: *Geophysical surveys*, vol. 5(1), p.37-82.

Hunt, C. P., Moskowitz, B. M., and Banerjee, S. K., 1995, Magnetic properties of rocks and minerals, *in* Ahrens T.J. (ed.), *Rock Physics & Phase relations: A Handbook of Physical Constants (Vol. 3)*: American Geophysical Union (Washington, DC), p. 189-204.

Ingersoll, R. V., 2001, Structural and stratigraphic evolution of the Rio Grande Rift, northern New Mexico and southern Colorado: *International Geology Review*, vol. 43, no. 10, p. 867-891.

Isac, A., Mandea, M., Purucker, M., and Langlais, B., 2015 (in press), A comparative analysis of the magnetic field signals over impact structures on the Earth, Mars and the Moon: *Advances in Space Research*.

Keller, G. R., Morgan, P., and Seager, W. R., 1990, Crustal structure, gravity anomalies and heat flow in the southern Rio Grande rift and their relationship to extensional tectonics: *Tectonophysics*, vol. 174, no. 1, p. 21-37.

Li, X. and Götze, H. J., 2001, Ellipsoid, geoid, gravity, geodesy, and geophysics: *Geophysics*, vol. 66, no. 6, p. 1,660-1,668.

Lorenz, V., 1986, On the growth of maars and diatremes and its relevance to the formation of tuff rings: *Bulletin of Volcanology*, vol. 48, no. 5, p. 265-274.

Mack, G. H., Cole, D. R., James, W. C., Giordano, T. H., and Salyards, S. L., 1994, Stable oxygen and carbon isotopes of pedogenic carbonate as indicators of Plio-Pleistocene paleoclimate in the southern Rio Grande Rift, south-central New Mexico: *American Journal of Science*, vol. 294, p. 621-640.

Michalski, J. R., Cuadros, J., Niles, P. B., Parnell, J., Rogers, A. D., and Wright, S. P., 2013, Groundwater activity on Mars and implications for a deep biosphere. *Nature Geoscience*, vol. 6(2), p. 133-138.

Miller, H. G. and Singh, V., 1994, Potential field tilt: A new concept for location of potential field sources: *Journal of Applied Geophysics*, vol. 32, no. 2, p. 213-217.

Mohr, P. J. and Taylor, B. N., 2005, The fundamental physical constants: *Ingenierías*, vol. 8 no. 26, p. 49.

Moritz, H., 1980, Geodetic reference system 1980: *Journal of Geodesy*, vol. 54, no. 3, p. 395-405.

Mueller, S., Scheu, B., Spieler, O., and Dingwell, D. B., 2008, Permeability control on magma fragmentation: *Geology*, vol. 36, no. 5, p. 399-402.

Mushayandebvu, M. F., Van Driel, P., Reid, A. B., and Fairhead, J. D., 2001, Magnetic source parameters of two-dimensional structures using extended Euler deconvolution: *Geophysics*, vol. 66, no. 3, p. 814-823.

Naidu, P. S., 1969, Estimation of spectrum and cross-spectrum of aeromagnetic field using fast digital Fourier transform (FDFT) techniques: *Geophysical Prospecting*, vol. 17, no .3, p. 344-361.

Nagy D., 1966, The Prism Method for Terrain Corrections Using Digital Computers: *Pure Applied Geophysics*, vol. 63, p. 31-39.

NOAA, 1976, U.S. Standard Atmosphere. Government Printing Office (Washington DC).

Paterson, N. R. and Reeves, C. V., 1985, Applications of gravity and magnetic surveys: The state-of-the-art: *Geophysics*, vol. 50, no. 12, p. 2,558-2,594.

Purucker, M. E., Head III, J. W., and Wilson, L., 2012, Magnetic signature of the lunar South Pole-Aitken basin: Character, origin, and age: *Journal of Geophysical Research*, vol. 117, p. E05001-1-E05001-8.

Ramberg, I. B., Cook, F. A., and Smithson, S. B., 1978, Structure of the Rio Grande rift in southern New Mexico and West Texas based on gravity interpretation: *Geological Society of America Bulletin*, vol. 89, no. 1, p. 107-123.

Reiche, P., 1940, The origin of Kilbourne Hole, New Mexico: *American Journal of Science*, vol. 238, no. 3, p. 212-225.

Rhodes, N. and Hurtado, J. M. (Jr.), 2012, A magnetic survey of Kilbourne Hole, southern New Mexico: implications for near surface geophysical exploration of Mars and the Moon: *Proceedings of the 43rd Lunar and Planetary Science Conference*, vol. 43, p. 2914.

Rhodes, N. and Hurtado, J. M. (Jr.), 2014. A GPR Survey of Kilbourne Hole, Southern New Mexico: Implications for Near Surface Geophysical Exploration of Mars and the Moon: *Proceedings of the 45th Lunar and Planetary Science Conference*, vol. 45, p. 2,912.

Robson, S. G. and Banta, E. R., 1995, Ground Water Atlas of the United States: Arizona, Colorado, New Mexico, Utah: US Geological Survey Open-File Report HA 730-C, http. *pubs. usgs. gov/ha/ha730/ch_c/C-text4. htm l [accessed 11 May 2015]*.

Hubbert, M.K. and Rubey, W.W., 1959, Role of fluid pressure in mechanics of overthrust faulting I. Mechanics of fluid-filled porous solids and its application to overthrust faulting: *Geological Society of America Bulletin*, vol. 70(2), p.115-166.

Shearer, S. E., 2005, *Three-Dimensional Inversion of Magnetic Data in the Presence of Remanent Magnetization* [Ph.D. dissertation]: Colorado School of Mines, 142 p.

Sinno, Y.A., Daggett, P.H., Keller, G.R., Morgan, P., and Harder, S.H., 1986, Crustal structure of the southern Rio Grande rift determined from seismic refraction profiling: *Journal of Geophysical Research*, vol. 91, p. 6,143-6,156.

Seager, W. R., 1987, Caldera-like collapse at Kilbourne Hole maar, New Mexico: *New Mexico Geology Science and Service*, vol. 9, no. 4, p. 69-73.

Sheridan, M.F. and Wohletz, K.H., 1981, Hydrovolcanic Explosions: The Systematics of Water-Pyroclast Equilibration: *Science*, vol. 212, no. 4,501, p. 1,387-1,389.

Spieler, O., Kennedy, B., Kueppers, U., Dingwell, D. B., Scheu, B., and Taddeucci, J., 2004, The fragmentation threshold of pyroclastic rocks: *Earth and Planetary Science Letters*, vol. 226, no. 1, p. 139-148.

Shannon, C. E., 1948, A mathematical theory of communication: *Bell System Technical Journal*, vol. 27, p. 379-423.

Shannon, C. E., 1949, Communication in the presence of noise: *Proceedings of the Institute of Radio Engineers Journal,* vol. 37, p. 10-21.

Spector, A. and Grant, F. S., 1970, Statistical models for interpreting aeromagnetic data: *Geophysics*, vol. 35, no. 2, p. 293-302.

Sjogren, W. L., 1979, Mars gravity: High-resolution results from Viking Orbiter 2: *Science*, vol. 203, no. 4,384, p. 1,006-1,010.

Solomon, S. C. and Head, J. W., 1979, Vertical movement in mare basins- Relation to mare emplacement, basin tectonics, and lunar thermal history: *Journal of Geophysical Research*, vol. 84 (B4), p. 1,667-1,682.

Solomon, S. C. and Head, J. W., 1982, Mechanisms for lithospheric heat transport on Venus Implications for tectonic style and volcanism: *Journal of Geophysical Research*, vol. 87, p. 9,236-9,246.

Stoeser, D. B., Green, G. N., Morath, L. C., Heran, W. D., Wilson, A. B., Moore, D. W., and Gosen, B. S. V., 2005, Preliminary integrated geologic map databases for the United States: *US Geological Survey Open-File Report 2005-1351*, 1,351 p.

Tanaka, K. L., Scott, D. H., and Greeley, R., 1992, Global stratigraphy, *in* Kieffer, H.H., B.M. Jakosky, B.M., Snyder, C.W., M. Matthews, M. (eds.), *Mars*: University of Arizona Press (Tuscon, AZ), p. 345-382.

Taylor, J.R., 1997, Introduction to error analysis, the study of uncertainties in physical measurements (Volume 1), *2nd Ed.*: University Science Books (New York**),** 327 p.

Telford, W. M., Geldart, L. P., and Sheriff, R. E., 1990, Applied Geophysics (Volume1): Cambridge University Press (Cambridge), 751 p.

Tenzer, R., Sirguey, P., Rattenbury, M., and Nicolson, J., 2011, A digital rock density map of New Zealand: *Computers & Geosciences*, vol. 37, p. 1,181-1,191.

New Mexico Bureau of Geology and Mineral Resources, 2003, *Geologic Map of New Mexico*, scale 1:500,000.

U.S. Geological Survey, 2009, National Elevation Dataset (NED). Retrieved from http://seamless.usgs.gov.

U.S. Geological Survey, 2010, *Kilbourne Hole Quadrangle*: USGS 7.5 Minute Series, scale 1:24,000.

Verduzco, B., Fairhead, J. D., Green, C. M., and MacKenzie, C., 2004, New insights into magnetic derivatives for structural mapping: *The Leading Edge*, vol. 23, no. 2, p. 116-119.

White, J. D. L. and Ross, P. S., 2011, Maar-diatreme volcanoes: A review: *Journal of Volcanology and Geothermal Research*, v. 201, no. 1, p. 1-29.

Wieczorek, M. A., 2007, The gravity and topography of the terrestrial planets, *in* Spohn, T. (ed.), 2007, *Planets and Moons: Treatise on Geophysics Volume 10*: Elsevier (Amsterdam The Netherlands), p.165-206.

Wilson, L. and Head, J. W., 2004, Evidence for a massive phreatomagmatic eruption in the initial stages of formation of the Mangala Valles outflow channel, Mars: *Geophysical Research Letters*, vol. 31, no. 15, p. 1,051-1,054.

Wohletz, K. and Heiken, G., 1992, *Volcanology and Geothermal Energy*: University of California Press (Berkeley, CA), 432 p.

Wohletz, K. H. and McQueen, R. G., 1984, Experimental studies of hydromagmatic volcanism, *in* Woods, C. A. (ed.) *Explosive Volcanism: Inception, Evolution, and Hazards*: The National Academies Press (Washington, DC), p. 158-169.

Wohletz, K. H., 1986, Explosive magma-water interactions: Thermodynamics, explosion mechanisms, and field studies: *Bulletin of Volcanology*, vol. 48, no. 5, p. 245-264.

Wohletz K. H. and Sheridan M. F., 1982, Melt-water interactions: Series II experimental design: *Reports of the Planetary Geology Program 1981-1982 (NASA Technical Memo 84211)*, p. 169-171.

Wohletz, K. H. and Sheridan, M. F., 1983, Hydrovolcanic explosions: II, Evolution of basaltic tuff rings and tuff cones: *American Journal of Science*, vol. 283, no. 5, p. 385-413.

Table 1. Rock unit descriptions and physical properties

Rock units description and legend	Magnetic Susceptibility (10^{-3} SI)		Density (g/cm^3)	
	*ref	model	*ref	model
Post eruption deposit (Quaternary) Young alluvium, reworked pyroclastic deposits	0-20.9 [a, c]	26	1.69-2.58 [a, d]	2.174
Pyroclastic deposit of Kilbourne Hole (Quaternary) Ash flow tuffs, tuff ring, air fall (tephra)	0.65 -37.8 [a, b]	-7 to -16	1.13-2.35 [a, d]	2.2-2.3
Diatreme filling of Kilbourne Hole (Quaternary) body of brecciated rock formed by explosive or hydro-static forces, whether or not it is related to volcanism.	? ?	13-18	1.78-3.06 [a, d]	2.58-2.64
Potrillo volcanic field (Mid-Miocene - Quaternary) Basalt, basaltic andesites, andesites, and silicic tuffs	2-175 [a, b, c]	48 -147	1.54-3.00 [d]	2.820-2.996
Clastic -Camp Rice Fm. and Fort Stockton Fm. (Middle -Tertiary -Quaternary) Boulder, conglomerate, breccia, sandstone, alluvium	0-20.9 [a, c]	26-30	1.69-2.58 [a, d]	2.16
Volcanic intrusion (Middle -Tertiary - Quaternary) Diabase with peridotite xenoliths	0.2-175 [a, b, c]	174.99	2.34-3.34 [a, d]	3.28
Laramide fault-block uplift (Cambrian to Permian). marine limestone, dolomite, shale, and sandstone.	-10 - 30 [a, b,]	-2.5 to 24	1.89-3.01 [a, d]	2.07-2.16
Basement rock (Pre Cambrain) Granite	0-50 [a, b]	74.97	2.30-2.94 [a, d]	2.67

***** *Note :* These numbers are the maximum and minimum values of similar rock types reported by [a] Hunt et al. (1995), [b] Gidley and Stuart (1980), [c] Gubbins and Herrero-Bervera (2007), [d] Tenzer et al. (2011)

Table 2. List of physical parameters.

Variables	Units	Descriptions
CR	-	The conversion rate or the efficiency of the eruption
ΔKE	J	Kinetic energy of the eruption
ΔPE_{dia}	J	Potential energy inside the diatreme during the eruption
ΔPE_{sys}	J	Potential energy of the masses that were released by the eruption
ΔPE_{exc}	J	Potential energy of the masses that were excavated by the eruption
dia	-	Value for surrounding of volcanic vent structure and the atmosphere
exc	-	Value for excavated masses of magmatic particles and water vapor
p_1	bar	Litho-static load pressure in the magma source region
p_o	bar	Atmospheric pressure at the surface of the volcano
λ	-	Pore pressure as a fraction of lithostatic load
τ_o	bar	Cohesive strength of rock or other material
m_f	kg	Mass of volcanic fragments including melt and pyroclastic deposit
m_w	kg	Mass of meteoric water in a phreatomagmatic eruption
m_m	kg	Mass of magma or melt in a phreatomagmatic eruption
m_w / m_m	-	Water to magma mass ratio
v_{max}	m/s	Initial gas expansion velocity
C_{vm}	$J.kg^{-1}.K^{-1}$	Heat capacity of molten basalt
p_o	MPa	Gas pressure at the final stage of the eruption
p_1	MPa	Gas pressure at the time of eruption
V_{dia}	m^3	Volume of the entire volcanic system (the diatreme)
V_{exc}	m^3	Volume of the material excavated form the eruption
T_m	K	Temparature of molten basaltic magma
T_e	K	Temperature of an idealized Earth surface
ΔW_{sys}	J	Works in a volcanic system that causes the masses to release
ΔU	J	Magma thermal energy
θ	radian	The tilt angle derivative in vertical direction
$\partial M/\partial x$	m	The first order derivatives of the magnetic field M in the x direction
$\partial M/\partial y$	m	The first order derivatives of the magnetic field M in the y direction
$\partial M/\partial z$	m	The first order derivatives of the magnetic field M in the z direction

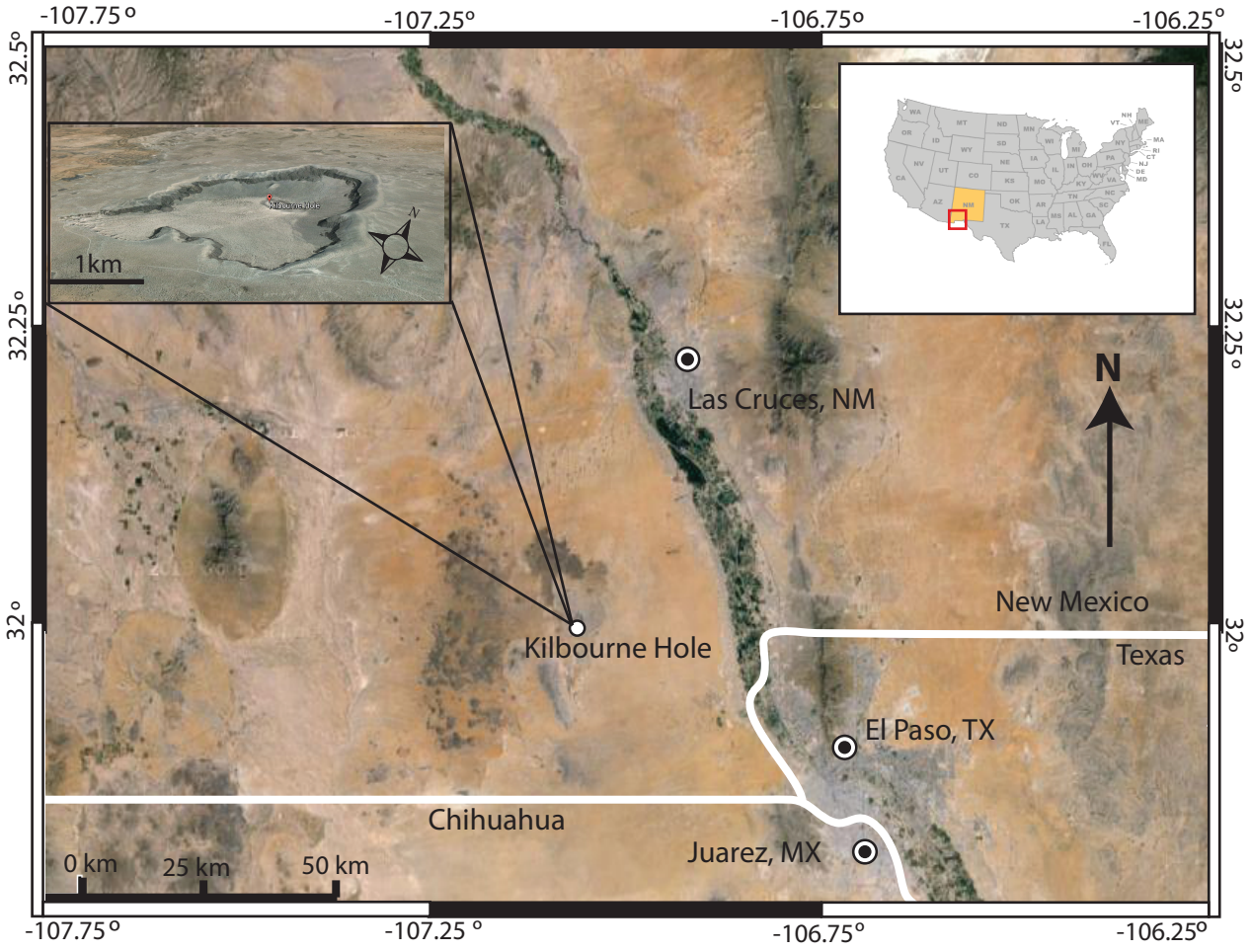

Figure 1. Location of Kilbourne Hole in southern Doña Ana County, New Mexico (imagery from Google Earth, 2008).

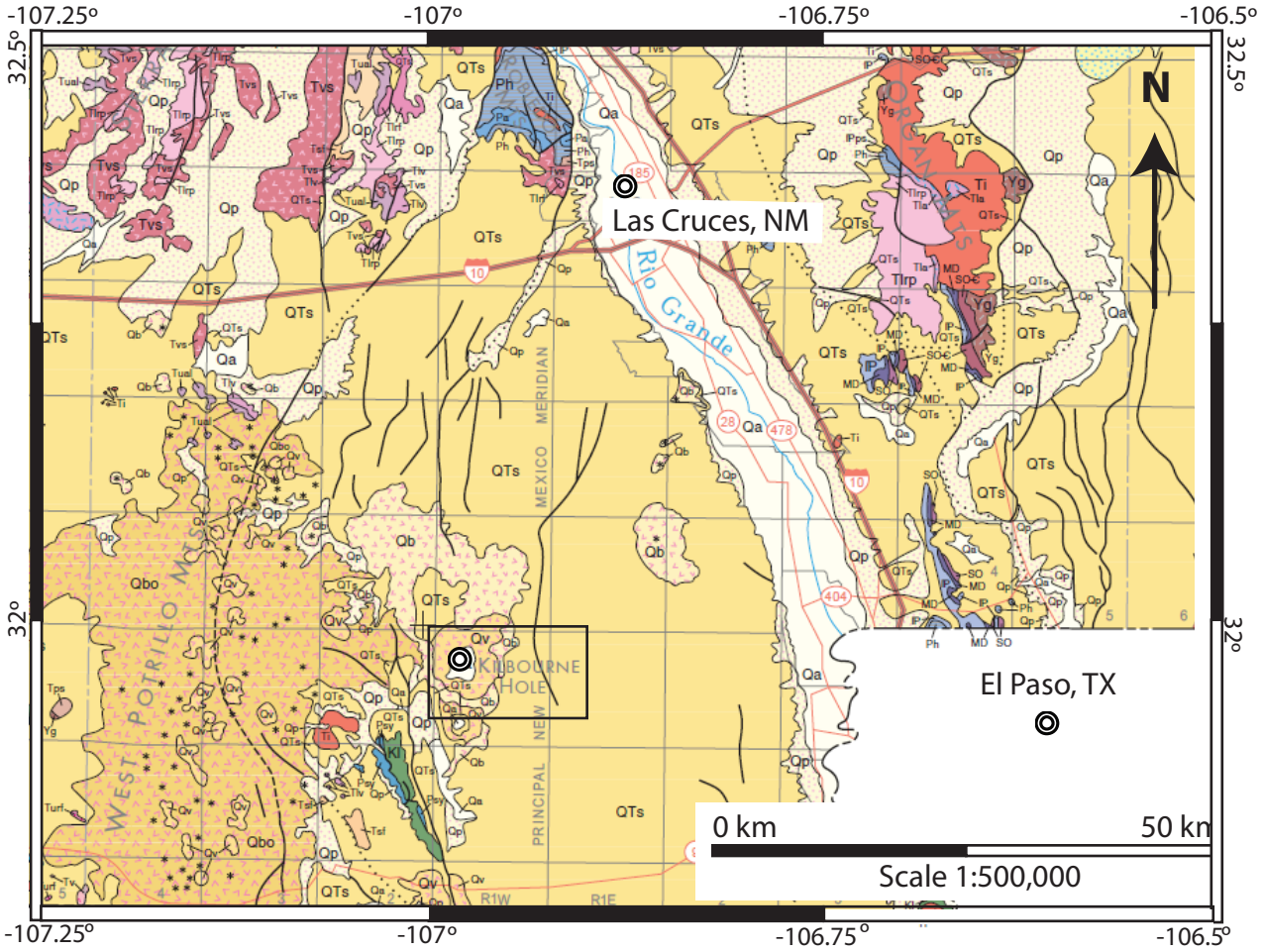

Figure 2. Geologic map of the Mesilla Basin. The Mesilla basin is the southern end of the Rio Grande basin. The box shows the location of Kilbourne Hole. Modified from Scholle (2003).

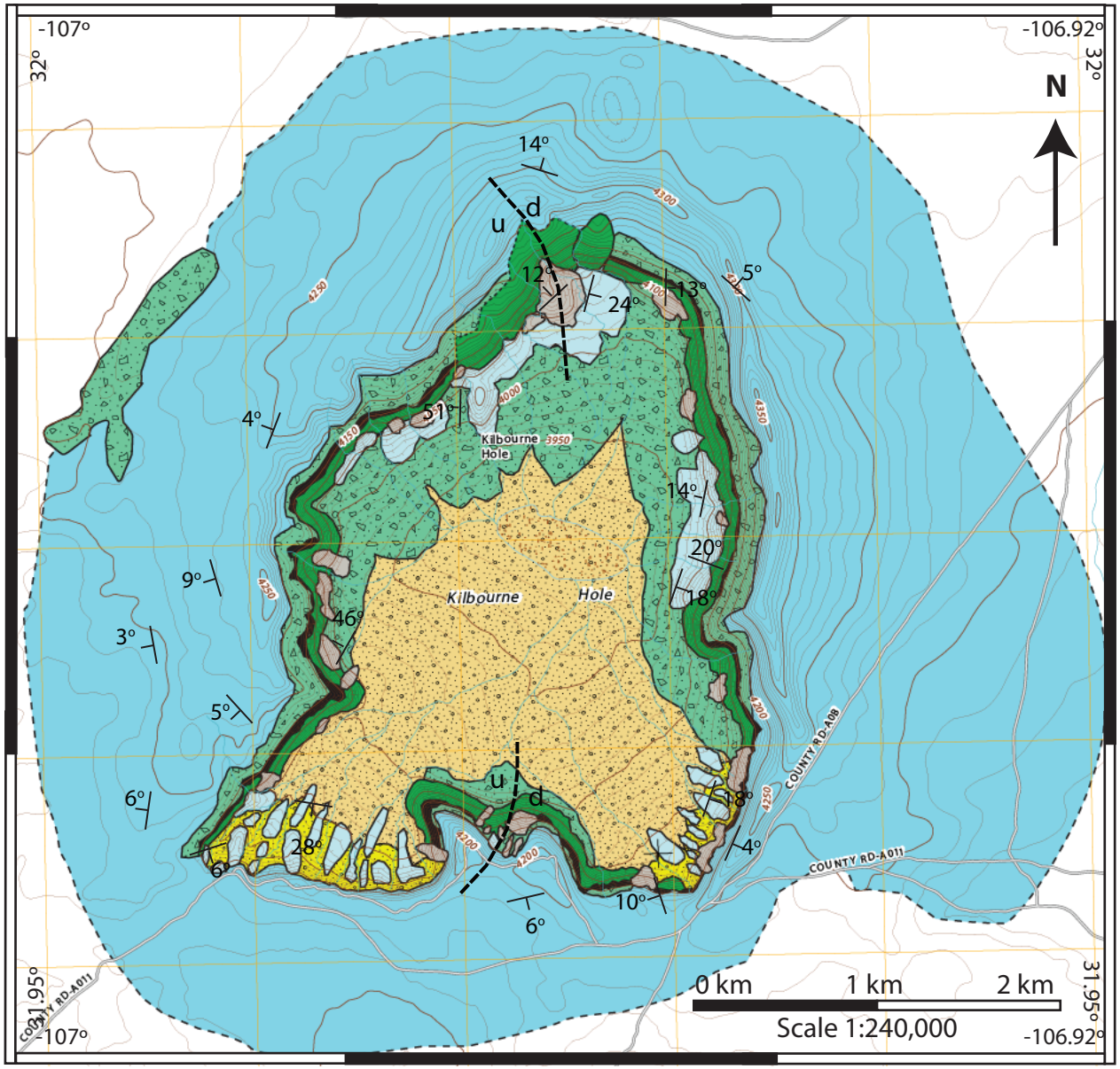

Legend

- Young Alluvium
- Talus
- Tuff Ring
- Volcanic Breccia
- Potrillo Basalt
- Camp Rice Fm.
- Contact
- Fault (u / d)
- Strike and Dip
- Rotated Blocks of Tuff Ring
- Rotated Blocks of Potrillo Basalt

Figure 3. Geologic Map of Kilbourne Hole, NM. Base map is U.S Geological Survey Kilbourne Hole Quadrangle 1:24,000 scale topographic map (USGS, 2010).

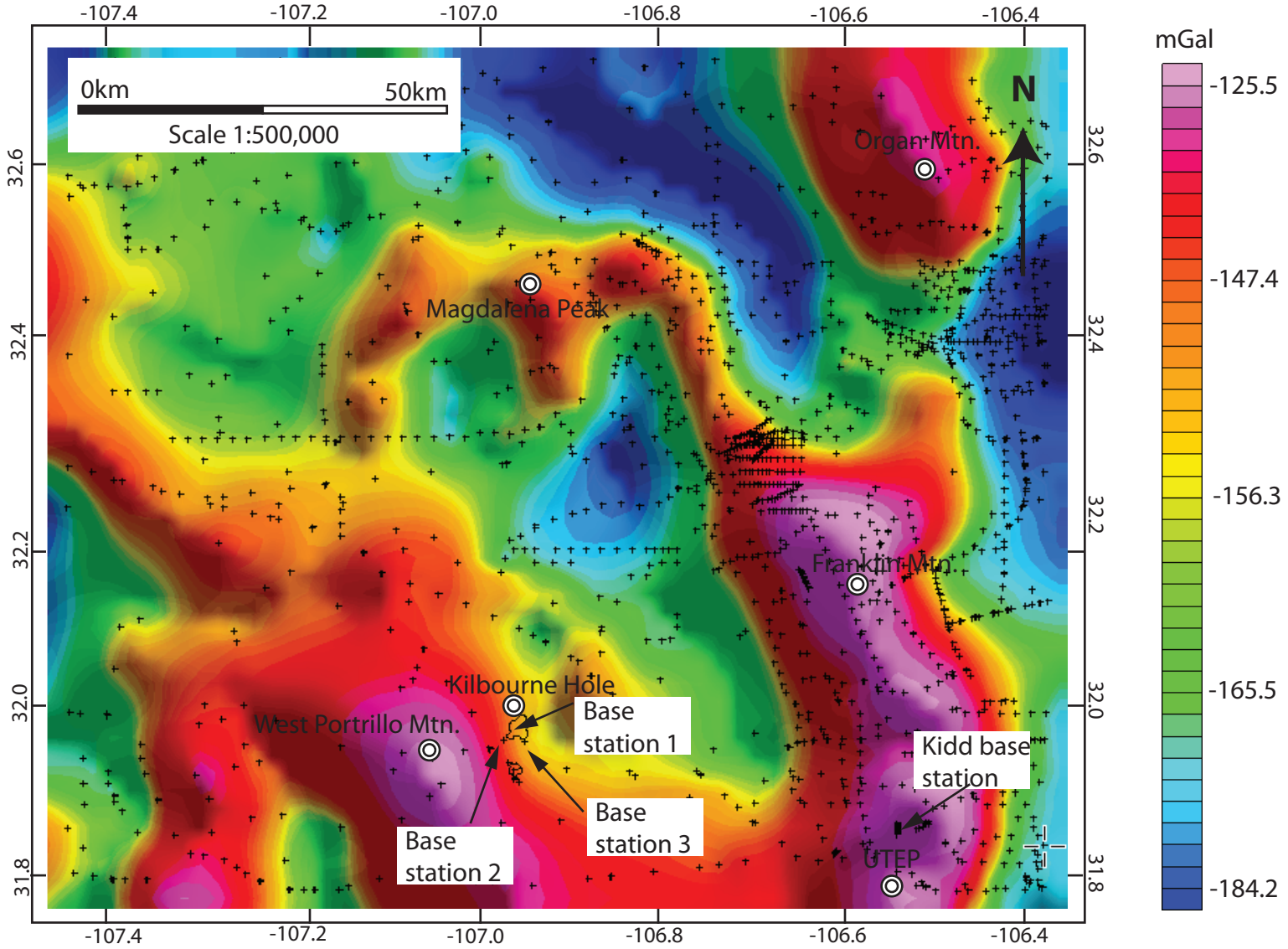

Figure 4. Bouguer gravity anomaly map of the Mesilla basin. Locations of base stations used during the gravity survey are shown. Reducing density of 2670 kg/m^3 is used for Bouguer correction. We generated this map using a set of gravity data obtained from the North American Gravity Database (Hildenbrand et al., 2002a). Black crosses are gravity stations.

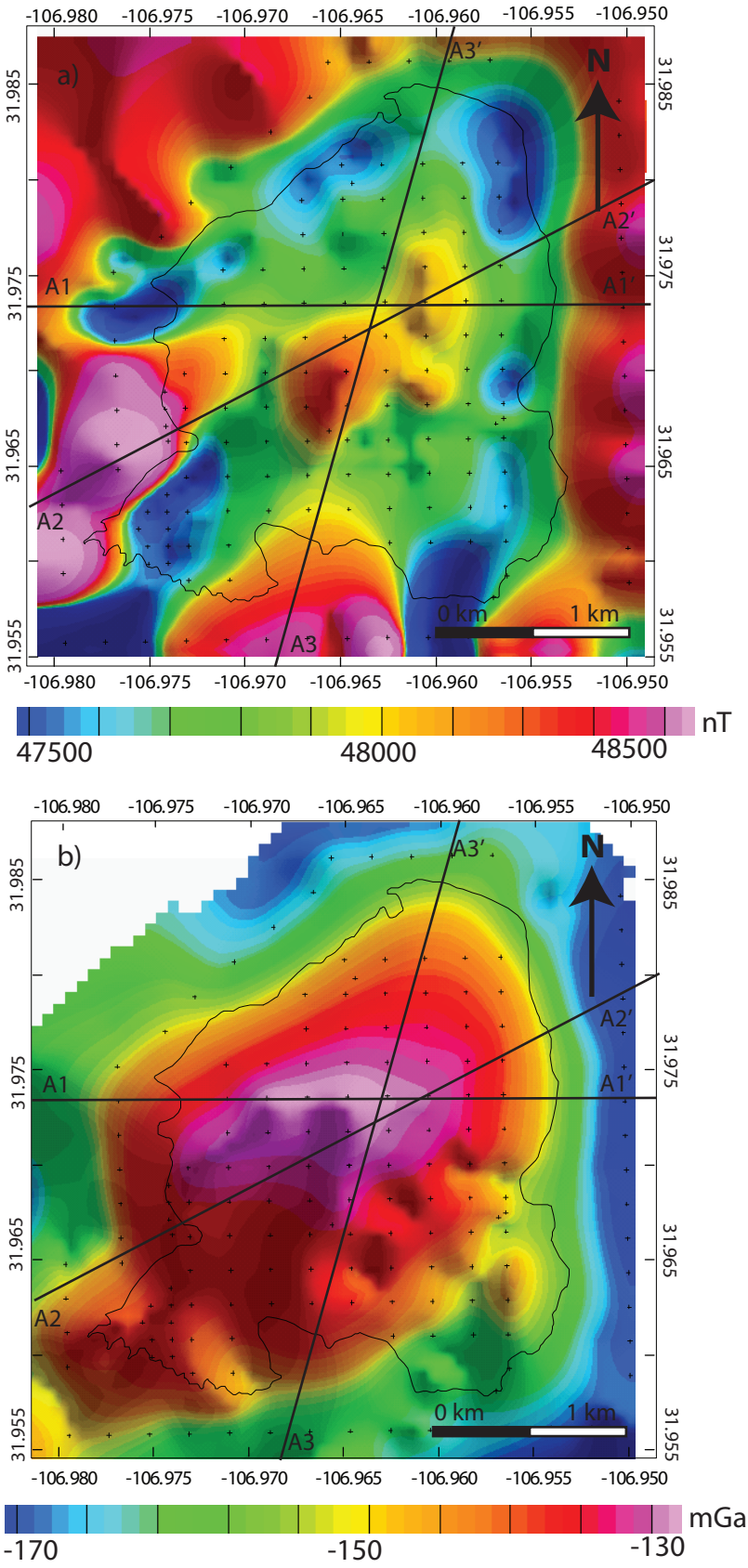

Figure 5. (a) Reduced to pole magnetic anomaly map of Kilbourne Hole (our data). (b) Bouguer gravity anomaly map of Kilbourne Hole (our data). Black lines represent the transects along which the inversion models in Figures 7-9 were constructed.

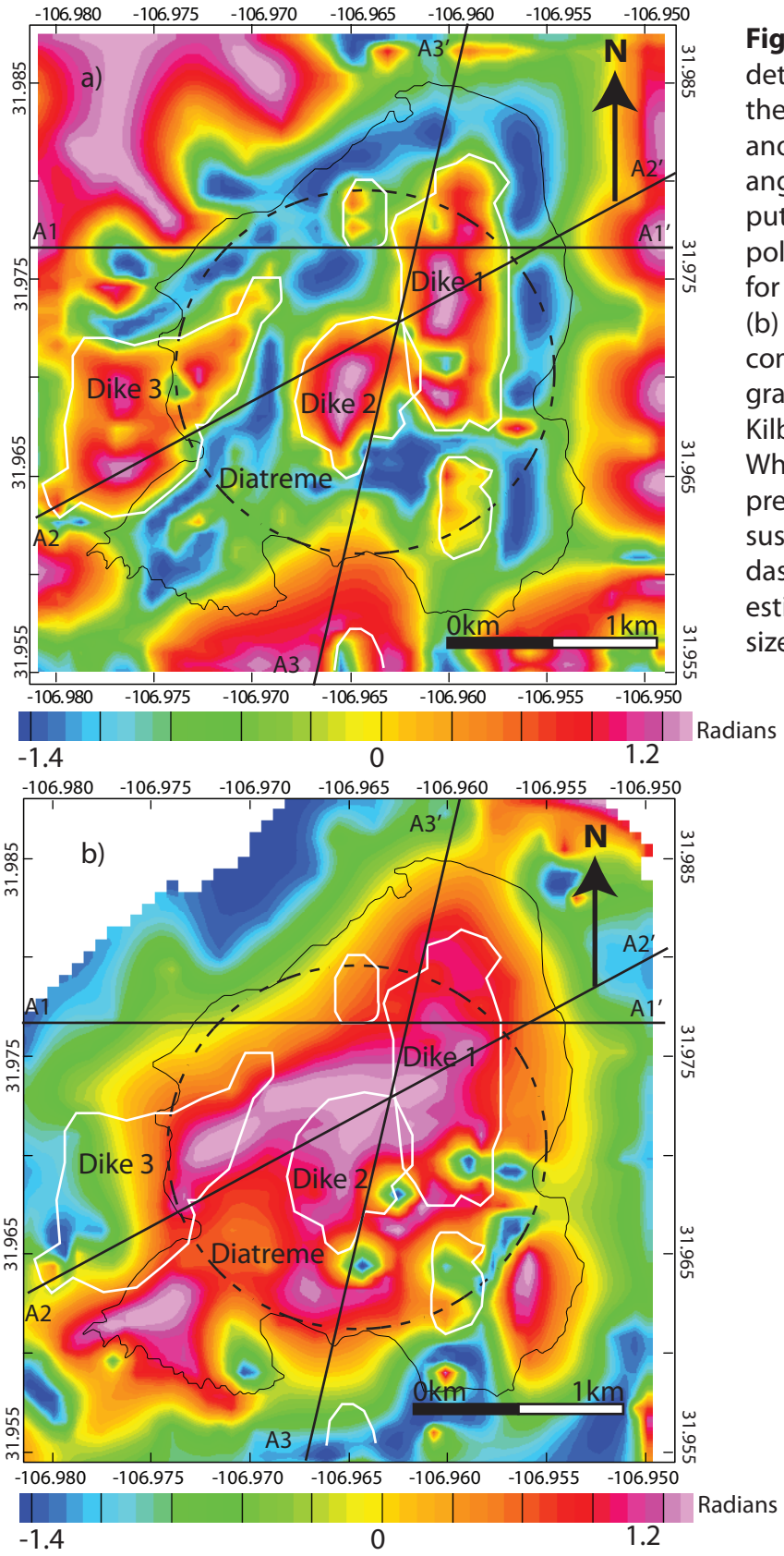

Figure 6. Results of edge detection methods applied to the magnetic and gravity anomalies in Figure 5. (a) Tilt angle derivative map computed from the reduced-to-pole magnetic anomaly data for Kilbourne Hole (our data). (b) Tilt angle derivative map computed from the Bouguer gravity anomaly data for Kilbourne Hole (our data). White outlines show the interpreted boundaries of suspected intrusions. The dashed circle denotes the best estimate for the original crater size.

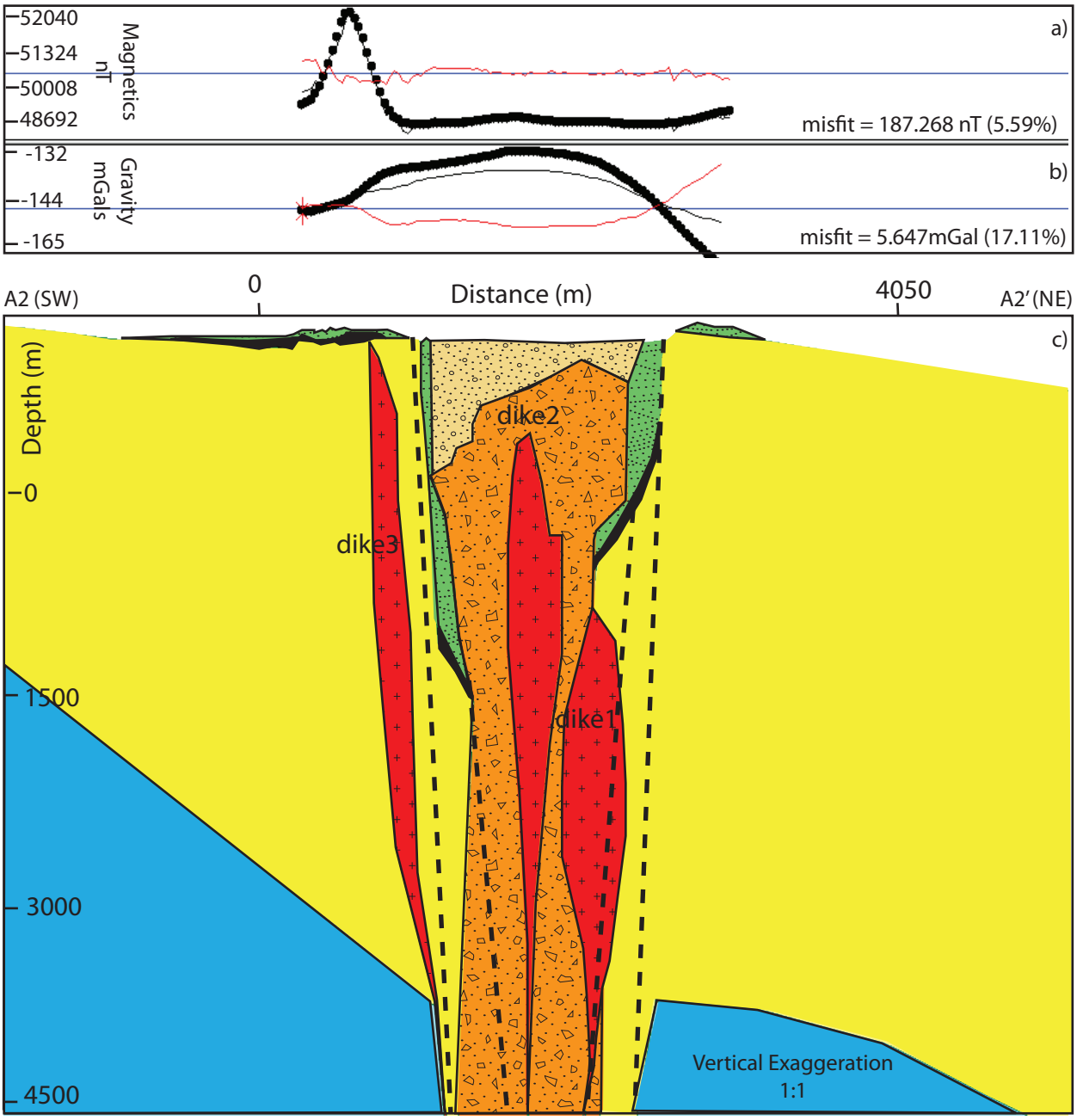

Figure 8. (a) 2D magnetic inverse model along transect A2-A2′ of Kibourne Hole from the reduced to pole magnetic anomaly map (Rhodes and Hurtado, 2012). (b) 2D gravity inverse model along transect A2-A2′ of Kilbourne Hole (our data). (c) Geologic cross-section of Kilbourne Hole arranged from south west to north east across Kilbourne Hole along transect A2-A2′. Location of along transect A2-A2′ is shown in Figure 5. This cross-section of Kilbourne Hole was developed using the two-dimensional integrated gravity and magnetic inversion method using our gravity and magnetic data. Density and magnetization constraints are given in Table 1. Dots are observed gravity values in b) and observed magnetic intensity in a). Black lines are the calculated gravity and magnetic anomaly. Red lines show the misfit values between the observed and calculated data. Dashed black lines in c) are the estimated locations of buriedfault zones from caldara-like collapsing of Kilbourne Hole after the eruption.

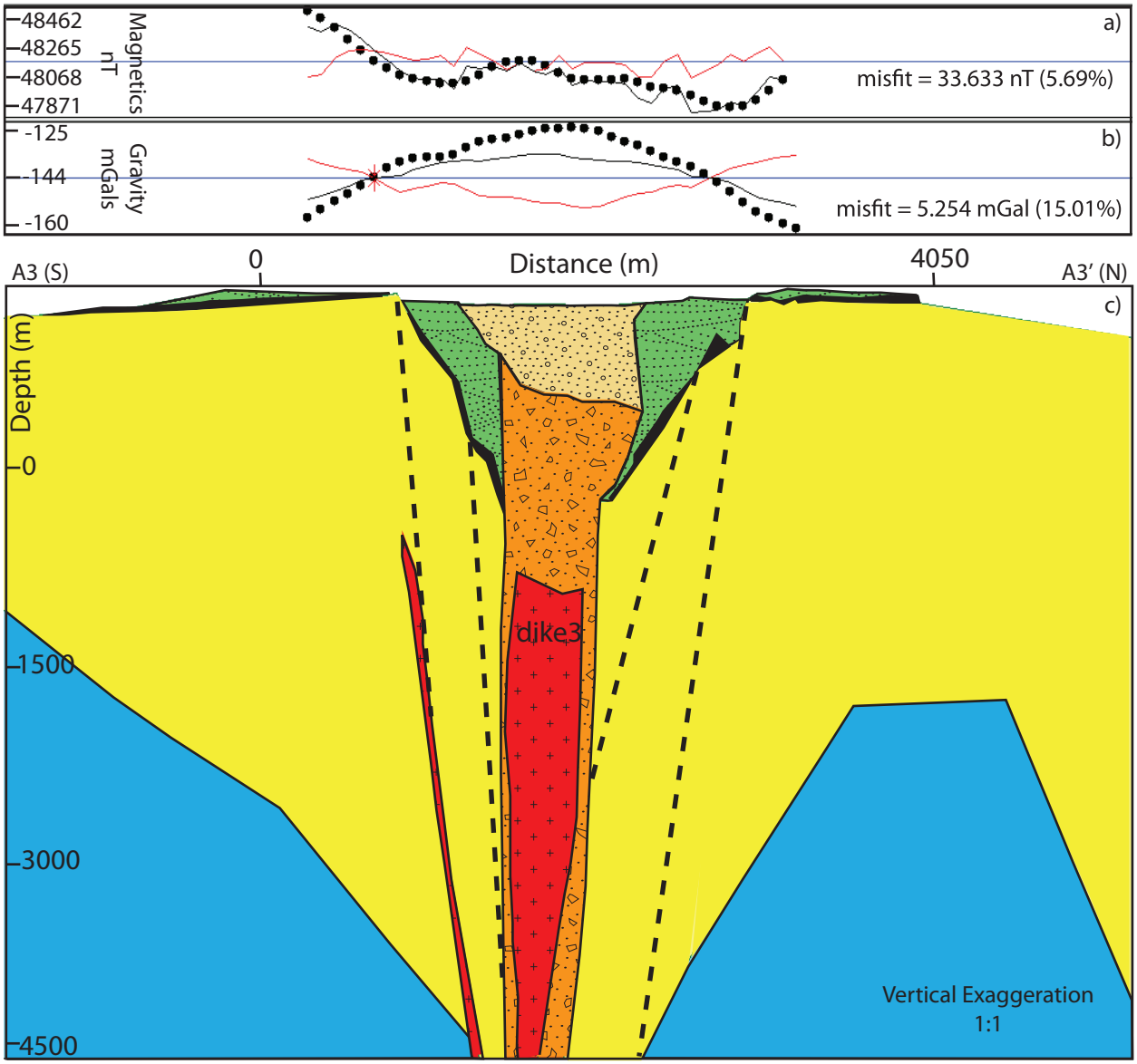

Figure 9. (a) 2D magnetic inverse model along transect A3-A3' of Kibourne Hole from the reduced to pole magnetic anomaly map (Rhodes and Hurtado, 2012). (b) 2D gravity inverse model along transect A3-A3' of Kilbourne Hole (our data). (c) Geologic cross-section of Kilbourne Hole arranged from south to north across Kilbourne Hole along transect A3-A3'. Location of along transect A3-A3' is shown in Figure 5. This cross-section of Kilbourne Hole was developed using the two-dimensional integrated gravity and magnetic inversion method using our gravity and magnetic data. Density and magnetization constraints are given in Table 1. Dots are observed gravity values in b) and observed magnetic intensity in a). Black lines are the calculated gravity and magnetic anomaly. Red lines show the misfit values between the observed and calculated data. Dashed black lines in c) are the estimated locations of buried-fault zones from caldara-like collapsing of Kilbourne Hole after the eruption.

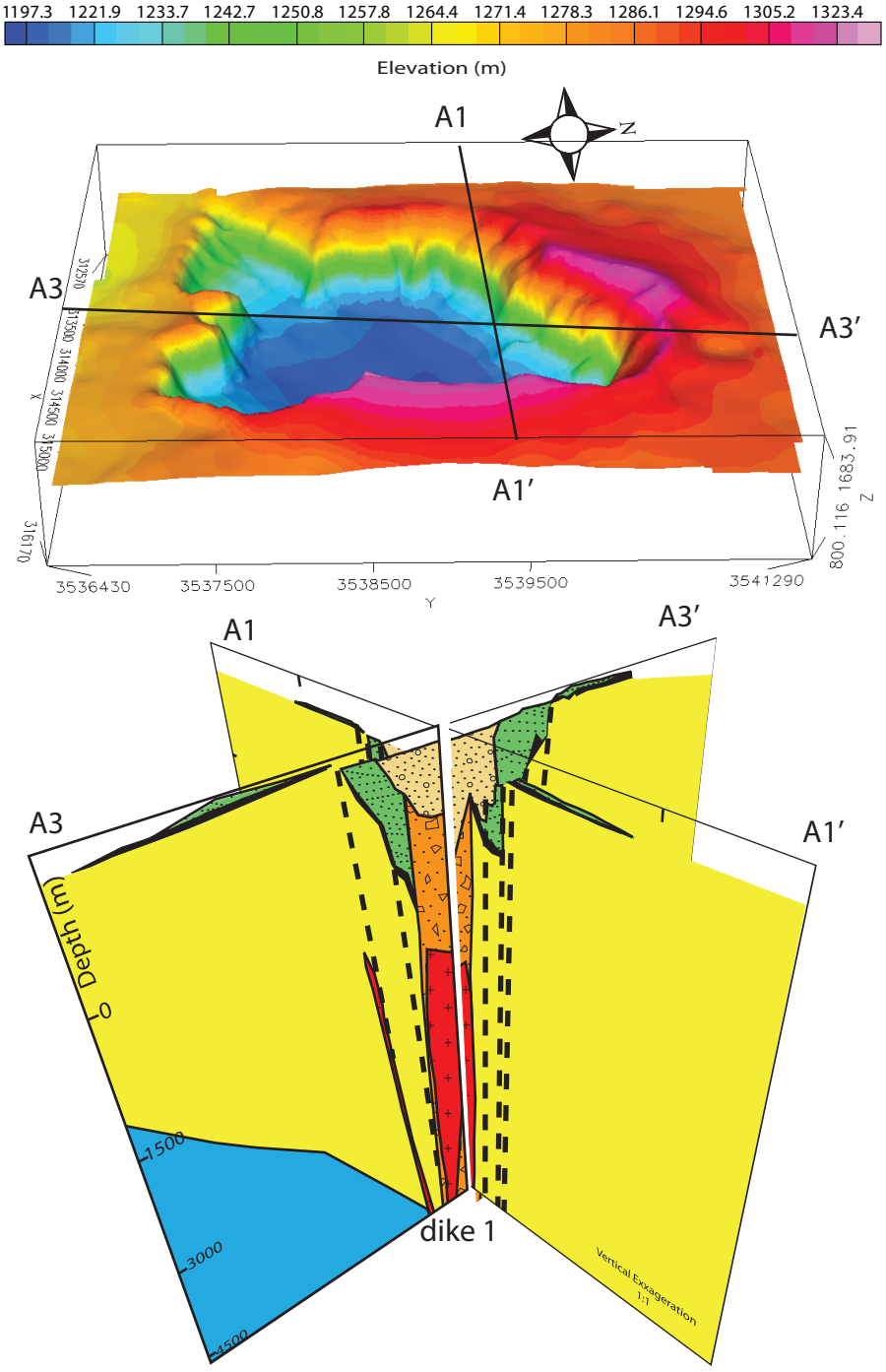

Figure 10. A fence diagram showing connectivity of dike 1 on cross-sections A1-A1′ and A3-A3′. The 3D perspective view of the surface topography of Kilbourne Hole is shown above the fence diagram for geographic context.

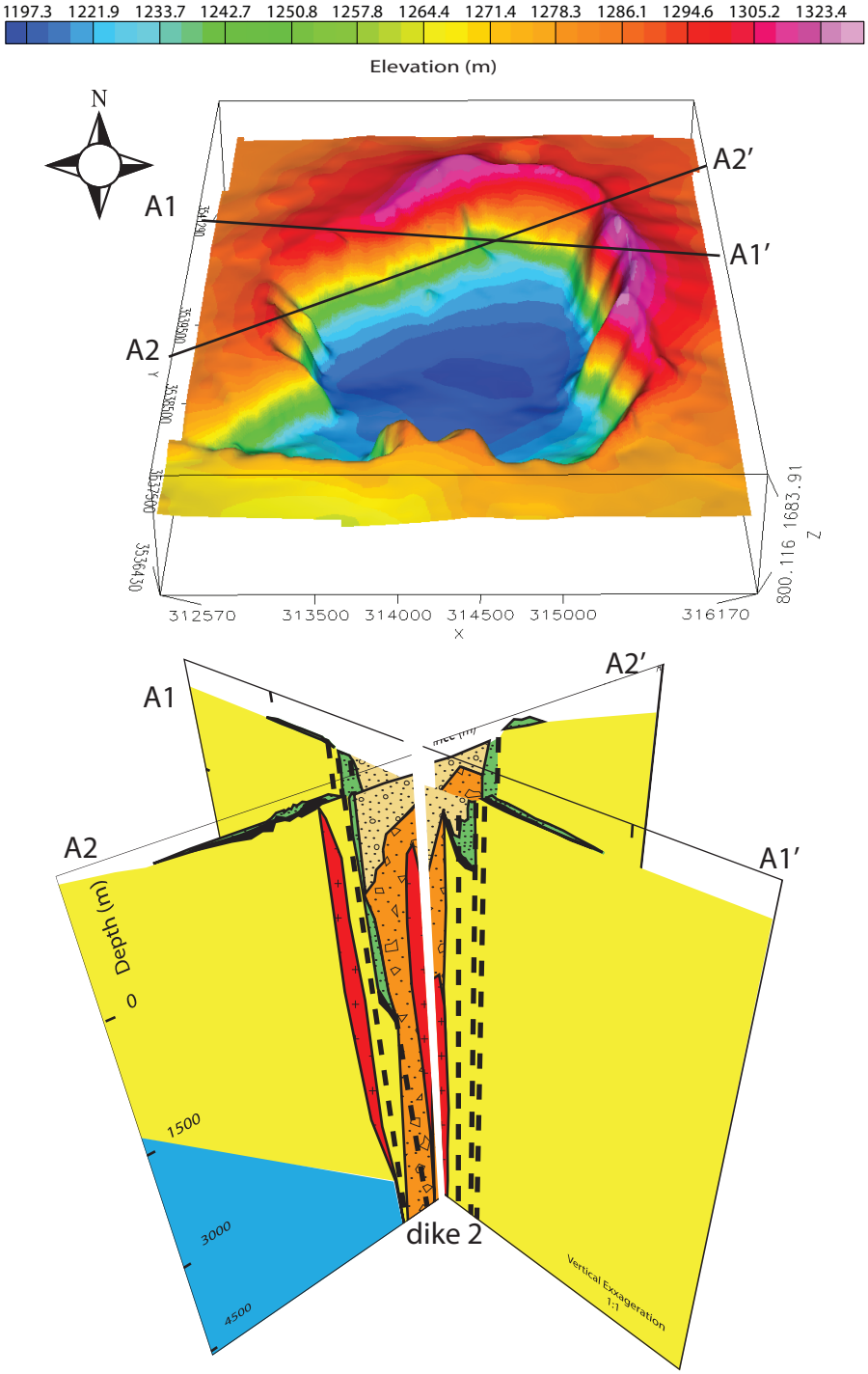

Figure 11. A fence diagram showing connectivity of dike 2 on cross-sections A1-A1′ and A2-A2′. The 3D perspective view of the surface topography of Kilbourne Hole is shown above the fence diagram for geographic context.

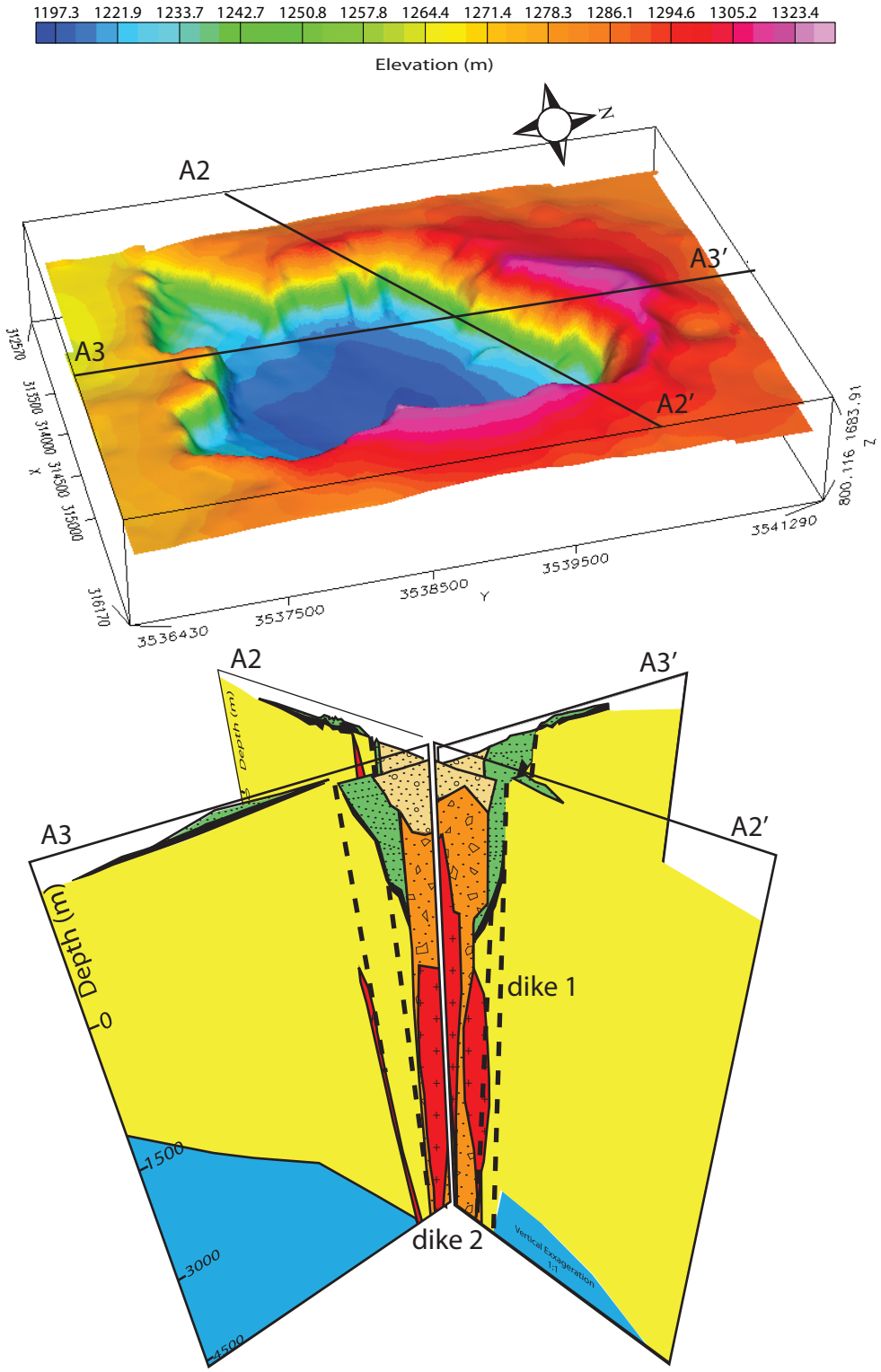

Figure 12. A fence diagram showing connectivity of dike 2 on cross-sections A2-A2′ and A3-A3′. The 3D perspective view of the surface topography of Kilbourne Hole is shown above the fence diagram for geographic context.

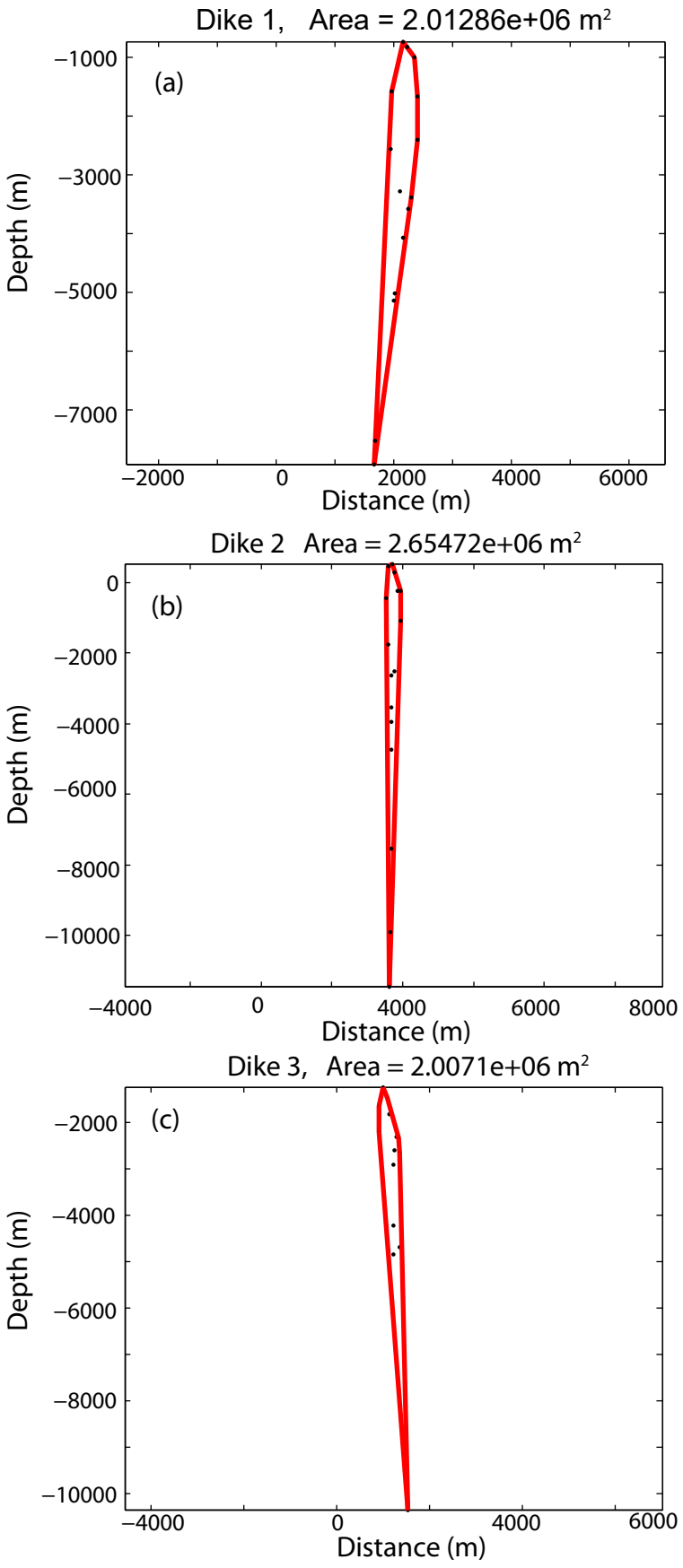

Figure 13. MAT LAB profiles of intrusion zones separated from integrated gravity-magnetic models of Kilbourne Hole. Black dots showed locations of where the intrusion zone appeared on the models. Red lines are the best fit geometrical shapes to the intrustion bodies generated by MAT LAB. The areas of intrusion zones were calculated using this overestimated-best fit of the geometrical bodies (red lines). In (a) profile of dike 1 derived from cross-section A2-A2′, (b) profile of dike 2 derived from cross-section A2-A2′, and (c) profile of dike 3 derived from cross-section A1-A1′.

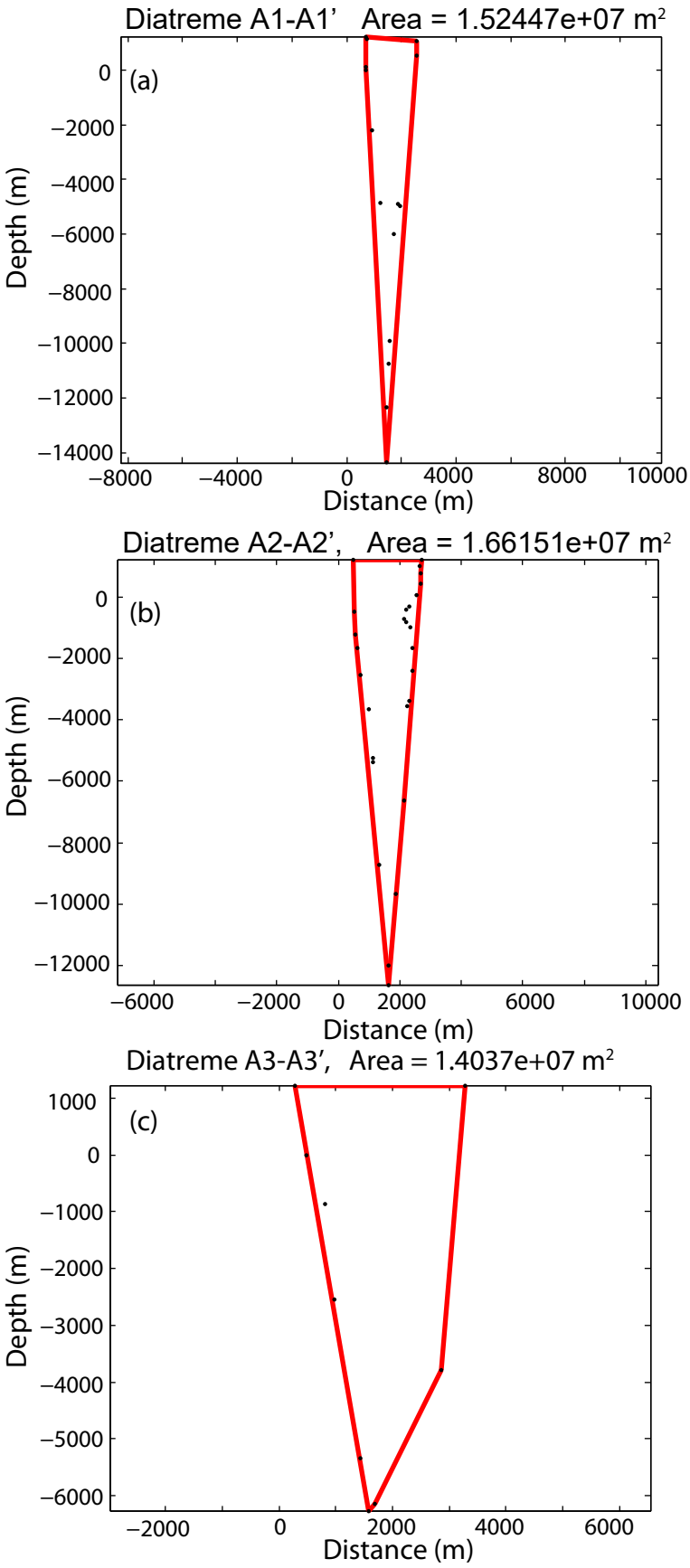

Figure 14. MAT LAB profiles of the diatreme separated from the integrated gravity-magnetic models of Kilbourne Hole. Black dots show locations of where the diatreme appeared on the models. Red lines are the best fit geometrical shapes to the diatreme bodies generated by MAT LAB. The areas of diatreme were calculated using this overestimated-best fit of geometrical bodies (red lines). In (a) profile of diatreme derived from cross-section A1-A1′, (b) profile of diatreme derived from cross-section A2-A2′, and (c) profile of diatreme derived from cross-section A3-A3′.

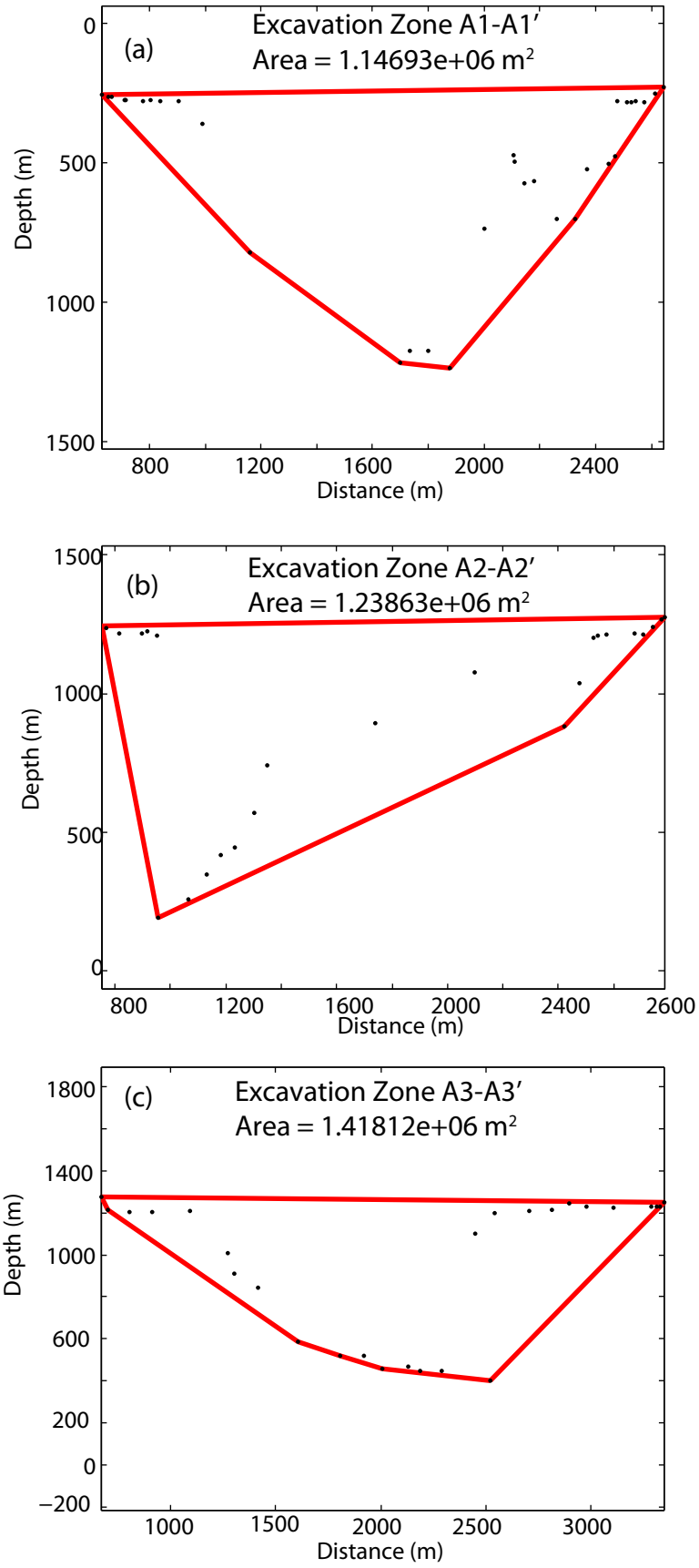

Figure 15. MAT LAB profiles of the excavation zone separated from the integrated gravity-magnetic models of Kilbourne Hole. The zone of excavation is considered to be the area of the present day crater and young alluvial material that is filling the crater. The bodies of young alluvial filling the crater are shown in all three models. Black dots show locations of where the excavation zone appeared on the models. Red lines are the best fit geometrical shape to the excavation zone generated by MAT LAB. The area of excavation zones were calculated using this overestimated-best fit of geometrical bodies (red lines). In (a) the profile of excavation zone derivedfrom cross-section A1-A1′, (b) profile of excavation zone derived from cross-section A2-A2′, and (c) profile of excavation zone derived from cross-section A3-A3′.

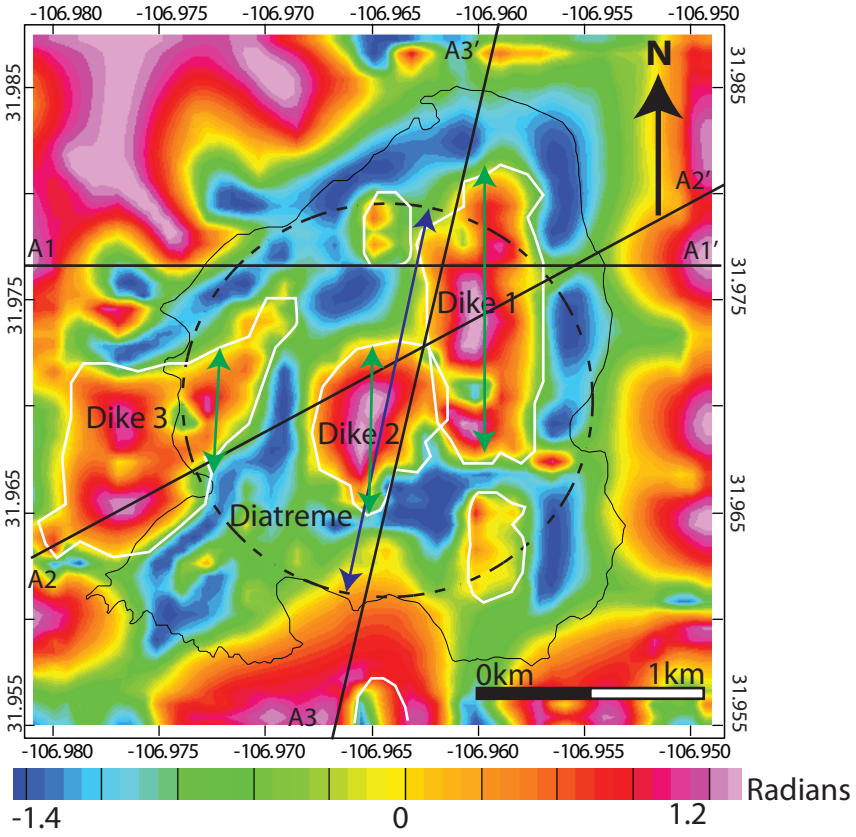

Figure 16. Edge detection results of magnetic anomalies on a tilt angle derivative map computed from the reduced to pole magnetic anomaly data for Kilbourne Hole (our data). White outlines show the boundaries of possible intrusion zones. Dashed circle is the best estimated boundary of the original crater at the time of eruption. Black lines are location of inversion models A1-A1′ and A2-A2′ and A3-A3′. Green arrows indicate the length of dike1, dike2, and dike 3. Blue arrow indicates the length of diatreme body, and excavation zone.

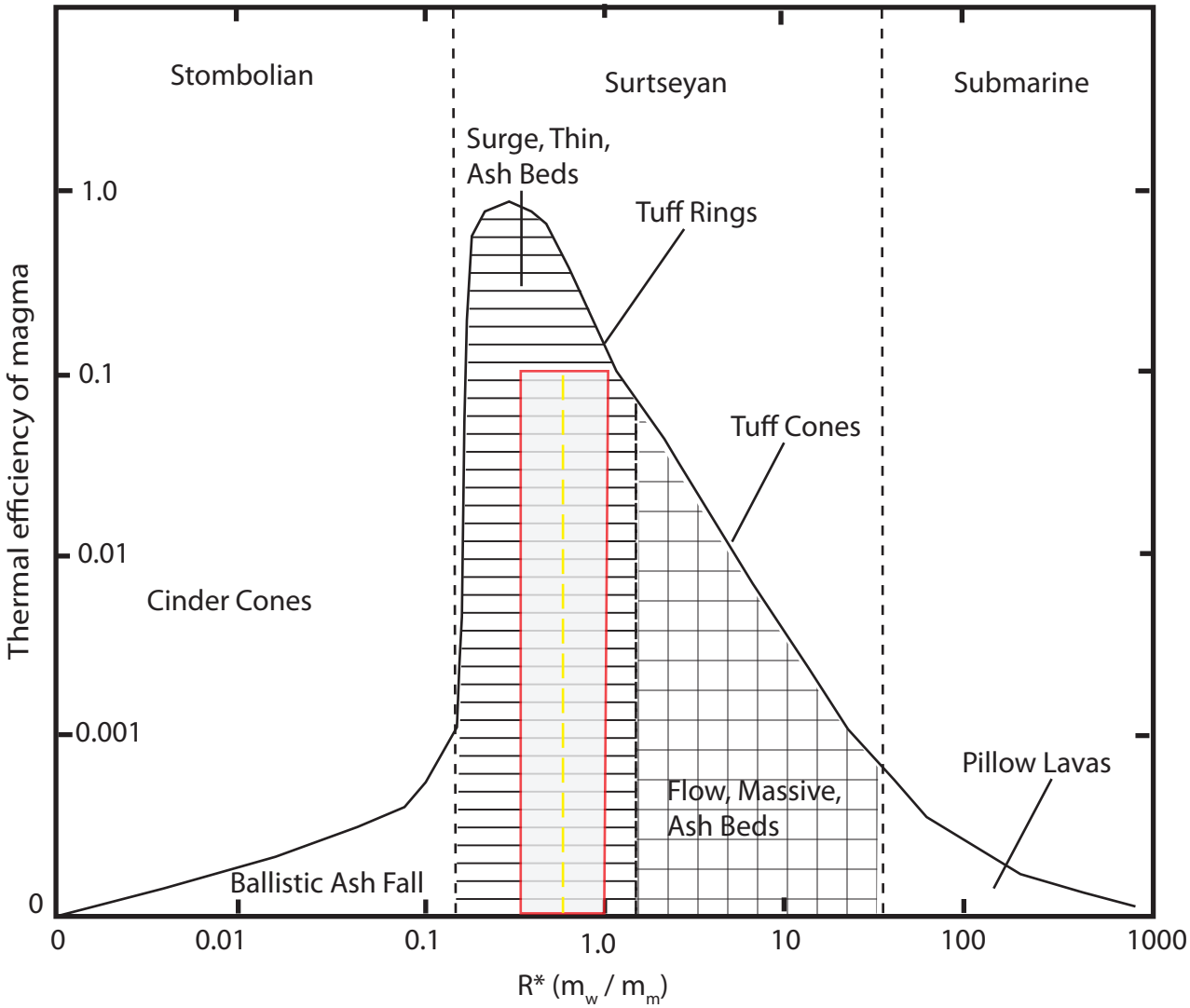

Figure 17. Ranges of thermal efficiency of phreatomagmatic eruptions shown as a function of water to magma mass ratio. Ranges are indicated types of eruptions (Strombolian, Surtseyan, and submarine) as well as the corresponding landforms and depositional facies (adapted from Wohletz and McQueen, 1984). Shaded red box indicates ranges of water to magma mass ratio (0.79 ± 0.23) predicted for Kilbourne Hole eruption.

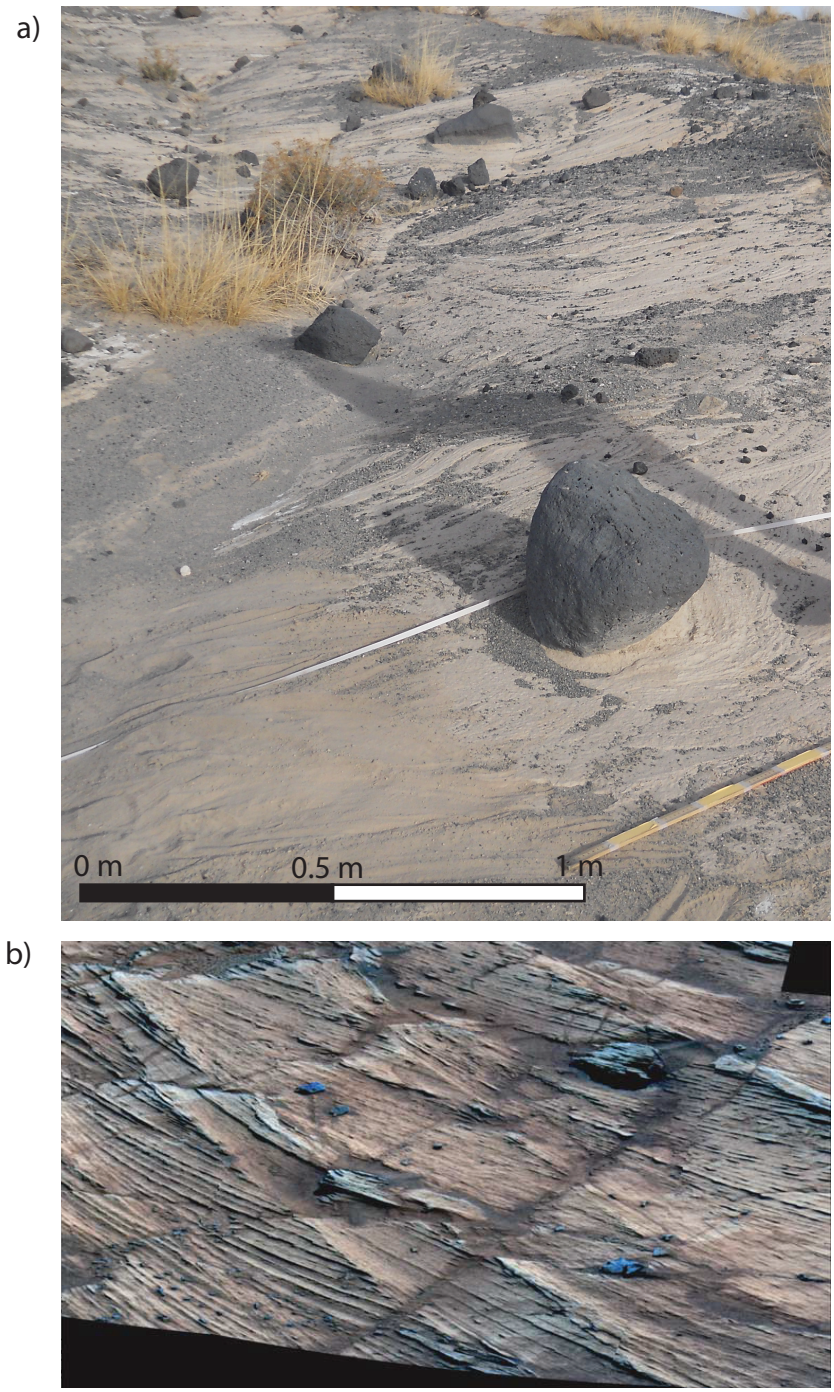

Figure 18. (a) Cross bedded tuff ring, volcanic blocks, and volcanic sags found on the west rim of Kilbourne Hole. The image is a true color photograph taken by the authors in November 2014. (b) High-angle cross bedding, volcanic blocks, and volcanic sags found on Home Plate, Mars. The mosaic image is a false color stretch photograph. The horizontal distance across the lower part of both images is approximately 1.5 m. (mosaic credit Squyres et al., 2007).

Appendix A: Kilbourne Hole Gravity Survey Data and Data Correction

A total of 172 gravity readings from Kilbourne Hole are included in this appendix. In this appendix, all the data and data corrections are displayed in an excel spreadsheet file. Field data collected for gravity station include latitudes, longitudes, the gravity meter reading from the Lacoste and Romberg G-30 unit, and elevation measurement from the Topcon GB-1000 unit. All gravity readings from Lacoste and Romberg G-30 unit are adjusted for the dial constant (LaCoste and Romberg, 2004). Corrected data also included in this appendix are: (1) terrain correction, (2) tidal drift correction, (3) atmospheric correction, 4) free-air correction, and 5) Bouguer correction using a reduce density of 2670 kg/m^3. The formula and constants used in our data correction process are based on Briesacher et al. (2002) and Hildenbrand et al. (2002).

References

Briesacher, A., Flanagan, G., Hinze, W. J., Hittelman, A. M., Keller, G. R., Kucks, R. P., and Webring, M., 2002, *Rationale and operational plan to upgrade the US gravity database*. US Department of the Interior, US Geological Survey.

Hildenbrand, T. G., Briesacher, Allen, Flanagan, Guy, Hinze, W.J., Hittelman, A.M., Keller, G.R., Kucks, R.P., Plouff, Don, Roest, W.R., Seeley, John, Smith, D.A., and Webring, Mike, 2002, Rationale and Operational Plan to Upgrade the U.S. Gravity Database: U. S. Geological Survey, Open-File Report 02-463, 12p.

LaCoste and Romberg, 2004, Instruction Manual Model G & D GravityMeters. LaCoste&Romberg, Ver. 4-2004, 127 p.

date	Station	Lat	Long	Elev. Height	time	time (julian	B1 time diff	B2timediff	kidds timediff	delta G-reading	G-milligals	B1 drift	B1-diff	B2drift	B2-diff	kidds drift	kidds-diff	total-drift	abs G (milliGals	Latitude correction	FA correction	B correction	terrain correction	ATM effects	G-theory	c-b anomaly
6/6/13	Kidds	31.7719	-106.506	1186.5	6:36	6.60	0.00	0.00	0.00	2647.21	2707.63	0.00	0.00	0.00	0.00	2707.63	0.00	0.00	979107.52	0.529833608	-366.108334	132.83235	*	0.77	979465.86	#VALUE!
6/6/13	B2	31.957892	-106.9798	1247.385	9:04	9.07	0.00	0.00	2.47	2623.01	2682.86	0.00	0.00	2682.86	0.00	2682.93	-24.71	-24.71	979082.8139	0.716764691	-384.888032	139.64862	0.647316	0.76	979480.92	-151.46231
6/6/13	B1	31.966394	-106.9666	1181.038	10:43	10.72	0.00	1.65	4.12	2634.54	2694.66	2694.66	0.00	2694.75	11.90	2694.78	-12.86	-0.96	979106.5593	0.723113032	-364.421855	132.22087	6.764922	0.77	979481.61	-135.31767
6/6/13	B2	31.957892	-106.9798	1247.385	9:04	9.07	0.00	0.00	2.47	2616.08	2675.76	0.00	0.00	2675.76	-7.09	2675.83	-31.80	-38.90	979068.6245	0.716764691	-384.888032	139.64862	0.647316	0.76	979480.92	-165.65176
6/6/13	B1	31.966394	-106.9666	1181.038	10:43	10.72	0.00	1.65	4.12	2635.65	2695.80	2695.80	1.14	2695.89	13.03	2695.91	-11.72	2.45	979109.9684	0.723113032	-364.421855	132.22087	6.764922	0.77	979481.61	-131.90852
6/6/13	M101	31.968225	-106.9668	1178.124	11:04	11.07	0.35	2.00	4.47	2635.56	2695.71	2695.72	1.06	2695.82	12.96	2695.83	-11.80	2.22	979109.7375	0.724452225	-363.522942	131.89463	7.090988	0.77	979481.76	-132.53455
6/6/13	M102	31.96996	-106.9668	1174.944	11:21	11.35	0.63	2.28	4.75	2636.36	2696.52	2696.55	1.89	2696.65	13.79	2696.66	-10.97	4.71	979112.2314	0.725713009	-362.541974	131.53862	7.446819	0.77	979481.9	-130.4506
6/6/13	M103	31.971813	-106.9669	1172.514	11:37	11.62	0.90	2.55	5.02	2636.87	2697.05	2697.09	2.43	2697.19	14.33	2697.19	-10.45	6.31	979113.8325	0.727049615	-361.792361	131.26658	7.718727	0.77	979482.05	-129.20558
6/6/13	M104	31.973613	-106.9669	1173.32	11:53	11.88	1.17	2.82	5.28	2637.23	2697.41	2697.47	2.81	2697.57	14.71	2697.56	-10.07	7.45	979114.9728	0.728338691	-362.040978	131.35681	7.628539	0.77	979482.2	-128.14313
6/6/13	M105	31.975466	-106.967	1180.813	12:07	12.12	1.40	3.05	5.52	2635.82	2695.97	2696.04	1.38	2696.14	13.28	2696.13	-11.51	3.15	979110.6726	0.729655845	-364.352374	132.19568	6.790098	0.77	979482.35	-131.95965
6/6/13	M106	31.977229	-106.9666	1190.526	12:29	12.48	1.77	3.42	5.88	2633.58	2693.68	2693.76	-0.90	2693.87	11.01	2693.84	-13.79	-3.68	979103.8406	0.730899312	-367.348575	133.28308	5.703248	0.77	979482.49	-138.11281
6/6/13	M108	31.979108	-106.9649	1196.67	12:45	12.75	2.03	3.68	6.15	2632.41	2692.48	2692.58	-2.09	2692.68	9.83	2692.65	-14.98	-7.24	979100.2818	0.732215028	-369.243821	133.97092	5.015754	0.77	979482.64	-141.30417
6/6/13	M109	31.977156	-106.9649	1186.038	13:01	13.02	2.30	3.95	6.42	2634.63	2694.75	2694.86	0.20	2694.97	12.11	2694.93	-12.70	-0.39	979107.1348	0.730847894	-365.964142	132.78063	6.20544	0.77	979482.49	-135.19243
6/6/13	M110	31.975488	-106.9648	1177.434	13:18	13.30	2.58	4.23	6.70	2636.35	2696.51	2696.64	1.97	2696.75	13.89	2696.70	-10.93	4.93	979112.4543	0.729671469	-363.310034	131.81739	7.168196	0.77	979482.35	-130.4657
6/6/13	M111	31.973645	-106.9649	1171.348	13:31	13.52	2.80	4.45	6.92	2637.39	2697.58	2697.71	3.05	2697.82	14.97	2697.77	-9.86	8.16	979115.6767	0.728361616	-361.432662	131.13604	7.849198	0.77	979482.2	-127.6088
6/6/13	M112	31.971821	-106.9648	1171.102	13:47	13.78	3.07	4.72	7.18	2637.17	2697.35	2697.50	2.84	2697.61	14.76	2697.55	-10.08	7.52	979115.0356	0.727055511	-361.356792	131.1085	7.876725	0.77	979482.05	-128.12256
6/6/13	M113	31.970075	-106.9648	1172.523	14:00	14.00	3.28	4.93	7.40	2636.73	2696.90	2697.06	2.40	2697.18	14.32	2697.11	-10.52	6.19	979113.7124	0.725796306	-361.795151	131.26758	7.71772	0.77	979481.91	-129.1838
6/6/13	M114	31.968218	-106.9648	1175.483	14:11	14.18	3.47	5.12	7.58	2635.91	2696.06	2696.23	1.57	2696.35	13.49	2696.28	-11.36	3.70	979111.2178	0.724447422	-362.708257	131.59897	7.386506	0.77	979481.76	-131.27723
6/6/13	M115	31.966476	-106.9647	1178.204	14:21	14.35	3.63	5.28	7.75	2634.95	2695.08	2695.25	0.59	2695.37	12.52	2695.30	-12.33	0.77	979108.291	0.723173018	-363.547634	131.90359	7.082036	0.77	979481.62	-133.83237
6/6/13	B1	31.966394	-106.9666	1181.038	14:39	14.65	3.93	5.58	8.05	2634.72	2694.85	2695.03	0.37	2695.15	12.30	2695.07	-12.56	0.10	979107.6237	0.723113032	-364.421855	132.22087	6.764922	0.77	979481.61	-134.2533
6/6/13	B2	31.957892	-106.9798	1247.385	15:34	15.57	0.00	6.50	8.97	2623.36	2683.22	0.00	0.00	2683.57	0.72	2683.47	-24.17	-23.45	979084.0711	0.716764691	-384.888032	139.64862	0.647316	0.76	979480.92	-150.20511
6/6/13	Kidds	31.7719	-106.506	1186.5	17:55	17.92	0.00	0.00	11.32	2647.52	2707.95	0.00	0.00	0.00	0.00	2708.27	0.63	0.00	979107.52	0.529833608	-366.108334	132.83235	*	0.77	979465.86	#VALUE!
6/7/13	Kidds	31.7719	-106.506	1186.5	6:22	6.37	0.00	0.00	0.00	2646.67	2707.08	0.00	0.00	0.00	0.00	2707.08	0.00	0.00	979107.52	0.529833608	-366.108334	132.83235	*	0.77	979465.86	#VALUE!
6/7/13	B2	31.957892	-106.9798	1247.385	8:08	8.13	0.00	0.00	1.77	2623.43	2683.29	0.00	0.00	2683.29	0.00	2683.46	-23.62	-23.62	979083.9001	0.716764691	-384.888032	139.64862	0.647316	0.76	979480.92	-150.37616
6/7/13	B1	31.966394	-106.9666	1181.038	9:31	9.52	0.00	1.38	3.15	2635.04	2695.17	2695.17	0.00	2695.20	11.92	2695.48	-11.60	0.32	979107.8374	0.723113032	-364.421855	132.22087	6.764922	0.77	979481.61	-134.0396
6/7/13	M126	31.966462	-106.9625	1176.944	9:56	9.93	0.42	1.80	3.57	2634.89	2695.02	2695.03	-0.15	2695.06	11.77	2695.37	-11.71	-0.09	979107.4335	0.723162353	-363.158954	131.76253	7.223026	0.77	979481.62	-134.79532
6/7/13	M127	31.968256	-106.9624	1173.725	10:01	10.02	0.50	1.88	3.65	2635.92	2696.07	2696.08	0.91	2696.12	12.83	2696.43	-10.65	3.09	979110.6084	0.724475391	-362.165955	131.40215	7.58322	0.77	979481.76	-132.03857
6/7/13	M128	31.970054	-106.9626	1171.966	10:11	10.18	0.67	2.05	3.82	2636.46	2696.63	2696.64	1.47	2696.67	13.38	2697.00	-10.08	4.77	979112.2896	0.725781563	-361.62333	131.20523	7.780046	0.77	979481.91	-130.6521
6/7/13	M129	31.971889	-106.9627	1171.148	10:24	10.40	0.88	2.27	4.03	2636.87	2697.05	2697.06	1.89	2697.10	13.81	2697.44	-9.64	6.06	979113.5784	0.727104189	-361.370981	131.11365	7.871578	0.77	979482.06	-129.58137
6/7/13	M130	31.973723	-106.9627	1172.351	10:38	10.63	1.12	2.50	4.27	2637.02	2697.20	2697.22	2.05	2697.25	13.97	2697.62	-9.46	6.55	979114.071	0.728417475	-361.742064	131.24833	7.736966	0.77	979482.21	-129.13593
6/7/13	M131	31.975602	-106.9626	1177.447	10:50	10.83	1.32	2.70	4.47	2636.18	2696.34	2696.36	1.19	2696.40	13.11	2696.78	-10.30	4.00	979111.5184	0.729752101	-363.314044	131.81884	7.166742	0.77	979482.36	-131.40977
6/7/13	M132	31.977311	-106.9628	1184.736	11:01	11.02	1.50	2.88	4.65	2634.73	2694.86	2694.88	-0.29	2694.92	11.63	2695.31	-11.77	-0.43	979107.09	0.730957102	-365.562507	132.63487	6.351129	0.77	979482.5	-135.36001
6/7/13	M133	31.979085	-106.9627	1191.304	11:13	11.22	1.70	3.08	4.85	2633.55	2693.65	2693.68	-1.50	2693.72	10.43	2694.12	-12.96	-4.03	979103.4932	0.732199219	-367.588552	133.37018	5.616193	0.77	979482.64	-138.54506
6/7/13	MX1	31.981324	-106.9615	1199.82	11:28	11.47	1.95	3.33	5.10	2632.05	2692.11	2692.14	-3.03	2692.18	8.90	2692.61	-14.47	-8.60	979098.9204	0.733753209	-370.215492	134.32357	4.663282	0.77	979482.82	-142.57897
6/7/13	MX2	31.982233	-106.9596	1200.293	11:47	11.78	2.27	3.65	5.42	2631.19	2691.23	2691.27	-3.90	2691.31	8.02	2691.76	-15.32	-11.20	979096.3223	0.734379922	-370.361392	134.37652	4.610355	0.77	979482.9	-145.21081
6/7/13	M216	31.979177	-106.9586	1190.748	12:20	12.33	2.82	4.20	5.97	2633.10	2693.19	2693.23	-1.94	2693.28	9.99	2693.77	-13.31	-5.26	979102.2635	0.732262959	-367.41704	133.30793	5.678408	0.77	979482.65	-139.82918
6/7/13	M134	31.979157	-106.9606	1191.023	12:31	12.52	3.00	4.38	6.15	2633.37	2693.46	2693.51	-1.66	2693.56	10.27	2694.06	-13.02	-4.40	979103.1178	0.732249399	-367.50187	133.33872	5.647636	0.77	979482.65	-138.95004
6/7/13	M135	31.977343	-106.9607	1184.436	12:42	12.70	3.18	4.57	6.33	2634.84	2694.97	2695.02	-0.15	2695.07	11.78	2695.59	-11.49	0.14	979107.6577	0.730979785	-365.469964	132.60128	6.384698	0.77	979482.5	-134.82036
6/7/13	M215	31.97732	-106.9586	1185.077	12:57	12.95	3.43	4.82	6.58	2633.92	2694.03	2694.08	-1.09	2694.13	10.84	2694.67	-12.41	-2.65	979104.8662	0.730963031	-365.667697	132.67304	6.312972	0.77	979482.5	-137.55566
6/7/13	M214	31.975578	-106.9587	1179.258	13:07	13.12	3.60	4.98	6.75	2635.34	2695.48	2695.54	0.37	2695.59	12.30	2696.14	-10.94	1.73	979109.2502	0.729734673	-363.872694	132.02159	6.964097	0.77	979482.36	-133.52269
6/7/13	M136	31.975514	-106.9606	1178.973	13:18	13.30	3.78	5.17	6.93	2635.54	2695.68	2695.75	0.58	2695.80	12.51	2696.36	-10.72	2.37	979109.8895	0.729689671	-363.784778	131.98968	6.995988	0.77	979482.35	-132.90235
6/7/13	M137	31.973649	-106.9608	1173.948	13:29	13.48	3.97	5.35	7.12	2636.71	2696.88	2696.95	1.78	2697.00	13.71	2697.58	-9.50	5.99	979113.508	0.728364575	-362.234701	131.42712	7.558267	0.77	979482.2	-129.55779
6/7/13	B1	31.966394	-106.9666	1181.038	14:20	14.33	4.82	6.20	7.97	2635.12	2695.25	2695.34	0.16	2695.39	12.10	2696.03	-11.05	1.22	979108.7406	0.723113032	-364.421855	132.22087	6.764922	0.77	979481.61	-133.13632
6/7/13	B2	31.957892	-106.9798	1247.385	15:37	15.62	0.00	7.48	9.25	2623.59	2683.45	0.00	0.00	2683.61	0.33	2684.35	-22.73	-22.40	979085.1221	0.716764691	-384.888032	139.64862	0.647316	0.76	979480.92	-149.15408
6/7/13	Kidds	31.7719	-106.506	1186.5	17:48	17.80	0.00	0.00	11.43	2647.76	2708.20	0.00	0.00	0.00	0.00	2709.31	2.23	0.00	979107.52	0.529833608	-366.108334	132.83235	*	0.77	979465.86	#VALUE!
6/11/13	Kidds	31.7719	-106.506	1186.5	5:01	5.02			0.00	2648.57	2709.02	0.00	0.00	0.00	0.00	2709.02	0.00	0.00	979107.52	0.529833608	-366.108334	132.83235	*	0.77	979465.86	#VALUE!
6/11/13	B2	31.957892	-106.9798	1247.385	6:46	6.77		0.00	1.75	2624.46	2684.34	0.00	0.00	2684.34	0.00	2684.31	-24.71	-24.71	979082.8103	0.716764691	-384.888032	139.64862	0.647316	0.76	979480.92	-151.46594
6/11/13	B1	31.966394	-106.9666	1181.038	7:46	7.77	0.00	1.00	2.75	2635.98	2696.14	2696.14	0.00	2696.20	11.86	2696.09	-12.93	-1.07	979106.4507	0.723113032	-364.421855	132.22087	6.764922	0.77	979481.61	-135.42625
6/11/13	M141	31.966488	-106.9605	1180.391	8:14	8.23	0.47	1.47	3.22	2634.73	2694.86	2694.84	-1.29	2694.96	10.61	2694.81	-14.22	-4.90	979102.6215	0.723181663	-364.22227	132.14843	6.837319	0.77	979481.62	-139.31782
6/11/13	M140	31.968349	-106.9605	1175.774	8:25	8.42	0.65	1.65	3.40	2635.96	2696.11	2696.09	-0.04	2696.23	11.89	2696.06	-12.96	-1.12	979106.4031	0.724543289	-362.798022	131.63154	7.353945	0.77	979481.77	-136.07802
6/11/13	M139	31.970111	-106.9605	1171.614	8:35	8.58	0.82	1.82	3.57	2637.14	2697.32	2697.30	1.16	2697.45	13.10	2697.27	-11.76	2.51	979110.0308	0.725822247	-361.514746	131.16582	7.819434	0.77	979481.91	-132.94533
6/11/13	M138	31.971959	-106.9605	1171.365	8:48	8.80	1.03	2.03	3.78	2637.61	2697.80	2697.77	1.64	2697.94	13.60	2697.75	-11.28	3.96	979111.4789	0.727154916	-361.43792	131.13794	7.847296	0.77	979482.06	-131.66832
6/11/13	M213	31.973729	-106.9585	1176.283	9:03	9.05	1.28	2.28	4.03	2636.63	2696.80	2696.76	0.62	2696.96	12.61	2696.74	-12.29	0.95	979108.4743	0.728421691	-362.954993	131.68853	7.296989	0.77	979482.21	-134.40037
6/11/13	M212	31.971929	-106.9584	1175.84	9:15	9.25	1.48	2.48	4.23	2636.41	2696.58	2696.53	0.39	2696.74	12.40	2696.51	-12.51	0.28	979107.8028	0.727133187	-362.818352	131.63893	7.346559	0.77	979482.06	-134.96318
6/11/13	M211	31.97015	-106.9584	1177.763	9:28	9.47	1.70	2.70	4.45	2635.62	2695.77	2695.71	-0.42	2695.95	11.61	2695.70	-13.33	-2.14	979105.3811	0.725850576	-363.411566	131.85422	7.131383	0.77	979481.92	-137.07778
6/11/13	M210	31.968378	-106.9583	1180.506	9:44	9.73	1.97	2.97	4.72	2634.30	2694.42	2694.35	-1.78	2694.62	10.28	2694.34	-14.68	-6.19	979101.3326	0.724564231	-364.25773	132.16131	6.824451	0.77	979481.77	-140.75034
6/11/13	M209	31.966546	-106.9583	1186.143	9:56	9.93	2.17	3.17	4.92	2632.96	2693.04	2692.98	-3.16	2693.26	8.92	2692.97	-16.06	-10.30	979097.2213	0.723224314	-365.996619	132.79239	6.19369	0.77	979481.63	-144.23591
6/11/13	M308	31.966662	-106.9564	1198.048	10:10	10.17	2.40	3.40	5.15	2630.08	2690.10	2690.02	-6.12	2690.33	5.98	2690.02	-19.01	-19.14	979088.3809	0.723309217	-369.668999	134.12519	4.861562	0.77	979481.63	-152.07827
6/11/13	M208	31.96478	-106.9583	1190.112	10:23	10.38	2.62	3.62	5.37	2631.80	2691.86	2691.77	-4.36	2692.10	7.76	2691.77	-17.25	-13.85	979093.6682	0.721923793	-367.220968	133.23673	5.749574	0.77	979481.48	-147.3099
6/11/13	M207	31.96294	-106.9583	1196.922	10:36	10.60	2.83	3.83	5.58	2630.21	2690.23	2690.14	-6.00	2690.49	6.15	2690.14	-18.88	-18.73	979088.7894	0.720558874	-369.321689	133.99913	4.987557	0.77	979481.33	-151.46306
6/11/13	M206	31.961137	-106.9582	1203.268	10:49	10.82	3.05	4.05	5.80	2628.60	2688.58	2688.48	-7.65	2688.86	4.51	2688.49	-20.53	-23.67	979083.8492	0.719212247	-371.279272	134.70958	4.277464	0.77	979481.19	-155.71995
6/11/13	M205	31.959994	-106.9605	1202.523	10:59	10.98	3.22	4.22	5.97	2626.70	2686.63	2686.53	-9.60	2686.92	2.58	2686.54	-22.48	-29.50	979078.0172	0.718353692	-371.04947	134.62618	4.360826	0.77	979481.09	-161.52221
6/11/13	M204	31.959271	-106.9603	1203.91	11:11	11.18	3.42	4.42	6.17	2628.75	2688.73	2688.63	-7.51	2689.03	4.69	2688.64	-20.38	-23.20	979084.3176	0.717808866	-371.477327	134.78146	4.205627	0.76	979481.03	-155.05576
6/11/13	M203	31.961096	-106.9603	1198.228	11:35	11.58	3.82	4.82	6.57	2630.09	2690.11	2689.98	-6.15	2690.43	6.09	2690.01	-19.02	-19.08	979088.4417	0.719181425	-369.724571	134.14534	4.841421	0.77	979481.18	-151.5506
6/11/13	M202	31.962888	-106.9604	1191.615	11:46	11.77	4.00	5.00	6.75	2631.67	2691.72	2691.60	-4.54	2692.06	7.72	2691.62	-17.40	-14.22	979093.2982	0.72051995	-367.684621	133.40499	5.581393	0.77	979481.33	-147.39905
6/11/13	M201	31.964696	-106.9604	1185.945	11:56	11.93	4.17	5.17	6.92	2633.08	2693.17	2693.03	-3.10	2693.52	9.18	2693.06	-15.96	-9.89	979097.6323	0.721861573	-365.935556	132.77022	6.215846	0.77	979481.48	-143.69154
6/11/13	M125	31.964653	-106.9625	1181.97	12:11	12.18	4.42	5.42	7.17	2634.58	2694.70	2694.56	-1.57	2695.07	10.73	2694.59	-14.43	-5.28	979102.2446	0.721829649	-364.709368	132.32521	6.660634	0.77	979481.47	-139.41215
6/11/13	M116	31.964633	-106.9646	1180.176	12:20	12.33	4.57	5.57	7.32	2635.39	2695.53	2695.39	-0.75	2695.91	11.57	2695.42	-13.60	-2.78	979104.7355	0.721814808	-364.155963	132.12436	6.861376	0.77	979481.47	-137.0714
6/11/13	B1	31.966394	-106.9666	1181.038	12:38	12.63	4.87	5.87	7.62	2635.83	2695.98	2695.83	-0.31	2696.38	12.04	2695.87	-13.16	-1.43	979106.0933	0.723113032	-364.421855	132.22087	6.764922	0.77	979481.61	-135.78367
6/11/13	B2	31.957892	-106.9798	1247.385	13:51	13.85	0.00	7.08	8.83	2624.06	2683.93	0.00	0.00	2684.41	0.07	2683.80	-25.23	-25.16	979082.3649	0.716764691	-384.888032	139.64862	0.647316	0.76	979480.92	-151.91129
6/11/13	Kidds	31.7719	-106.506	1186.5	15:47	15.78	0.00	0.00	10.77	2648.41	2708.86	0.00	0.00	0.00	0.00	2708.70	-0.33	0.00	979107.52	0.529833608	-366.108334	132.83235	*	0.77	979465.86	#VALUE!
6/12/13	Kidds	31.7719	-106.506	1186.5	5:00	5.00	0.00	0.00	0.00	2648.55	2709.00	0.00	0.00	0.00	0.00	2709.00	0.00	0.00	979107.52	0.529833608	-366.108334	132.83235	*	0.77	979465.86	#VALUE!
6/12/13	B2	31.957892	-106.9798	1247.385	6:50	6.83	0.00	0.00	1.83	2624.59	2684.47	0.00	0.00	2684.47	0.00	2684.51	-24.49	-24.49	979083.0254	0.716764691	-384.888032	139.64862	0.647316	0.76	979480.92	-151.25078
6/12/13	B1	31.966394	-106.9666	1181.038	7:36	7.60	0.00	0.77	2.60	2636.19	2696.35	2696.35	0.00	2696.33	11.86	2696.40	-12.60	-0.75	979106.7726	0.723113032	-364.421855	132.22087	6.764922	0.77	979481.61	-135.10437
6/12/2013	M122	31.959214	-106.9626	1202.188	7:54	7.90	0.30	1.07	2.90	2629.52	2689.52	2689.52	-6.83	2689.50	5.02	2689.58	-19.43	-21.24	979086.2807	0.717765178	-370.946138	134.58867	4.398312	0.77	979481.03	-153.22376
6/12/2013	M123	31.961161	-106.9625	1192.651	8:04	8.07	0.47	1.23	3.07	2632.16	2692.22	2692.22	-4.13	2692.19	7.72	2692.28	-16.72	-13.13	979094.3854	0.719229926	-368.004214	133.52098	5.465469	0.77	979481.19	-146.08405
6/12/2013	M124	31.962974	-106.9624	1187.398	8:12	8.20	0.60	1.37	3.20	2633.53	2693.63	2693.62	-2.73	2693.59	9.12	2693.69	-15.32	-8.93	979098.5903	0.720583985	-366.383784	132.93289	6.05326	0.77	979481.34	-142.47081
6/12/2013	M117	31.963068	-106.9646	1184.529	8:20	8.33	0.73	1.50	3.33	2634.58	2694.70	2694.69	-1.66	2694.66	10.19	2694.77	-14.24	-5.71	979101.8124	0.720653951	-365.498769	132.61169	6.374291	0.77	979481.34	-139.49915
6/12/2013	M118	31.961234	-106.9647	1188.458	8:30	8.50	0.90	1.67	3.50	2633.45	2693.55	2693.53	-2.82	2693.50	9.03	2693.61	-15.39	-9.18	979098.3383	0.719284575	-366.710781	133.05156	5.93465	0.77	979481.19	-142.4919
6/12/2013	M248	31.961057	-106.9667	1188.229	8:38	8.63	1.03	1.80	3.63	2634.00	2694.11	2694.09	-2.26	2694.06	9.59	2694.18	-14.83	-7.50	979100.0248	0.719152387	-366.640142	133.02592	5.960274	0.77	979481.18	-140.81054
6/12/2013	M249	31.962784	-106.9667	1183.819	8:46	8.77	1.17	1.93	3.77	2635.08	2695.21	2695.20	-1.15	2695.17	10.69	2695.29	-13.72	-4.18	979103.339	0.720442715	-365.279754	132.53221	6.453738	0.77	979481.32	-138.00963
6/12/2013	M250	31.964626	-106.9667	1182.397	8:50	8.83	1.23	2.00	3.83	2635.63	2695.78	2695.76	-0.59	2695.73	11.25	2695.85	-13.15	-2.49	979105.0268	0.721809853	-364.841087	132.37301	6.612854	0.77	979481.47	-136.59164
6/12/2013	M247	31.961269	-106.9687	1189.974	9:06	9.10	1.50	2.27	4.10	2633.85	2693.95	2693.93	-2.42	2693.90	9.42	2694.03	-14.97	-7.97	979099.5543	0.719310815	-367.178428	133.22128	5.765015	0.77	979481.2	-141.1505
6/12/2013	M246	31.962803	-106.9689	1189.453	9:15	9.25	1.65	2.42	4.25	2634.59	2694.71	2694.69	-1.66	2694.65	10.18	2694.79	-14.21	-5.70	979101.8239	0.720456817	-367.0177	133.16295	5.823313	0.77	979481.32	-139.04947
6/12/2013	M245	31.964582	-106.969	1187.419	9:21	9.35	1.75	2.52	4.35	2635.04	2695.17	2695.15	-1.20	2695.11	10.64	2695.26	-13.75	-4.32	979103.2039	0.721777054	-366.390249	132.93524	6.050911	0.77	979481.47	-137.98596
6/12/2013	M217	31.966488	-106.969	1184.534	9:30	9.50	1.90	2.67	4.50	2635.95	2696.10	2696.08	-0.27	2696.04	11.56	2696.19	-12.81	-1.52	979105.9956	0.723181672	-365.500283	132.61225	6.373732	0.77	979481.62	-135.59305
6/12/2013	M218	31.968174	-106.9689	1181.246	9:38	9.63	2.03	2.80	4.63	2636.78	2696.95	2696.92	0.57	2696.89	12.41	2697.04	-11.96	1.02	979108.542	0.724415329	-364.486003	132.24415	6.741647	0.77	979481.76	-133.46174
6/12/2013	M219	31.969945	-106.969	1177.907	9:45	9.75	2.15	2.92	4.75	2637.72	2697.92	2697.88	1.53	2697.84	13.37	2698.01	-11.00	3.91	979111.4266	0.725701961	-363.455989	131.87034	7.115269	0.77	979481.9	-131.00343
6/12/2013	M220	31.971837	-106.9689	1175.163	9:53	9.88	2.28	3.05	4.88	2638.70	2698.92	2698.88	2.53	2698.84	14.37	2699.01	-9.99	6.91	979114.4337	0.72706692	-362.609515	131.56314	7.422313	0.77	979482.05	-128.38213
6/12/2013	M224	31.973623	-106.9711	1187.59	10:04	10.07	2.47	3.23	5.07	2636.58	2696.75	2696.71	0.36	2696.67	12.20	2696.85	-12.16	0.40	979107.9187	0.728346215	-366.442924	132.95438	6.031776	0.77	979482.2	-133.99052
6/12/2013	M221	31.973574	-106.9691	1179.362	10:14	10.23	2.63	3.40	5.23	2638.97	2699.20	2699.16	2.81	2699.11	14.64	2699.30	-9.71	7.74	979115.2556	0.728310791	-363.904791	132.03323	6.95246	0.77	979482.2	-127.34585
6/12/2013	M222	31.975432	-106.9694	1189.159	10:22	10.37	2.77	3.53	5.37	2635.93	2696.08	2696.04	-0.31	2696.00	11.52	2696.19	-12.82	-1.60	979105.916	0.729631444	-366.926905	133.13004	5.856211	0.77	979482.35	-136.00716
6/12/2013	M223	31.975395	-106.9713	1197.565	10:34	10.57	2.97	3.73	5.57	2634.46	2694.58	2694.53	-1.82	2694.49	10.01	2694.69	-14.32	-6.12	979101.397	0.72960554	-369.519935	134.07111	4.915607	0.77	979482.34	-139.81186
6/12/2013	M244	31.975268	-106.9732	1205.427	11:17	11.28	3.68	4.45	6.28	2633.08	2693.17	2693.11	-3.24	2693.06	8.58	2693.29	-15.72	-10.38	979097.1436	0.729515273	-371.945146	134.95129	4.035879	0.76	979482.33	-143.39964
6/12/2013	M242	31.971665	-106.9732	1186.457	11:36	11.60	4.00	4.77	6.60	2637.08	2697.26	2697.20	0.85	2697.14	12.67	2697.39	-11.62	1.90	979109.4222	0.726943737	-366.093438	132.82754	6.158555	0.77	979482.04	-132.42397
6/12/2013	M225	31.971893	-106.9711	1180.15	11:44	11.73	4.13	4.90	6.73	2638.08	2698.29	2698.22	1.87	2698.16	13.69	2698.41	-10.59	4.97	979112.4907	0.727107683	-364.147884	132.12145	6.864286	0.77	979482.06	-129.9077
6/12/2013	M226	31.970103	-106.9712	1179.67	11:54	11.90	4.30	5.07	6.90	2638.01	2698.21	2698.15	1.80	2698.09	13.61	2698.35	-10.66	4.75	979112.2722	0.725816628	-363.99983	132.06771	6.917996	0.77	979481.91	-130.02148
6/12/2013	M241	31.969932	-106.9731	1182.975	12:05	12.08	4.48	5.25	7.08	2637.78	2697.98	2697.91	1.56	2697.85	13.37	2698.11	-10.89	4.04	979111.562	0.725692748	-365.019343	132.43772	6.548178	0.77	979481.9	-130.43815
6/12/2013	M240	31.968023	-106.9728	1186.974	12:22	12.37	4.77	5.53	7.37	2636.55	2696.72	2696.65	0.30	2696.58	12.11	2696.86	-12.14	0.26	979107.7783	0.724305162	-366.252949	132.88542	6.100704	0.77	979481.75	-133.72846
6/12/2013	M227	31.96813	-106.9711	1183.841	12:35	12.58	4.98	5.75	7.58	2636.71	2696.88	2696.81	0.46	2696.74	12.27	2697.03	-11.98	0.75	979108.2652	0.724383664	-365.286497	132.53467	6.451276	0.77	979481.75	-133.51546
6/12/2013	M228	31.966323	-106.9712	1189.112	12:45	12.75	5.15	5.92	7.75	2635.52	2695.66	2695.59	-0.76	2695.52	11.04	2695.81	-13.19	-2.91	979104.6068	0.723060356	-366.912482	133.12477	5.86147	0.77	979481.61	-136.58103
6/12/2013	M330	31.967123	-106.9743	1189.804	12:55	12.92	5.32	6.08	7.92	2636.05	2696.21	2696.13	-0.22	2696.06	11.58	2696.36	-12.65	-1.29	979106.2311	0.723647142	-367.125939	133.20225	5.784038	0.77	979481.67	-134.9631
6/12/2013	M239	31.966348	-106.9732	1190.61	13:08	13.13	5.53	6.30	8.13	2635.50	2695.64	2695.56	-0.79	2695.49	11.01	2695.80	-13.21	-2.98	979104.5374	0.72307907	-367.374576	133.29248	5.693849	0.77	979481.61	-136.52579
6/12/2013	M238	31.964426	-106.9732	1195.145	13:21	13.35	5.75	6.52	8.35	2634.32	2694.44	2694.35	-2.00	2694.27	9.80	2694.60	-14.41	-6.61	979100.9087	0.721661614	-368.77352	133.80019	5.186399	0.77	979481.45	-139.61469
6/12/2013	M229	31.964606	-106.971	1190.774	13:33	13.55	5.95	6.72	8.55	2634.74	2694.87	2694.77	-1.58	2694.70	10.23	2695.03	-13.98	-5.33	979102.1944	0.721795162	-367.42518	133.31084	5.675498	0.77	979481.47	-138.71348
6/12/2013	M230	31.962861	-106.9709	1193.252	13:40	13.67	6.07	6.83	8.67	2634.05	2694.16	2694.07	-2.28	2693.99	9.52	2694.32	-14.68	-7.45	979100.0728	0.720500363	-368.189592	133.58826	5.398219	0.77	979481.33	-140.48383
6/12/2013	M231	31.961187	-106.9708	1196.964	13:49	13.82	6.22	6.98	8.82	2632.89	2692.97	2692.88	-3.47	2692.80	8.32	2693.14	-15.86	-11.01	979096.5069	0.719249369	-369.33466	134.00383	4.982857	0.77	979481.19	-143.59967
6/12/2013	M232	31.959179	-106.9707	1206.063	14:01	14.02	6.42	7.18	9.02	2630.86	2690.89	2690.80	-5.56	2690.72	6.24	2691.07	-17.94	-17.25	979090.268	0.717739217	-372.141468	135.02249	3.964714	0.76	979481.03	-148.91574
6/12/13	B1	31.966394	-106.9666	1181.038	14:17	14.28	6.68	7.45	9.28	2636.09	2696.25	2696.15	-0.20	2696.06	11.59	2696.42	-12.58	-1.19	979106.3253	0.723113032	-364.421855	132.22087	6.764922	0.77	979481.61	-135.55162
6/12/13	B2	31.957892	-106.9798	1247.385	14:42	14.70	0.00	7.87	9.70	2624.40	2684.28	0.00	0.00	2684.09	-0.39	2684.47	-24.54	-24.93	979082.592	0.716764691	-384.888032	139.64862	0.647316	0.76	979480.92	-151.68418
6/12/13	Kidds	31.7719	-106.506	1186.5	16:16	16.27	0.00	0.00	11.27	2648.76	2709.22	0.00	0.00	0.00	0.00	2709.43	0.43	0.00	979107.52	0.529833608	-366.108334	132.83235	*	0.77	979465.86	#VALUE!
6/18/13	Kidds	31.7719	-106.506	1186.5	4:56	4.93	0.00	0.00	0.00	2649.48	2709.96	0.00	0.00	0.00	0.00	2709.96	0.00	0.00	979107.52	0.529833608	-366.108334	132.83235	*	0.77	979465.86	#VALUE!
6/18/13	B2	31.957892	-106.97981	1247.385	6:27	6.45	0.00	0.00	1.52	2625.35	2685.25	0.00	0.00	2685.25	0.00	2685.29	-24.67	-24.67	979082.8514	0.716764694	-384.888032	139.64862	0.647316	0.76	979480.92	-151.4248
6/18/13	M506	31.969003	-106.95117	1283.437	7:21	7.35	0.00	0.90	2.42	2611.88	2671.46	0.00	0.00	2671.49	-13.77	2671.52	-38.44	-52.20	979055.3157	0.725019133	-396.008655	143.68475	4.681236	0.76	979481.82	-168.7437
6/18/13	M507	31.969775	-106.95146	1286.089	7:28	7.47	0.00	1.02	2.53	2611.38	2670.95	0.00	0.00	2670.98	-14.28	2671.01	-38.95	-53.22	979054.2978	0.725579449	-396.826685	143.98165	4.977989	0.76	979481.89	-169.00645
6/18/13	M508	31.972718	-106.9512	1287.598	7:48	7.80	0.00	1.35	2.87	2611.46	2671.03	0.00	0.00	2671.07	-14.18	2671.10	-38.86	-53.04	979054.4781	0.72769906	-397.292126	144.15059	5.146838	0.76	979482.13	-168.59956
6/12/13	M509	31.973828	-106.95119	1286.912	7:54	7.90	0.00	1.45	2.97	2611.78	2671.36	0.00	0.00	2671.40	-13.85	2671.43	-38.53	-52.38	979055.1383	0.728492189	-397.080512	144.07379	5.070075	0.76	979482.22	-168.24106
6/18/13	M510	31.975256	-106.95102	1285.777	8:00	8.00	0.00	1.55	3.07	2612.28	2671.87	0.00	0.00	2671.91	-13.34	2671.94	-38.01	-51.35	979056.167	0.729506794	-396.730397	143.94672	4.94307	0.76	979482.33	-167.67824
6/18/13	M511	31.976651	-106.95142	1287.293	8:08	8.13	0.00	1.68	3.20	2612.24	2671.83	0.00	0.00	2671.88	-13.38	2671.90	-38.05	-51.43	979056.0917	0.730492598	-397.19801	144.11644	5.112706	0.76	979482.45	-167.39922
6/18/13	M512	31.977902	-106.95215	1287.551	8:13	8.22	0.00	1.77	3.28	2612.38	2671.97	0.00	0.00	2672.02	-13.23	2672.05	-37.91	-51.14	979056.3825	0.731371969	-397.277582	144.14533	5.141575	0.76	979482.55	-167.13044
6/12/13	M513	31.979217	-106.95262	1286.339	8:19	8.32	0.00	1.87	3.38	2612.80	2672.40	0.00	0.00	2672.45	-12.80	2672.48	-37.47	-50.27	979057.2474	0.732291146	-396.903717	144.00964	5.005954	0.76	979482.65	-166.74604
6/18/13	M514	31.980671	-106.95303	1283.593	8:25	8.42	0.00	1.97	3.48	2613.68	2673.31	0.00	0.00	2673.36	-11.90	2673.39	-36.57	-48.47	979059.0542	0.73330157	-396.056672	143.70222	4.698676	0.76	979482.77	-165.90416
6/18/13	M515	31.983055	-106.95343	1274.566	8:32	8.53	0.00	2.08	3.60	2616.04	2675.72	0.00	0.00	2675.78	-9.48	2675.80	-34.15	-43.63	979063.8922	0.734944876	-393.272171	142.69161	3.688586	0.76	979482.97	-164.04367
6/18/13	M516	31.985245	-106.95439	1273.523	8:39	8.65	0.00	2.20	3.72	2616.76	2676.46	0.00	0.00	2676.52	-8.74	2676.54	-33.41	-42.15	979065.3722	0.736439695	-392.950426	142.57485	3.571876	0.76	979483.14	-163.06311
6/18/13	X3	31.986135	-106.9557	1272.494	8:46	8.77	0.00	2.32	3.83	2617.27	2676.98	0.00	0.00	2677.04	-8.21	2677.07	-32.89	-41.10	979066.4223	0.737042618	-392.633011	142.45965	3.456736	0.76	979483.21	-162.40261
6/18/13	M421	31.987369	-106.95764	1274.288	8:53	8.88	0.00	2.43	3.95	2617.30	2677.01	0.00	0.00	2677.08	-8.18	2677.10	-32.85	-41.03	979066.4895	0.737875693	-393.186381	142.66049	3.657477	0.76	979483.32	-161.88232
6/18/13	X4	31.983824	-106.95469	1287.795	9:09	9.15	0.00	2.70	4.22	2613.13	2672.74	0.00	0.00	2672.81	-12.44	2672.84	-37.12	-49.56	979057.9645	0.735471126	-397.352794	144.17264	5.168875	0.76	979483.03	-165.95391
6/18/13	M420	31.987096	-106.95995	1288.808	9:17	9.28	0.00	2.83	4.35	2614.02	2673.65	0.00	0.00	2673.73	-11.52	2673.75	-36.20	-47.73	979059.7934	0.737692135	-397.665234	144.28605	5.282231	0.76	979483.29	-164.07823
6/18/13	M419	31.986547	-106.96217	1288.263	9:27	9.45	0.00	3.00	4.52	2614.55	2674.20	0.00	0.00	2674.28	-10.98	2674.30	-35.66	-46.63	979060.8869	0.737321131	-397.497129	144.22504	5.221238	0.76	979483.25	-163.10821
6/18/13	M418	31.986446	-106.96395	1298.114	9:35	9.58	0.00	3.13	4.65	2612.43	2672.03	0.00	0.00	2672.11	-13.14	2672.13	-37.82	-50.97	979056.5527	0.737253011	-400.535761	145.32789	6.323584	0.76	979483.24	-164.39606
6/18/13	M417	31.986043	-106.96589	1299.517	9:42	9.70	0.00	3.25	4.77	2612.28	2671.87	0.00	0.00	2671.96	-13.29	2671.98	-37.97	-51.27	979056.2514	0.736980854	-400.968531	145.48496	6.480577	0.76	979483.21	-164.23205
6/18/13	M416	31.984185	-106.96687	1300.088	9:48	9.80	0.00	3.35	4.87	2612.12	2671.71	0.00	0.00	2671.80	-13.46	2671.82	-38.14	-51.59	979055.9287	0.735717689	-401.144678	145.54888	6.544471	0.76	979483.06	-164.22773
6/18/13	M415	31.981937	-106.96894	1292.97	9:56	9.93	0.00	3.48	5.00	2613.67	2673.29	0.00	0.00	2673.39	-11.87	2673.41	-36.55	-48.41	979059.109	0.734175954	-398.949089	144.752	5.747967	0.76	979482.87	-163.06015
6/18/13	M414	31.980072	-106.97147	1285.681	10:06	10.10	0.00	3.65	5.17	2615.77	2675.44	0.00	0.00	2675.54	-9.71	2675.56	-34.39	-44.10	979063.4172	0.732886006	-396.700742	143.93597	4.932308	0.76	979482.72	-160.84868
6/18/13	M413	31.979616	-106.97374	1274.821	10:15	10.25	0.00	3.80	5.32	2619.05	2678.80	0.00	0.00	2678.90	-6.35	2678.93	-31.03	-37.38	979070.1405	0.732568536	-393.350859	142.72016	3.717131	0.76	979482.69	-157.43749
6/18/13	M412	31.976966	-106.9769	1274.765	10:25	10.42	0.00	3.97	5.48	2619.80	2679.57	0.00	0.00	2679.68	-5.58	2679.70	-30.26	-35.84	979071.6845	0.730714706	-393.333609	142.71389	3.710868	0.76	979482.47	-155.69579
6/18/13	M411	31.975106	-106.97804	1268.398	10:32	10.53	0.00	4.08	5.60	2621.38	2681.19	0.00	0.00	2681.30	-3.96	2681.32	-28.64	-32.59	979074.9254	0.729400948	-391.369645	142.00109	2.998391	0.76	979482.32	-154.26757
6/18/13	M410	31.972714	-106.97889	1270.392	10:38	10.63	0.00	4.18	5.70	2620.98	2680.78	0.00	0.00	2680.89	-4.36	2680.91	-29.05	-33.41	979074.1113	0.727696504	-391.984741	142.22432	3.22154	0.76	979482.13	-154.27248
6/18/13	M409	31.970926	-106.97851	1271.731	10:46	10.77	0.00	4.32	5.83	2620.27	2680.05	0.00	0.00	2680.17	-5.09	2680.19	-29.77	-34.86	979072.6642	0.726411226	-392.397788	142.37423	3.37137	0.76	979481.98	-155.1615
6/18/13	M408	31.964856	-106.9791	1262.753	10:53	10.88	0.00	4.43	5.95	2619.03	2678.78	0.00	0.00	2678.90	-6.35	2678.92	-31.04	-37.39	979070.131	0.721979914	-389.62846	141.36911	2.366758	0.76	979481.49	-159.97092
6/18/13	M407	31.967817	-106.9782	1270.255	10:59	10.98	0.00	4.53	6.05	2620.30	2680.08	0.00	0.00	2680.20	-5.05	2680.22	-29.73	-34.78	979072.7364	0.724154767	-391.942524	142.20899	3.206207	0.76	979481.73	-155.2922
6/18/13	M406	31.966115	-106.97781	1266.308	11:07	11.12	0.00	4.67	6.18	2620.91	2680.71	0.00	0.00	2680.83	-4.42	2680.85	-29.11	-33.53	979073.992	0.722907858	-390.725036	141.76711	2.764537	0.76	979481.59	-155.11577
6/18/13	M405	31.964857	-106.9791	1262.647	11:16	11.27	0.00	4.82	6.33	2622.23	2682.06	0.00	0.00	2682.19	-3.07	2682.20	-27.75	-30.82	979076.7022	0.721980476	-389.595762	141.35725	2.354899	0.76	979481.49	-153.43251
6/18/13	M404	31.964114	-106.98003	1258.324	11:22	11.37	0.00	4.92	6.43	2623.53	2683.39	0.00	0.00	2683.52	-1.73	2683.54	-26.42	-28.15	979079.3689	0.721430792	-388.262279	140.87327	1.871223	0.76	979481.43	-152.03865
6/18/13	M403	31.962952	-106.98015	1253.998	11:29	11.48	0.00	5.03	6.55	2624.48	2684.36	0.00	0.00	2684.50	-0.76	2684.51	-25.44	-26.20	979081.3199	0.720567891	-386.927871	140.38896	1.387186	0.76	979481.33	-151.32755
6/18/13	M402	31.961146	-106.98108	1255.458	11:37	11.62	0.00	5.17	6.68	2624.56	2684.44	0.00	0.00	2684.58	-0.67	2684.60	-25.36	-26.03	979081.4903	0.719219274	-387.378245	140.55242	1.550539	0.76	979481.19	-150.56035
6/18/13	M401	31.959473	-106.98076	1246.467	11:44	11.73	0.00	5.28	6.80	2625.22	2685.12	0.00	0.00	2685.26	0.01	2685.28	-24.68	-24.67	979082.8475	0.717960951	-384.604847	139.54584	0.544622	0.76	979481.05	-151.84014
6/18/13	M503	31.962275	-106.95052	1263.619	12:27	12.45	0.00	6.00	7.52	2615.27	2674.93	0.00	0.00	2675.09	-10.16	2675.11	-34.85	-45.01	979062.51	0.720063162	-389.895612	141.46606	2.46366	0.76	979481.28	-167.11535
6/18/13	M502	31.960801	-106.95158	1259.204	12:33	12.55	0.00	6.10	7.62	2616.28	2675.97	0.00	0.00	2676.13	-9.12	2676.14	-33.81	-42.94	979064.583	0.718960467	-388.533756	140.97179	1.969688	0.76	979481.16	-166.28437
6/18/13	M501	31.957796	-106.9525	1253.08	12:40	12.67	0.00	6.22	7.73	2617.42	2677.13	0.00	0.00	2677.30	-7.95	2677.31	-32.64	-40.60	979066.923	0.716691989	-386.644744	140.28619	1.284478	0.76	979480.92	-165.58917
6/18/13	MX6	31.957331	-106.95038	1253.34	12:48	12.80	0.00	6.35	7.87	2617.14	2676.85	0.00	0.00	2677.02	-8.24	2677.03	-32.93	-41.16	979066.3563	0.716338329	-386.724949	140.3153	1.313569	0.76	979480.88	-166.03791
6/18/13	M517	31.957225	-106.95322	1252.698	12:55	12.92	0.00	6.47	7.98	2617.48	2677.20	0.00	0.00	2677.37	-7.89	2677.38	-32.58	-40.46	979067.0582	0.716257695	-386.526916	140.24342	1.241736	0.76	979480.87	-165.52535
6/18/13	M518	31.956418	-106.95468	1253.025	13:01	13.02	0.00	6.57	8.08	2617.61	2677.33	0.00	0.00	2677.50	-7.75	2677.52	-32.44	-40.19	979067.3294	0.715643165	-386.627791	140.28003	1.27832	0.76	979480.8	-165.08792
6/18/13	M519	31.956145	-106.95697	1253.199	13:08	13.13	0.00	6.68	8.20	2618.12	2677.85	0.00	0.00	2678.03	-7.22	2678.04	-31.92	-39.14	979068.3794	0.715434529	-386.681466	140.29951	1.297786	0.76	979480.78	-163.96205
6/18/13	M520	31.956049	-106.95872	1253.425	13:19	13.32	0.00	6.87	8.38	2618.37	2678.11	0.00	0.00	2678.29	-6.96	2678.30	-31.66	-38.62	979068.9004	0.715361391	-386.75118	140.32481	1.323071	0.76	979480.77	-163.3636
6/18/13	M521	31.956182	-106.96082	1246.819	13:26	13.43	0.00	6.98	8.50	2620.33	2680.11	0.00	0.00	2680.30	-4.95	2680.31	-29.65	-34.60	979072.9194	0.715462676	-384.713455	139.58525	0.583999	0.76	979480.78	-161.39262
6/18/13	M522	31.956213	-106.96308	1255.6	13:34	13.57	0.00	7.12	8.63	2618.99	2678.74	0.00	0.00	2678.93	-6.32	2678.94	-31.02	-37.34	979070.1823	0.715487016	-387.42209	140.56831	1.566423	0.76	979480.79	-161.42429
6/18/13	M527	31.956126	-106.97375	1249.74	13:48	13.80	0.00	7.35	8.87	2623.00	2682.85	0.00	0.00	2683.04	-2.21	2683.05	-26.90	-29.12	979078.4045	0.715419908	-385.614484	139.91227	0.910788	0.76	979480.78	-155.00214
6/18/13	M526	31.955866	-106.97171	1251.738	13:55	13.92	0.00	7.47	8.98	2621.88	2681.70	0.00	0.00	2681.90	-3.35	2681.91	-28.05	-31.40	979076.1171	0.715221711	-386.230801	140.13595	1.134327	0.76	979480.76	-156.65239
6/18/13	M525	31.956271	-106.96961	1249.934	14:01	14.02	0.00	7.57	9.08	2621.73	2681.55	0.00	0.00	2681.75	-3.51	2681.76	-28.20	-31.71	979075.8149	0.715531189	-385.674326	139.93399	0.932494	0.76	979480.79	-157.54376
6/18/13	M523	31.953952	-106.9646	1251.418	14:11	14.18	0.00	7.73	9.25	2620.35	2680.13	0.00	0.00	2680.34	-4.91	2680.35	-29.61	-34.52	979072.9976	0.713752424	-386.132108	140.10012	1.098525	0.76	979480.6	-159.71522
6/18/13	M524	31.953876	-106.96671	1246.948	14:19	14.32	0.00	7.87	9.38	2621.65	2681.46	0.00	0.00	2681.67	-3.58	2681.68	-28.28	-31.85	979075.666	0.713693816	-384.753267	139.59969	0.598429	0.76	979480.6	-158.41913
6/18/13	M528	31.955906	-106.97523	1247.357	14:25	14.42	0.00	7.97	9.48	2624.10	2683.97	0.00	0.00	2684.18	-1.07	2684.19	-25.76	-26.83	979080.6874	0.715252142	-384.879412	139.64548	0.644183	0.76	979480.76	-153.43632
6/18/13	M529	31.955902	-106.97775	1246.747	14:33	14.55	0.00	8.10	9.62	2625.09	2684.99	0.00	0.00	2685.20	-0.05	2685.21	-24.75	-24.80	979082.7211	0.715248954	-384.691248	139.57719	0.575944	0.76	979480.76	-151.59042
6/18/13	M531	31.955784	-106.98216	1245.298	14:44	14.73	0.00	8.28	9.80	2626.98	2686.92	0.00	0.00	2687.14	1.89	2687.15	-22.81	-20.92	979086.6	0.715158769	-384.244282	139.41497	0.413867	0.76	979480.75	-148.14872
6/18/13	B2	31.957892	-106.97981	1247.385	14:56	14.93	0.00	8.48	10.00	2625.57	2685.48	0.00	0.00	2685.70	0.45	2685.71	-24.25	-23.80	979083.7229	0.716764694	-384.888032	139.64862	0.647316	0.76	979480.92	-150.55329
6/18/13	Kidds	31.7719	-106.506	1186.5	16:55	16.92	0.00	0.00	11.98	2649.75	2710.23	0.00	0.00	0.00	0.00	2710.51	0.55	0.00	979107.52	0.529833608	-366.108334	132.83235	*	0.77	979465.86	#VALUE!
6/19/13	Kidds	31.7719	-106.506	1186.5	5:03	5.05	0.00	0.00	0.00	2649.74	2710.22	0.00	0.00	0.00	0.00	2710.22	0.00	0.00	979107.52	0.529833608	-366.108334	132.83235	*	0.77	979465.86	#VALUE!
6/19/13	B2	31.957892	-106.97981	1247.385	6:53	6.88	0.00	0.00	1.83	2625.64	2685.55	0.00	0.00	2685.55	0.00	2685.55	-24.67	-24.67	979082.851	0.716764694	-384.888032	139.64862	0.647316	0.76	979480.92	-151.42527
6/19/13	B1	31.966394	-106.96661	1181.038	7:40	7.67	0.00	0.78	2.62	2637.09	2697.27	0.00	0.00	2697.24	11.69	2697.28	-12.95	-1.25	979106.269	0.723113031	-364.421855	132.22087	6.764922	0.77	979481.61	-135.60792
6/19/13	M302	31.97695	-106.95712	1184.48	7:58	7.97	0.00	1.08	2.92	2635.51	2695.65	0.00	0.00	2695.62	10.07	2695.66	-14.56	-4.50	979103.0239	0.730702955	-365.48354	132.60621	6.379774	0.77	979482.47	-139.4185
6/19/13	M301	31.978921	-106.95675	1194.008	8:10	8.17	0.00	1.28	3.12	2633.30	2693.39	0.00	0.00	2693.35	7.80	2693.40	-16.82	-9.03	979098.4921	0.732084166	-368.422666	133.6729	5.313625	0.77	979482.63	-143.30395
6/19/13	M303	31.975624	-106.95676	1185.021	8:25	8.42	0.00	1.53	3.37	2635.34	2695.48	0.00	0.00	2695.43	9.88	2695.49	-14.74	-4.86	979102.6607	0.729767311	-365.650436	132.66677	6.319238	0.77	979482.36	-139.62826
6/19/13	M304	31.973967	-106.95693	1184.012	8:32	8.53	0.00	1.65	3.48	2635.46	2695.60	0.00	0.00	2695.54	9.99	2695.61	-14.61	-4.62	979102.9025	0.728590812	-365.339198	132.55381	6.432142	0.77	979482.23	-139.33735
6/19/13	M305	31.972153	-106.95673	1186.894	8:40	8.67	0.00	1.78	3.62	2634.47	2694.59	0.00	0.00	2694.53	8.98	2694.60	-15.63	-6.65	979100.871	0.727293816	-366.228238	132.87646	6.109656	0.77	979482.08	-140.97778
6/19/13	M306	31.97064	-106.95614	1192.877	8:50	8.83	0.00	1.95	3.78	2632.53	2692.60	0.00	0.00	2692.53	6.98	2692.61	-17.61	-10.63	979096.8931	0.726204796	-368.073851	133.54628	5.44018	0.77	979481.96	-144.3265
6/19/13	M307	31.967493	-106.9569	1191.184	9:03	9.05	0.00	2.17	4.00	2632.47	2692.54	0.00	0.00	2692.46	6.92	2692.55	-17.67	-10.76	979096.763	0.723917856	-367.55163	133.35674	5.629621	0.77	979481.7	-144.34446
6/19/13	M309	31.964842	-106.95629	1198.466	9:19	9.32	0.00	2.43	4.27	2630.57	2690.60	0.00	0.00	2690.51	4.96	2690.61	-19.62	-14.66	979092.8638	0.721969282	-369.797956	134.17198	4.814789	0.77	979481.49	-147.41235
6/19/13	M310	31.963026	-106.95633	1201.776	9:28	9.47	0.00	2.58	4.42	2629.79	2689.80	0.00	0.00	2689.71	4.16	2689.81	-20.42	-16.26	979091.2616	0.720622814	-370.819016	134.54255	4.444413	0.77	979481.34	-148.587
6/19/13	M311	31.961311	-106.95646	1207.794	9:38	9.63	0.00	2.75	4.58	2628.33	2688.30	0.00	0.00	2688.21	2.66	2688.31	-21.91	-19.25	979088.2666	0.719342269	-372.675415	135.21628	3.771022	0.76	979481.2	-150.94354
6/19/13	M312	31.959453	-106.95601	1218.3	9:45	9.75	0.00	2.87	4.70	2625.57	2685.48	0.00	0.00	2685.38	-0.17	2685.49	-24.73	-24.91	979082.6115	0.717945932	-375.916226	136.39246	2.595447	0.76	979481.05	-155.55889
6/19/13	M332	31.961032	-106.97726	1208.546	10:10	10.17	0.00	3.28	5.12	2633.44	2693.53	0.00	0.00	2693.42	7.87	2693.55	-16.68	-8.81	979098.7117	0.719133518	-372.907388	135.30047	3.686875	0.76	979481.18	-140.41226
6/19/13	M320	31.960897	-106.97643	1209.601	10:25	10.42	0.00	3.53	5.37	2632.89	2692.97	0.00	0.00	2692.85	7.30	2692.98	-17.24	-9.94	979097.5772	0.719032533	-373.232827	135.41858	3.568824	0.76	979481.17	-141.44658
6/19/13	M316	31.960118	-106.97416	1208.079	10:38	10.63	0.00	3.75	5.58	2632.64	2692.72	0.00	0.00	2692.58	7.03	2692.73	-17.49	-10.46	979097.058	0.718447046	-372.763339	135.24819	3.73913	0.76	979481.1	-142.03129
6/19/13	M235	31.959164	-106.97304	1208.038	10:49	10.82	0.00	3.93	5.77	2632.27	2692.34	0.00	0.00	2692.20	6.65	2692.35	-17.87	-11.23	979096.2943	0.717727832	-372.7507	135.2436	3.743718	0.76	979481.03	-142.72108
6/19/13	M233	31.957438	-106.97071	1214.168	11:02	11.03	0.00	4.15	5.98	2629.90	2689.91	0.00	0.00	2689.76	4.21	2689.92	-20.30	-16.09	979091.4343	0.716420117	-374.641643	135.92987	3.057797	0.76	979480.89	-146.92223
6/19/13	M234	31.957466	-106.97213	1214.992	11:13	11.22	0.00	4.33	6.17	2630.23	2690.25	0.00	0.00	2690.09	4.54	2690.26	-19.96	-15.42	979092.1039	0.716440929	-374.895822	136.02212	2.965595	0.76	979480.89	-146.18518
6/19/13	M322	31.958232	-106.97485	1216.946	11:29	11.48	0.00	4.60	6.43	2630.85	2690.88	0.00	0.00	2690.72	5.17	2690.90	-19.33	-14.16	979093.3644	0.717022755	-375.498567	136.24088	2.746952	0.76	979480.95	-144.8215
6/19/13	M326	31.958964	-106.9761	1216.824	11:46	11.77	0.00	4.88	6.72	2631.32	2691.36	0.00	0.00	2691.19	5.64	2691.38	-18.84	-13.20	979094.3173	0.717576437	-375.460928	136.22722	2.760603	0.76	979481.01	-143.93834
6/19/13	M334	31.959323	-106.97684	1218.663	11:59	11.98	0.00	5.10	6.93	2630.53	2690.56	0.00	0.00	2690.37	4.82	2690.57	-19.65	-14.83	979092.6924	0.717848064	-376.028202	136.4331	2.554828	0.76	979481.04	-145.43673
6/19/13	MX7	31.961476	-106.97711	1206.113	12:12	12.20	0.00	5.32	7.15	2633.63	2693.73	0.00	0.00	2693.54	7.99	2693.74	-16.48	-8.49	979099.0326	0.719466511	-372.156873	135.02809	3.959118	0.76	979481.21	-140.33335
6/19/13	MX8	31.960229	-106.97916	1215.48	12:20	12.33	0.00	5.45	7.28	2631.82	2691.88	0.00	0.00	2691.68	6.13	2691.89	-18.33	-12.20	979095.322	0.718530426	-375.046333	136.07675	2.910989	0.76	979481.11	-143.14998
6/19/13	B2	31.957892	-106.97981	1247.385	12:38	12.63	0.00	5.75	7.58	2625.44	2685.34	0.00	0.00	2685.14	-0.41	2685.36	-24.86	-25.27	979082.2487	0.716764694	-384.888032	139.64862	0.647316	0.76	979480.92	-152.02755
6/19/13	Kidds	31.7719	-106.506	1186.5	14:53	14.88	0.00	0.00	9.83	2649.76	2710.24	0.00	0.00	0.00	0.00	2710.26	0.04	0.00	979107.52	0.529833608	-366.108334	132.83235	*	0.77	979465.86	#VALUE!
11/7/2015	Kidds	31.7719	-106.506	1186.5	7:41	7.68	0.00	0.00	0.00	2651.23	2711.75	0.00	0.00	0.00	0.00	2711.75	0.00	0.00	979107.52	0.529833608	-366.108334	132.83235	*	0.77	979465.86	#VALUE!
11/7/2015	M116	31.964659	-106.96455	1180.12	12:14	12.23	0.00	0.00	4.55	2638.01	2698.21	0.00	0.00	0.00	0.00	2698.21	-13.53	-13.53	979093.9858	0.721834135	-364.138688	132.11809	6.867643	0.77	979481.47	-147.82803
11/7/2015	M201	31.964694	-106.96033	1186.085	12:36	12.60	0.00	0.00	4.92	2635.73	2695.88	0.00	0.00	0.00	0.00	2695.88	-15.87	-15.87	979091.6516	0.721859959	-365.978743	132.78589	6.20018	0.77	979481.47	-149.66027
11/7/2015	M203	31.961133	-106.96038	1198.008	1:01	13.02	0.00	0.00	5.34	2632.77	2692.85	0.00	0.00	0.00	0.00	2692.85	-18.90	-18.90	979088.6212	0.719208983	-369.656706	134.12071	4.866038	0.77	979481.19	-151.39267
11/7/2015	M701	31.96193	-106.95921	1197.35	1:16	16.27	0.00	0.00	8.59	2632.73	2692.81	0.00	0.00	0.00	0.00	2692.81	-18.94	-18.94	979088.5803	0.719806033	-369.453724	134.04704	4.939665	0.77	979481.25	-151.55404
11/7/2015	M702	31.963613	-106.95856	1193.926	1:30	13.50	0.00	0.00	5.82	2633.51	2693.61	0.00	0.00	0.00	0.00	2693.61	-18.14	-18.14	979089.3788	0.721059135	-368.397498	133.66372	5.322801	0.77	979481.39	-151.18177
11/7/2015	M703	31.965252	-106.95776	1190.508	1:57	13.95	0.00	0.00	6.27	2634.31	2694.43	0.00	0.00	0.00	0.00	2694.43	-17.32	-17.32	979090.1978	0.722272109	-367.34312	133.28106	5.705263	0.77	979481.52	-150.78502
11/7/2015	M704	31.967082	-106.95743	1190.003	2:14	14.23	0.00	0.00	6.55	2634.47	2694.59	0.00	0.00	0.00	0.00	2694.59	-17.16	-17.16	979090.3616	0.723617004	-367.187326	133.22452	5.76177	0.77	979481.67	-150.81244
11/7/2015	M705	31.969445	-106.95692	1202.825	2:33	14.55	0.00	0.00	6.87	2631.88	2691.94	0.00	0.00	0.00	0.00	2691.94	-19.81	-19.81	979087.7101	0.725339696	-371.14255	134.65999	4.327034	0.77	979481.86	-152.57075
11/7/2015	M706	31.970485	-106.95405	1198.183	2:50	14.83	0.00	0.00	7.15	2639.29	2699.80	0.00	0.00	0.00	0.00	2699.80	-11.95	-11.95	[illegible]	[illegible]	[illegible]	[illegible]	7.495046	0.77	979482.01	[illegible]
11/7/2015	M707	31.96783	-106.9628	1174.57	3:09	15.15	0.00	0.00	7.47	2640.45	2700.71	0.00	0.00	0.00	0.00	2700.71	-11.04	-11.04	[illegible]	[illegible]	[illegible]	[illegible]	7.488668	0.77	979481.73	-146.05568
11/7/2015	Kidds	31.7719	-106.506	1186.5	8:06	20.10	0.00	0.00	12.42	2651.23	2711.75	0.00	0.00	0.00	0.00	2711.75	0.00	0.00	979107.52	0.529833608	-366.108334	132.83235	*	0.77	979465.86	#VALUE!

Appendix B: Kilbourne Hole Reduced to Pole Magnetic Data

In this appendix B, we include our reduced to pole magnetic data from Kibourne Hole in an excel spreadsheet. The reduced to pole magnetic data were derived from a total of 166 magnetic measurements form our field magnetic surveys at Kilbourne Hole. Our magnetic field works were completed over 1 year time span with surveys in March, 2011, May 2011, and January 2012 (Rhodes and Hurtado, 2012). We used the reference total magnetic field derived by Finlay et al. (2010) and corrected our field magnetic data to the reduced pole magnetic data using the `RTP` extension implemented in the *Geosoft Oasis Montaj 6.0* software suite. The spreadsheet include: (1) latitudes, (2) longitudes, and (3) the reduced to pole magnetic intensity value in (nT).

References

Finlay, C. C., Maus, S., Beggan, C. D., Hamoudi, M., Lowes, F. J., Olsen, N., and Thébault, E., 2010, Evaluation of candidate geomagnetic field models for IGRF-11. *Earth Planets Space*, vol. 62, no. 10, p. 787-804.

Rhodes, N. and Hurtado, J. M. (Jr.), 2012, A magnetic survey of Kilbourne Hole, southern New Mexico: implications for near surface geophysical exploration of Mars and the Moon: Lunar and Planetary Science Conference, Abstracts, vol. 43, p. 2914.

Line	X	Y	Z
L1	312900	3537050	45865.87
L1	312950	3537050	46140.35
L1	313000	3537050	46444.19
L1	313050	3537050	46706.79
L1	313100	3537050	46909.34
L1	313150	3537050	47034.07
L1	313200	3537050	47161.45
L1	313250	3537050	47350.14
L1	313300	3537050	47584.22
L1	313350	3537050	47747.57
L1	313400	3537050	47899.74
L1	313450	3537050	48073.38
L1	313500	3537050	48162.55
L1	313550	3537050	48202.57
L1	313600	3537050	48248.67
L1	313650	3537050	48299.02
L1	313700	3537050	48342.16
L1	313750	3537050	48366.99
L1	313800	3537050	48383.11
L1	313850	3537050	48394.39
L1	313900	3537050	48406.66
L1	313950	3537050	48432.6
L1	314000	3537050	48474.36
L1	314050	3537050	48508.11
L1	314100	3537050	48497.16
L1	314150	3537050	48417.1
L1	314200	3537050	48321.8
L1	314250	3537050	48278.91
L1	314300	3537050	48355.4
L1	314350	3537050	48629.21
L1	314400	3537050	49009.52
L1	314450	3537050	49284.07
L1	314500	3537050	49208.47
L1	314550	3537050	48625.06
L1	314600	3537050	47714.82
L1	314650	3537050	46767.25
L1	314700	3537050	46107.52
L1	314750	3537050	46026.6
L1	314800	3537050	46416.72
L1	314850	3537050	47058.02
L1	314900	3537050	47665.18
L1	314950	3537050	48024.5
L1	315000	3537050	48174.64
L1	315050	3537050	48176.45
L1	315100	3537050	48134.95
L1	315150	3537050	48148.64

L1	315200	3537050	48218.95
L1	315250	3537050	48306.87
L1	315300	3537050	48368.29
L1	315350	3537050	48360.47
L1	315400	3537050	48292.45
L1	315450	3537050	48188.61
L1	315500	3537050	48079.09
L1	315550	3537050	47996.37
L1	315600	3537050	47943.89
L1	315650	3537050	47911.86
L1	315700	3537050	47889.07
L1	315750	3537050	47894.73
L2	312900	3537100	46173.3
L2	312950	3537100	46372.66
L2	313000	3537100	46594.93
L2	313050	3537100	46808.11
L2	313100	3537100	46989.98
L2	313150	3537100	47140.81
L2	313200	3537100	47278.66
L2	313250	3537100	47438.37
L2	313300	3537100	47600.41
L2	313350	3537100	47748.76
L2	313400	3537100	47884.3
L2	313450	3537100	48003.55
L2	313500	3537100	48097.57
L2	313550	3537100	48163.77
L2	313600	3537100	48215.78
L2	313650	3537100	48263.13
L2	313700	3537100	48302.89
L2	313750	3537100	48330.6
L2	313800	3537100	48349.96
L2	313850	3537100	48365.35
L2	313900	3537100	48381.85
L2	313950	3537100	48406.64
L2	314000	3537100	48435.91
L2	314050	3537100	48456.64
L2	314100	3537100	48449.24
L2	314150	3537100	48402.55
L2	314200	3537100	48345.67
L2	314250	3537100	48327.73
L2	314300	3537100	48398.15
L2	314350	3537100	48597.22
L2	314400	3537100	48844.04
L2	314450	3537100	48997.25
L2	314500	3537100	48905.4
L2	314550	3537100	48450.36
L2	314600	3537100	47755.61

L2	314650	3537100	47033.65
L2	314700	3537100	46515.19
L2	314750	3537100	46406.82
L2	314800	3537100	46658.19
L2	314850	3537100	47110.14
L2	314900	3537100	47581.01
L2	314950	3537100	47897.91
L2	315000	3537100	48056.1
L2	315050	3537100	48106.35
L2	315100	3537100	48110.02
L2	315150	3537100	48135.8
L2	315200	3537100	48189.06
L2	315250	3537100	48250.78
L2	315300	3537100	48292.92
L2	315350	3537100	48289.12
L2	315400	3537100	48242.76
L2	315450	3537100	48169.68
L2	315500	3537100	48089.34
L2	315550	3537100	48022.01
L2	315600	3537100	47974.07
L2	315650	3537100	47943.46
L2	315700	3537100	47927.68
L2	315750	3537100	47929.8
L3	312900	3537150	46602.33
L3	312950	3537150	46703.22
L3	313000	3537150	46838.29
L3	313050	3537150	46981.4
L3	313100	3537150	47117.4
L3	313150	3537150	47240.34
L3	313200	3537150	47362.94
L3	313250	3537150	47485.7
L3	313300	3537150	47617.99
L3	313350	3537150	47743.22
L3	313400	3537150	47857.08
L3	313450	3537150	47962.83
L3	313500	3537150	48047.99
L3	313550	3537150	48113.64
L3	313600	3537150	48169.06
L3	313650	3537150	48216.08
L3	313700	3537150	48255.06
L3	313750	3537150	48285.54
L3	313800	3537150	48309.24
L3	313850	3537150	48329.08
L3	313900	3537150	48348.65
L3	313950	3537150	48370.41
L3	314000	3537150	48393.17
L3	314050	3537150	48407.85

L3	314100	3537150	48404.38
L3	314150	3537150	48380.84
L3	314200	3537150	48355.07
L3	314250	3537150	48357.21
L3	314300	3537150	48417.71
L3	314350	3537150	48542.59
L3	314400	3537150	48685.35
L3	314450	3537150	48749.44
L3	314500	3537150	48632.7
L3	314550	3537150	48291.55
L3	314600	3537150	47784.91
L3	314650	3537150	47258.98
L3	314700	3537150	46877.76
L3	314750	3537150	46755.63
L3	314800	3537150	46891.64
L3	314850	3537150	47191.15
L3	314900	3537150	47523.67
L3	314950	3537150	47788.16
L3	315000	3537150	47951.34
L3	315050	3537150	48031.81
L3	315100	3537150	48071.48
L3	315150	3537150	48106.52
L3	315200	3537150	48151.42
L3	315250	3537150	48196.98
L3	315300	3537150	48226.74
L3	315350	3537150	48227.39
L3	315400	3537150	48198.07
L3	315450	3537150	48148.04
L3	315500	3537150	48090.89
L3	315550	3537150	48039.74
L3	315600	3537150	48001.27
L3	315650	3537150	47976.45
L3	315700	3537150	47964.79
L3	315750	3537150	47970.82
L4	312900	3537200	47124.12
L4	312950	3537200	47114.31
L4	313000	3537200	47147.92
L4	313050	3537200	47209.55
L4	313100	3537200	47283.92
L4	313150	3537200	47364.83
L4	313200	3537200	47448.63
L4	313250	3537200	47545.76
L4	313300	3537200	47642.95
L4	313350	3537200	47740.92
L4	313400	3537200	47837.15
L4	313450	3537200	47922.93
L4	313500	3537200	47999.43

L4	313550	3537200	48065.37
L4	313600	3537200	48120.09
L4	313650	3537200	48167.2
L4	313700	3537200	48206.81
L4	313750	3537200	48239.29
L4	313800	3537200	48265.7
L4	313850	3537200	48288.25
L4	313900	3537200	48309.18
L4	313950	3537200	48330.31
L4	314000	3537200	48349.27
L4	314050	3537200	48362.16
L4	314100	3537200	48364.05
L4	314150	3537200	48355.27
L4	314200	3537200	48346.3
L4	314250	3537200	48356.08
L4	314300	3537200	48400.27
L4	314350	3537200	48478.88
L4	314400	3537200	48553.63
L4	314450	3537200	48563.68
L4	314500	3537200	48449.85
L4	314550	3537200	48182.02
L4	314600	3537200	47807.62
L4	314650	3537200	47421.42
L4	314700	3537200	47131.89
L4	314750	3537200	47020.08
L4	314800	3537200	47089.35
L4	314850	3537200	47283.18
L4	314900	3537200	47521.51
L4	314950	3537200	47728.74
L4	315000	3537200	47875.3
L4	315050	3537200	47966.81
L4	315100	3537200	48022.8
L4	315150	3537200	48067.49
L4	315200	3537200	48109.27
L4	315250	3537200	48146.51
L4	315300	3537200	48171.07
L4	315350	3537200	48175.23
L4	315400	3537200	48158.52
L4	315450	3537200	48126.66
L4	315500	3537200	48088.52
L4	315550	3537200	48052.91
L4	315600	3537200	48025.39
L4	315650	3537200	48008.16
L4	315700	3537200	48002.18
L4	315750	3537200	48007.14
L5	312900	3537250	47741.17
L5	312950	3537250	47594.6

L5	313000	3537250	47515.53
L5	313050	3537250	47483.84
L5	313100	3537250	47485.66
L5	313150	3537250	47509.73
L5	313200	3537250	47553.69
L5	313250	3537250	47605.05
L5	313300	3537250	47672.03
L5	313350	3537250	47745.43
L5	313400	3537250	47818.3
L5	313450	3537250	47890.94
L5	313500	3537250	47957.02
L5	313550	3537250	48015.48
L5	313600	3537250	48068.77
L5	313650	3537250	48114.82
L5	313700	3537250	48154.49
L5	313750	3537250	48188.27
L5	313800	3537250	48217.55
L5	313850	3537250	48242.82
L5	313900	3537250	48265.54
L5	313950	3537250	48286.03
L5	314000	3537250	48304.35
L5	314050	3537250	48317.5
L5	314100	3537250	48323.68
L5	314150	3537250	48324.08
L5	314200	3537250	48325.71
L5	314250	3537250	48338.25
L5	314300	3537250	48369.2
L5	314350	3537250	48411.65
L5	314400	3537250	48442.61
L5	314450	3537250	48421.88
L5	314500	3537250	48311.29
L5	314550	3537250	48103.78
L5	314600	3537250	47825.48
L5	314650	3537250	47541.35
L5	314700	3537250	47324.69
L5	314750	3537250	47224.23
L5	314800	3537250	47251.11
L5	314850	3537250	47373.69
L5	314900	3537250	47537.24
L5	314950	3537250	47696.5
L5	315000	3537250	47823.85
L5	315050	3537250	47913.84
L5	315100	3537250	47977.11
L5	315150	3537250	48024.7
L5	315200	3537250	48065.5
L5	315250	3537250	48099.14
L5	315300	3537250	48121.83

L5	315350	3537250	48130.18
L5	315400	3537250	48123.79
L5	315450	3537250	48106.17
L5	315500	3537250	48083.55
L5	315550	3537250	48062.14
L5	315600	3537250	48046.54
L5	315650	3537250	48038.75
L5	315700	3537250	48039.02
L5	315750	3537250	48048.3
L6	312900	3537300	48430.79
L6	312950	3537300	48127.23
L6	313000	3537300	47919.73
L6	313050	3537300	47785.33
L6	313100	3537300	47704.81
L6	313150	3537300	47664.64
L6	313200	3537300	47652.79
L6	313250	3537300	47671.5
L6	313300	3537300	47704.01
L6	313350	3537300	47749.13
L6	313400	3537300	47804.26
L6	313450	3537300	47859.2
L6	313500	3537300	47913.75
L6	313550	3537300	47966.97
L6	313600	3537300	48016.55
L6	313650	3537300	48061.85
L6	313700	3537300	48101.62
L6	313750	3537300	48136.56
L6	313800	3537300	48167.6
L6	313850	3537300	48195.15
L6	313900	3537300	48219.44
L6	313950	3537300	48241.12
L6	314000	3537300	48259.21
L6	314050	3537300	48273.52
L6	314100	3537300	48283.33
L6	314150	3537300	48289.58
L6	314200	3537300	48295.54
L6	314250	3537300	48306.8
L6	314300	3537300	48325.62
L6	314350	3537300	48346.91
L6	314400	3537300	48351.57
L6	314450	3537300	48315.24
L6	314500	3537300	48217.96
L6	314550	3537300	48051.88
L6	314600	3537300	47841.45
L6	314650	3537300	47628.38
L6	314700	3537300	47460.71
L6	314750	3537300	47375.79

L6	314800	3537300	47380.27
L6	314850	3537300	47455.74
L6	314900	3537300	47570.64
L6	314950	3537300	47689.66
L6	315000	3537300	47792.56
L6	315050	3537300	47873.94
L6	315100	3537300	47934.46
L6	315150	3537300	47983.43
L6	315200	3537300	48023.43
L6	315250	3537300	48055.71
L6	315300	3537300	48079.07
L6	315350	3537300	48091.58
L6	315400	3537300	48093.46
L6	315450	3537300	48087.52
L6	315500	3537300	48078.09
L6	315550	3537300	48069.58
L6	315600	3537300	48065.51
L6	315650	3537300	48067.83
L6	315700	3537300	48076.11
L6	315750	3537300	48088.43
L7	312900	3537350	49175.39
L7	312950	3537350	48688.25
L7	313000	3537350	48342.97
L7	313050	3537350	48099.82
L7	313100	3537350	47934.78
L7	313150	3537350	47828.25
L7	313200	3537350	47768.66
L7	313250	3537350	47736.25
L7	313300	3537350	47735.91
L7	313350	3537350	47756.48
L7	313400	3537350	47787.97
L7	313450	3537350	47828.11
L7	313500	3537350	47870.84
L7	313550	3537350	47913.99
L7	313600	3537350	47960.78
L7	313650	3537350	48004.52
L7	313700	3537350	48043.98
L7	313750	3537350	48079.34
L7	313800	3537350	48113.69
L7	313850	3537350	48144.6
L7	313900	3537350	48171.64
L7	313950	3537350	48194.56
L7	314000	3537350	48214.07
L7	314050	3537350	48229.78
L7	314100	3537350	48242.15
L7	314150	3537350	48251.76
L7	314200	3537350	48260.5

L7	314250	3537350	48270.19
L7	314300	3537350	48280.93
L7	314350	3537350	48286.22
L7	314400	3537350	48275.24
L7	314450	3537350	48232.5
L7	314500	3537350	48144.97
L7	314550	3537350	48014.8
L7	314600	3537350	47854.33
L7	314650	3537350	47693.61
L7	314700	3537350	47565.68
L7	314750	3537350	47492.55
L7	314800	3537350	47482.97
L7	314850	3537350	47527.36
L7	314900	3537350	47603.52
L7	314950	3537350	47691.32
L7	315000	3537350	47773.91
L7	315050	3537350	47842.93
L7	315100	3537350	47898.56
L7	315150	3537350	47944.63
L7	315200	3537350	47983.81
L7	315250	3537350	48015.94
L7	315300	3537350	48040.57
L7	315350	3537350	48057.3
L7	315400	3537350	48066.29
L7	315450	3537350	48069.68
L7	315500	3537350	48070.82
L7	315550	3537350	48073.34
L7	315600	3537350	48080.2
L7	315650	3537350	48093.67
L7	315700	3537350	48112.75
L7	315750	3537350	48125.9
L8	312900	3537400	49905.98
L8	312950	3537400	49233.28
L8	313000	3537400	48747.9
L8	313050	3537400	48397.98
L8	313100	3537400	48148.37
L8	313150	3537400	47974.46
L8	313200	3537400	47856.52
L8	313250	3537400	47791.62
L8	313300	3537400	47757.61
L8	313350	3537400	47749.98
L8	313400	3537400	47767.48
L8	313450	3537400	47793.9
L8	313500	3537400	47824.41
L8	313550	3537400	47857.99
L8	313600	3537400	47902.95
L8	313650	3537400	47947.14

L8	313700	3537400	47986.44
L8	313750	3537400	48021.53
L8	313800	3537400	48059.55
L8	313850	3537400	48094.32
L8	313900	3537400	48124.09
L8	313950	3537400	48149.64
L8	314000	3537400	48170.11
L8	314050	3537400	48187.13
L8	314100	3537400	48201.26
L8	314150	3537400	48213.03
L8	314200	3537400	48222
L8	314250	3537400	48229.18
L8	314300	3537400	48233.43
L8	314350	3537400	48231.04
L8	314400	3537400	48212.36
L8	314450	3537400	48168.64
L8	314500	3537400	48094.95
L8	314550	3537400	47989.67
L8	314600	3537400	47865.87
L8	314650	3537400	47742.5
L8	314700	3537400	47641.45
L8	314750	3537400	47580.9
L8	314800	3537400	47564.79
L8	314850	3537400	47588.29
L8	314900	3537400	47639.98
L8	314950	3537400	47702.82
L8	315000	3537400	47764.05
L8	315050	3537400	47818.64
L8	315100	3537400	47864.38
L8	315150	3537400	47909.5
L8	315200	3537400	47948.22
L8	315250	3537400	47980.47
L8	315300	3537400	48006.93
L8	315350	3537400	48027.32
L8	315400	3537400	48041.83
L8	315450	3537400	48052.41
L8	315500	3537400	48061.82
L8	315550	3537400	48072.64
L8	315600	3537400	48086.85
L8	315650	3537400	48106.27
L8	315700	3537400	48129.21
L8	315750	3537400	48140.74
L9	312900	3537450	50551.34
L9	312950	3537450	49702.11
L9	313000	3537450	49095.25
L9	313050	3537450	48653.43
L9	313100	3537450	48332.14

L9	313150	3537450	48102.71
L9	313200	3537450	47945.57
L9	313250	3537450	47833.13
L9	313300	3537450	47767.27
L9	313350	3537450	47737.77
L9	313400	3537450	47740.18
L9	313450	3537450	47760.52
L9	313500	3537450	47784.93
L9	313550	3537450	47811.92
L9	313600	3537450	47852.95
L9	313650	3537450	47895.06
L9	313700	3537450	47934.12
L9	313750	3537450	47970.33
L9	313800	3537450	48010.38
L9	313850	3537450	48047.29
L9	313900	3537450	48079.07
L9	313950	3537450	48106.11
L9	314000	3537450	48128.25
L9	314050	3537450	48146.13
L9	314100	3537450	48161.14
L9	314150	3537450	48173.88
L9	314200	3537450	48183.31
L9	314250	3537450	48188.77
L9	314300	3537450	48189.42
L9	314350	3537450	48181.47
L9	314400	3537450	48159.35
L9	314450	3537450	48117.74
L9	314500	3537450	48053.35
L9	314550	3537450	47970.67
L9	314600	3537450	47874.72
L9	314650	3537450	47779.96
L9	314700	3537450	47701.96
L9	314750	3537450	47650.51
L9	314800	3537450	47630.66
L9	314850	3537450	47640.45
L9	314900	3537450	47671.56
L9	314950	3537450	47715.39
L9	315000	3537450	47761.28
L9	315050	3537450	47802.93
L9	315100	3537450	47841.24
L9	315150	3537450	47880.7
L9	315200	3537450	47917.57
L9	315250	3537450	47949.33
L9	315300	3537450	47976.77
L9	315350	3537450	48000.18
L9	315400	3537450	48019.23
L9	315450	3537450	48034.86

L9	315500	3537450	48049.66
L9	315550	3537450	48065.44
L9	315600	3537450	48082.65
L9	315650	3537450	48101.45
L9	315700	3537450	48120.13
L9	315750	3537450	48134.39
L10	312900	3537500	50890.74
L10	312950	3537500	49998.5
L10	313000	3537500	49328.13
L10	313050	3537500	48829.73
L10	313100	3537500	48457.45
L10	313150	3537500	48184.82
L10	313200	3537500	47985.65
L10	313250	3537500	47851.93
L10	313300	3537500	47757.36
L10	313350	3537500	47700.08
L10	313400	3537500	47710.44
L10	313450	3537500	47738.68
L10	313500	3537500	47761.19
L10	313550	3537500	47788.81
L10	313600	3537500	47821.48
L10	313650	3537500	47859.69
L10	313700	3537500	47898.74
L10	313750	3537500	47938.41
L10	313800	3537500	47975.12
L10	313850	3537500	48009.61
L10	313900	3537500	48040.36
L10	313950	3537500	48067.82
L10	314000	3537500	48090.06
L10	314050	3537500	48108.29
L10	314100	3537500	48123.45
L10	314150	3537500	48136.36
L10	314200	3537500	48144.94
L10	314250	3537500	48148.58
L10	314300	3537500	48146.37
L10	314350	3537500	48136.86
L10	314400	3537500	48114.61
L10	314450	3537500	48076.51
L10	314500	3537500	48023.11
L10	314550	3537500	47955.48
L10	314600	3537500	47881.73
L10	314650	3537500	47809.34
L10	314700	3537500	47747.89
L10	314750	3537500	47706.71
L10	314800	3537500	47686.32
L10	314850	3537500	47687.12
L10	314900	3537500	47706.42

L10	314950	3537500	47735.77
L10	315000	3537500	47765.97
L10	315050	3537500	47795.67
L10	315100	3537500	47825.43
L10	315150	3537500	47859.42
L10	315200	3537500	47892.83
L10	315250	3537500	47923.4
L10	315300	3537500	47951.32
L10	315350	3537500	47976.78
L10	315400	3537500	47999
L10	315450	3537500	48018.49
L10	315500	3537500	48036.86
L10	315550	3537500	48055.04
L10	315600	3537500	48071.95
L10	315650	3537500	48087.48
L10	315700	3537500	48103.11
L10	315750	3537500	48118.43
L11	312900	3537550	50831.46
L11	312950	3537550	50054.69
L11	313000	3537550	49414.34
L11	313050	3537550	48910.47
L11	313100	3537550	48524.09
L11	313150	3537550	48235.95
L11	313200	3537550	48026.18
L11	313250	3537550	47862.55
L11	313300	3537550	47752.75
L11	313350	3537550	47694.42
L11	313400	3537550	47699.07
L11	313450	3537550	47730.86
L11	313500	3537550	47755.23
L11	313550	3537550	47778.94
L11	313600	3537550	47806.25
L11	313650	3537550	47839.17
L11	313700	3537550	47877.36
L11	313750	3537550	47916.77
L11	313800	3537550	47951.09
L11	313850	3537550	47981.25
L11	313900	3537550	48009.09
L11	313950	3537550	48034.37
L11	314000	3537550	48056.22
L11	314050	3537550	48074.01
L11	314100	3537550	48088.91
L11	314150	3537550	48101.1
L11	314200	3537550	48109.21
L11	314250	3537550	48111.83
L11	314300	3537550	48108.49
L11	314350	3537550	48097.23

L11	314400	3537550	48075.33
L11	314450	3537550	48041.01
L11	314500	3537550	47994.44
L11	314550	3537550	47941.22
L11	314600	3537550	47885.66
L11	314650	3537550	47832.68
L11	314700	3537550	47788.2
L11	314750	3537550	47755.58
L11	314800	3537550	47735.63
L11	314850	3537550	47731.02
L11	314900	3537550	47739.85
L11	314950	3537550	47758
L11	315000	3537550	47776.5
L11	315050	3537550	47794.43
L11	315100	3537550	47815.68
L11	315150	3537550	47842.62
L11	315200	3537550	47872.47
L11	315250	3537550	47901.62
L11	315300	3537550	47929.7
L11	315350	3537550	47956.68
L11	315400	3537550	47981.69
L11	315450	3537550	48004.31
L11	315500	3537550	48025.49
L11	315550	3537550	48044.84
L11	315600	3537550	48060.14
L11	315650	3537550	48070.07
L11	315700	3537550	48076.74
L11	315750	3537550	48102.71
L12	312900	3537600	50444.87
L12	312950	3537600	49885.99
L12	313000	3537600	49349.45
L12	313050	3537600	48892.98
L12	313100	3537600	48524.61
L12	313150	3537600	48239.13
L12	313200	3537600	48015.44
L12	313250	3537600	47856.19
L12	313300	3537600	47746.68
L12	313350	3537600	47707.47
L12	313400	3537600	47711.22
L12	313450	3537600	47748.3
L12	313500	3537600	47767.38
L12	313550	3537600	47789.29
L12	313600	3537600	47805.3
L12	313650	3537600	47832.78
L12	313700	3537600	47871.94
L12	313750	3537600	47916.65
L12	313800	3537600	47941.31

L12	313850	3537600	47963.18
L12	313900	3537600	47986.06
L12	313950	3537600	48007.86
L12	314000	3537600	48027.55
L12	314050	3537600	48044.34
L12	314100	3537600	48058.62
L12	314150	3537600	48069.34
L12	314200	3537600	48075.91
L12	314250	3537600	48077.28
L12	314300	3537600	48072.95
L12	314350	3537600	48061.37
L12	314400	3537600	48040.91
L12	314450	3537600	48010.25
L12	314500	3537600	47971.37
L12	314550	3537600	47925.42
L12	314600	3537600	47887.16
L12	314650	3537600	47852.22
L12	314700	3537600	47822.19
L12	314750	3537600	47801.59
L12	314800	3537600	47781.52
L12	314850	3537600	47773.04
L12	314900	3537600	47777.62
L12	314950	3537600	47789.6
L12	315000	3537600	47792.41
L12	315050	3537600	47796.95
L12	315100	3537600	47806.3
L12	315150	3537600	47828.95
L12	315200	3537600	47856.17
L12	315250	3537600	47884.48
L12	315300	3537600	47913.27
L12	315350	3537600	47941.47
L12	315400	3537600	47969.03
L12	315450	3537600	47995.55
L12	315500	3537600	48020.59
L12	315550	3537600	48042.35
L12	315600	3537600	48058.93
L12	315650	3537600	48069.91
L12	315700	3537600	48079.95
L12	315750	3537600	48112.63
L13	312900	3537650	49842.62
L13	312950	3537650	49556.56
L13	313000	3537650	49177.26
L13	313050	3537650	48806.6
L13	313100	3537650	48489.53
L13	313150	3537650	48231.29
L13	313200	3537650	48021.91
L13	313250	3537650	47840.23

L13	313300	3537650	47720.26
L13	313350	3537650	47687.93
L13	313400	3537650	47700.78
L13	313450	3537650	47748.07
L13	313500	3537650	47772.02
L13	313550	3537650	47787.58
L13	313600	3537650	47801.21
L13	313650	3537650	47825
L13	313700	3537650	47863.46
L13	313750	3537650	47905.1
L13	313800	3537650	47929.73
L13	313850	3537650	47948.09
L13	313900	3537650	47967.78
L13	313950	3537650	47985.96
L13	314000	3537650	48003.83
L13	314050	3537650	48019.24
L13	314100	3537650	48032.54
L13	314150	3537650	48041.46
L13	314200	3537650	48046.94
L13	314250	3537650	48047.73
L13	314300	3537650	48043.26
L13	314350	3537650	48031.03
L13	314400	3537650	48011.58
L13	314450	3537650	47984.98
L13	314500	3537650	47951.83
L13	314550	3537650	47916.67
L13	314600	3537650	47889.66
L13	314650	3537650	47867.87
L13	314700	3537650	47850.12
L13	314750	3537650	47835.41
L13	314800	3537650	47818.18
L13	314850	3537650	47808.17
L13	314900	3537650	47806.91
L13	314950	3537650	47810.56
L13	315000	3537650	47806.29
L13	315050	3537650	47801.87
L13	315100	3537650	47804.49
L13	315150	3537650	47819.99
L13	315200	3537650	47843.95
L13	315250	3537650	47871.46
L13	315300	3537650	47901.02
L13	315350	3537650	47931.03
L13	315400	3537650	47962.01
L13	315450	3537650	47993.34
L13	315500	3537650	48023.73
L13	315550	3537650	48050.92
L13	315600	3537650	48074.35

L13	315650	3537650	48094.99
L13	315700	3537650	48117.22
L13	315750	3537650	48151.43
L14	312900	3537700	49263.45
L14	312950	3537700	49185.53
L14	313000	3537700	48961.96
L14	313050	3537700	48693.16
L14	313100	3537700	48440.7
L14	313150	3537700	48212.85
L14	313200	3537700	47994.27
L14	313250	3537700	47800.08
L14	313300	3537700	47637.59
L14	313350	3537700	47590.29
L14	313400	3537700	47641.46
L14	313450	3537700	47732.4
L14	313500	3537700	47764.44
L14	313550	3537700	47780.45
L14	313600	3537700	47793.27
L14	313650	3537700	47815.64
L14	313700	3537700	47851.65
L14	313750	3537700	47889.36
L14	313800	3537700	47915.65
L14	313850	3537700	47934.7
L14	313900	3537700	47953.39
L14	313950	3537700	47970.59
L14	314000	3537700	47986.09
L14	314050	3537700	47999.4
L14	314100	3537700	48010.95
L14	314150	3537700	48018.43
L14	314200	3537700	48022.25
L14	314250	3537700	48021.71
L14	314300	3537700	48016.91
L14	314350	3537700	48005.8
L14	314400	3537700	47988.78
L14	314450	3537700	47966.19
L14	314500	3537700	47941.28
L14	314550	3537700	47915.25
L14	314600	3537700	47895.75
L14	314650	3537700	47880.89
L14	314700	3537700	47868.53
L14	314750	3537700	47857.21
L14	314800	3537700	47844.43
L14	314850	3537700	47834.14
L14	314900	3537700	47829.44
L14	314950	3537700	47825.07
L14	315000	3537700	47815.52
L14	315050	3537700	47806.42

L14	315100	3537700	47804.49
L14	315150	3537700	47815.57
L14	315200	3537700	47836.22
L14	315250	3537700	47862.83
L14	315300	3537700	47893.56
L14	315350	3537700	47926.54
L14	315400	3537700	47961.77
L14	315450	3537700	47998.74
L14	315500	3537700	48036.21
L14	315550	3537700	48072.14
L14	315600	3537700	48106.33
L14	315650	3537700	48139.39
L14	315700	3537700	48172.39
L14	315750	3537700	48207.11
L15	312900	3537750	48849.83
L15	312950	3537750	48884.41
L15	313000	3537750	48781.11
L15	313050	3537750	48612.68
L15	313100	3537750	48435.53
L15	313150	3537750	48253.28
L15	313200	3537750	48050.63
L15	313250	3537750	47804.43
L15	313300	3537750	47579.81
L15	313350	3537750	47480.33
L15	313400	3537750	47544.63
L15	313450	3537750	47681.22
L15	313500	3537750	47744.32
L15	313550	3537750	47773.52
L15	313600	3537750	47789.32
L15	313650	3537750	47808.79
L15	313700	3537750	47841.23
L15	313750	3537750	47875.95
L15	313800	3537750	47903.22
L15	313850	3537750	47923.5
L15	313900	3537750	47942.64
L15	313950	3537750	47959.49
L15	314000	3537750	47973.67
L15	314050	3537750	47984.79
L15	314100	3537750	47994.17
L15	314150	3537750	48000.15
L15	314200	3537750	48003.21
L15	314250	3537750	48002.47
L15	314300	3537750	47997.98
L15	314350	3537750	47988.02
L15	314400	3537750	47972.45
L15	314450	3537750	47953.29
L15	314500	3537750	47932.82

L15	314550	3537750	47914.63
L15	314600	3537750	47901.09
L15	314650	3537750	47891.2
L15	314700	3537750	47883.46
L15	314750	3537750	47874.65
L15	314800	3537750	47863.86
L15	314850	3537750	47853.47
L15	314900	3537750	47844.4
L15	314950	3537750	47835.08
L15	315000	3537750	47821.98
L15	315050	3537750	47808.65
L15	315100	3537750	47803.1
L15	315150	3537750	47810.84
L15	315200	3537750	47830.32
L15	315250	3537750	47857.16
L15	315300	3537750	47889.63
L15	315350	3537750	47926.28
L15	315400	3537750	47966.94
L15	315450	3537750	48010.32
L15	315500	3537750	48055.79
L15	315550	3537750	48102.14
L15	315600	3537750	48149.93
L15	315650	3537750	48198.79
L15	315700	3537750	48247.79
L15	315750	3537750	48277.12
L16	312900	3537800	48648.43
L16	312950	3537800	48710.51
L16	313000	3537800	48688.14
L16	313050	3537800	48609.65
L16	313100	3537800	48509.13
L16	313150	3537800	48367.98
L16	313200	3537800	48155.41
L16	313250	3537800	47879.35
L16	313300	3537800	47566.23
L16	313350	3537800	47309.22
L16	313400	3537800	47414.35
L16	313450	3537800	47624.47
L16	313500	3537800	47714.55
L16	313550	3537800	47779.3
L16	313600	3537800	47793.13
L16	313650	3537800	47808.81
L16	313700	3537800	47837.94
L16	313750	3537800	47874.18
L16	313800	3537800	47897.38
L16	313850	3537800	47916.45
L16	313900	3537800	47935.9
L16	313950	3537800	47955.48

L16	314000	3537800	47966.97
L16	314050	3537800	47974.95
L16	314100	3537800	47981.65
L16	314150	3537800	47986.86
L16	314200	3537800	47988.99
L16	314250	3537800	47987.35
L16	314300	3537800	47983.04
L16	314350	3537800	47975.89
L16	314400	3537800	47962.29
L16	314450	3537800	47945.13
L16	314500	3537800	47928.91
L16	314550	3537800	47914.77
L16	314600	3537800	47906.27
L16	314650	3537800	47899.68
L16	314700	3537800	47893.73
L16	314750	3537800	47888.36
L16	314800	3537800	47879
L16	314850	3537800	47867.85
L16	314900	3537800	47857.45
L16	314950	3537800	47846.32
L16	315000	3537800	47827.06
L16	315050	3537800	47807.75
L16	315100	3537800	47795.32
L16	315150	3537800	47804.95
L16	315200	3537800	47826.16
L16	315250	3537800	47854.24
L16	315300	3537800	47889.2
L16	315350	3537800	47930.42
L16	315400	3537800	47976.86
L16	315450	3537800	48026.61
L16	315500	3537800	48080.15
L16	315550	3537800	48137.23
L16	315600	3537800	48197.13
L16	315650	3537800	48257
L16	315700	3537800	48312.09
L16	315750	3537800	48342.35
L17	312900	3537850	48653.3
L17	312950	3537850	48681.75
L17	313000	3537850	48714.79
L17	313050	3537850	48728.43
L17	313100	3537850	48720.09
L17	313150	3537850	48651.41
L17	313200	3537850	48477.96
L17	313250	3537850	48145.21
L17	313300	3537850	47737.65
L17	313350	3537850	47382.83
L17	313400	3537850	47373.54

L17	313450	3537850	47526.5
L17	313500	3537850	47635.76
L17	313550	3537850	47728.7
L17	313600	3537850	47769.11
L17	313650	3537850	47795.58
L17	313700	3537850	47828.03
L17	313750	3537850	47863.85
L17	313800	3537850	47888.76
L17	313850	3537850	47908.59
L17	313900	3537850	47928.78
L17	313950	3537850	47948.84
L17	314000	3537850	47960.53
L17	314050	3537850	47967.3
L17	314100	3537850	47972.54
L17	314150	3537850	47977.16
L17	314200	3537850	47978.87
L17	314250	3537850	47977.24
L17	314300	3537850	47972.92
L17	314350	3537850	47966.86
L17	314400	3537850	47954.37
L17	314450	3537850	47939.42
L17	314500	3537850	47925.06
L17	314550	3537850	47915.32
L17	314600	3537850	47909.52
L17	314650	3537850	47905.41
L17	314700	3537850	47901.99
L17	314750	3537850	47897.91
L17	314800	3537850	47889.12
L17	314850	3537850	47877.54
L17	314900	3537850	47864.55
L17	314950	3537850	47851
L17	315000	3537850	47830.23
L17	315050	3537850	47807.95
L17	315100	3537850	47794.14
L17	315150	3537850	47801.99
L17	315200	3537850	47823.93
L17	315250	3537850	47853.67
L17	315300	3537850	47891.3
L17	315350	3537850	47936.85
L17	315400	3537850	47988.66
L17	315450	3537850	48044.63
L17	315500	3537850	48105.63
L17	315550	3537850	48171.8
L17	315600	3537850	48240.95
L17	315650	3537850	48307.96
L17	315700	3537850	48365
L17	315750	3537850	48399.53

L18	312900	3537900	48699.5
L18	312950	3537900	48746.39
L18	313000	3537900	48853.38
L18	313050	3537900	48978.45
L18	313100	3537900	49089.39
L18	313150	3537900	49113.27
L18	313200	3537900	48969.03
L18	313250	3537900	48642.74
L18	313300	3537900	48179.37
L18	313350	3537900	47727.82
L18	313400	3537900	47468.22
L18	313450	3537900	47343.47
L18	313500	3537900	47474.64
L18	313550	3537900	47605.98
L18	313600	3537900	47696.29
L18	313650	3537900	47760.55
L18	313700	3537900	47809.58
L18	313750	3537900	47852.58
L18	313800	3537900	47879
L18	313850	3537900	47901.2
L18	313900	3537900	47921.55
L18	313950	3537900	47940.8
L18	314000	3537900	47952.8
L18	314050	3537900	47961.14
L18	314100	3537900	47966.3
L18	314150	3537900	47969.74
L18	314200	3537900	47969.44
L18	314250	3537900	47966.78
L18	314300	3537900	47961.08
L18	314350	3537900	47952.95
L18	314400	3537900	47943.67
L18	314450	3537900	47933.34
L18	314500	3537900	47923.45
L18	314550	3537900	47915.41
L18	314600	3537900	47911.21
L18	314650	3537900	47909.52
L18	314700	3537900	47907.11
L18	314750	3537900	47903.28
L18	314800	3537900	47894.91
L18	314850	3537900	47883.83
L18	314900	3537900	47871
L18	314950	3537900	47854.69
L18	315000	3537900	47832.06
L18	315050	3537900	47810.54
L18	315100	3537900	47798.09
L18	315150	3537900	47804
L18	315200	3537900	47824.44

L18	315250	3537900	47855.95
L18	315300	3537900	47896.5
L18	315350	3537900	47945.09
L18	315400	3537900	48000.54
L18	315450	3537900	48062.57
L18	315500	3537900	48130.52
L18	315550	3537900	48203.49
L18	315600	3537900	48279.55
L18	315650	3537900	48354
L18	315700	3537900	48416.66
L18	315750	3537900	48453.38
L19	312900	3537950	48670.46
L19	312950	3537950	48841.63
L19	313000	3537950	49078.32
L19	313050	3537950	49362.05
L19	313100	3537950	49653.04
L19	313150	3537950	49852.21
L19	313200	3537950	49843.36
L19	313250	3537950	49459.04
L19	313300	3537950	48876.61
L19	313350	3537950	48266.55
L19	313400	3537950	47782.67
L19	313450	3537950	47459.38
L19	313500	3537950	47441.18
L19	313550	3537950	47521.74
L19	313600	3537950	47621.96
L19	313650	3537950	47715.52
L19	313700	3537950	47787.66
L19	313750	3537950	47843.79
L19	313800	3537950	47873.64
L19	313850	3537950	47896.49
L19	313900	3537950	47916.52
L19	313950	3537950	47935.39
L19	314000	3537950	47947.2
L19	314050	3537950	47956.68
L19	314100	3537950	47962.26
L19	314150	3537950	47964.93
L19	314200	3537950	47962.54
L19	314250	3537950	47958.56
L19	314300	3537950	47950.27
L19	314350	3537950	47940.1
L19	314400	3537950	47931.89
L19	314450	3537950	47925.95
L19	314500	3537950	47918.95
L19	314550	3537950	47913.79
L19	314600	3537950	47910.77
L19	314650	3537950	47911.35

L19	314700	3537950	47911.58
L19	314750	3537950	47908.47
L19	314800	3537950	47899.63
L19	314850	3537950	47889.2
L19	314900	3537950	47875.8
L19	314950	3537950	47858.74
L19	315000	3537950	47835.23
L19	315050	3537950	47813.39
L19	315100	3537950	47801.34
L19	315150	3537950	47806.32
L19	315200	3537950	47826.14
L19	315250	3537950	47858.96
L19	315300	3537950	47901.83
L19	315350	3537950	47952.8
L19	315400	3537950	48010.78
L19	315450	3537950	48076.82
L19	315500	3537950	48149.56
L19	315550	3537950	48227.39
L19	315600	3537950	48309.01
L19	315650	3537950	48392.04
L19	315700	3537950	48466.58
L19	315750	3537950	48498.64
L20	312900	3538000	48567.05
L20	312950	3538000	48930.07
L20	313000	3538000	49347.97
L20	313050	3538000	49839.3
L20	313100	3538000	50365.91
L20	313150	3538000	50792.9
L20	313200	3538000	50928.87
L20	313250	3538000	50522.36
L20	313300	3538000	49797.91
L20	313350	3538000	49008.73
L20	313400	3538000	48317.21
L20	313450	3538000	47814.98
L20	313500	3538000	47569.82
L20	313550	3538000	47483.63
L20	313600	3538000	47569.13
L20	313650	3538000	47682.16
L20	313700	3538000	47777.94
L20	313750	3538000	47858.87
L20	313800	3538000	47882.18
L20	313850	3538000	47897.99
L20	313900	3538000	47915.37
L20	313950	3538000	47933.6
L20	314000	3538000	47945.29
L20	314050	3538000	47954.46
L20	314100	3538000	47960.19

L20	314150	3538000	47962.42
L20	314200	3538000	47958.72
L20	314250	3538000	47950.89
L20	314300	3538000	47937.64
L20	314350	3538000	47918.89
L20	314400	3538000	47918.66
L20	314450	3538000	47918.64
L20	314500	3538000	47915.17
L20	314550	3538000	47909.78
L20	314600	3538000	47909.96
L20	314650	3538000	47912.98
L20	314700	3538000	47914.77
L20	314750	3538000	47914.34
L20	314800	3538000	47905.55
L20	314850	3538000	47895.06
L20	314900	3538000	47883.5
L20	314950	3538000	47868.59
L20	315000	3538000	47840.93
L20	315050	3538000	47815.78
L20	315100	3538000	47800.43
L20	315150	3538000	47807.95
L20	315200	3538000	47828.99
L20	315250	3538000	47862.38
L20	315300	3538000	47906.72
L20	315350	3538000	47959.27
L20	315400	3538000	48018.45
L20	315450	3538000	48085.47
L20	315500	3538000	48159.85
L20	315550	3538000	48239.09
L20	315600	3538000	48321.43
L20	315650	3538000	48404.8
L20	315700	3538000	48479.69
L20	315750	3538000	48510.95
L21	312900	3538050	48402.14
L21	312950	3538050	48981.36
L21	313000	3538050	49611.91
L21	313050	3538050	50324.05
L21	313100	3538050	51127.28
L21	313150	3538050	51876.5
L21	313200	3538050	52440.77
L21	313250	3538050	51768.2
L21	313300	3538050	50776.34
L21	313350	3538050	49782.88
L21	313400	3538050	48903.57
L21	313450	3538050	48235.6
L21	313500	3538050	47809.66
L21	313550	3538050	47593.63

L21	313600	3538050	47594.9
L21	313650	3538050	47681.89
L21	313700	3538050	47774.71
L21	313750	3538050	47858.5
L21	313800	3538050	47883.52
L21	313850	3538050	47897.52
L21	313900	3538050	47914.07
L21	313950	3538050	47934.16
L21	314000	3538050	47944.39
L21	314050	3538050	47953.38
L21	314100	3538050	47960.29
L21	314150	3538050	47965.85
L21	314200	3538050	47961.96
L21	314250	3538050	47954.42
L21	314300	3538050	47939.65
L21	314350	3538050	47921.93
L21	314400	3538050	47917.18
L21	314450	3538050	47917.33
L21	314500	3538050	47914.64
L21	314550	3538050	47912.29
L21	314600	3538050	47910.5
L21	314650	3538050	47913.33
L21	314700	3538050	47917.59
L21	314750	3538050	47919.35
L21	314800	3538050	47909.61
L21	314850	3538050	47898.64
L21	314900	3538050	47887.71
L21	314950	3538050	47873.94
L21	315000	3538050	47845.69
L21	315050	3538050	47819.13
L21	315100	3538050	47805.38
L21	315150	3538050	47813.29
L21	315200	3538050	47832.58
L21	315250	3538050	47864.64
L21	315300	3538050	47910.01
L21	315350	3538050	47963.93
L21	315400	3538050	48021.03
L21	315450	3538050	48085.66
L21	315500	3538050	48158.98
L21	315550	3538050	48235.98
L21	315600	3538050	48310.17
L21	315650	3538050	48382.28
L21	315700	3538050	48445.66
L21	315750	3538050	48486.1
L22	312900	3538100	48297.34
L22	312950	3538100	49002.1
L22	313000	3538100	49782.6

L22	313050	3538100	50646.48
L22	313100	3538100	51574.36
L22	313150	3538100	52419.52
L22	313200	3538100	52972.15
L22	313250	3538100	52419.52
L22	313300	3538100	51410.16
L22	313350	3538100	50353.88
L22	313400	3538100	49374.6
L22	313450	3538100	48595.44
L22	313500	3538100	48067.28
L22	313550	3538100	47779.54
L22	313600	3538100	47687.88
L22	313650	3538100	47716.9
L22	313700	3538100	47783.22
L22	313750	3538100	47849.88
L22	313800	3538100	47878.23
L22	313850	3538100	47894.96
L22	313900	3538100	47912.75
L22	313950	3538100	47933.33
L22	314000	3538100	47944.89
L22	314050	3538100	47954.64
L22	314100	3538100	47963.42
L22	314150	3538100	47971.71
L22	314200	3538100	47972.15
L22	314250	3538100	47966.19
L22	314300	3538100	47951.71
L22	314350	3538100	47933.62
L22	314400	3538100	47925.05
L22	314450	3538100	47922.21
L22	314500	3538100	47919.4
L22	314550	3538100	47915.97
L22	314600	3538100	47913.01
L22	314650	3538100	47914.47
L22	314700	3538100	47917.95
L22	314750	3538100	47919.21
L22	314800	3538100	47910.77
L22	314850	3538100	47900.09
L22	314900	3538100	47889.89
L22	314950	3538100	47874.96
L22	315000	3538100	47849.08
L22	315050	3538100	47826.33
L22	315100	3538100	47816.68
L22	315150	3538100	47823.22
L22	315200	3538100	47839.28
L22	315250	3538100	47868.89
L22	315300	3538100	47912.9
L22	315350	3538100	47965.39

L22	315400	3538100	48019.67
L22	315450	3538100	48080.68
L22	315500	3538100	48149.55
L22	315550	3538100	48219.43
L22	315600	3538100	48281.84
L22	315650	3538100	48339.54
L22	315700	3538100	48393.74
L22	315750	3538100	48439.96
L23	312900	3538150	48234.74
L23	312950	3538150	48978.47
L23	313000	3538150	49798.37
L23	313050	3538150	50672.69
L23	313100	3538150	51503.35
L23	313150	3538150	52147.62
L23	313200	3538150	52414.53
L23	313250	3538150	52140.88
L23	313300	3538150	51418.55
L23	313350	3538150	50501.74
L23	313400	3538150	49571.42
L23	313450	3538150	48770.82
L23	313500	3538150	48221.61
L23	313550	3538150	47900.61
L23	313600	3538150	47771.42
L23	313650	3538150	47761.02
L23	313700	3538150	47802.66
L23	313750	3538150	47853.98
L23	313800	3538150	47880.58
L23	313850	3538150	47897
L23	313900	3538150	47914.14
L23	313950	3538150	47933.02
L23	314000	3538150	47947.89
L23	314050	3538150	47959.64
L23	314100	3538150	47970.05
L23	314150	3538150	47980.8
L23	314200	3538150	47990.39
L23	314250	3538150	47989.66
L23	314300	3538150	47967.59
L23	314350	3538150	47938.22
L23	314400	3538150	47929
L23	314450	3538150	47926.68
L23	314500	3538150	47920.96
L23	314550	3538150	47914.65
L23	314600	3538150	47912.73
L23	314650	3538150	47914.47
L23	314700	3538150	47916.25
L23	314750	3538150	47914.67
L23	314800	3538150	47908.8

L23	314850	3538150	47900.27
L23	314900	3538150	47888.42
L23	314950	3538150	47872.82
L23	315000	3538150	47853.64
L23	315050	3538150	47837.44
L23	315100	3538150	47830
L23	315150	3538150	47833.85
L23	315200	3538150	47848.46
L23	315250	3538150	47875.77
L23	315300	3538150	47915.06
L23	315350	3538150	47962.9
L23	315400	3538150	48015.48
L23	315450	3538150	48073.48
L23	315500	3538150	48134.85
L23	315550	3538150	48194.32
L23	315600	3538150	48244.8
L23	315650	3538150	48285.66
L23	315700	3538150	48317.28
L23	315750	3538150	48380.71
L24	312900	3538200	48161.07
L24	312950	3538200	48886.27
L24	313000	3538200	49646.89
L24	313050	3538200	50395.72
L24	313100	3538200	50974.3
L24	313150	3538200	51252.64
L24	313200	3538200	51114.4
L24	313250	3538200	51191.45
L24	313300	3538200	50897.29
L24	313350	3538200	50261.48
L24	313400	3538200	49479.82
L24	313450	3538200	48697.23
L24	313500	3538200	48232.61
L24	313550	3538200	47948.22
L24	313600	3538200	47822.08
L24	313650	3538200	47799.77
L24	313700	3538200	47831.52
L24	313750	3538200	47880.3
L24	313800	3538200	47896.73
L24	313850	3538200	47906.35
L24	313900	3538200	47920.07
L24	313950	3538200	47934.57
L24	314000	3538200	47952.76
L24	314050	3538200	47966.45
L24	314100	3538200	47978.25
L24	314150	3538200	47987.95
L24	314200	3538200	48011.58
L24	314250	3538200	48015.7

L24	314300	3538200	47978.66
L24	314350	3538200	47916.89
L24	314400	3538200	47920.43
L24	314450	3538200	47926.38
L24	314500	3538200	47919.8
L24	314550	3538200	47905.53
L24	314600	3538200	47908.52
L24	314650	3538200	47913.29
L24	314700	3538200	47912.49
L24	314750	3538200	47906.73
L24	314800	3538200	47904.24
L24	314850	3538200	47898.82
L24	314900	3538200	47887.92
L24	314950	3538200	47872.48
L24	315000	3538200	47860.29
L24	315050	3538200	47852.4
L24	315100	3538200	47847.75
L24	315150	3538200	47848.91
L24	315200	3538200	47860.73
L24	315250	3538200	47884.89
L24	315300	3538200	47918.45
L24	315350	3538200	47960.59
L24	315400	3538200	48010.96
L24	315450	3538200	48066.89
L24	315500	3538200	48122.21
L24	315550	3538200	48173.64
L24	315600	3538200	48217.77
L24	315650	3538200	48252.87
L24	315700	3538200	48282.39
L24	315750	3538200	48349.93
L25	312900	3538250	48118
L25	312950	3538250	48743.67
L25	313000	3538250	49389.37
L25	313050	3538250	49957.48
L25	313100	3538250	50300.12
L25	313150	3538250	50323.21
L25	313200	3538250	50067.97
L25	313250	3538250	50217.77
L25	313300	3538250	50204.3
L25	313350	3538250	49842.1
L25	313400	3538250	49277
L25	313450	3538250	48645.77
L25	313500	3538250	48237.85
L25	313550	3538250	47979.3
L25	313600	3538250	47860.68
L25	313650	3538250	47831.71
L25	313700	3538250	47854.65

L25	313750	3538250	47894.5
L25	313800	3538250	47909.68
L25	313850	3538250	47915.9
L25	313900	3538250	47926.77
L25	313950	3538250	47939.43
L25	314000	3538250	47959
L25	314050	3538250	47975.71
L25	314100	3538250	47991.61
L25	314150	3538250	48010.49
L25	314200	3538250	48049.12
L25	314250	3538250	48075.32
L25	314300	3538250	48021.06
L25	314350	3538250	47944.52
L25	314400	3538250	47934.81
L25	314450	3538250	47936.65
L25	314500	3538250	47925.74
L25	314550	3538250	47909.15
L25	314600	3538250	47910.3
L25	314650	3538250	47915.18
L25	314700	3538250	47914.11
L25	314750	3538250	47906.66
L25	314800	3538250	47904.28
L25	314850	3538250	47900.02
L25	314900	3538250	47889.85
L25	314950	3538250	47876.91
L25	315000	3538250	47871.63
L25	315050	3538250	47870.3
L25	315100	3538250	47870.39
L25	315150	3538250	47867.02
L25	315200	3538250	47874.2
L25	315250	3538250	47893.33
L25	315300	3538250	47921.55
L25	315350	3538250	47959.01
L25	315400	3538250	48007.76
L25	315450	3538250	48062.1
L25	315500	3538250	48114.9
L25	315550	3538250	48164.07
L25	315600	3538250	48210.58
L25	315650	3538250	48252.47
L25	315700	3538250	48294.12
L25	315750	3538250	48354.76
L26	312900	3538300	48079.24
L26	312950	3538300	48589.04
L26	313000	3538300	49101.17
L26	313050	3538300	49514.83
L26	313100	3538300	49730.88
L26	313150	3538300	49722.34

L26	313200	3538300	49620.87
L26	313250	3538300	49654.11
L26	313300	3538300	49664.7
L26	313350	3538300	49481.85
L26	313400	3538300	49131.87
L26	313450	3538300	48745.09
L26	313500	3538300	48343.88
L26	313550	3538300	48076.46
L26	313600	3538300	47929.65
L26	313650	3538300	47874.96
L26	313700	3538300	47877.23
L26	313750	3538300	47898.96
L26	313800	3538300	47913.75
L26	313850	3538300	47920.96
L26	313900	3538300	47930.45
L26	313950	3538300	47943.95
L26	314000	3538300	47964.47
L26	314050	3538300	47985.64
L26	314100	3538300	48008.81
L26	314150	3538300	48040.64
L26	314200	3538300	48084.17
L26	314250	3538300	48115.23
L26	314300	3538300	48074.53
L26	314350	3538300	48012.88
L26	314400	3538300	47980.07
L26	314450	3538300	47962.17
L26	314500	3538300	47943.59
L26	314550	3538300	47925
L26	314600	3538300	47922.15
L26	314650	3538300	47925.89
L26	314700	3538300	47927.38
L26	314750	3538300	47924.36
L26	314800	3538300	47917.9
L26	314850	3538300	47909.64
L26	314900	3538300	47900.87
L26	314950	3538300	47891.21
L26	315000	3538300	47885.16
L26	315050	3538300	47885.9
L26	315100	3538300	47897.45
L26	315150	3538300	47884.3
L26	315200	3538300	47882.66
L26	315250	3538300	47896.64
L26	315300	3538300	47922.3
L26	315350	3538300	47959.16
L26	315400	3538300	48006.34
L26	315450	3538300	48059.93
L26	315500	3538300	48114.45

L26	315550	3538300	48168.26
L26	315600	3538300	48221.67
L26	315650	3538300	48274.11
L26	315700	3538300	48326.53
L26	315750	3538300	48383.03
L27	312900	3538350	48037.31
L27	312950	3538350	48445.83
L27	313000	3538350	48846.01
L27	313050	3538350	49157.37
L27	313100	3538350	49323.98
L27	313150	3538350	49346.09
L27	313200	3538350	49298.55
L27	313250	3538350	49313.93
L27	313300	3538350	49311.33
L27	313350	3538350	49202.05
L27	313400	3538350	48992.82
L27	313450	3538350	48740.6
L27	313500	3538350	48427.12
L27	313550	3538350	48177.05
L27	313600	3538350	48017.65
L27	313650	3538350	47935.14
L27	313700	3538350	47912.61
L27	313750	3538350	47916.74
L27	313800	3538350	47922.54
L27	313850	3538350	47925.03
L27	313900	3538350	47931.74
L27	313950	3538350	47944.2
L27	314000	3538350	47968.14
L27	314050	3538350	47994.89
L27	314100	3538350	48025.5
L27	314150	3538350	48062.26
L27	314200	3538350	48103.86
L27	314250	3538350	48127.64
L27	314300	3538350	48107.63
L27	314350	3538350	48060.98
L27	314400	3538350	48022.5
L27	314450	3538350	47990.6
L27	314500	3538350	47960.93
L27	314550	3538350	47938.5
L27	314600	3538350	47936.74
L27	314650	3538350	47945.16
L27	314700	3538350	47954.09
L27	314750	3538350	47956.53
L27	314800	3538350	47946.13
L27	314850	3538350	47931.4
L27	314900	3538350	47917.08
L27	314950	3538350	47902.52

L27	315000	3538350	47886.84
L27	315050	3538350	47874.71
L27	315100	3538350	47874.47
L27	315150	3538350	47866.14
L27	315200	3538350	47869.7
L27	315250	3538350	47887.67
L27	315300	3538350	47916.29
L27	315350	3538350	47955.59
L27	315400	3538350	48004.73
L27	315450	3538350	48060.05
L27	315500	3538350	48118.4
L27	315550	3538350	48179.12
L27	315600	3538350	48243.77
L27	315650	3538350	48311.48
L27	315700	3538350	48381.71
L27	315750	3538350	48426.62
L28	312900	3538400	47993.14
L28	312950	3538400	48329.72
L28	313000	3538400	48650.52
L28	313050	3538400	48906.77
L28	313100	3538400	49083.61
L28	313150	3538400	49192.28
L28	313200	3538400	49289.87
L28	313250	3538400	49214.17
L28	313300	3538400	49127
L28	313350	3538400	49013.13
L28	313400	3538400	48847.13
L28	313450	3538400	48656.61
L28	313500	3538400	48453.82
L28	313550	3538400	48292.49
L28	313600	3538400	48117.81
L28	313650	3538400	48008.02
L28	313700	3538400	47960.14
L28	313750	3538400	47946.55
L28	313800	3538400	47936.79
L28	313850	3538400	47930.52
L28	313900	3538400	47930.41
L28	313950	3538400	47937.18
L28	314000	3538400	47966.95
L28	314050	3538400	48002.77
L28	314100	3538400	48041.04
L28	314150	3538400	48083.09
L28	314200	3538400	48117.62
L28	314250	3538400	48139.2
L28	314300	3538400	48131.18
L28	314350	3538400	48102.09
L28	314400	3538400	48057.14

L28	314450	3538400	48013.2
L28	314500	3538400	47973.86
L28	314550	3538400	47942.36
L28	314600	3538400	47949.53
L28	314650	3538400	47970.9
L28	314700	3538400	47993.5
L28	314750	3538400	48013.49
L28	314800	3538400	47989.19
L28	314850	3538400	47961.79
L28	314900	3538400	47939.41
L28	314950	3538400	47917.45
L28	315000	3538400	47872.86
L28	315050	3538400	47825.12
L28	315100	3538400	47779.43
L28	315150	3538400	47800.5
L28	315200	3538400	47830.65
L28	315250	3538400	47863.55
L28	315300	3538400	47903.52
L28	315350	3538400	47948.98
L28	315400	3538400	48001.64
L28	315450	3538400	48059.91
L28	315500	3538400	48124.31
L28	315550	3538400	48191.84
L28	315600	3538400	48264.23
L28	315650	3538400	48340.26
L28	315700	3538400	48415.97
L28	315750	3538400	48458.83
L29	312900	3538450	47968.43
L29	312950	3538450	48246.81
L29	313000	3538450	48515.21
L29	313050	3538450	48742.04
L29	313100	3538450	48927.72
L29	313150	3538450	49076.71
L29	313200	3538450	49179.34
L29	313250	3538450	49117.3
L29	313300	3538450	48995.69
L29	313350	3538450	48854.3
L29	313400	3538450	48693.01
L29	313450	3538450	48533.16
L29	313500	3538450	48409.21
L29	313550	3538450	48309.43
L29	313600	3538450	48172.95
L29	313650	3538450	48063.24
L29	313700	3538450	48003.24
L29	313750	3538450	47975.46
L29	313800	3538450	47953.92
L29	313850	3538450	47938.96

L29	313900	3538450	47934.05
L29	313950	3538450	47939.74
L29	314000	3538450	47969.95
L29	314050	3538450	48009.96
L29	314100	3538450	48052.4
L29	314150	3538450	48093.66
L29	314200	3538450	48124.2
L29	314250	3538450	48141.91
L29	314300	3538450	48141.11
L29	314350	3538450	48118.56
L29	314400	3538450	48077.28
L29	314450	3538450	48031.2
L29	314500	3538450	47988.87
L29	314550	3538450	47959.38
L29	314600	3538450	47968.22
L29	314650	3538450	47995.17
L29	314700	3538450	48024.16
L29	314750	3538450	48044.95
L29	314800	3538450	48020.5
L29	314850	3538450	47986.11
L29	314900	3538450	47953.7
L29	314950	3538450	47916.83
L29	315000	3538450	47855.5
L29	315050	3538450	47786.09
L29	315100	3538450	47729.55
L29	315150	3538450	47747.64
L29	315200	3538450	47790.73
L29	315250	3538450	47836.38
L29	315300	3538450	47886.66
L29	315350	3538450	47939.15
L29	315400	3538450	47996.5
L29	315450	3538450	48058.65
L29	315500	3538450	48127.32
L29	315550	3538450	48199.25
L29	315600	3538450	48275.02
L29	315650	3538450	48352.1
L29	315700	3538450	48423.68
L29	315750	3538450	48472.47
L30	312900	3538500	47958.41
L30	312950	3538500	48194.23
L30	313000	3538500	48422.4
L30	313050	3538500	48626.64
L30	313100	3538500	48809.17
L30	313150	3538500	48963.29
L30	313200	3538500	49060.87
L30	313250	3538500	49009.61
L30	313300	3538500	48876.77

L30	313350	3538500	48710.61
L30	313400	3538500	48526.86
L30	313450	3538500	48345.38
L30	313500	3538500	48296.93
L30	313550	3538500	48260.19
L30	313600	3538500	48176.95
L30	313650	3538500	48092.58
L30	313700	3538500	48032.18
L30	313750	3538500	47994.95
L30	313800	3538500	47967.37
L30	313850	3538500	47949.4
L30	313900	3538500	47942.09
L30	313950	3538500	47949.72
L30	314000	3538500	47976.47
L30	314050	3538500	48016.15
L30	314100	3538500	48058.17
L30	314150	3538500	48097.14
L30	314200	3538500	48126.4
L30	314250	3538500	48145.86
L30	314300	3538500	48148.72
L30	314350	3538500	48132.73
L30	314400	3538500	48094.25
L30	314450	3538500	48050.21
L30	314500	3538500	48012.48
L30	314550	3538500	47990.09
L30	314600	3538500	47993.2
L30	314650	3538500	48013.16
L30	314700	3538500	48033.71
L30	314750	3538500	48041.85
L30	314800	3538500	48025.71
L30	314850	3538500	47995.66
L30	314900	3538500	47959.75
L30	314950	3538500	47912.92
L30	315000	3538500	47846.87
L30	315050	3538500	47778.47
L30	315100	3538500	47732.09
L30	315150	3538500	47735.38
L30	315200	3538500	47770.77
L30	315250	3538500	47819.03
L30	315300	3538500	47873.35
L30	315350	3538500	47930.45
L30	315400	3538500	47990.72
L30	315450	3538500	48056.29
L30	315500	3538500	48127.04
L30	315550	3538500	48200.81
L30	315600	3538500	48276.55
L30	315650	3538500	48353.02

L30	315700	3538500	48423.03
L30	315750	3538500	48476.02
L31	312900	3538550	47972.43
L31	312950	3538550	48164.52
L31	313000	3538550	48360.07
L31	313050	3538550	48543.84
L31	313100	3538550	48716.85
L31	313150	3538550	48859.99
L31	313200	3538550	48931.84
L31	313250	3538550	48888.72
L31	313300	3538550	48759.46
L31	313350	3538550	48585.11
L31	313400	3538550	48400.93
L31	313450	3538550	48239.34
L31	313500	3538550	48217.59
L31	313550	3538550	48220.63
L31	313600	3538550	48173.16
L31	313650	3538550	48108.02
L31	313700	3538550	48052.36
L31	313750	3538550	48012.03
L31	313800	3538550	47979.46
L31	313850	3538550	47957.21
L31	313900	3538550	47947.09
L31	313950	3538550	47952.05
L31	314000	3538550	47978.22
L31	314050	3538550	48017.36
L31	314100	3538550	48059.08
L31	314150	3538550	48096.91
L31	314200	3538550	48127.11
L31	314250	3538550	48148.9
L31	314300	3538550	48158.03
L31	314350	3538550	48147.21
L31	314400	3538550	48112.46
L31	314450	3538550	48070.62
L31	314500	3538550	48034.51
L31	314550	3538550	48012.45
L31	314600	3538550	48010.15
L31	314650	3538550	48019.32
L31	314700	3538550	48027.99
L31	314750	3538550	48027.23
L31	314800	3538550	48015.58
L31	314850	3538550	47993.87
L31	314900	3538550	47961.43
L31	314950	3538550	47915.54
L31	315000	3538550	47853.81
L31	315050	3538550	47793.09
L31	315100	3538550	47753.15

L31	315150	3538550	47747.83
L31	315200	3538550	47772.14
L31	315250	3538550	47814.71
L31	315300	3538550	47867.17
L31	315350	3538550	47924.25
L31	315400	3538550	47985.41
L31	315450	3538550	48051.67
L31	315500	3538550	48122.17
L31	315550	3538550	48194.77
L31	315600	3538550	48268.83
L31	315650	3538550	48343.13
L31	315700	3538550	48411.72
L31	315750	3538550	48466.52
L32	312900	3538600	47997.46
L32	312950	3538600	48150.36
L32	313000	3538600	48313.6
L32	313050	3538600	48479.64
L32	313100	3538600	48644.88
L32	313150	3538600	48786.06
L32	313200	3538600	48873.77
L32	313250	3538600	48806.27
L32	313300	3538600	48664.76
L32	313350	3538600	48499.01
L32	313400	3538600	48338.11
L32	313450	3538600	48229.77
L32	313500	3538600	48212.41
L32	313550	3538600	48243.46
L32	313600	3538600	48189.99
L32	313650	3538600	48123.6
L32	313700	3538600	48067.87
L32	313750	3538600	48023.79
L32	313800	3538600	47987.72
L32	313850	3538600	47961.12
L32	313900	3538600	47946.27
L32	313950	3538600	47944.7
L32	314000	3538600	47972.77
L32	314050	3538600	48013.09
L32	314100	3538600	48055.12
L32	314150	3538600	48094.18
L32	314200	3538600	48127.5
L32	314250	3538600	48155.93
L32	314300	3538600	48174.21
L32	314350	3538600	48178.7
L32	314400	3538600	48138.48
L32	314450	3538600	48091.91
L32	314500	3538600	48054.59
L32	314550	3538600	48028.39

L32	314600	3538600	48018.39
L32	314650	3538600	48014.63
L32	314700	3538600	48007.9
L32	314750	3538600	47991.46
L32	314800	3538600	47992.29
L32	314850	3538600	47985.35
L32	314900	3538600	47965.6
L32	314950	3538600	47932.69
L32	315000	3538600	47876.23
L32	315050	3538600	47825.25
L32	315100	3538600	47795.76
L32	315150	3538600	47780.41
L32	315200	3538600	47790.68
L32	315250	3538600	47823.11
L32	315300	3538600	47869.23
L32	315350	3538600	47922.87
L32	315400	3538600	47981.31
L32	315450	3538600	48045.37
L32	315500	3538600	48113.17
L32	315550	3538600	48182.61
L32	315600	3538600	48252.42
L32	315650	3538600	48322.87
L32	315700	3538600	48389.34
L32	315750	3538600	48445.1
L33	312900	3538650	48031.25
L33	312950	3538650	48142.32
L33	313000	3538650	48275.41
L33	313050	3538650	48420.62
L33	313100	3538650	48566.82
L33	313150	3538650	48684.97
L33	313200	3538650	48741.55
L33	313250	3538650	48678.3
L33	313300	3538650	48550.82
L33	313350	3538650	48406.85
L33	313400	3538650	48280.11
L33	313450	3538650	48203.17
L33	313500	3538650	48201.05
L33	313550	3538650	48230.85
L33	313600	3538650	48188.88
L33	313650	3538650	48126.13
L33	313700	3538650	48073.2
L33	313750	3538650	48029.44
L33	313800	3538650	47992.15
L33	313850	3538650	47963.04
L33	313900	3538650	47945.8
L33	313950	3538650	47941.96
L33	314000	3538650	47967.63

L33	314050	3538650	48006.33
L33	314100	3538650	48047.72
L33	314150	3538650	48087.36
L33	314200	3538650	48123.09
L33	314250	3538650	48154.17
L33	314300	3538650	48177.43
L33	314350	3538650	48184.28
L33	314400	3538650	48150.11
L33	314450	3538650	48104.84
L33	314500	3538650	48065.69
L33	314550	3538650	48035.54
L33	314600	3538650	48019.11
L33	314650	3538650	48007.04
L33	314700	3538650	47992.92
L33	314750	3538650	47974.98
L33	314800	3538650	47976.88
L33	314850	3538650	47978.04
L33	314900	3538650	47967.23
L33	314950	3538650	47943.34
L33	315000	3538650	47898.94
L33	315050	3538650	47856.98
L33	315100	3538650	47830.85
L33	315150	3538650	47813.21
L33	315200	3538650	47815.17
L33	315250	3538650	47838.14
L33	315300	3538650	47876.25
L33	315350	3538650	47923.73
L33	315400	3538650	47977.49
L33	315450	3538650	48036.74
L33	315500	3538650	48099.29
L33	315550	3538650	48162.9
L33	315600	3538650	48226.47
L33	315650	3538650	48289.91
L33	315700	3538650	48350.09
L33	315750	3538650	48406.25
L34	312900	3538700	48056.84
L34	312950	3538700	48131.49
L34	313000	3538700	48229
L34	313050	3538700	48340.1
L34	313100	3538700	48440.93
L34	313150	3538700	48504.18
L34	313200	3538700	48515.22
L34	313250	3538700	48471.55
L34	313300	3538700	48384.71
L34	313350	3538700	48286.78
L34	313400	3538700	48203.41
L34	313450	3538700	48160.33

L34	313500	3538700	48156.9
L34	313550	3538700	48169.73
L34	313600	3538700	48149.39
L34	313650	3538700	48107.61
L34	313700	3538700	48064.9
L34	313750	3538700	48026.52
L34	313800	3538700	47992.67
L34	313850	3538700	47966.01
L34	313900	3538700	47950.43
L34	313950	3538700	47950.15
L34	314000	3538700	47968.29
L34	314050	3538700	47999.47
L34	314100	3538700	48035.61
L34	314150	3538700	48072.6
L34	314200	3538700	48108.69
L34	314250	3538700	48139.66
L34	314300	3538700	48159.74
L34	314350	3538700	48162.37
L34	314400	3538700	48139.41
L34	314450	3538700	48103.17
L34	314500	3538700	48067.94
L34	314550	3538700	48038.92
L34	314600	3538700	48018.94
L34	314650	3538700	48004.2
L34	314700	3538700	47990.22
L34	314750	3538700	47978.78
L34	314800	3538700	47976.93
L34	314850	3538700	47976.63
L34	314900	3538700	47968.55
L34	314950	3538700	47947.96
L34	315000	3538700	47914.04
L34	315050	3538700	47880.05
L34	315100	3538700	47854.98
L34	315150	3538700	47839.58
L34	315200	3538700	47838.63
L34	315250	3538700	47854.85
L34	315300	3538700	47885.39
L34	315350	3538700	47926.09
L34	315400	3538700	47973.68
L34	315450	3538700	48026.43
L34	315500	3538700	48082.07
L34	315550	3538700	48138.42
L34	315600	3538700	48194.1
L34	315650	3538700	48248.99
L34	315700	3538700	48303.78
L34	315750	3538700	48359.35
L35	312900	3538750	48071.39

L35	312950	3538750	48109.53
L35	313000	3538750	48165.16
L35	313050	3538750	48221.21
L35	313100	3538750	48245.51
L35	313150	3538750	48222.13
L35	313200	3538750	48165.2
L35	313250	3538750	48150.46
L35	313300	3538750	48134.71
L35	313350	3538750	48105.45
L35	313400	3538750	48079.27
L35	313450	3538750	48068.59
L35	313500	3538750	48082.87
L35	313550	3538750	48100.28
L35	313600	3538750	48096.14
L35	313650	3538750	48074.09
L35	313700	3538750	48047.33
L35	313750	3538750	48020.11
L35	313800	3538750	47992.18
L35	313850	3538750	47968.93
L35	313900	3538750	47955.76
L35	313950	3538750	47954.62
L35	314000	3538750	47967.58
L35	314050	3538750	47989.89
L35	314100	3538750	48017.8
L35	314150	3538750	48048.41
L35	314200	3538750	48081.76
L35	314250	3538750	48109.37
L35	314300	3538750	48125.99
L35	314350	3538750	48126.97
L35	314400	3538750	48112.56
L35	314450	3538750	48086.96
L35	314500	3538750	48057.7
L35	314550	3538750	48031.86
L35	314600	3538750	48015.11
L35	314650	3538750	48003.77
L35	314700	3538750	47995.02
L35	314750	3538750	47988.52
L35	314800	3538750	47985.07
L35	314850	3538750	47981.48
L35	314900	3538750	47971.79
L35	314950	3538750	47953.36
L35	315000	3538750	47925.87
L35	315050	3538750	47896.68
L35	315100	3538750	47873.24
L35	315150	3538750	47858.77
L35	315200	3538750	47857.13
L35	315250	3538750	47869.13

L35	315300	3538750	47893.28
L35	315350	3538750	47927.19
L35	315400	3538750	47968.53
L35	315450	3538750	48014.45
L35	315500	3538750	48062.4
L35	315550	3538750	48110.61
L35	315600	3538750	48157.41
L35	315650	3538750	48202.08
L35	315700	3538750	48245.63
L35	315750	3538750	48307.96
L36	312900	3538800	48069.84
L36	312950	3538800	48074.88
L36	313000	3538800	48078.57
L36	313050	3538800	48062.52
L36	313100	3538800	47985.31
L36	313150	3538800	47846.69
L36	313200	3538800	47675.11
L36	313250	3538800	47742.51
L36	313300	3538800	47829.18
L36	313350	3538800	47886.6
L36	313400	3538800	47927.21
L36	313450	3538800	47961.45
L36	313500	3538800	47993.21
L36	313550	3538800	48019.39
L36	313600	3538800	48034.02
L36	313650	3538800	48033.69
L36	313700	3538800	48025.16
L36	313750	3538800	48012.37
L36	313800	3538800	47990.95
L36	313850	3538800	47971.82
L36	313900	3538800	47961.71
L36	313950	3538800	47962
L36	314000	3538800	47966.48
L36	314050	3538800	47977.18
L36	314100	3538800	47993.14
L36	314150	3538800	48011.16
L36	314200	3538800	48043.22
L36	314250	3538800	48068.79
L36	314300	3538800	48080.45
L36	314350	3538800	48077.36
L36	314400	3538800	48074
L36	314450	3538800	48060.32
L36	314500	3538800	48039.86
L36	314550	3538800	48019.25
L36	314600	3538800	48010.09
L36	314650	3538800	48006.46
L36	314700	3538800	48004.94

L36	314750	3538800	48006.51
L36	314800	3538800	47999.3
L36	314850	3538800	47990.71
L36	314900	3538800	47978.93
L36	314950	3538800	47961.27
L36	315000	3538800	47935.46
L36	315050	3538800	47908.29
L36	315100	3538800	47884.5
L36	315150	3538800	47872
L36	315200	3538800	47870.71
L36	315250	3538800	47880.16
L36	315300	3538800	47899.25
L36	315350	3538800	47927.2
L36	315400	3538800	47962.7
L36	315450	3538800	48002.54
L36	315500	3538800	48043.53
L36	315550	3538800	48084.61
L36	315600	3538800	48124.59
L36	315650	3538800	48163.16
L36	315700	3538800	48203.74
L36	315750	3538800	48266.8
L37	312900	3538850	48063.27
L37	312950	3538850	48034.48
L37	313000	3538850	47989.3
L37	313050	3538850	47904.96
L37	313100	3538850	47752.18
L37	313150	3538850	47546.73
L37	313200	3538850	47348.04
L37	313250	3538850	47417.15
L37	313300	3538850	47558.34
L37	313350	3538850	47674.59
L37	313400	3538850	47768.8
L37	313450	3538850	47838.25
L37	313500	3538850	47898.75
L37	313550	3538850	47943.12
L37	313600	3538850	47974.16
L37	313650	3538850	47989.95
L37	313700	3538850	47996.99
L37	313750	3538850	47996.15
L37	313800	3538850	47983.77
L37	313850	3538850	47969.5
L37	313900	3538850	47961.41
L37	313950	3538850	47958.8
L37	314000	3538850	47959.3
L37	314050	3538850	47962.17
L37	314100	3538850	47969.1
L37	314150	3538850	47979.37

L37	314200	3538850	48004.45
L37	314250	3538850	48025.62
L37	314300	3538850	48035.28
L37	314350	3538850	48033.74
L37	314400	3538850	48035.53
L37	314450	3538850	48031.14
L37	314500	3538850	48018.95
L37	314550	3538850	48006.13
L37	314600	3538850	48004.37
L37	314650	3538850	48007.65
L37	314700	3538850	48012.01
L37	314750	3538850	48015.87
L37	314800	3538850	48009.5
L37	314850	3538850	47999.04
L37	314900	3538850	47985.01
L37	314950	3538850	47966.75
L37	315000	3538850	47942.98
L37	315050	3538850	47916.96
L37	315100	3538850	47894.01
L37	315150	3538850	47880.86
L37	315200	3538850	47879.32
L37	315250	3538850	47886.83
L37	315300	3538850	47902.14
L37	315350	3538850	47925.21
L37	315400	3538850	47956.12
L37	315450	3538850	47991.04
L37	315500	3538850	48026.78
L37	315550	3538850	48062.66
L37	315600	3538850	48099.11
L37	315650	3538850	48136.06
L37	315700	3538850	48177.91
L37	315750	3538850	48235.79
L38	312900	3538900	48056.09
L38	312950	3538900	48002.36
L38	313000	3538900	47919.85
L38	313050	3538900	47794.11
L38	313100	3538900	47622.16
L38	313150	3538900	47436.16
L38	313200	3538900	47311.25
L38	313250	3538900	47320.1
L38	313300	3538900	47421.88
L38	313350	3538900	47542.89
L38	313400	3538900	47652.87
L38	313450	3538900	47746.13
L38	313500	3538900	47818.17
L38	313550	3538900	47874.8
L38	313600	3538900	47917.41

L38	313650	3538900	47947
L38	313700	3538900	47964.68
L38	313750	3538900	47971.83
L38	313800	3538900	47968.97
L38	313850	3538900	47961.7
L38	313900	3538900	47955.75
L38	313950	3538900	47952.64
L38	314000	3538900	47949.02
L38	314050	3538900	47947.04
L38	314100	3538900	47948.66
L38	314150	3538900	47956.14
L38	314200	3538900	47972
L38	314250	3538900	47987.86
L38	314300	3538900	47996.52
L38	314350	3538900	47999.91
L38	314400	3538900	48003.61
L38	314450	3538900	48004.65
L38	314500	3538900	48001.96
L38	314550	3538900	47999.39
L38	314600	3538900	48001.66
L38	314650	3538900	48007.83
L38	314700	3538900	48013.92
L38	314750	3538900	48017.3
L38	314800	3538900	48013.32
L38	314850	3538900	48003.63
L38	314900	3538900	47990.07
L38	314950	3538900	47971.74
L38	315000	3538900	47947.55
L38	315050	3538900	47921.88
L38	315100	3538900	47899.55
L38	315150	3538900	47886.89
L38	315200	3538900	47884.02
L38	315250	3538900	47889.65
L38	315300	3538900	47902.78
L38	315350	3538900	47923.18
L38	315400	3538900	47950.12
L38	315450	3538900	47981.3
L38	315500	3538900	48014.32
L38	315550	3538900	48048.09
L38	315600	3538900	48082.55
L38	315650	3538900	48118.68
L38	315700	3538900	48161.1
L38	315750	3538900	48215.91
L39	312900	3538950	48066.99
L39	312950	3538950	47991.17
L39	313000	3538950	47892.34
L39	313050	3538950	47762.17

L39	313100	3538950	47617.66
L39	313150	3538950	47488.49
L39	313200	3538950	47404.79
L39	313250	3538950	47382.93
L39	313300	3538950	47425.55
L39	313350	3538950	47504.34
L39	313400	3538950	47596.31
L39	313450	3538950	47682.5
L39	313500	3538950	47761.13
L39	313550	3538950	47824.45
L39	313600	3538950	47873.68
L39	313650	3538950	47910
L39	313700	3538950	47936.04
L39	313750	3538950	47951.61
L39	313800	3538950	47954.56
L39	313850	3538950	47951.58
L39	313900	3538950	47947.82
L39	313950	3538950	47943.43
L39	314000	3538950	47937.59
L39	314050	3538950	47932.03
L39	314100	3538950	47930
L39	314150	3538950	47933
L39	314200	3538950	47942.93
L39	314250	3538950	47953.79
L39	314300	3538950	47962.12
L39	314350	3538950	47967.66
L39	314400	3538950	47974.89
L39	314450	3538950	47981.41
L39	314500	3538950	47985.79
L39	314550	3538950	47990.35
L39	314600	3538950	47997.44
L39	314650	3538950	48005.79
L39	314700	3538950	48013.33
L39	314750	3538950	48017.16
L39	314800	3538950	48014.34
L39	314850	3538950	48006.28
L39	314900	3538950	47993.41
L39	314950	3538950	47975.48
L39	315000	3538950	47950.77
L39	315050	3538950	47923.66
L39	315100	3538950	47900.75
L39	315150	3538950	47887.53
L39	315200	3538950	47884.15
L39	315250	3538950	47888.86
L39	315300	3538950	47900.94
L39	315350	3538950	47919.88
L39	315400	3538950	47944.94

L39	315450	3538950	47974.39
L39	315500	3538950	48006.57
L39	315550	3538950	48040.17
L39	315600	3538950	48074.66
L39	315650	3538950	48111.07
L39	315700	3538950	48152.42
L39	315750	3538950	48208.52
L40	312900	3539000	48086.81
L40	312950	3539000	48006.14
L40	313000	3539000	47910.23
L40	313050	3539000	47806.08
L40	313100	3539000	47724.95
L40	313150	3539000	47690.21
L40	313200	3539000	47720.98
L40	313250	3539000	47614.56
L40	313300	3539000	47554.7
L40	313350	3539000	47563.89
L40	313400	3539000	47608.8
L40	313450	3539000	47674.38
L40	313500	3539000	47736.15
L40	313550	3539000	47794.64
L40	313600	3539000	47842.56
L40	313650	3539000	47883.33
L40	313700	3539000	47913.84
L40	313750	3539000	47935.75
L40	313800	3539000	47941.74
L40	313850	3539000	47942.35
L40	313900	3539000	47940.77
L40	313950	3539000	47938.91
L40	314000	3539000	47928.23
L40	314050	3539000	47918.46
L40	314100	3539000	47912.46
L40	314150	3539000	47911.74
L40	314200	3539000	47917.04
L40	314250	3539000	47924.93
L40	314300	3539000	47931.96
L40	314350	3539000	47939.03
L40	314400	3539000	47949.8
L40	314450	3539000	47961.5
L40	314500	3539000	47973.06
L40	314550	3539000	47985.01
L40	314600	3539000	47994.07
L40	314650	3539000	48003.48
L40	314700	3539000	48011.34
L40	314750	3539000	48015.97
L40	314800	3539000	48014.06
L40	314850	3539000	48007.7

L40	314900	3539000	47997.56
L40	314950	3539000	47982.69
L40	315000	3539000	47952.91
L40	315050	3539000	47921.47
L40	315100	3539000	47894.57
L40	315150	3539000	47883.59
L40	315200	3539000	47880.76
L40	315250	3539000	47885.55
L40	315300	3539000	47898.06
L40	315350	3539000	47917.48
L40	315400	3539000	47941.91
L40	315450	3539000	47971.57
L40	315500	3539000	48005.34
L40	315550	3539000	48041.55
L40	315600	3539000	48077.93
L40	315650	3539000	48116.55
L40	315700	3539000	48159.69
L40	315750	3539000	48216.16
L41	312900	3539050	48113.36
L41	312950	3539050	48041.17
L41	313000	3539050	47962.21
L41	313050	3539050	47894.21
L41	313100	3539050	47864.55
L41	313150	3539050	47882.79
L41	313200	3539050	47921.2
L41	313250	3539050	47814.93
L41	313300	3539050	47707.41
L41	313350	3539050	47660.43
L41	313400	3539050	47660.68
L41	313450	3539050	47691.36
L41	313500	3539050	47737.47
L41	313550	3539050	47785.91
L41	313600	3539050	47828.49
L41	313650	3539050	47865.59
L41	313700	3539050	47895.96
L41	313750	3539050	47919.86
L41	313800	3539050	47928.27
L41	313850	3539050	47931.16
L41	313900	3539050	47931.38
L41	313950	3539050	47928.54
L41	314000	3539050	47917.53
L41	314050	3539050	47905.83
L41	314100	3539050	47897.71
L41	314150	3539050	47894.02
L41	314200	3539050	47896.15
L41	314250	3539050	47901.3
L41	314300	3539050	47908.09

L41	314350	3539050	47916.22
L41	314400	3539050	47929.62
L41	314450	3539050	47945.25
L41	314500	3539050	47960.71
L41	314550	3539050	47976.1
L41	314600	3539050	47988.47
L41	314650	3539050	47999.52
L41	314700	3539050	48008.79
L41	314750	3539050	48014.26
L41	314800	3539050	48013.04
L41	314850	3539050	48007.46
L41	314900	3539050	47997.47
L41	314950	3539050	47981.53
L41	315000	3539050	47951.61
L41	315050	3539050	47918.31
L41	315100	3539050	47890.88
L41	315150	3539050	47878.33
L41	315200	3539050	47875.66
L41	315250	3539050	47880.84
L41	315300	3539050	47894.32
L41	315350	3539050	47914.85
L41	315400	3539050	47941.11
L41	315450	3539050	47973.01
L41	315500	3539050	48010.24
L41	315550	3539050	48050.66
L41	315600	3539050	48092.7
L41	315650	3539050	48137.18
L41	315700	3539050	48185.76
L41	315750	3539050	48237.67
L42	312900	3539100	48146.22
L42	312950	3539100	48086.45
L42	313000	3539100	48024.43
L42	313050	3539100	47980.7
L42	313100	3539100	47968.04
L42	313150	3539100	47981.14
L42	313200	3539100	47984.71
L42	313250	3539100	47914
L42	313300	3539100	47818.4
L42	313350	3539100	47755.03
L42	313400	3539100	47730
L42	313450	3539100	47738.18
L42	313500	3539100	47760.03
L42	313550	3539100	47791.6
L42	313600	3539100	47823.28
L42	313650	3539100	47852.1
L42	313700	3539100	47874.58
L42	313750	3539100	47891.13

L42	313800	3539100	47905.58
L42	313850	3539100	47915.01
L42	313900	3539100	47919.02
L42	313950	3539100	47917.59
L42	314000	3539100	47907.59
L42	314050	3539100	47896.03
L42	314100	3539100	47887.4
L42	314150	3539100	47883.29
L42	314200	3539100	47882.71
L42	314250	3539100	47886.04
L42	314300	3539100	47892.37
L42	314350	3539100	47902.58
L42	314400	3539100	47916.4
L42	314450	3539100	47933.06
L42	314500	3539100	47951.07
L42	314550	3539100	47968.51
L42	314600	3539100	47983.34
L42	314650	3539100	47996.39
L42	314700	3539100	48006.75
L42	314750	3539100	48012.94
L42	314800	3539100	48012.15
L42	314850	3539100	48005.64
L42	314900	3539100	47994.01
L42	314950	3539100	47974.84
L42	315000	3539100	47945.71
L42	315050	3539100	47914.45
L42	315100	3539100	47888.86
L42	315150	3539100	47874.99
L42	315200	3539100	47871.2
L42	315250	3539100	47876.61
L42	315300	3539100	47891.07
L42	315350	3539100	47913.63
L42	315400	3539100	47942.9
L42	315450	3539100	47978.91
L42	315500	3539100	48021.02
L42	315550	3539100	48067.77
L42	315600	3539100	48117.6
L42	315650	3539100	48170.34
L42	315700	3539100	48223.84
L42	315750	3539100	48274.21
L43	312900	3539150	48195.71
L43	312950	3539150	48134.28
L43	313000	3539150	48081.3
L43	313050	3539150	48042.4
L43	313100	3539150	48017.85
L43	313150	3539150	47997.95
L43	313200	3539150	47963.89

L43	313250	3539150	47918.05
L43	313300	3539150	47860.65
L43	313350	3539150	47811.46
L43	313400	3539150	47784.45
L43	313450	3539150	47776.26
L43	313500	3539150	47787.46
L43	313550	3539150	47805.22
L43	313600	3539150	47824.13
L43	313650	3539150	47837.95
L43	313700	3539150	47847.02
L43	313750	3539150	47855.37
L43	313800	3539150	47874.11
L43	313850	3539150	47892.73
L43	313900	3539150	47904.26
L43	313950	3539150	47906.75
L43	314000	3539150	47899.71
L43	314050	3539150	47889.76
L43	314100	3539150	47881.93
L43	314150	3539150	47877.25
L43	314200	3539150	47875.22
L43	314250	3539150	47876.42
L43	314300	3539150	47881.87
L43	314350	3539150	47891.2
L43	314400	3539150	47905.93
L43	314450	3539150	47923.5
L43	314500	3539150	47941.58
L43	314550	3539150	47959.58
L43	314600	3539150	47977.36
L43	314650	3539150	47993.44
L43	314700	3539150	48006.59
L43	314750	3539150	48014.16
L43	314800	3539150	48012.27
L43	314850	3539150	48003.17
L43	314900	3539150	47987.58
L43	314950	3539150	47965.49
L43	315000	3539150	47938.33
L43	315050	3539150	47910.1
L43	315100	3539150	47886.91
L43	315150	3539150	47871.64
L43	315200	3539150	47866.92
L43	315250	3539150	47872.39
L43	315300	3539150	47887.82
L43	315350	3539150	47912.48
L43	315400	3539150	47945.93
L43	315450	3539150	47986.99
L43	315500	3539150	48034.91
L43	315550	3539150	48088.7

L43	315600	3539150	48148.38
L43	315650	3539150	48212.23
L43	315700	3539150	48276.9
L43	315750	3539150	48319.03
L44	312900	3539200	48241.89
L44	312950	3539200	48179.47
L44	313000	3539200	48121.87
L44	313050	3539200	48071.26
L44	313100	3539200	48013.34
L44	313150	3539200	47941.45
L44	313200	3539200	47852.18
L44	313250	3539200	47854.79
L44	313300	3539200	47851.39
L44	313350	3539200	47837.11
L44	313400	3539200	47825.17
L44	313450	3539200	47820.74
L44	313500	3539200	47818.49
L44	313550	3539200	47821.14
L44	313600	3539200	47824.96
L44	313650	3539200	47822.36
L44	313700	3539200	47811.65
L44	313750	3539200	47796.68
L44	313800	3539200	47831.36
L44	313850	3539200	47867
L44	313900	3539200	47890.49
L44	313950	3539200	47903.98
L44	314000	3539200	47897.58
L44	314050	3539200	47888.11
L44	314100	3539200	47880.88
L44	314150	3539200	47877.59
L44	314200	3539200	47873.27
L44	314250	3539200	47872.46
L44	314300	3539200	47875.85
L44	314350	3539200	47884.29
L44	314400	3539200	47898.68
L44	314450	3539200	47915.92
L44	314500	3539200	47934.29
L44	314550	3539200	47952.89
L44	314600	3539200	47973.24
L44	314650	3539200	47992.77
L44	314700	3539200	48008.7
L44	314750	3539200	48019.41
L44	314800	3539200	48013.75
L44	314850	3539200	47999.98
L44	314900	3539200	47980.96
L44	314950	3539200	47956.63
L44	315000	3539200	47930.27

L44	315050	3539200	47904.71
L44	315100	3539200	47883.83
L44	315150	3539200	47867.89
L44	315200	3539200	47862.38
L44	315250	3539200	47868.02
L44	315300	3539200	47884.52
L44	315350	3539200	47911.73
L44	315400	3539200	47949.43
L44	315450	3539200	47995.77
L44	315500	3539200	48049.51
L44	315550	3539200	48110.13
L44	315600	3539200	48177.73
L44	315650	3539200	48248.84
L44	315700	3539200	48316.38
L44	315750	3539200	48358.39
L45	312900	3539250	48287.39
L45	312950	3539250	48219.17
L45	313000	3539250	48153.32
L45	313050	3539250	48085.13
L45	313100	3539250	48000.5
L45	313150	3539250	47898.3
L45	313200	3539250	47794.12
L45	313250	3539250	47800.78
L45	313300	3539250	47830.84
L45	313350	3539250	47846.57
L45	313400	3539250	47856.05
L45	313450	3539250	47854.65
L45	313500	3539250	47852.35
L45	313550	3539250	47844.57
L45	313600	3539250	47835.66
L45	313650	3539250	47818.45
L45	313700	3539250	47795.65
L45	313750	3539250	47776.63
L45	313800	3539250	47807.66
L45	313850	3539250	47848.21
L45	313900	3539250	47877.71
L45	313950	3539250	47895.06
L45	314000	3539250	47893.24
L45	314050	3539250	47885.71
L45	314100	3539250	47879.34
L45	314150	3539250	47875.67
L45	314200	3539250	47871.5
L45	314250	3539250	47869.75
L45	314300	3539250	47872.38
L45	314350	3539250	47879.29
L45	314400	3539250	47893.33
L45	314450	3539250	47910.23

L45	314500	3539250	47927.73
L45	314550	3539250	47946.6
L45	314600	3539250	47968.74
L45	314650	3539250	47990.02
L45	314700	3539250	48007.13
L45	314750	3539250	48017.13
L45	314800	3539250	48010.36
L45	314850	3539250	47994.46
L45	314900	3539250	47972.96
L45	314950	3539250	47947.1
L45	315000	3539250	47921.13
L45	315050	3539250	47895.25
L45	315100	3539250	47873.98
L45	315150	3539250	47857.52
L45	315200	3539250	47852.78
L45	315250	3539250	47860.01
L45	315300	3539250	47878.54
L45	315350	3539250	47908.88
L45	315400	3539250	47950.98
L45	315450	3539250	48002.35
L45	315500	3539250	48061.2
L45	315550	3539250	48127.27
L45	315600	3539250	48199.9
L45	315650	3539250	48273.8
L45	315700	3539250	48339.47
L45	315750	3539250	48386.43
L46	312900	3539300	48327.57
L46	312950	3539300	48256.95
L46	313000	3539300	48181.2
L46	313050	3539300	48099.8
L46	313100	3539300	48004.7
L46	313150	3539300	47903.73
L46	313200	3539300	47828.31
L46	313250	3539300	47818.43
L46	313300	3539300	47847.44
L46	313350	3539300	47884.2
L46	313400	3539300	47913.95
L46	313450	3539300	47930.68
L46	313500	3539300	47914.06
L46	313550	3539300	47888.5
L46	313600	3539300	47862.05
L46	313650	3539300	47835.73
L46	313700	3539300	47810.08
L46	313750	3539300	47796.66
L46	313800	3539300	47813.36
L46	313850	3539300	47843.53
L46	313900	3539300	47868.95

L46	313950	3539300	47883.78
L46	314000	3539300	47884.98
L46	314050	3539300	47879.36
L46	314100	3539300	47872.94
L46	314150	3539300	47868.5
L46	314200	3539300	47866.74
L46	314250	3539300	47867.9
L46	314300	3539300	47872.46
L46	314350	3539300	47881.52
L46	314400	3539300	47892.8
L46	314450	3539300	47907.23
L46	314500	3539300	47924.58
L46	314550	3539300	47944.16
L46	314600	3539300	47964.79
L46	314650	3539300	47984.11
L46	314700	3539300	47998.04
L46	314750	3539300	48003.82
L46	314800	3539300	47999.67
L46	314850	3539300	47986.8
L46	314900	3539300	47968.08
L46	314950	3539300	47943.61
L46	315000	3539300	47909.95
L46	315050	3539300	47874.94
L46	315100	3539300	47845.64
L46	315150	3539300	47832.5
L46	315200	3539300	47832.68
L46	315250	3539300	47844.67
L46	315300	3539300	47868.12
L46	315350	3539300	47903.21
L46	315400	3539300	47949.45
L46	315450	3539300	48005.22
L46	315500	3539300	48068.94
L46	315550	3539300	48139.59
L46	315600	3539300	48215.26
L46	315650	3539300	48290.94
L46	315700	3539300	48358.41
L46	315750	3539300	48409.39
L47	312900	3539350	48380.67
L47	312950	3539350	48295.74
L47	313000	3539350	48213.79
L47	313050	3539350	48125.88
L47	313100	3539350	48031.5
L47	313150	3539350	47941.02
L47	313200	3539350	47874.12
L47	313250	3539350	47867.2
L47	313300	3539350	47903.17
L47	313350	3539350	47957.59

L47	313400	3539350	48012.68
L47	313450	3539350	48041.63
L47	313500	3539350	48014.56
L47	313550	3539350	47963.87
L47	313600	3539350	47916.01
L47	313650	3539350	47874.3
L47	313700	3539350	47842.78
L47	313750	3539350	47826.11
L47	313800	3539350	47832.07
L47	313850	3539350	47849.31
L47	313900	3539350	47865.66
L47	313950	3539350	47874.74
L47	314000	3539350	47874.88
L47	314050	3539350	47869.16
L47	314100	3539350	47862.35
L47	314150	3539350	47857.89
L47	314200	3539350	47859.62
L47	314250	3539350	47865.25
L47	314300	3539350	47874.2
L47	314350	3539350	47884.97
L47	314400	3539350	47894.99
L47	314450	3539350	47906.71
L47	314500	3539350	47921.5
L47	314550	3539350	47939.2
L47	314600	3539350	47957.53
L47	314650	3539350	47973.02
L47	314700	3539350	47983.2
L47	314750	3539350	47987.09
L47	314800	3539350	47986.19
L47	314850	3539350	47979.57
L47	314900	3539350	47965.36
L47	314950	3539350	47940.38
L47	315000	3539350	47895.23
L47	315050	3539350	47843.09
L47	315100	3539350	47801.21
L47	315150	3539350	47789.38
L47	315200	3539350	47798.34
L47	315250	3539350	47819.38
L47	315300	3539350	47850.47
L47	315350	3539350	47891.63
L47	315400	3539350	47943.02
L47	315450	3539350	48002.9
L47	315500	3539350	48070.27
L47	315550	3539350	48143.95
L47	315600	3539350	48222.15
L47	315650	3539350	48300.16
L47	315700	3539350	48371.63

L47	315750	3539350	48422.87
L48	312950	3539400	48337.29
L48	313000	3539400	48250.27
L48	313050	3539400	48163.08
L48	313100	3539400	48075
L48	313150	3539400	48000.69
L48	313200	3539400	47958.19
L48	313250	3539400	47957.06
L48	313300	3539400	47998.12
L48	313350	3539400	48075.36
L48	313400	3539400	48163.41
L48	313450	3539400	48244
L48	313500	3539400	48166.29
L48	313550	3539400	48068.26
L48	313600	3539400	47987.54
L48	313650	3539400	47927.64
L48	313700	3539400	47887.28
L48	313750	3539400	47864.25
L48	313800	3539400	47858.15
L48	313850	3539400	47861.25
L48	313900	3539400	47866.73
L48	313950	3539400	47868.68
L48	314000	3539400	47865.27
L48	314050	3539400	47856.78
L48	314100	3539400	47847.23
L48	314150	3539400	47839.81
L48	314200	3539400	47848.55
L48	314250	3539400	47862.12
L48	314300	3539400	47877.95
L48	314350	3539400	47896.75
L48	314400	3539400	47900.95
L48	314450	3539400	47906.98
L48	314500	3539400	47919.09
L48	314550	3539400	47935.19
L48	314600	3539400	47948.77
L48	314650	3539400	47958.86
L48	314700	3539400	47963.26
L48	314750	3539400	47962.29
L48	314800	3539400	47969.54
L48	314850	3539400	47973.25
L48	314900	3539400	47968.72
L48	314950	3539400	47953.21
L48	315000	3539400	47880.96
L48	315050	3539400	47797.81
L48	315100	3539400	47724.98
L48	315150	3539400	47726.88
L48	315200	3539400	47752.68

L48	315250	3539400	47785.93
L48	315300	3539400	47827.23
L48	315350	3539400	47875.52
L48	315400	3539400	47932.08
L48	315450	3539400	47995.02
L48	315500	3539400	48065.1
L48	315550	3539400	48140.29
L48	315600	3539400	48218.84
L48	315650	3539400	48296.33
L48	315700	3539400	48368.26
L48	315750	3539400	48421.53
L49	313000	3539450	48291.76
L49	313050	3539450	48208.27
L49	313100	3539450	48131.08
L49	313150	3539450	48070.68
L49	313200	3539450	48035.54
L49	313250	3539450	48046.55
L49	313300	3539450	48099.02
L49	313350	3539450	48184.32
L49	313400	3539450	48283.63
L49	313450	3539450	48356.57
L49	313500	3539450	48280.43
L49	313550	3539450	48159.98
L49	313600	3539450	48057.99
L49	313650	3539450	47980
L49	313700	3539450	47929.32
L49	313750	3539450	47897.63
L49	313800	3539450	47882.01
L49	313850	3539450	47873.97
L49	313900	3539450	47869.62
L49	313950	3539450	47864.01
L49	314000	3539450	47856.14
L49	314050	3539450	47845.12
L49	314100	3539450	47834.43
L49	314150	3539450	47828
L49	314200	3539450	47838.5
L49	314250	3539450	47855.8
L49	314300	3539450	47875.58
L49	314350	3539450	47894.66
L49	314400	3539450	47899.49
L49	314450	3539450	47902.99
L49	314500	3539450	47911.88
L49	314550	3539450	47924.79
L49	314600	3539450	47936.01
L49	314650	3539450	47943.3
L49	314700	3539450	47946.3
L49	314750	3539450	47946.77

L49	314800	3539450	47956.01
L49	314850	3539450	47963.8
L49	314900	3539450	47961.04
L49	314950	3539450	47939.32
L49	315000	3539450	47859.9
L49	315050	3539450	47762.54
L49	315100	3539450	47683.01
L49	315150	3539450	47679.77
L49	315200	3539450	47711.75
L49	315250	3539450	47753.05
L49	315300	3539450	47801.86
L49	315350	3539450	47855.97
L49	315400	3539450	47916.7
L49	315450	3539450	47981.91
L49	315500	3539450	48052.68
L49	315550	3539450	48126.99
L49	315600	3539450	48202.87
L49	315650	3539450	48275.88
L49	315700	3539450	48342.22
L49	315750	3539450	48398.29
L50	313050	3539500	48259.07
L50	313100	3539500	48190.05
L50	313150	3539500	48141.43
L50	313200	3539500	48125.18
L50	313250	3539500	48140.4
L50	313300	3539500	48189.75
L50	313350	3539500	48265.73
L50	313400	3539500	48341.47
L50	313450	3539500	48377.67
L50	313500	3539500	48315.04
L50	313550	3539500	48200.34
L50	313600	3539500	48087.47
L50	313650	3539500	48007.92
L50	313700	3539500	47955.67
L50	313750	3539500	47921.96
L50	313800	3539500	47899.96
L50	313850	3539500	47884.32
L50	313900	3539500	47872.12
L50	313950	3539500	47860.73
L50	314000	3539500	47848.2
L50	314050	3539500	47834.44
L50	314100	3539500	47822.45
L50	314150	3539500	47817.86
L50	314200	3539500	47828.17
L50	314250	3539500	47846.84
L50	314300	3539500	47867.1
L50	314350	3539500	47884.37

L50	314400	3539500	47889.88
L50	314450	3539500	47893.01
L50	314500	3539500	47900.63
L50	314550	3539500	47911.66
L50	314600	3539500	47921.93
L50	314650	3539500	47929.73
L50	314700	3539500	47934.62
L50	314750	3539500	47939.17
L50	314800	3539500	47946.79
L50	314850	3539500	47951.25
L50	314900	3539500	47943.15
L50	314950	3539500	47909.64
L50	315000	3539500	47836.07
L50	315050	3539500	47747.86
L50	315100	3539500	47681.22
L50	315150	3539500	47665.95
L50	315200	3539500	47689
L50	315250	3539500	47729.75
L50	315300	3539500	47780.34
L50	315350	3539500	47837.43
L50	315400	3539500	47899.62
L50	315450	3539500	47965.72
L50	315500	3539500	48035.5
L50	315550	3539500	48107.26
L50	315600	3539500	48178.11
L50	315650	3539500	48245.21
L50	315700	3539500	48307.56
L50	315750	3539500	48363.96
L51	313100	3539550	48247.7
L51	313150	3539550	48206.6
L51	313200	3539550	48189.55
L51	313250	3539550	48207.78
L51	313300	3539550	48253.16
L51	313350	3539550	48310.66
L51	313400	3539550	48360.64
L51	313450	3539550	48367.26
L51	313500	3539550	48301.34
L51	313550	3539550	48186.43
L51	313600	3539550	48071.08
L51	313650	3539550	47997.17
L51	313700	3539550	47954
L51	313750	3539550	47925.8
L51	313800	3539550	47905.42
L51	313850	3539550	47887.89
L51	313900	3539550	47871.59
L51	313950	3539550	47855.05
L51	314000	3539550	47838.3

L51	314050	3539550	47821.04
L51	314100	3539550	47806.32
L51	314150	3539550	47800.18
L51	314200	3539550	47812.74
L51	314250	3539550	47834.51
L51	314300	3539550	47857.36
L51	314350	3539550	47874.82
L51	314400	3539550	47879.01
L51	314450	3539550	47880.3
L51	314500	3539550	47885.49
L51	314550	3539550	47894.79
L51	314600	3539550	47905.98
L51	314650	3539550	47916.01
L51	314700	3539550	47924.42
L51	314750	3539550	47931.84
L51	314800	3539550	47938.62
L51	314850	3539550	47939.97
L51	314900	3539550	47927.22
L51	314950	3539550	47891.55
L51	315000	3539550	47824.66
L51	315050	3539550	47748.31
L51	315100	3539550	47690.2
L51	315150	3539550	47669.66
L51	315200	3539550	47683.08
L51	315250	3539550	47717.63
L51	315300	3539550	47765.21
L51	315350	3539550	47821.09
L51	315400	3539550	47882.91
L51	315450	3539550	47948.15
L51	315500	3539550	48015.49
L51	315550	3539550	48083.06
L51	315600	3539550	48148
L51	315650	3539550	48207.39
L51	315700	3539550	48260.41
L51	315750	3539550	48322.23
L52	313150	3539600	48256.55
L52	313200	3539600	48250.17
L52	313250	3539600	48265.07
L52	313300	3539600	48294.84
L52	313350	3539600	48332.25
L52	313400	3539600	48351.09
L52	313450	3539600	48332.15
L52	313500	3539600	48250.29
L52	313550	3539600	48124.35
L52	313600	3539600	47985.91
L52	313650	3539600	47943.25
L52	313700	3539600	47926.04

L52	313750	3539600	47913.2
L52	313800	3539600	47900.72
L52	313850	3539600	47885.57
L52	313900	3539600	47868.24
L52	313950	3539600	47848.78
L52	314000	3539600	47828.09
L52	314050	3539600	47805.87
L52	314100	3539600	47784.56
L52	314150	3539600	47770.1
L52	314200	3539600	47790.36
L52	314250	3539600	47820.8
L52	314300	3539600	47849.52
L52	314350	3539600	47874.42
L52	314400	3539600	47869.6
L52	314450	3539600	47866
L52	314500	3539600	47869.38
L52	314550	3539600	47877.59
L52	314600	3539600	47890.27
L52	314650	3539600	47903.71
L52	314700	3539600	47915.29
L52	314750	3539600	47925.46
L52	314800	3539600	47931.28
L52	314850	3539600	47931.16
L52	314900	3539600	47918.93
L52	314950	3539600	47888.78
L52	315000	3539600	47826.98
L52	315050	3539600	47762.2
L52	315100	3539600	47715.27
L52	315150	3539600	47687.73
L52	315200	3539600	47689.93
L52	315250	3539600	47716.05
L52	315300	3539600	47757.61
L52	315350	3539600	47809.64
L52	315400	3539600	47868.74
L52	315450	3539600	47932.21
L52	315500	3539600	47996.72
L52	315550	3539600	48060.43
L52	315600	3539600	48120.88
L52	315650	3539600	48176.62
L52	315700	3539600	48228.49
L52	315750	3539600	48291.34
L53	313200	3539650	48277.19
L53	313250	3539650	48291.89
L53	313300	3539650	48312.91
L53	313350	3539650	48330.52
L53	313400	3539650	48329.11
L53	313450	3539650	48289.01

L53	313500	3539650	48197.94
L53	313550	3539650	48067.95
L53	313600	3539650	47937.43
L53	313650	3539650	47898.85
L53	313700	3539650	47895.35
L53	313750	3539650	47894.45
L53	313800	3539650	47890.97
L53	313850	3539650	47881.19
L53	313900	3539650	47864.91
L53	313950	3539650	47843.28
L53	314000	3539650	47819.85
L53	314050	3539650	47795.07
L53	314100	3539650	47770.73
L53	314150	3539650	47754.99
L53	314200	3539650	47774.03
L53	314250	3539650	47805.72
L53	314300	3539650	47834.38
L53	314350	3539650	47855.42
L53	314400	3539650	47849.49
L53	314450	3539650	47846.04
L53	314500	3539650	47849.9
L53	314550	3539650	47858.91
L53	314600	3539650	47873.95
L53	314650	3539650	47890.32
L53	314700	3539650	47904.49
L53	314750	3539650	47915.53
L53	314800	3539650	47921.48
L53	314850	3539650	47921.26
L53	314900	3539650	47909.53
L53	314950	3539650	47882.74
L53	315000	3539650	47830.07
L53	315050	3539650	47774.27
L53	315100	3539650	47731.55
L53	315150	3539650	47703.28
L53	315200	3539650	47699.79
L53	315250	3539650	47719.21
L53	315300	3539650	47754.64
L53	315350	3539650	47801.56
L53	315400	3539650	47857.59
L53	315450	3539650	47918.75
L53	315500	3539650	47980.64
L53	315550	3539650	48041.38
L53	315600	3539650	48100.56
L53	315650	3539650	48157.18
L53	315700	3539650	48212.2
L53	315750	3539650	48272.66
L54	313250	3539700	48312.28

L54	313300	3539700	48319.52
L54	313350	3539700	48321.63
L54	313400	3539700	48301.44
L54	313450	3539700	48252.29
L54	313500	3539700	48159.38
L54	313550	3539700	48043.26
L54	313600	3539700	47938.89
L54	313650	3539700	47893.21
L54	313700	3539700	47885.46
L54	313750	3539700	47889.07
L54	313800	3539700	47891.06
L54	313850	3539700	47884.84
L54	313900	3539700	47868.73
L54	313950	3539700	47846.33
L54	314000	3539700	47820.79
L54	314050	3539700	47795.34
L54	314100	3539700	47771.57
L54	314150	3539700	47759.63
L54	314200	3539700	47769.24
L54	314250	3539700	47791.52
L54	314300	3539700	47808.96
L54	314350	3539700	47815.42
L54	314400	3539700	47808.35
L54	314450	3539700	47816.43
L54	314500	3539700	47828.49
L54	314550	3539700	47842.38
L54	314600	3539700	47859.27
L54	314650	3539700	47877.58
L54	314700	3539700	47892.23
L54	314750	3539700	47902.35
L54	314800	3539700	47908.12
L54	314850	3539700	47907.33
L54	314900	3539700	47894.67
L54	314950	3539700	47866.18
L54	315000	3539700	47822.02
L54	315050	3539700	47774.43
L54	315100	3539700	47734.24
L54	315150	3539700	47709.45
L54	315200	3539700	47705.57
L54	315250	3539700	47722.47
L54	315300	3539700	47754.06
L54	315350	3539700	47797
L54	315400	3539700	47849.68
L54	315450	3539700	47908.91
L54	315500	3539700	47969.08
L54	315550	3539700	48028.5
L54	315600	3539700	48087.85

L54	315650	3539700	48147.17
L54	315700	3539700	48205.2
L54	315750	3539700	48265.52
L55	313300	3539750	48314.14
L55	313350	3539750	48305.48
L55	313400	3539750	48278.11
L55	313450	3539750	48222.49
L55	313500	3539750	48138.16
L55	313550	3539750	48037.4
L55	313600	3539750	47950.21
L55	313650	3539750	47907.34
L55	313700	3539750	47896.92
L55	313750	3539750	47901.58
L55	313800	3539750	47907.46
L55	313850	3539750	47902.37
L55	313900	3539750	47884.41
L55	313950	3539750	47858.89
L55	314000	3539750	47831.15
L55	314050	3539750	47805.28
L55	314100	3539750	47781.5
L55	314150	3539750	47766.98
L55	314200	3539750	47768.77
L55	314250	3539750	47778.98
L55	314300	3539750	47784.22
L55	314350	3539750	47781.58
L55	314400	3539750	47776.62
L55	314450	3539750	47790.32
L55	314500	3539750	47808.13
L55	314550	3539750	47825.82
L55	314600	3539750	47845.09
L55	314650	3539750	47864.21
L55	314700	3539750	47878.71
L55	314750	3539750	47887.79
L55	314800	3539750	47892.62
L55	314850	3539750	47891.15
L55	314900	3539750	47876.95
L55	314950	3539750	47848.89
L55	315000	3539750	47807.43
L55	315050	3539750	47762.37
L55	315100	3539750	47723
L55	315150	3539750	47702.87
L55	315200	3539750	47703.44
L55	315250	3539750	47721.95
L55	315300	3539750	47752.57
L55	315350	3539750	47793.34
L55	315400	3539750	47844.15
L55	315450	3539750	47902

L55	315500	3539750	47960.91
L55	315550	3539750	48020.05
L55	315600	3539750	48080.98
L55	315650	3539750	48144.01
L55	315700	3539750	48205.77
L55	315750	3539750	48265.62
L56	313350	3539800	48290.26
L56	313400	3539800	48258.01
L56	313450	3539800	48209.05
L56	313500	3539800	48131.42
L56	313550	3539800	48048.63
L56	313600	3539800	47978.54
L56	313650	3539800	47939.84
L56	313700	3539800	47929.01
L56	313750	3539800	47936.82
L56	313800	3539800	47949.35
L56	313850	3539800	47937.81
L56	313900	3539800	47913.69
L56	313950	3539800	47885.27
L56	314000	3539800	47854.91
L56	314050	3539800	47826.68
L56	314100	3539800	47800.46
L56	314150	3539800	47782.7
L56	314200	3539800	47773.83
L56	314250	3539800	47771.09
L56	314300	3539800	47763.72
L56	314350	3539800	47752.25
L56	314400	3539800	47757.04
L56	314450	3539800	47774.31
L56	314500	3539800	47794.93
L56	314550	3539800	47816.43
L56	314600	3539800	47834.91
L56	314650	3539800	47853.23
L56	314700	3539800	47865.68
L56	314750	3539800	47872.88
L56	314800	3539800	47876.47
L56	314850	3539800	47873.85
L56	314900	3539800	47858.4
L56	314950	3539800	47829.69
L56	315000	3539800	47786.68
L56	315050	3539800	47739.73
L56	315100	3539800	47695.21
L56	315150	3539800	47685.91
L56	315200	3539800	47694.99
L56	315250	3539800	47718.13
L56	315300	3539800	47750.52
L56	315350	3539800	47791.51

L56	315400	3539800	47841.13
L56	315450	3539800	47898.04
L56	315500	3539800	47956.49
L56	315550	3539800	48016.32
L56	315600	3539800	48078.2
L56	315650	3539800	48143.32
L56	315700	3539800	48206.49
L56	315750	3539800	48268.5
L57	313400	3539850	48250.25
L57	313450	3539850	48201.07
L57	313500	3539850	48137.53
L57	313550	3539850	48068.97
L57	313600	3539850	48010.56
L57	313650	3539850	47978.99
L57	313700	3539850	47969.89
L57	313750	3539850	47978.46
L57	313800	3539850	47989.69
L57	313850	3539850	47978.02
L57	313900	3539850	47951.73
L57	313950	3539850	47921.93
L57	314000	3539850	47889.97
L57	314050	3539850	47859.47
L57	314100	3539850	47828.99
L57	314150	3539850	47803.98
L57	314200	3539850	47786.05
L57	314250	3539850	47772.73
L57	314300	3539850	47757.7
L57	314350	3539850	47744.76
L57	314400	3539850	47749.41
L57	314450	3539850	47767.51
L57	314500	3539850	47787.78
L57	314550	3539850	47809.05
L57	314600	3539850	47827.26
L57	314650	3539850	47843.78
L57	314700	3539850	47854.81
L57	314750	3539850	47860.78
L57	314800	3539850	47862.36
L57	314850	3539850	47857.78
L57	314900	3539850	47840.75
L57	314950	3539850	47811.97
L57	315000	3539850	47769.05
L57	315050	3539850	47721.7
L57	315100	3539850	47679.88
L57	315150	3539850	47673.35
L57	315200	3539850	47687.79
L57	315250	3539850	47714.31
L57	315300	3539850	47748.88

L57	315350	3539850	47790.69
L57	315400	3539850	47840.38
L57	315450	3539850	47896.28
L57	315500	3539850	47954.53
L57	315550	3539850	48014.66
L57	315600	3539850	48077.38
L57	315650	3539850	48142.34
L57	315700	3539850	48205.04
L57	315750	3539850	48266.82
L58	313450	3539900	48215.7
L58	313500	3539900	48154.54
L58	313550	3539900	48097.6
L58	313600	3539900	48051.57
L58	313650	3539900	48023.91
L58	313700	3539900	48015.67
L58	313750	3539900	48021.08
L58	313800	3539900	48026.61
L58	313850	3539900	48018.47
L58	313900	3539900	47998.59
L58	313950	3539900	47974.66
L58	314000	3539900	47946.73
L58	314050	3539900	47910.96
L58	314100	3539900	47873.04
L58	314150	3539900	47839.68
L58	314200	3539900	47811.38
L58	314250	3539900	47788.57
L58	314300	3539900	47768.81
L58	314350	3539900	47756.48
L58	314400	3539900	47758.53
L58	314450	3539900	47771.48
L58	314500	3539900	47789.02
L58	314550	3539900	47807.84
L58	314600	3539900	47824.54
L58	314650	3539900	47838.84
L58	314700	3539900	47848.1
L58	314750	3539900	47852.69
L58	314800	3539900	47852.16
L58	314850	3539900	47844.52
L58	314900	3539900	47826.33
L58	314950	3539900	47796.65
L58	315000	3539900	47757.21
L58	315050	3539900	47715.64
L58	315100	3539900	47683.45
L58	315150	3539900	47675.59
L58	315200	3539900	47688.67
L58	315250	3539900	47715.36
L58	315300	3539900	47750.59

L58	315350	3539900	47793.37
L58	315400	3539900	47842.62
L58	315450	3539900	47897.58
L58	315500	3539900	47955.4
L58	315550	3539900	48016.1
L58	315600	3539900	48078.66
L58	315650	3539900	48143.03
L58	315700	3539900	48205.27
L58	315750	3539900	48265.75
L59	313500	3539950	48180.8
L59	313550	3539950	48129.76
L59	313600	3539950	48091.32
L59	313650	3539950	48068.71
L59	313700	3539950	48061.71
L59	313750	3539950	48065.32
L59	313800	3539950	48070.2
L59	313850	3539950	48066.71
L59	313900	3539950	48056.91
L59	313950	3539950	48043.8
L59	314000	3539950	48023.32
L59	314050	3539950	47982.65
L59	314100	3539950	47934.06
L59	314150	3539950	47888.26
L59	314200	3539950	47849.71
L59	314250	3539950	47818.07
L59	314300	3539950	47793.6
L59	314350	3539950	47778.93
L59	314400	3539950	47776.35
L59	314450	3539950	47784.08
L59	314500	3539950	47796.62
L59	314550	3539950	47811.61
L59	314600	3539950	47825.99
L59	314650	3539950	47837.55
L59	314700	3539950	47845.14
L59	314750	3539950	47848.38
L59	314800	3539950	47845.91
L59	314850	3539950	47836.19
L59	314900	3539950	47817.01
L59	314950	3539950	47789.38
L59	315000	3539950	47754.14
L59	315050	3539950	47718.08
L59	315100	3539950	47691.2
L59	315150	3539950	47684.86
L59	315200	3539950	47696.93
L59	315250	3539950	47722.04
L59	315300	3539950	47756.5
L59	315350	3539950	47798.95

L59	315400	3539950	47847.76
L59	315450	3539950	47901.34
L59	315500	3539950	47958.25
L59	315550	3539950	48018.52
L59	315600	3539950	48080.91
L59	315650	3539950	48144.38
L59	315700	3539950	48206.32
L59	315750	3539950	48263.91
L60	313550	3540000	48163.96
L60	313600	3540000	48133.02
L60	313650	3540000	48114.57
L60	313700	3540000	48108.33
L60	313750	3540000	48112.09
L60	313800	3540000	48117.56
L60	313850	3540000	48121.75
L60	313900	3540000	48125.71
L60	313950	3540000	48131.28
L60	314000	3540000	48130.82
L60	314050	3540000	48075.72
L60	314100	3540000	48009.67
L60	314150	3540000	47951.14
L60	314200	3540000	47900.16
L60	314250	3540000	47859.85
L60	314300	3540000	47828.62
L60	314350	3540000	47810.23
L60	314400	3540000	47802.8
L60	314450	3540000	47804.49
L60	314500	3540000	47811.6
L60	314550	3540000	47822.76
L60	314600	3540000	47833.28
L60	314650	3540000	47842.19
L60	314700	3540000	47846.87
L60	314750	3540000	47848.39
L60	314800	3540000	47844.18
L60	314850	3540000	47833.16
L60	314900	3540000	47814.05
L60	314950	3540000	47788.25
L60	315000	3540000	47757.66
L60	315050	3540000	47728.29
L60	315100	3540000	47707.45
L60	315150	3540000	47702.07
L60	315200	3540000	47712.16
L60	315250	3540000	47735.21
L60	315300	3540000	47767.7
L60	315350	3540000	47809.04
L60	315400	3540000	47856.24
L60	315450	3540000	47908.21

L60	315500	3540000	47963.45
L60	315550	3540000	48022.68
L60	315600	3540000	48083.61
L60	315650	3540000	48145.52
L60	315700	3540000	48205.83
L60	315750	3540000	48263.45
L61	313600	3540050	48167.15
L61	313650	3540050	48155.35
L61	313700	3540050	48151.98
L61	313750	3540050	48157.13
L61	313800	3540050	48166.93
L61	313850	3540050	48177.77
L61	313900	3540050	48191.33
L61	313950	3540050	48206.23
L61	314000	3540050	48210.16
L61	314050	3540050	48156.69
L61	314100	3540050	48083.59
L61	314150	3540050	48015.28
L61	314200	3540050	47956.44
L61	314250	3540050	47908.23
L61	314300	3540050	47870.74
L61	314350	3540050	47846.61
L61	314400	3540050	47833.69
L61	314450	3540050	47829.89
L61	314500	3540050	47831.19
L61	314550	3540050	47837.34
L61	314600	3540050	47844.74
L61	314650	3540050	47850.21
L61	314700	3540050	47852.44
L61	314750	3540050	47852.13
L61	314800	3540050	47847.07
L61	314850	3540050	47835.61
L61	314900	3540050	47816.87
L61	314950	3540050	47794.26
L61	315000	3540050	47768.66
L61	315050	3540050	47743.97
L61	315100	3540050	47726.09
L61	315150	3540050	47722.43
L61	315200	3540050	47732.34
L61	315250	3540050	47753.2
L61	315300	3540050	47783.07
L61	315350	3540050	47822.07
L61	315400	3540050	47867.62
L61	315450	3540050	47917.25
L61	315500	3540050	47969.82
L61	315550	3540050	48026.63
L61	315600	3540050	48085.45

L61	315650	3540050	48144.34
L61	315700	3540050	48200.68
L61	315750	3540050	48257.69
L62	313650	3540100	48190.29
L62	313700	3540100	48191.73
L62	313750	3540100	48198.82
L62	313800	3540100	48211.74
L62	313850	3540100	48226.79
L62	313900	3540100	48243.47
L62	313950	3540100	48257.71
L62	314000	3540100	48253.98
L62	314050	3540100	48211.34
L62	314100	3540100	48144.21
L62	314150	3540100	48075.28
L62	314200	3540100	48013
L62	314250	3540100	47959.34
L62	314300	3540100	47915.76
L62	314350	3540100	47885.92
L62	314400	3540100	47868.91
L62	314450	3540100	47859.52
L62	314500	3540100	47855.64
L62	314550	3540100	47856.87
L62	314600	3540100	47860.71
L62	314650	3540100	47863.18
L62	314700	3540100	47862.21
L62	314750	3540100	47859.61
L62	314800	3540100	47854.42
L62	314850	3540100	47843.13
L62	314900	3540100	47825.73
L62	314950	3540100	47805.18
L62	315000	3540100	47784.41
L62	315050	3540100	47764.89
L62	315100	3540100	47750.82
L62	315150	3540100	47747.61
L62	315200	3540100	47756.91
L62	315250	3540100	47775.94
L62	315300	3540100	47802.79
L62	315350	3540100	47838.75
L62	315400	3540100	47881.94
L62	315450	3540100	47928.95
L62	315500	3540100	47978.16
L62	315550	3540100	48031.57
L62	315600	3540100	48087.52
L62	315650	3540100	48143.09
L62	315700	3540100	48196.15
L62	315750	3540100	48251.09
L63	313700	3540150	48222.74

L63	313750	3540150	48233.58
L63	313800	3540150	48249.11
L63	313850	3540150	48266.85
L63	313900	3540150	48282.27
L63	313950	3540150	48292.24
L63	314000	3540150	48286.93
L63	314050	3540150	48250.21
L63	314100	3540150	48190.55
L63	314150	3540150	48124.88
L63	314200	3540150	48064.11
L63	314250	3540150	48008.75
L63	314300	3540150	47961.22
L63	314350	3540150	47926.2
L63	314400	3540150	47904.2
L63	314450	3540150	47890.66
L63	314500	3540150	47881.25
L63	314550	3540150	47877.45
L63	314600	3540150	47878.33
L63	314650	3540150	47878.24
L63	314700	3540150	47874.98
L63	314750	3540150	47870.67
L63	314800	3540150	47865.34
L63	314850	3540150	47855.26
L63	314900	3540150	47838.9
L63	314950	3540150	47821.32
L63	315000	3540150	47804.89
L63	315050	3540150	47789.31
L63	315100	3540150	47776.83
L63	315150	3540150	47774.48
L63	315200	3540150	47783.93
L63	315250	3540150	47801.55
L63	315300	3540150	47825.31
L63	315350	3540150	47857.62
L63	315400	3540150	47898.18
L63	315450	3540150	47942.37
L63	315500	3540150	47987.61
L63	315550	3540150	48036.73
L63	315600	3540150	48089.24
L63	315650	3540150	48141.14
L63	315700	3540150	48189.3
L63	315750	3540150	48241.55
L64	313750	3540200	48260.62
L64	313800	3540200	48278.28
L64	313850	3540200	48294.97
L64	313900	3540200	48308.69
L64	313950	3540200	48314.16
L64	314000	3540200	48305.91

L64	314050	3540200	48275.39
L64	314100	3540200	48224.45
L64	314150	3540200	48165.43
L64	314200	3540200	48108.93
L64	314250	3540200	48053.55
L64	314300	3540200	48003.26
L64	314350	3540200	47964.07
L64	314400	3540200	47939.06
L64	314450	3540200	47921.65
L64	314500	3540200	47908.7
L64	314550	3540200	47900.68
L64	314600	3540200	47898.5
L64	314650	3540200	47896.55
L64	314700	3540200	47891.06
L64	314750	3540200	47884.7
L64	314800	3540200	47879.6
L64	314850	3540200	47870.88
L64	314900	3540200	47856.84
L64	314950	3540200	47840.86
L64	315000	3540200	47827.95
L64	315050	3540200	47816.61
L64	315100	3540200	47807.2
L64	315150	3540200	47804.71
L64	315200	3540200	47813.43
L64	315250	3540200	47829.86
L64	315300	3540200	47850.88
L64	315350	3540200	47879.39
L64	315400	3540200	47916.6
L64	315450	3540200	47957.82
L64	315500	3540200	47999.23
L64	315550	3540200	48043.81
L64	315600	3540200	48092.42
L64	315650	3540200	48141.01
L64	315700	3540200	48185.86
L64	315750	3540200	48234.34
L65	313800	3540250	48296.3
L65	313850	3540250	48314.78
L65	313900	3540250	48325.14
L65	313950	3540250	48326.18
L65	314000	3540250	48318.12
L65	314050	3540250	48291.25
L65	314100	3540250	48246.84
L65	314150	3540250	48193.39
L65	314200	3540250	48141.68
L65	314250	3540250	48088.81
L65	314300	3540250	48038.06
L65	314350	3540250	47996.39

L65	314400	3540250	47968.77
L65	314450	3540250	47950.4
L65	314500	3540250	47935
L65	314550	3540250	47923.66
L65	314600	3540250	47919.11
L65	314650	3540250	47915.38
L65	314700	3540250	47908.54
L65	314750	3540250	47900.95
L65	314800	3540250	47896.11
L65	314850	3540250	47889.77
L65	314900	3540250	47877.7
L65	314950	3540250	47864.27
L65	315000	3540250	47854.49
L65	315050	3540250	47846.43
L65	315100	3540250	47838.42
L65	315150	3540250	47836.2
L65	315200	3540250	47844.51
L65	315250	3540250	47859.75
L65	315300	3540250	47878.13
L65	315350	3540250	47902.63
L65	315400	3540250	47936.41
L65	315450	3540250	47974.54
L65	315500	3540250	48012.07
L65	315550	3540250	48051.86
L65	315600	3540250	48096.62
L65	315650	3540250	48142.11
L65	315700	3540250	48183.29
L65	315750	3540250	48225.94
L66	313850	3540300	48322.77
L66	313900	3540300	48332.32
L66	313950	3540300	48331.01
L66	314000	3540300	48320.7
L66	314050	3540300	48297.55
L66	314100	3540300	48258.43
L66	314150	3540300	48210.09
L66	314200	3540300	48160.46
L66	314250	3540300	48109.07
L66	314300	3540300	48057.67
L66	314350	3540300	48017.25
L66	314400	3540300	47992.7
L66	314450	3540300	47976.85
L66	314500	3540300	47963.16
L66	314550	3540300	47949.84
L66	314600	3540300	47941.9
L66	314650	3540300	47935.83
L66	314700	3540300	47926.55
L66	314750	3540300	47918.23

L66	314800	3540300	47915.1
L66	314850	3540300	47912.09
L66	314900	3540300	47904.08
L66	314950	3540300	47892.32
L66	315000	3540300	47884.79
L66	315050	3540300	47880.01
L66	315100	3540300	47874.66
L66	315150	3540300	47871.72
L66	315200	3540300	47878.29
L66	315250	3540300	47891.88
L66	315300	3540300	47907.55
L66	315350	3540300	47928.29
L66	315400	3540300	47958.16
L66	315450	3540300	47993
L66	315500	3540300	48026.81
L66	315550	3540300	48062.2
L66	315600	3540300	48102.92
L66	315650	3540300	48145.16
L66	315700	3540300	48183.19
L66	315750	3540300	48220.5
L67	313900	3540350	48333.47
L67	313950	3540350	48328.86
L67	314000	3540350	48318.72
L67	314050	3540350	48296.59
L67	314100	3540350	48260.15
L67	314150	3540350	48213.45
L67	314200	3540350	48164.53
L67	314250	3540350	48112.1
L67	314300	3540350	48060.18
L67	314350	3540350	48025.24
L67	314400	3540350	48008.13
L67	314450	3540350	48000.52
L67	314500	3540350	47991.75
L67	314550	3540350	47976.91
L67	314600	3540350	47965.22
L67	314650	3540350	47954.77
L67	314700	3540350	47943.11
L67	314750	3540350	47935.84
L67	314800	3540350	47936.18
L67	314850	3540350	47938.4
L67	314900	3540350	47934.87
L67	314950	3540350	47926
L67	315000	3540350	47920.66
L67	315050	3540350	47918.04
L67	315100	3540350	47913.64
L67	315150	3540350	47910.02
L67	315200	3540350	47914.73

L67	315250	3540350	47925.62
L67	315300	3540350	47938.15
L67	315350	3540350	47955.06
L67	315400	3540350	47981.32
L67	315450	3540350	48012.43
L67	315500	3540350	48042.39
L67	315550	3540350	48073.45
L67	315600	3540350	48110.38
L67	315650	3540350	48148.91
L67	315700	3540350	48182.99
L67	315750	3540350	48214.82
L68	313850	3540400	48329.34
L68	313900	3540400	48329.45
L68	313950	3540400	48322.95
L68	314000	3540400	48310.54
L68	314050	3540400	48288.81
L68	314100	3540400	48253.61
L68	314150	3540400	48207.71
L68	314200	3540400	48155.9
L68	314250	3540400	48098.52
L68	314300	3540400	48039.58
L68	314350	3540400	48018.33
L68	314400	3540400	48017.52
L68	314450	3540400	48022.61
L68	314500	3540400	48026.19
L68	314550	3540400	48008
L68	314600	3540400	47989.78
L68	314650	3540400	47973.66
L68	314700	3540400	47956.61
L68	314750	3540400	47952.78
L68	314800	3540400	47959.34
L68	314850	3540400	47968.34
L68	314900	3540400	47973.96
L68	314950	3540400	47965.37
L68	315000	3540400	47960.67
L68	315050	3540400	47959.89
L68	315100	3540400	47958.71
L68	315150	3540400	47952.56
L68	315200	3540400	47953.71
L68	315250	3540400	47961.3
L68	315300	3540400	47970.48
L68	315350	3540400	47984
L68	315400	3540400	48006.24
L68	315450	3540400	48033.38
L68	315500	3540400	48059.5
L68	315550	3540400	48086.88
L68	315600	3540400	48119.72

L68	315650	3540400	48154.35
L68	315700	3540400	48184.99
L68	315750	3540400	48214.31
L69	313900	3540450	48320.88
L69	313950	3540450	48312.82
L69	314000	3540450	48299.85
L69	314050	3540450	48277.57
L69	314100	3540450	48241.66
L69	314150	3540450	48195.22
L69	314200	3540450	48143.72
L69	314250	3540450	48085.73
L69	314300	3540450	48030.01
L69	314350	3540450	48016.05
L69	314400	3540450	48024.17
L69	314450	3540450	48038.77
L69	314500	3540450	48047.89
L69	314550	3540450	48031.3
L69	314600	3540450	48011.11
L69	314650	3540450	47990.76
L69	314700	3540450	47973.08
L69	314750	3540450	47972.17
L69	314800	3540450	47983.24
L69	314850	3540450	47996.9
L69	314900	3540450	48005.18
L69	314950	3540450	48001.3
L69	315000	3540450	47999.23
L69	315050	3540450	48000.76
L69	315100	3540450	48000.03
L69	315150	3540450	47994.54
L69	315200	3540450	47994.02
L69	315250	3540450	47997.91
L69	315300	3540450	48003.39
L69	315350	3540450	48013.64
L69	315400	3540450	48032.43
L69	315450	3540450	48055.2
L69	315500	3540450	48077.18
L69	315550	3540450	48100.69
L69	315600	3540450	48129.66
L69	315650	3540450	48159.77
L69	315700	3540450	48186.1
L69	315750	3540450	48210.67

Appendix C: Area of Polygon Calculation

Included in Appendix C is a computer code we used to estimate the area of geometrical bodies from the inversion model. The code was written for MATLAB R.2012b. We adopted a procedure developed by Lundgren (2005). The input data for this code routine is an excel file containing x and z coordinate vector of the polygon of interest. The output of this code yields a resulting vector including: (1) the radius of the best fit, (2) the area of the best fit polygon.

References

Lundgren, J., 2005, *Alpha Shapes*. http://www.mathworks.com/matlabcentral/fileexchange/28851-alpha-shapes/content/alphavol.zip, MATLAB Central File Exchange. Retreived April 18th 2015.

```
%%Appendix D- Routine to calculate volume of the buried geometry



%%

clc
clear

% read body profile data
%B_G_K = csvread('gravity_kilbourne_revised_2015_3.csv',',', 171, 13);
body_profile = load ('dike2_profile_test.csv');

z = body_profile (:,2); %depth peak
z = -z;
x = body_profile (:,1); %distance
y = x;
[m n] = size (z);
X = [x z];

figure (1)
plot (x,z)
%%
%make plot coordinate
xlin = linspace(min(x),max(x),m);
ylin = linspace(min(y),max(y),m);
[x,y] = meshgrid(xlin, ylin);% R or reference matrix in ASCII format

%%
tri = delaunay(x,y);
%figure (1)
%h = plot3(x,z,y,'.-')
%%

figure (2)
V= alphavol(X,inf,1);
% [x,y,z] = sphere;
%    ii = abs(z) < 0.4;
%    X = [x(ii),y(ii),z(ii)];
%  X = [X; 0.8*X];
  figure (3)
   subplot(211), alphavol(X,inf,1);
   subplot(212), alphavol(X,0.1,1);

%%
figure (4)
w = ones(m,1);
peak = w*z';
surf (x,y,peak)
```

```
%%
%%
% How many triangles are there?
figure (4)
[r,c] = size(tri);
disp(r)

%% Plot it with TRISURF

 trisurf(tri,x,y,peak)
axis vis3d

%% Clean it up

axis off
l = light('Position',[-50 -15 29])
set(gca,'CameraPosition',[208 -50 7687])
lighting phong
shading interp
colorbar EastOutside
```

Appendix D: Volume and Mass Estimation

Included in Appendix D is an excel spreadsheet we use to calculate the volume and mass of volcanic dikes, the diatreme and, the excavation zone. Using Equation 8 (see Chapter 2) implemented in this excel spreadsheet, we also calculated mass of water and the ratio of mass of water to mass of magma. The input of this spreadsheet are area of polygon obtained from Appendix C, the initial velocity from Chapter 3, rock density (table 1; see Chapter 2), and temperature and atmospheric pressure constants (Wohletz, 1986). The uncertainties of each variable are also propagated into the final result. The methods used in error and uncertainty analysis are form Taylor (1997) and Bevington and Robinson (2002). The formula used in our error and uncertainty analysis is also implemented in third page of this excel spreadsheet. The output products of this spread sheet are 1) mass of water, 2) mass of water to mass of magma ratio, and 3) volume and percent of water in groundwater reservoir, 4) the uncertainties of the obtained variables.

References

Bevington, P. R. and Robinson, K.D., 2002, *Data Reduction and Error Analysis for the Physical Sciences (3rd ed.)*: McGraw-Hill Education (New York), 336 p.

Taylor, J.R., 1997, Introduction to error analysis, the study of uncertainties in physical measurements (Volume 1), *2nd Ed.*: University Science Books (New York), 327 p.

Wohletz, K. H., 1986, Explosive magma-water interactions: Thermodynamics, explosion mechanisms, and field studies: *Bulletin of Volcanology*, vol. 48, no. 5, p. 245-264.

Appendix D-Mass of Water Calculation

Length of Dike 1 = 0.0137deg			area of dike 1	2013000	m2	Volume of dike 1	1.98E+09	m3	1.977229 km3
	982.23	m							
Length of Dike 2 = 0.0077 deg			area of dike 2	2655000	m2	Volume of dike 2	1.47E+09	m3	1.465719 km3
	552.06	m							
Length of Dike 3 = 0.0071 deg			area of dike 3	2007000	m2	Volume of dike 3	1.02E+09	m3	1.021643 km3
	509.04	m							
Length of excavation zone = 0.0170 deg			area of excavation A1	1146930	m2	Volume of excavation	1.55E+09	m3	1.55E+00 km3
A3	1218.82	m	area of excavation A2	1238600					
			Area of excavation A3	1418100	m2				
			Average	1267876.667	m2				
Length of Diatreme = 0.0170 deg			area of Diatreme A1	15244700	m2	Volume of Diatreme	1.86E+10	m3	1.86E+01 km3
A3	1218.82	m	area of diatreme A3	14037000	m2				
			Area of Diatreme A2	16600000	m2				
			Average	15293900	m2				

volume of all dikes	4.46E+09	m3	density	3100	kg/ m3		mass of all dike	1.38E+13	kg
Volume of excavation zone	1.55E+09	m3	density	2178.431373	kg/m3	solid volume	mass of excavation zone	2.52E+12	kg
						0.75			
Volume of Diatreme	1.42E+10	m3	density	2560	kg/m3		mass of diatreme	3.63E+13	kg

Calucaltion for mas of water						calculate	P1			
Cvm	1000	$N.m\,kg^{-1}\,K^{-1}$					p-litho	8.81E+02	bar	3580 m
Te	298	K					p-litho	3.21E+02		1500 m
Tm	1273	K					error p-litho	2.95E+01	2.95E+06	kg.m-1.s-2
P1	8.81E+07	kg.m-1.s-2	8.81E+02	bar						
Vmax	132.21	m/s	113.46	vmin	Vmean	122.835	Verr	9.375	m/s	
p0	89000	kg.m-1.s-2	0.89	bar						

$$m_w = \frac{2\,(CR.\,m_m C_{vm}(T_m - T_e) - p_1 V_{dia} - p_0 V_{exc})}{v_{max}^2} - m_f$$

Equation. (8)

term1	1.33E-04	2.86141E-05	error propagation
term 2	1.34942E+18	1.43E+17	
term3	1.25E+18	1.59E+17	
term4	1.03E+14	1.55E+13	
mw	1.09E+13 kg	3.12E+12	
vol	1.09E+10 m3	3.12E+09	
	10.86793282 km3	3.12E+00	
mw/mm	0.79	2.25E-01	

now calculate uncertainty

Calucaltion for mas of water

	crossection (km^2	length (km)	density (kg/m^3	volume(km^3)	volume(m^3)	delta_volume	mass (kg)	delta_mass	delta _area	delta volume
dike 1	2.013	0.98223	3100	1.98E+00	1.98E+09	0.296494139	6.129E+12	9.1913E+11	1729.26463	2.96E+08
dike 2	2.655	0.55206	3100	1.47E+00	1.47E+09	0.294403719	4.544E+12	9.1265E+11	1985.96612	2.94E+08
dike 3	2.007	0.50904	3100	1.02E+00	1.02E+09	0.225125822	3.167E+12	6.9789E+11	1726.68556	2.25E+08
diatreme	15.2939	1.21882	2560	1.86E+01	1.86E+10	1.671353442	4.772E+13	4.2787E+12	4766.4901	1.67E+09
Volcanic system	1.267876667	1.21882	2178.431373	1.55E+00	1.55E+09	0.23182815	2.52E+12	3.7877E+11	1372.39168	2.32E+08
Volcanic sur	na	na	2560	1.42E+01	1.42E+10	1.737436701	3.63E+13	4.45E+12	na	1.74E+09
total dike	na	na	3100	4.46E+00	4.46E+09	0.474619806	1.38E+13	1.47E+12	na	4.75E+08

error analysis

delta x (km)	0.1
delta z (km)	0.12
delta y (km)	0.1

	crossection (m^2)
dike 1	2013000
dike 2	2655000
dike 3	2007000
diatreme	15293900
Volcanic system	1267877

Chapter 3: GPR Surveys at Kilbourne Hole, NM: Implications for Paleoclimatology and Planetary Exploration

[1] Nisa Maksim, [2] José M. Hurtado, Jr, and [3] Diane I. Doser

The University of Texas at El Paso, 500 West University Avenue, El Paso, TX 79662

[1] nrhodes@miners.utep,edu, [2] jhurtado@utep.edu, [3] doser@utep.edu

Abstract

We hypothesize that the sizes of volcanic blocks ejected by a phreatomagmatic eruption are indicative of explosion behavior and characteristics of the groundwater reservoir involved. In this research we develop a non-invasive geophysical survey technique using ground-penetrating radar (GPR) to quantitatively map the size distribution of volcanic blocks and sags at an analog phreatomagmatic volcano site with the goal of understanding the hydrologic conditions that were involved in its eruption. We determined the distribution of volcanic block sizes as a function of radial distance from the crater rim at Kilourne Hole, NM using GPR. We collected the size distribution of volcanic blocks along six survey transects, and estimated that volcanic blocks were ejected by the Kilbourne Hole eruption at an initial velocity of 123 ± 9 m s^{-1} and that the duration of the gas expansion phase of the eruption was as long as 92 ± 11 s. The initial pressure inside the vent at the time of eruption was 163 ± 9 bar. Using an empirical relationship between the maximum gas expansion velocity and the initial pressure, we estimate that the ratio between the mass of gas and the mass of solid material that was released during the eruption was 0.01-0.02 (1-2%). Assuming that the all gases were

derived from groundwater, we applied this gas-to-rock mass ratio to the independent estimates of the mass of ejected volcanic fragments and determined the amount of water involved in the Kilbourne Hole eruption. Our results suggest that the mass of water in the Plio-Pleistocene groundwater reservoir that fed the Kilbourne Hole contained a minimum of $7.7 \pm 1.0 \times 10^9$ kg (~ 0.008 kg^3) of water. We have successfully utilized geophysical mapping results of phreatomagmatic outcrop as climate proxies. The implication of our geophysical approaches for planetary exploration is also discussed.

Keywords: phreatomagmatic volcano, ground-penetrating radar, pyroclastic deposits, volcanic blocks, Kilbourne Hole, planetary geophysics, gas-to-rock mass ratio, groundwater, paleohydrology

1. Introduction

The search for water on Mars has focused mainly on surface water, ice water, or groundwater (Ezell and Ezell, 2013, Hobbs et al., 2015, Marra, 2015). Observations indicate that rivers and groundwater may have been prominent features in its early history (Marra, 2015). Features such as Home Plate plateau, a suspected remnant of a phreatomagmatic eruption located in Gusev Crater on Mars (Squyres et al., 2007), can reveal important information about paleohydrologic conditions. When magma interacts with a groundwater source, a phreatomagmatic eruption can occur. The resulting explosion can be so strong that it excavates a volcanic crater (Wohletz and Sherridan, 1981) and creates a high volume of pyroclastic material (Wilson and Head, 1994). The existence of phreatomagmatic features like Home Plate on Mars implies the existence of groundwater in the past (Squyres et al., 2007). In a phreatomagmatic eruption, the heated water will flash into steam, which, if confined, will build up pressure, potentially to the point of explosive release. The resulting explosion will excavate a crater and eject pyroclastic material (Wohletz and Sherridan, 1981). Because the initial gas ejection velocity is the direct result of the water vapor pressure trapped inside the volcanic vent, it can be used to determine the size of the groundwater reservoir that interacted with the magma source. Knowledge of the physics governing phreatomagmatic eruptions offers a unique opportunity to make quantitative estimates of the amount of water involved. To be able to quantify the amount of groundwater involved in the early volcanic activity on Mars is the goal of this research.

In this research, we hypothesized that the size distribution of pyroclastic material ejected by a phreatomagmatic eruption is indicative of the behavior of the explosion and

the characteristics of the groundwater reservoir involved (Wohletz and Sheridan, 1983). To test the hypothesis, we mapped the radial size distribution of volcanic blocks ejected from Kilbourne Hole using a GPR. The radial size distributions of volcanic blocks data were used to determine the initial gas ejection velocity (Fagents and Wilson, 1996; Wilson, 1999; Sparks, 1976; Wilson, 1972). We present here the results of a GPR study of a phreatomagmatic volcano – Kilbourne Hole in New Mexico – designed specifically to decipher the paleohydrogeological conditions at the time of eruption. The techniques used in this research can serve as an analog for similar studies applied to the paleohydrologic exploration of other planets, like Mars. Our GPR surveys were designed specifically to work on a phreatomagmatic setting as an implication to future Mars exploration. The majority of the Martian surface has been shaped by extensive volcanism (Tanaka et al., 1992; Mouginis-Mark et al., 1992). The accumulated fine-grained material from volcanic activity on Mars resembles terrestrial volcanic ash on Earth (Grant and Schultz, 1990). The fine-grained materials from volcanic activity on Mars are distinguished by their easily eroded surfaces, their low thermal inertia, and continuous, regular layering that are similar to terrestrial sedimentary deposits (Grant and Schultz, 1990; Tanaka, 2000). Because of this similarity, we first designed a GPR study on an analog phreatomagmatic volcanic site on Earth and then later we can potentially adapt our survey design on the Martian site. To evaluate the potential of future GPR investigations on Mars, we designed medium-frequency (250 MHz) GPR surveys to map volcanic block size distribution at Kilbourne Hole, NM. The implications of these integrated surveys for the exploration Mars are to improve the ability to characterize volcanic activity on Mars and to quantify the amount of Martian ancient groundwater.

We performed an experiment at an analogous site to determine the relationship between the volcanic block size distribution and the terminal velocity of the volcanic clasts that were dropped at the time of eruption. We then used the obtained relationship to determine the following: the initial velocity of eruption, the time duration of the eruption phase, the initial vent pressure at the time of eruption and the amount of groundwater that fed the eruption. In this paper we describe: (1) our strategy for imaging and measuring the sizes of volcanic blocks and associated sags from GPR profiles; (2) how to quantify the initial gas ejection velocity based on the size distribution of volcanic blocks; (3) a method for calculating the volume of the groundwater reservoir that fed the Kilbourne Hole eruption; and (4) the use of GPR for similar applications in planetary exploration.

One obstacle that could prevent GPR and other electrical surveys on Mars to become successful is that the application of electrical techniques on the Martian subsurface heavily depends on the knowledge of the subsurface electromagnetic characteristics and how these will affect wave propagation (Wainstein et al., 2008). As such, further investigations and other complimentary approaches on Martian subsurface electrical properties are still required to adapt Earth techniques to properly work under Martian conditions (Wainstein et al., 2008).

2. Background

2.1 Phreatomagmatic Volcanoes on Earth and Mars

A phreatomagmatic eruption is caused by the explosive interaction between rising magma and an external source of water such as groundwater, surface water, seawater, meteoric water, hydrothermal water, ice-melt water, or lake water (Morrissey et al., 2000;Wilson and Head, 2003). Prior to the eruption, vapor produced by heating the water source can be trapped, building up tremendous gas pressure. The trap can be a cap of resistant rock, for example a lava flow, overlying a groundwater reservoir. As gas accumulates in the confined aquifer beneath the cap rock, the pressure rises. Once the pressure exceeds the tensile strength of the cap rock, an explosive release of the pressurized gas can occur. Water heated by lava then flashes in steam and expands violently; fragmenting the magma it is in contact with into fine-grained ash. As the gas radially expands from the vent, it pushes the cap rocks and other solid material outward with it. The style of phreatomagmatic eruptions range from relatively mild inflows of low viscosity lava into a lake or the ocean to form pillow lavas to extremely high-energy explosions that produce pyroclastic deposits consisting of more than 90% fragmented country rock (Wohletz and Zimanowski, 2000). The resulting eruptive products can include airfall tephra (e.g. ash and pumice), ejected volcanic blocks, pyroclastic flow-and-surge deposits, and debris flows (Barberi et al., 1989). Landforms produced by phreatomagmatic eruptions include the excavated crater, called a maar, and a surrounding tuff ring or cone (White and Ross, 2011). Tuff cone, mainly composed of thick-bedded pyroclastic flow and surge deposits, are characterized by high profiles feature and steepness of the bedding (>25 degrees). Wetter eruptions (with a water-rock ratio >1)

result in larger diameter tuff rings and tuff cones than those that formed by dryer eruptions (Wohletz and Sherridan, 1981). A tuff ring is formed from an explosion at a shallower depth (less than 0.5 km) than a tuff cone. Tuff ring mainly composed of thin-bedded pyroclastic flow and surge deposits and characterized by low profiles features and less steepness of the bedding <10 degrees). Wohletz and Sherridan (1981) suggest that fluid dynamic interactions between groundwater and magma control the strength of the resulting volcanic eruption.

Pyroclastic surge deposits are similar to pyroclastic flow deposits in composition, except that surge deposits are generally richer in lithic fragments than flow deposits and are better sorted. Both pyroclastic surge and flow deposits are derived from ignimbrite or deposited during the same ignimbrite-forming eruption (Fisher and Heiken, 1982). The pyroclastic deposits produced by a phreatomagmatic eruption often contain ejected blocks of basalt and other lithologies measuring up to 1 m or more in diameter (Walker and Groasdale, 1971). These volcanic blocks were ballistically ejected from the vent at the time of eruption and, when they land, they deform the unconsolidated pyroclastic deposits into asymmetric depressions called sags. The asymmetry of the sag can be used to determine the trajectory of the blocks and the location of the vent (Walker and Groasdel, 1971). Volcanic sags on Earth typically indicate that the deformed pyroclastic deposit were unconsolidated and wet at the time it was bombarded by the volcanic blocks.

What has been interpreted to be an outcrop of material deposited by a phreatomagmatic eruption was identified by the Mars Exploration Rover Spirit at Home Plate Plateau in Gusev Crater, near the Martian equator (Squyres et al., 2007). Squyres et

al. (2007) interpreted that the layers at Home Plate are composed of clastic rocks of moderately altered alkali basalt composition and suggested that Home Plate is a result of a phreatomagmatic activity that occurred when the alkali-rich basaltic magma came into contact with a subsurface fluid. The stratigraphically lowest unit at Home Plate is likely pyroclastic material, while the uppermost unit represents eolian reworking of those pyroclastic materials (Vaucher et al., 2009). In the lower unit, cross-stratified surge deposits are found which contain what are interpreted to be volcanic blocks and sags (Squyres et al., 2007). The chemical composition of the volcanic blocks is similar to those of basalts that are found nearby and suggest that the deposits lay close to the source vent (Squyres et al., 2007).

Ennis et al. (2007) compared the stratigraphy at Home Plate to that at Zuni Salt Lake, a phreatomagmatic crater in Arizona, and found some similarities between the two sites, including: (1) both have tephra layers with low-angle cross bedding; (2) both show occurrences of volcanic ejecta impacting wet cohesive tephra beds, producing sag features; and (3) both are capped by massive basalt blocks. One difference between the sites is that the bedding at Home Plate dips 6°, whereas the bedding at Zuni Salt Lake dips more steeply (25°). Ennis et al. (2007) suggested that under the weak gravity field and thin atmospheric pressure on Mars, the ash ejected from a phreatomagmatic eruption would be expected to be more widespread and to have shallower dips. Because no evidence of surface excavation, collapse, or slump features have been found at Home Plate, Ennis et al. (2007) suggested that Home Plate is a phreatomagmatic volcano with a shallower basaltic source than that which produced Zuni Salt Lake.

2.2 Previous Geophysical Study on Mars

Among the previous the design of geophysical research on Mars (Picardi et al., 2004; Seu et al., 2007; Hamran et al., Kobayashi et al., 2014; 2015), ground-penetrating radar (GPR) is a popular method for its mobility and its applications on ground ice and permafrost material (Picardi et al., 2004; Seu et al., 2007). There are several types of GPR equipment that have been deployed on Mars and the Moon. The Shallow Subsurface Radar (SHARAD) on board the Mars Reconnaissance Orbiter has probed the Martian subsurface to a depth of about 1 km (Hamran et al., 2015; Seu et al., 2007). The lower-frequency Mars Advanced Radar for Subsurface and Ionosphere Sounding (MARSIS) instrument is orbiting Mars surfaces on Mars Express satellite (Picardi et al., 2004). The Moon's Lunar Radar Sounder (LRS) was also installed and orbited on a Kaguya lunar exploration platform in 2007. LRS operated in a frequency range of 4-6 MHz. It provides 150 m resolution and ~5 km depth of penetration (Kobayashi et al., 2014). A ground-based GPR unit will be boarded on the NASA Mars 2020 rover mission. This ground-based radar will operate at 150-1200 MHz frequency and is using an ultra-wide band with bow-tie slot antenna at 60 cm above the ground surface. Depending on ground conditions, this radar will have the ability to penetrate to more than 10 meters depth.

2.3 Ground-Penetrating Radar

Ground-penetrating radar (GPR) is a non-invasive geophysical tool that has been used primarily for subsurface stratigraphic studies (e.g., Beres, and Haeni, 1991; Bristow

and Jol, 2003; Coma et al, 2005; Barone et al., 2007; Ferguson and Piece, 2012). GPR uses microwave frequency electromagnetic waves to probe the subsurface.

Most of the successful GPR surveys on Mars have been done in Martian polar ice (Hamran et al., 2015; Seu et al., 2007). The Shallow Subsurface Radar (SHARAD) on board the Mars Reconnaissance Orbiter has probed the Martian subsurface to a depth of about 1 km using a 20 MHz center frequency and 10 MHz bandwidths (Hamran et al., 2015; Seu et al., 2007). A GPR unit is comprised of a pair of antennas, a transmitter that emits electromagnetic waves into the subsurface, and a receiver that records the returned signal. When the transmitted radar signal encounters inhomogeneities in subsurface dielectric properties, some of the energy is reflected or scattered back to the surface and the receiver. In addition, the characteristics of the transmitted radar signal (e.g. polarity, phase, etc.) can change as it interacts with and is reflected by materials in the subsurface. The GPR receiver amplifies and records the returned radar signal detected at the surface. The recorded radar signals can be processed and displayed as an image called a radargram (Figures 3, 4, and 6).

For a stratigraphic layer that has homogenous dielectric properties, the reflected electrical wave is strong and continuous and is seen in a radargram as a bright continuous line called "a reflector" (Beres, and Haeni, 1991). For an inhomogeneous or poor sorting stratigraphic layer, the reflected wave is scattered and weak and may not be seen on the radargram. In nonmagnetic and homogeneous geologic media, radar waves travel at a velocity (v) that is a function of electrical permittivity (ε) (Thomson et al., 2012):

$$v = \frac{c}{\sqrt{\varepsilon}} \qquad (1),$$

where c is the velocity of radar waves in free space (0.2998 m/ns in a vacuum; Grote et al., 2003). The velocity can be used to determine the depth to the reflector, z (in m), using (Thomson et al., 2012):

$$z = \frac{Tv}{2} \qquad (2),$$

where T is the two-way travel time (in ns). To accurately calculate depth, however, a detailed velocity model is required, but it is difficult to derive such a velocity model because most geologic media is highly variable and inhomogeneous. For example, variations in moisture content can greatly attenuate radar waves (Russell et al., 2013). A solution to this problem is to directly measure the velocity of radar waves in situations where the depth of the reflector is known, i.e. using Equation (2) instead of Equation (1) to solve for v. As the radar wave propagated into the medium, the signal can be absorbed, lost, or attenuated. The rate of signal attenuation (β) significantly depends on mineral composition of the geological layer such as the percent of pore water, the chemical properties of the pore water, and percent of clay minerals. The attenuation rate normally decreases as both frequency and conductivity increase. Attenuation rate dictates how deep the radargram is.

The ability of GPR to identify subsurface layers or an object depends on (Davis and Annan 1989): (1) the frequency used; (2) the electrical permittivity contrasts among the subsurface materials; and (3) low attenuation rate. The pyroclastic deposits produced by phreatomagmatic eruptions are complex and vary in porosity, thickness, and grain size. The inhomogeneity in phreatomagmatic eruptions may greatly affect the ability of GPR surveys. In some exceptional cases, researchers have found that some basalt rich pyroclastic flows from a phreatomagmatic eruption attenuate much of the radar signal

within the first 1-2 m (Conyers and Connell, 2007). In most cases, a GPR survey can successfully perform on pyroclastic deposits because the pyroclastic deposits are typically thin (~10-100 m), electrically resistive, and likely to be located near the surface (Neal, 2004). The exceptional case in which GPR survey can perform on basaltic-andesitic ash flow deposits is because the material is very dried. Using 100 MHz GPR on dried basaltic-andesitic ash flow deposits, radar waves can penetrate up to 4-6 m (Conyers, 1995; Russell and Stasiuk, 1997). Listed here are the conditions of pyroclastic deposits that are GPR probable suggested by previous worker; in volcanic ash that has a permittivity that ranges between 4-7 F/m (Haggy et al., 2007), in the Bishop tuff (Grimm et al., 2007), Tumalo tuff (Haggy et al., 2007), and Tambora tuff (Abrams and Sigurdsson, 2007), where the attenuation rate of low frequency (50-150 MHz) radar signals varies between 10-50 F/m.

2.4 Physical Properties of Phreatomagmatic Eruption

2.4.1 Initial Gas Expansion Velocity

During a phreatomagmatic explosion, volcanic blocks are launched at an initial velocity equal to the maximum velocity of the expanding gas (Wilson, 1995). As their velocity decreases, volcanic blocks that were launched along with the gas are deposited when the gravitational force exceeds the drag force, which is dependent on atmospheric pressure and density. The important factors that determine the maximum gas expansion velocity, as well as the distribution of ejected volcanic blocks, include the mass ratio of water to magma (Wilson, 1995), the density of the mixture of fluid (water vapor) and pyroclastic particles (Sheridan, 1981), and atmospheric pressure (Fagents and Wilson

1995). Fagents and Wilson (1995) present a model for calculating the maximum velocity of volcanic blocks in a phreatomagmatic explosion from these parameters.

The relationship between gas expansion velocity (V_e) and radial distance from center of the eruption (R) is (Fagents and Wilson, 1995):

$$V_e = V_0 \left(\frac{R_0}{R}\right)^2 e^{-\frac{t}{\tau}} \qquad (3),$$

where V_0 is the initial gas expansion velocity of the gas i.e., the velocity at time zero (t_0) at radial distance R_0 from the center of the explosion; t is time; and τ is a time constant defined as the duration of the gas expansion phase (Fagents and Wilson, 1995). Equation (3) shows that the gas expansion velocity exponentially decreases as a function of time.

Assuming that the volcanic blocks were released from the vent at a velocity equal to the initial gas expansion velocity (V_0), both the gas and the volcanic blocks then decelerate (Equation (3)) as the gas plume propagates away from the vent and expands. If a volcanic block is dropped at a distance R from the vent, we can take the velocity V_e of the block at distance R to be an estimate of the volcanic block's velocity at impact. Quantitatively, V_0 is a direct result of water vapor that was released after the rupture of the volcanic vent. With known energy and the initial gas expansion velocity of an eruption, we can relate the size of volcanic blocks to the amount of groundwater that interacted with the magma source (Zimanowski et al., 1995). The time constant of the gas expansion phase also help us define the physical condition of a groundwater reservoir, for example the porosity and hydraulic conductivity of the aquifer (Fagents and Wilson, 1995). The long duration of gas expansion phase indicates that groundwater may be able to flow continuously to feed the eruption. A high flow rate of groundwater indicates a good hydraulic conductivity of the groundwater reservoir.

2.4.2 Block Size Distribution

Based on a semi-numerical model relating pyroclastic block sizes to their ejection velocities in Hawaiian and Plinian eruptions, Wilson (1999) show that clast size also exponentially decreases as a function of a decreasing expansion velocity (Figure 1). As volcanic gas and a volcanic block travel away from the vent, the gas is decelerated by frictions until it no longer has enough kinetic energy to carry the volcanic block; Once the kinetic energy is no longer strong enough to carry the weight of the blocks, the gravitational force overcomes aerodynamic forces and the volcanic block drops to the ground (Wilson and Bowell, 1971).

The largest volcanic blocks are found near the vent, where the gas velocity is the highest, and the smallest volcanic blocks are found further from the vent (Wilson, 1976). In the field, we can directly measure the sizes of dropped volcanic blocks (φ) and the distance of the blocks from the vent (R). With these two parameters we can calculate the velocity of the volcanic block at impact, which is also the velocity of the volcanic blocks at the time $V_e(R)$ it was dropped. Previous workers (e.g., Walker et al., 1971; Wilson and Bowell, 1971; Wilson 1999) have defined a relationship between volcanic block size and distance from the vents (Figure 1).

The gravity acceleration of a falling pyroclastic block ($g(y)$) is a function of its diameter (φ_i) and density (ρ_i); assuming that the block is a sphere shape. The aerodynamic force of the volcanic gas ($w(y)$) is controlled by the friction factor, C_d. The friction factor is a dimensionless quantity that is used to quantify the drag or resistance of a volcanic block in the plume of gas. Friction factor depends on the size and shape of a volcanic block. If a volcanic block is close to spherical, then the gas motion around a

block will be uniform and less turbulent than if the block is angular. In this case, C_d will have a value within about 30 percent of 0.7 (Wilson and Huang 1979). By balancing the gravitational force acting on the volcanic blocks and the drag force and kinetic energy exerted on it by the expanding gas, one can derive the impact velocity of the volcanic block (Walker, 1971):

$$V_e = \sqrt{[(4\varphi_i \rho_i g)/\,(3C_d \rho_g)]} \qquad (4),$$

where ρ_i is the density of volcanic blocks (3100 kg/m^3 for basalt); g is Earth's gravitational acceleration (9.81 m/s^2); C_d is an empirically-derived friction factor (~0.7; Wilson and Huang 1979); φ is volcanic block size (in m); and ρ_g is atmospheric density (4.7 ± 1.2 kg m^{-3}; Steiner and Babenko, 1978). We neglect lift forces in Equation (4) because the density of a pyroclastic block is much greater than that of air and the pyroclastic blocks are rarely observed to be spinning rapidly (Walker et al., 1971). The average Earth's atmospheric density at sea level is 1.225 kg m^{-3} at 15 °C. The atmospheric density at the time of Kilbourne Hole eruption is unknown but can be estimated using previous observations of other volcanoes (Patrick, 2007; Steiner and Babenko, 1978). If one can determine how the size of dropped volcanic blocks (φ) changes with distance from the explosion center (R), one can calculate the velocity of the blocks at the time they impacted using Equation (4). With that relationship, the initial gas expansion velocity can be determined using Equation (3).

2.4.3 Initial Gas Pressure

In a phreatomagmatic eruption, a sudden released of gas pressure and a vast expansion of volatile constituents occurred at the time of rupture (Fudali and Melson, 1970). Therefore, in addition to the initial velocity of the eruption, another important factor that determines the efficiency of the eruption is the initial pressure of volcanic vent prior the eruption. A number of investigators (Koelle, 1961; Fudali and Melson, 1970) have estimated the initial gas pressure within the vent ($P_{chamber}$) prior to an explosive eruption using the modified Bernoulli equation:

$$P_{chamber} = \frac{1}{2}\rho_d (V_0)^2 \qquad (5),$$

where ρ_d is the density of the material lying between the magma body and the surface.

2.4.4 Explosive energy

The explosive energy of an eruption can be expressed in terms of kinetic energy. The kinetic energy of an eruption is in the form of pyroclastic material moving away from the vent. At the moment of eruption, the potential energy associated with the accumulated gas pressure is converted to kinetic energy (E_k) (Zimanowski et al., 1995), which is quantified as:

$$E_k = \frac{1}{2}(M_f + M_w)V_0^2 \qquad (6),$$

where M_f is the mass of pyroclastic fragments and M_w is the mass of water. By knowing the kinetic energy, the maximum velocity of the gas (water vapor) and the pyroclastic fragments, and the mass of pyroclastic fragments, we can solve for the mass of water in the system.

2.4.5 Gas to Rock Mass Ratio

Several eruption models suggest various relationships and ratios between water gas to the solid fragment that could potentially produce large eruption. This gas to rock mass ratio in a phreatomagmatic eruption specifically refers to the weight of the water vapor to the weight of the rock fragment excavated and expelled from the vent during the explosion. Fagents and Wilson (1993) generated a model to define percent of gas to solid rock fragments in relation to the initial gas expansion velocity and the initial pressure. Self et al (1993) documented cloud gas of several eruptions. Self et al (1979) suggested maximum 10-30% of gas to rock mass ratio while Fagents and Wilson (1993) suggested only 1-5% of gas to rock mass ratio could resulting in large-scale explosion. How magma would interact with such high percentage of water in a very short period of time in the case of Self et al (1979) is still uncertain. Self et al (1979) explicated the long cylindrical geometry of the magma vent, maximized the chances of groundwater being involved in the eruption. Where Fagents and Wilson (1993) argued that the initial pressure of the eruption is limited by the rock strength and the maximum amount of water vapor that can be contained in the rock formation is limited by its porosity. Hence It is likely that a high gas to rock mass ratio in a large-scale explosion is instead associated to the large size of the magma region. In this research we utilized the eruption model of Fagents and Wilson (1993) to derive the gas to rock mass ratio and the amount of groundwater at Kilbourne Hole during the time of eruption. Fagents and Wilson (1993)'s explosion model provides a mathematic relationship between various initial velocities, initial pressure, and the ratio of gas to rock fragments that were released from the eruption.

Fagents and Wilson (1993)'s eruption model of Vulcanian eruption suggested a volatile rich (1-10 wt%) mixture of magma, vaporized groundwater and exsolved volatiles, must be trapped at high pressure ranges between 1-100 bars in order to initiate the initial gas expansion velocities at the time of rupture to be between 100-400 ms^{-1} (Fudali and Melson, 1970; Self, 1979; Fagents and Wilson, 1993). The weight percent between the mass of vaporizing gas to an initial mass flux of rock fragments that were released at rupture is gas to rock fragments mass ratio (n). High initial gas expansion velocity and high initial pressure at the time of rupture indicates high gas to rock fragments mass ratio. Vice versa, the low initial gas expansion velocity and low initial pressure indicates low gas to rock fragments mass ratio (n).

The sizes of the volcanic blocks and the internal structure of Kilbourne Hole are the keys to understanding how explosive Kilbourne was at the time of eruption. We can derive the initial velocity of the volcanic blocks by knowing the size of the volcanic blocks and its location from the vent. We can also derive the initial pressure within the vent by knowing the initial velocity and the density of the cap rock material. The derived initial pressure and the initial velocity can be used to estimate the weight ratio of water vapor to the weight of rock fragments that were released from the eruption (Self et al., 1979; Fagents and Wilson, 1993). Hence, we can estimate the weight of liquid water in the ancient groundwater reservoir.

3. Study Area

Kilbourne Hole is a well-known phreatomagmatic volcanic crater located in Southern Doña Ana County, New Mexico (Figure 2). This maar crater is a 2-km wide depression, and it is about 200-m deep (Reiche, 1940). The area around Kilbourne Hole is covered with 50-150 m of pyroclastic deposits. Underneath this volcanic ash are the Aden and Afton basalt flow lava flows. The Kilbourne Hole eruption occurred during the mid-Pleistocene (0.02-0.1 Ma; Seager, 1984). Seager (1984) and Lorenz (1973) suggest that the excavation of Kilbourne Hole was caused by catastrophic subsidence, similar to caldera collapse, following phreatomagmatic explosive activity.

Kilbourne Hole is located along the southwest margin of the Rio Grande rift. The Rio Grande rift, and the series of basins related to it, is a major tectonic feature of the North American continent that extends from Colorado through New Mexico, and into northern Chihuahua, Mexico, covering a distance of about 950 km (Ramberg et al., 1978; Keller et al., 1990). The extension that formed the Rio Grande rift, and the associated volcanism, began about 30 million years ago (Ingersoll, 2001) and still continues today (Keller et al., 1990). Volcanic activity can be found throughout the Rio Grande rift (Lipman, 1969). The volcanic activity along the Rio Grande rift varies from alkalic to tholeiitic basaltic volcanism activity. The changes in types of volcanism composition indicate the magma source of volcanic activity within the Rio Grande Rift is derived from various depths. Tholeiitic basalts originate at shallower depths than alkalic basalts (Lipman, 1969), suggesting the movement within the vent. During the Pliocene to Quaternary, volcanic activity in the Rio Grande Rift mostly erupted alkali-olivine basalt and, in some localities, tholeiitic basalts (Keller et al., 1990).

The Kilbourne Hole eruption occurred during the Pliocene to Quaternary Rio Grande rift phase (5 Ma to present). Prior to the Kilbourne Hole eruption, the area was already covered with at a series of volcanic flows that erupted from Aden and Afton craters (Hoffer, 1972; Seager, 1984). Below the Afton-Aden basalt flows is the Late Quaternary (2-3 Ma) Santa Fe group (Figure 2), a 1.5-2 km thick package of fluvial sediments deposited by the ancestral Rio Grande River (Seager, 1984). There are two parts of the Santa Fe group. The younger unit is the Camp Rice Formation, which contains fluvial and piedmont sediments (Lorenz, 1986). The older unit is the Fort Hancock formation, which contains alluvial sediments (Hawley, 1975).

The Kilbourne Hole eruption is the most recent event of in the Pliocene-Quaternary rifting period (Hoffer, 1972). The Kilbouren Hole eruption excavated the Santa Fe group and the overlying Afton-Aden basalt flows. Both pre-eruptive units can be seen exposed inside Kilbourne Hole. The Kilbourne Hole explosion deposited 50-150 m of air-fall and pyroclastic surge deposits around the crater rim (Lorenz, 1986). Pieces of alkali olivine can be found within the pyroclastic deposits, indicating that there is basaltic intrusion located underneath Kilbourne Hole (Hoffer, 1972; Hawley, 1975). The pyroclastic deposits can be traced 800-1000 m radially away from the modern crater rim (Seager, 1987). There are two sets of pyroclastic layers: one that deposited around the crater rim, and one that has collapsed into the crater (Figure 3). The dips of both sets of pyroclastic strata range from 8° to 35° (Seager, 1987). After the Kilbourne Hole eruption, aeolian and fluvial sediments were deposited throughout the area, including the interior of Kilboune hole, and these deposits mantle all of the older units (Figure 3).

4. Methodology

4.1 GPR Survey Design for Kilbourne Hole

In November 2014 we performed several initial GPR experiments at Kilbourne Hole using a 250-MHz Noggins Plus GPR unit to determine the radar wave velocity, sampling frequencies, gain, and filtering methods that would provide the best results. The GPR surveys to map the size distribution of volcanic block at Kilbourne Hole is possible because of the high electrical permittivity contrast between mafic volcanic blocks and the pyroclastic deposit. We also evaluated the electrical properties of the geologic materials at the survey sites in order to properly design the detailed GPR surveys that followed. We used these parameters in the processing of data from our GPR surveys to locate and determine the sizes of buried volcanic blocks.

Our approach to estimate the radar wave velocity of the pyroclastic deposit at Kilbourne Hole was to use a 250-MHz Noggins Plus GPR unit to acquire several GPR profiles over a 10-mm diameter and 30-cm long iron metal rod buried to a known depth of 0.45 m and then calculate the radar wave velocity using Equation (2). The rod was buried to a known depth of 0.45 m in the pyroclastic material at Kilbourne Hole. Because the rod has a large electrical permittivity (e > 100 F/m) and a high attenuation ratio (β > 1000 dB/m), radar waves are poorly transmitted though it and are instead directly reflected back to the GPR receiver. This produces a hyperbolic reflector in the resulting radargram (Figure 4). The apex of the hyperbolic reflector is located at the bottom of the buried metal rod. Using a modified exponential curve fitting routine (Milsom, 2003) in the *Ekko Pulse* software suite, we estimate the wave velocity in the pyroclastic deposits above the metal rod at Kilbourne Hole to be 0.13 m ns^{-1}.

This data for a known target also allowed us to determine the permittivity of the pyroclastic material at Kilbourne Hole. Using Equation (1), we calculate the electrical permittivity of the pyroclastic deposits at Kilbourne Hole to be ~2.2 F/m. This relatively low permittivity means that most of the GPR signal will not be propagated into the media, most signals will instead be scattered and some small signal attenuation may occur.

To make sure that the radar waves can reach the desired survey depth of more than 1m, we also must know the attenuation constant of the pyroclastic deposits. Empirically determined signal attenuation values were provided by previous workers (i.e., Ulaby et al., 1996; Davis and Annan, 1989; Milsom, 2003). For silty materials with permittivity of ~2.2 F/m, the attenuation rate (β) is between 100-300 dB/m. We did not perform a laboratory study to measure the attenuation rate of volcanic ash at Kilbourne Hole, but, by applying an AGC of 300 dB to the radargrams, we were able to regain the deeper part of the radargrams that previously before the data processing were too weak for photointerpretation. Based on the electrical properties of the geological material at Kilbourne Hole, the GPR receiver was set to sample at 1-ns intervals during data collection and data processing to retrieve the best quality GPR image. Using the Shannon-Nyquist theorem, we estimate the sampling frequency to be ~1000 MHz.

All GPR data was imported into and processed with the *Ekko Pulse* software suite to improve the quality of the resulting GPR radargram. The processing steps were: (1) temporal filtering (de-wowing) to increase contrast and sharpness; (2) stacking the returned signal to remove very low-frequency components; and (3) AGC (automatic gain control) at 300 dB to compensate for attenuation of the radar signal and to gain visibility

of the weak radargram trace. We stacked the arrival radar signal four times to eliminate background noise while maintaining the best image quality. The penetration depth of the 250-MHz instrument at Kilbourne Hole seen in the radargram was between ~2.54-3.58 m based on our field calculation using two way travel time of 0.13 ns/m. Our processed radargrams provide high-resolution images that allow us to identify and measure the sag features that are preserved in the tephra units at Kilbourne Hole.

4.2 Short GPR Surveys and Radargram Calibration

To learn how to recognize volcanic blocks and associated sags on our processed GPR images, we made GPR measurements over outcrops with exposed volcanic blocks and associated sags along 29 short (<10-m long) transects on the rim of Kilbourne Hole (Figure 5). These short profiles were collected in January 2013 and in January 2014 using a 250-MHz Noggins Plus GPR unit and the acquisition parameters and data processing workflow described in Section 4.1. The resulting radargrams were displayed with 2x vertical exaggeration at a scale of 1:39 and were manually photointerpreted to trace the locations of both sags and volcanic blocks (Figure 3).

By comparing the exposed outcrops to their GPR profiles, we found two prominent types of reflectors in the resulting radargrams (Figure 3). The first type (Type 1) includes strong, continuous, smooth, undulating reflectors that correspond to the horizontal layers in the pyroclastic flow deposits. Basaltic volcanic blocks appear as the second type of reflector (Type 2), which are very dim and weak. The basaltic volcanic blocks appear this way because they have higher permittivity due to their high iron and magnesium content (Russell et al., 2013) and, as a result, they attenuate the GPR signal.

These two distinctive types of reflectors allow us to discriminate volcanic blocks from sags on GPR profiles. Knowing what they look like we can measure the apparent widths of buried volcanic blocks and sags directly from GPR radargrams.

The remaining question, however, is the relationship between the apparent widths of these features on GPR radargrams and their actual widths. To answer this question, we compared the widths of exposed volcanic sags and blocks in the field to the apparent widths of the same features as observed on the GPR radargrams obtained from our short profiles. Because volcanic sags are wider at the top than at the bottom, an objective and consistent definition for width was needed. The width is defined as the length of the imaginary line drawn through the middle part of the sag between the top and the bottom of the sag and through the center of the volcanic block (Figure 4a). Using this definition, a calibrated screen ruler application (*Ruler 1.0* for Windows) was used to measure the apparent width of the sags identified in the short transect radargrams. The field measurements of the widths of the volcanic sags and blocks were obtained with a measuring tape using the same width definition used for measuring sags on the radargrams (Figure 4b). The uncertainty of these measurements both in the field and on the radargrams is 0.05 cm, which is the margin of error for the ruler. Other possible sources of error include human error and subjectivity when choosing points of measurement.

Because the Type 2 reflectors associated with volcanic blocks are difficult to interpret, we are unable to reliably identify blocks in the GPR radargrams and are therefore unable to accurately determine their widths using the GPR radargrams. However, the apparent widths of the Type 1 reflectors associated with sags can be

accurately measured on the radargrams and related to their actual widths as measured in the field. Based on the assumption (Walker and Croasdale, 1971) that the size of a sag is proportional to the size of the volcanic block that created it, we establish an empirical relationship between the widths of sags and the widths of volcanic blocks as they appear in the outcrop. With this intermediate step, we can then relate the widths of sags measured in GPR radargrams to the actual widths of the volcanic blocks that created them.

4.3 Long GPR Surveys at Kilboune Hole

In January 2012, January 2013, and January 2014, we collected GPR data along 6 long transects extending radially away from the rim of Kilbourne Hole in each cardinal direction (Figure 5). The transects varied in length from 250 m to 1,000 m, depending on accessibility, each extending a distance sufficient to include the entire area covered by the Kilbourne Hole pyroclastic deposits. We used the same 250-MHz Noggins Plus GPR equipment and the same GPR instrument parameters and processing steps described in Section 4.1. The purpose of GPR surveys on these long transects was to collect the sizes distribution of the volcanic blocks and sags that were buried within the pyroclastic deposits around the rim of Kilbourne Hole crater (Figure 6). The length of these long surveys line is long enough to reveal the changing trend in sizes of the volcanic blocks and sags.

4.4 Velocity at Impact of Volcanic Blocks

We calculate the impact velocity of a volcanic block from its size and location using Equation (4). The atmospheric density at the time of Kilbourne Hole eruption is unknown. We do know that the average Earth's atmospheric density at sea level is 1.225 kg/m^3 at 15 °C. However, during the Kilbourne Hole eruption, the atmosphere was mixed with the volcanic gas plume. As a result, it was hotter than the ambient atmosphere and was probably filled with volcanic particles. Steiner and Babenko (1978) observed that the atmospheric density of the volcanic gas in a Strombolian eruption can be as much as 4.7 kg/m^3, and Patrick (2007) modeled the density of the volcanic gas in a Plinian eruption to be >3.5 kg/m^3. Based on this, we chose a density of 4.7±1.2 kg m^{-3} to represent the atmospheric density at the time of Kilbourne Hole eruption. The impact velocity is then used to calculate the initial velocity when the gas and volcanic blocks were first released from the vent. The workflow of how to calculate the initial velocity of the gas and volcanic blocks from its impact velocity is shown in the following paragraph.

4.5 Initial Pressures of the Volcanic Vent

In the case of Kilbourne Hole, the initial gas pressure (P) was trapped under the weight of cap rocks before the rupture. The density of cap rocks is varied; we used a weighted average density of both Aden and Afton basalt (3,100 $kg.m^{-3}$) and the Camp Rice formation (2,160 $kg.m^{-3}$). At Kilbourne Hole ρ_d used in the initial pressure estimate (Equation (6)) is 2,164.7 $kg.m^{-3}$.

4.6 Initial Velocity of the Eruption Analysis

In addition to the size of the blocks, our GPR survey provides the lateral distance from the vent for each volcanic block we found. In order to apply Fagents and Wilson (1995)'s velocity model to retrieve the initial gas expansion velocity (Equation (3)), we convert lateral distance from the crater rim (in Cartesian coordinates (x, y)) into radial distance from the vent (in polar coordinates (r, θ)) (Figure 7). Assuming that the volcanic block is denser than the gas plume and was ejected following ballistic trajectories, the coordinate transformation from Cartesian coordinates to polar is given by:

$$r = \frac{\cos\theta}{x} \qquad (7),$$

where x is lateral distance between the volcanic block and crater rim, and r is a radial distance between the volcanic block and the vent. The location of the vent was estimated using a magnetic anomaly map of Kilbourne Hole (Rhodes and Hurtado, 2012; see Chapter 2). The vent is the location where an eruption was originated. The vent is later filled by fragments of the diatreme filling including highly brecciated pre-eruptive rocks, volcanic origin rocks, and post eruptive material. The vent of Kilbourne Hole is not seen on the surface, but the can be seen on the magnetic and gravity anomaly map of Kilbourne hole due to its unique magnetic susceptibility and density properties of vent filling material. We define that the present location of Kilbourne Hole's vent is where the body of diatreme filling material were buried near the center of Kilbourne Hole. The extensions of the diatreme filling normally are from the pre-eruption surfaces to the top of the volcanic dikes. Our magnetic model provides a best estimate depth to the top of the dikes (which is also the thickness of the diatreme filling body) to be 920 ± 120 m and the radius of the vent to be (349.5 ± 40 m) (Rhodes and Hurtado, 2012). In the radial

distance calculation in Equation (7) the top of the volcanic dikes at the depth of 920 ± 120 km is considered to be the center point of ejection or the beginning of the vent of the volcano. The radius of the vent is expected to be smaller than the radius of present day crater because of erosion; the radius of the present day crater is larger than radius of the vent at the time of eruption. We draw the best-fit circle that inscribes the present day crater rim (Figure 7) and use the radius of that circle as our estimate for the radius of the vent at the time of eruption. We use this radius to convert lateral distance from the crater rim to dropping locations of the volcanic blocks to radial distance from the center of the vent to dropping locations of the volcanic blocks (Figure 7 and Equation (7)).

A MATLAB code (Appendix A) was written to plot impact velocity versus radial distance and to fit the explosion model of Fagents and Wilson (1995) to the data using a least-squares regression (York, 1968; York, 2004). To do this, we first linearize Equation (3) to yield:

$$\log V_e = 2\log V_0 \frac{R_0}{R} - \frac{t}{\tau} \qquad (8).$$

If we assume that the ejected gas and pyroclastic material both have velocity V_0 at a distance $R = R_0$, we can write:

$$\log V_e = 2\log V_0 - \frac{t}{\tau} \qquad (9).$$

Given that: $Y = a + bX$ (10).

Then we can write: $Y = logV_e$ (11),

$$X = t = \frac{R}{v_e} \qquad (12)$$

$$a = 2logV_o \qquad (13)$$

$$b = -\frac{1}{\tau} \qquad (14)$$

By replacing the calculated flight time (t) (using Equation (12)) and the impact velocity of the volcanic block into Equation (10), we can determine V_0 and τ by from the linear regression coefficients *a* and *b* using Equation (13) and (14).

4.7 Gas to Rock Mass Ratio

To determine the gas-to-rock mass ratio of Kilbourne Hole eruption we plotted our derived initial velocity of the volcanic blocks (V_0) and the initial pressure (P) of the vent on Fagents and Wilson (1993) 's eruption model. The major application of this model is for the prediction of the amount of water vapor (gas) that was released considering the initial conditions in the vent (Initial pressure, initial velocity of the volcanic blocks). This eruption model only described the simplest behavior of the eruption ignoring the presence of wind shear or the formation of a convection cloud above the vent. This model can best explain the behavior of the larger size and more dense ejected material (e.g., millimeters size particles) and large volcanic blocks, which are demonstrably less affected by the atmosphere. This model can only provide rough result for smaller and less dense ejected material or the material that are more vulnerable to atmospheric motion inside the convection cloud.

According to this Fagents and Wilson (1993)'s eruption model, in transient explosions where there is some meteoric water is in addition to magmatic volatiles, gas to rock mass ratio of 0.01 to 0.1 (1 to 10 percent) is commonly involved in order to generate initial velocities of large volcanic blocks span values from a few tens of $m.s^{-1}$ to 400 $m.s^{-1}$. This amount of gas-to-rock mass ratio is also required the initial gas pressures inside

the vent to be significantly less than 40 MPa and to be consistent with the strengths of the cap rocks under which pressure accumulation occurs (Fudali and Melson, 1972).

The gas-to-rock mass ratio allows us to calculate the amount of gas (predominantly water vapor) in the system at the time of the eruption. To do this, we must estimate the mass of the rock fragments that may be released from the vent of Kilbourne Hole at the time of rupture. Assuming that all the cap rock was later removed and excavated from the crater as rock fragments, we can estimate that the mass of rock fragments equals to the mass of the cap rock. By cross multiplying the mass of rock fragments to the gas-to-rock mass ratio, we then can resolve for the mass of gas, hence groundwater that fed the Kilbourne Hole eruption.

4.8 Propagation of Uncertainties

All measurement of the width of the volcanic sags and blocks at Kilbourne Hole contains uncertainties from both the GPR instrument and from measurements apparatus. The entire model derived quantities such as locations, depths, width and length of volcanic vent and dikes used in our calculation contains uncertainty from both gravity and magnetic surveys at Kilbourne Hole. Because our final results (initial velocity, initial pressure, mass of water) are depends on these those mentioned quantities, we must propagate the uncertainties from those quantities into our final results (Ku, 1966; Taylor, 1997). We follow a standard rule of uncertainties propagation by Ku (1966) and Taylor (1997). The rules of error propagation used in this research are under an assumption that all quantities that contain errors are uncorrelated and random.

5. Results

Using the 250 MHz noggins GPR unit, we are able to image sags, volcanic blocks, and crossbedding within the pyroclastic deposit at Kilbourne Hole. The retrieved GPR images provide a great resolution of objects as small as ~25 cm and bedding as thin as ~10-20 cm. Our GPR surveys at Kilbourne Hole achieved penetration depths into the pyroclastic deposit of 2.45 m to 3.78 m at most survey localities. The radar propagation velocity in the pyroclastic deposits at Kilbourne Hole is ~0.11-0.13 m/ns. We found that the radar signal in the pyroclastic deposits at Kilbourne Hole dissipated quickly after a certain depth (~ 3-4 m.), which may be due the development of caliche-rich B soil horizons, which are common in arid environments (Tatum and Francke, 2012).

5.1 Relationship Between the Widths of Volcanic Sags Measured with GPR and Measured in the Field

We obtained 29 measurements of exposed volcanic sags and associated blocks from the short GPR surveys. We then plotted the volcanic sag width as measured from the radargrams ($\varphi_{sag,GPR}$) versus the actual width of the sag as measured in the field ($\varphi_{sag,field}$). Figure 8 shows a linear regression ($r^2 = 0.91$) through this data:

$$\varphi_{sag,GPR} = 0.9185\varphi_{sag,field} + 5.8529 \quad (15).$$

We used this relationship to correct our GPR measurements result to be as close as our field measurement results (Appendix A).

5.2 Relationship Between the Actual Widths of Volcanic Sags and Associated Volcanic Blocks

At the field locations of volcanic blocks and sags we performed 29 width measurements of exposed volcanic sags and associated blocks. We then plotted the actual width of the volcanic sags ($\varphi_{sag,field}$) versus the actual width of the volcanic blocks ($\varphi_{block,field}$). The result of this measurement provided statistical evidence that the width of the volcanic sags is highly depending on the width of the volcanic blocks. Figure 9 shows a linear regression (r^2 = 0.54) through this data:

$$\varphi_{sag,GPR} = 0.9185\varphi_{sag,field} + 5.8529 \quad (16).$$

5.3 Relationship Between the GPR Widths of Volcanic Sags and Associated Volcanic Blocks

Because the volcanic blocks at Kilbourne Hole are mostly ultramafic basalt, their high iron contents prevent our GPR radargrams from yielding a clear and bright reflector of volcanic blocks. By plotting the GPR width measurements of volcanic sags to the field width measurement of the volcanic blocks, we are able to establish a direct relationship that allow us to relate the width of volcanic sags to the width of the volcanic blocks that created the volcanic sags.

The resulting relationship between the GPR width of volcanic sags ($\varphi_{sag,GPR}$) measured from GPR radargrams and the actual width of volcanic blocks as measured in the field ($\varphi_{sag,field}$) shows a linear regression (r^2 = 0.43) (Figure10) as describe in the following equation:

$$\varphi_{blocks} = 0.1604\varphi_{sags\_GPR} + 22.273 \quad (17).$$

5.4 Volcanic Block Size Distributions From Long GPR Transects at Kilbourne Hole

We collected a total of six long GPR surveys lines extended approximately ~ 600-1000 m long radially from the crater rim. We are able to detect and visualize volcanic sag features along those surveys ling. The length of the long survey line provides us the opportunity to recognize the distribution trend of the volcanic sags size. On the processed GPR radargrams, we measured the width of the volcanic sags found buried along the survey lines. We calibrated the volcanic sag width measurements from the GPR to its filed width using Equation (16). We converted the calibrated width of the volcanic sags into the width of the volcanic blocks that created the sags using Equation (16). Using the width of the volcanic blocks obtained from Equation (17), we calculated the impact velocity of the volcanic blocks at the dropping location using Equation (4). The lateral distance of the volcanic blocks and sags locations from the crater rim were also converted into its radial distance from the center of the vent using Equation (7). The volcanic blocks width and calculated radial distance are shown in Table 2 and Appendix A. We then plotted the result of volcanic blocks widths to its radial locations (Figure 10) and we then applied the Fagents and Wilson (1995) eruption velocity model to our results (Equation (3)). Figure 10 shows an example using data plot from long survey line 3. The data plots from other five long survey lines are included in Appendix B. Figure 11 shows calculated impact velocity of the volcanic blocks found along the survey line 3 plotted against radial distance from the crater rim. Figure 11 shows a negative exponential trend, which indicates that the gas expansion velocity decreases as the distance from the center of the eruption increases.

5.5 Initial Gas Expansion Velocity and Initial Pressure of the Vent

The York's least square regression between the result of volcanic blocks widths measurement and radial distance of the volcanic blocks and the Fagents and Wilson (1995) eruption velocity model (Figure 12), yields us two results: the initial gas expansion velocity (*Vo*) and the time constant of the gas expansion phase (*t*). The initial gas expansion velocity (*Vo*) and the time constant of the gas expansion phase (*t*) results retrieved from each of the six long GPR transects are listed in Table 3. Each result for *Vo* and for *t* are including their propagated uncertainties from each measurements and initial input data. We average results from all six long GPR transects to yield an average *Vo* of 123 ± 9 m s^{-1}; and an average *t* of 92 ± 11 s. With the now known initial velocity of the gas expansion, we can calculate the initial pressure inside the orifice using the modified Bernoulli equation (Equation (6)). The initial pressure inside of the vent prior to the eruption was 163 ± 9 bar.

5.6 Gas-to-Rock Mass Ratio and Groundwater in Kilbourne Hole Eruption

We applied our initial velocity of the volcanic blocks and initial pressure of the vent results to the theoretical models of phreatomagmatic explosions by Fagents and Wilson (1993) to determine the gas-to-rock mass ratio of Kilbourne Hole eruption (Figure 12). By plotting our results to the model, we predict that the gas (m_g)-to-rock (m_s) mass ratio during the Kilbourne Hole eruption was 1 – 2 % (0.01-0.02)(Figure 13).

Using this gas-to-rock mass ratio and the estimated masses of ejected rock fragments from the vent of Kilbourne Hole at the time of rupture, we were able to calculate the amount of gas (predominantly water vapor) in the system at the time of the

eruption. By assuming that the mass of rock fragments equals to the mass of the cap rock, we estimated that the mass of rock fragments release from the vent of Kilbourne Hole at the time of eruption contains ~15 ± 5 m thick of Aden and Afton basalt (Seager, 1984) and approximately 920 ± 120 m of the Camp Rice formation (Rhodes and Hurtado, 2012). The thickness of Camp Rice formation material that may be ejected as rock fragments is considered to be equivalent to the thickness of Camp Rice formation from the pre-eruptive surfaces to the top of the upper most dike appeared on our gravity and magnetic model of Kilbourne Hole (Rhodes and Hurtado, 2012). Also from our gravity and magnetic model of Kilbourne Hole (Rhodes and Hurtado, 2012), we estimated the radius of the cap rock (R_d) to be ~349.8 ± 40 m. The volume of the cap rock was calculated assuming a cylindrical shape and an average weighted density of the basalt and the Camp Rice formation of 2,175.32 kg m^{-3} using this equation:

$$vol = \pi R_d^2 h \qquad (18).$$

This gives a volume of 3.54 ± 0.46 x 10^8 m^3 and a mass of 7.69 ± 1.00 x 10^{11} kg cap rock. For a gas-to-rock mass ratio of 0.01, this yields 7.7 ± 1.0 x 10^9 kg of water vapor. For a gas-to-rock mass ratio of 0.02, this yields 14.1 ± 2.0 x 10^9 kg of water vapor

6. Discussion

6.1 Assessment of Radar Properties Kilbourne Hole and Mars-Analog Phreatomagmatic terrains

Our GPR data of Kilbourne Hole suggest GPR method is a suitable for subsurface imaging on pyroclastic flow deposit and probing basaltic volcanic blocks. The geological setting of Kilbourne Hole locating in Chihuahua desert also yields similar site conditions (e.g., high aridity) to Mars Home plate. We found that the permittivity of the pyroclastic deposits at Kilbourne Hole is ~2.2 F/m with an attenuation constant of ~100-300 dB. Picardi et al (2004) using a 2 MHz-SHARAD data and found that an average electrical permittivity of the Martian regolith is ~6 F/m with an attenuation constant as low as ~30-50 dB. Vaucher et al. (2009) tested two volcanic ash units and a basaltic lava flow in Elysium Planitia using data from SHARAD. The electrical permittivity of the basaltic lava flow is ~ 8.8 ± 1.0. The Martian subsurface has higher electrical permittivity and lower attenuation rate than at Kilbourne Hole. Based on these estimates, the Martian subsurface is suitable for using GPR method. It is likely to be able to obtain better radargrams and deep radar penetration ranges on Mars than at Kilbourne Hole using similar equipment and survey design. Our GPR result at Kilbourne Hole agrees with Stillman and Olhoeft (2006)'s suggestion that the lack of liquid water and its associated low conductivity in the Martian subsurface should result in a good GPR environment. Even though Heggy et al. (2006) and Olhoeft (2003) pointed out that the iron oxide rich Martian subsurface could attenuate the GPR signal propagation, we do convince that that high electrical permittivity of Mars surfaces (~3 times higher than Kilbourne Hole

surface) should overcome the radar attenuation due to dielectric and magnetic losses from iron oxide rich subsurface materials.

6.2 Assessment of GPR Image Quality at Kilbourne Hole and Mars-Analog Phreatomagmatic terrains

With our GPR radargrams, we were able to image three distinct volcanic features: (1) sags; (2) volcanic blocks; and (3) cross-bedding in pyroclastic deposits. The image of volcanic blocks, however, is dimmed and not as bright as other image's reflectors. Using 250 MHz frequency GPR unit, we achieved 2.54-3.68 m penetration depth and 0.25 m resolution. We are able to image sags as small as 25 cm wide and pyroclastic layers as thin as 25 cm. For comparison, in Figure 14 we show volcanic sags and volcanic blocks features at Kilbourne Hole in comparison to Home Plate. It is obvious that Martian volcanic blocks and volcanic sags are identical to the same features at Kilbourne Hole but may be smaller in sizes. One volcanic block identified at Home Plate on Mars is 3.8 cm wide (Lewis et al., 2008) (Figure 14). Our results also demonstrate a used of medium frequency GPR in mapping mafic volcanic blocks, and alkaline pyroclastic deposit that contain significant amount of calcium rich top soil. We suggest that 250 MHz is the most suitable frequency to perform a GPR survey on Mars Home Plate considering the geological setting and the size of volcanic bocks and sags we imaged. We may need to consider a higher frequency GPR on Mars in order to increase the survey resolution so that we can detect smaller sizes volcanic blocks (Lewis et al., 2008). Therefore we suggest that a similar GPR survey could be conducted on either a robotic or human exploration mission to study features such as Home Plate on Mars.

6.3 Kilbourne Hole Eruption

Our model velocity model indicates that after the rupture of the cap rocks, rock fragments and gas were expanded from the vent at the initial velocity of ~113-132 m s^{-1}. These initial velocities of the volcanic blocks are consistent with observations of historical eruptions (e.g., Iguchi et al., 1983; Ishihara, 1985, 1990; Morrissey and Mastin, 2000; Parfitt and Wilson, 2008) and empirical calculations of the dispersal of large clasts by Fagents (1993) and Fagents and Wilson (1993). Observed at Sakurajima volcano in Japan in 1982-1987, the initial velocities of volcanic blocks were estimated to be 110-240 m s^{-1} (Iguchi et al., 1983; Ishihara, 1985, 1990). Observed at Shinmoedake volcano in Kyushu, Japan on February 1, 2011**,** the initial velocity of volcanic blocks was 240-290 m s^{-1} (Maeno et al., 2013). Our calculation based on estimated strength and thickness of cap rock indicates that the initial pressure of the vent before the rupture of Kilbourne Hole was 163 ± 9 bar and that expansion event of the rupture lasted 92 ± 11 s after initiation. Observed during its two-day eruption event, the maximum time duration of the gas fexpansion at Usu volcano was 97.5 s during these two days (Yokoo, 2002).

6.4 Paleohydrological Interpretation of Kilbourne Hole

Following the eruption model proposed by Fagents and Wilson (1993), we plotted the range of obtained initial velocity of the volcanic blocks and the initial pressure of the vent on the model (Figure 15). Fagents and Wilson (1993)'s eruption model indicates that Kilbourne Hole eruption was supplied by the gas-to-rock mass ratio at 0.01-0.02 (1-2%). These results are adjacent to the other observations of recent phreatomagmatic volcanoes.

The observation at Ngauruhoe where at the time of its eruption has the initial pressures of 1 to l0 MPa and the initial velocities of the ejected volcanic blocks were 220 to 250 m s^{-1}. The eruption was estimated to have gas-to-rock mass ratio of 2-6% and have sent a 0.8 m volcanic blocks to the distance as far as 2.5 km. Another observation from the Ukinrek Maars eruption, were the initial pressure and the initial velocity of the volcanic blocks that are larger than 2 m in size at the time of eruption are 0.1 to 5 MPa and 82 to 85 m s^{-1}**,** yield gas-to-rock mass ratio of 1-5%.

Our results are still problematic, however, because the presence of tuff ring and abundant accretion lapilli in pyroclastic deposits at Kilbourne Hole suggests a wet eruption. In general, the porosity of consolidated sand, which is a typical aquifer material in Rio Grande basin, is 22% (Crilley et al., 2013). Assuming that the Kilbourne Hole groundwater reservoir was fully saturated at the time of the eruption, the explanation for this low percent of water we can suggest is that our estimated dry eruption at Kilbourne Hole is not representative of the entire eruption, but only the last stage of the eruption, where the previous eruption had depleted the majority of the water resources.

Additional explanation is that Fagents and Wilson (1993)‘s eruption model provided usually much smaller gas to rock mass ratio than values estimated by previous workers (Fudali and mason, 1972; Self et al., 1979; Wohletz, 1986). Fagents and Wilson (1993) discussed the limitation of their model that it can best explain the eruption phenomenon of coarse grain ejecta (>1 mm) or volcanic blocks because their velocity model did not considering the turbulent movement inside the eruption gas plume. Hence the model result on large volcanic block is more reliable for it has sufficient mass to not be effected by the turbulent or side way movement of the gas cloud. However, Wood

(1995) pointed out that the result on large volcanic blocks may not be more relaible because when large volcanic blocks are ballistic dispersed with other rock fragments, the heat cannot be transferred from the volcanic blocks to the gas in the timescale of an explosion (Woods, 1995). Therefor large size volcanic blocks do not remain in thermal equilibrium with the gas, thus leading to significantly lower velocities and temperatures than predicted by an equilibrium model (Wood, 1995).

It must be noted that the penetration depth of our GPR radar is ~2.54-3.58 m and that the volcanic blocks we detected are located at depths shallower than that. Our survey may have missed larger volcanic blocks (~> 2m diameter) that may have been deposited deeper in the pyroclastic deposits. Those deeper volcanic blocks may represent earlier phases of the eruption. It is possible that by the last stage of the eruption, the water source may have already been depleted and the magma source may have lost a substantial amount of internal heat energy. Both of these would lower the eruption efficiency in a manner consistent with our results while also explaining why the geology of the pyroclastic deposits at Kilbourne Hole is consistent with an overall wet eruption.

7. Conclusion

The phreatomagmatic activities suggested that ancient Mars was warm, wet, and dynamically active. Understanding past phreatomagmatic activity on Mars can potentially provide us with information about the ancient Martian hydrosphere. Not only does a phreatomagmatic volcano confirm the existence of an external source of water, but it also provides information of how Martian groundwater, surface water, and magmatic sources interacted. We conducted a geophysical survey at Kilbourne Hole, a well-known phreatomagmatic volcano in New Mexico, using GPR to demonstrate the use phreatomagmatic volcanic features as paleohydrological proxies. Our GPR surveys revealed buried volcanic sags and volcanic blocks around Kilbourne Hole. By measuring the size distribution of volcanic blocks as a function of distance from Kilbourne Hole, we determined the initial gas expansion velocity during the eruption to be 123 ± 9 m s^{-1} and the time duration of the entire gas expansion phase to be of 92 ± 11 s. The initial pressure prior to the eruption was calculated to be 163 ± 9 bars. The length of time duration of the gas expansion phase is a good indicator about the groundwater reservoir that fed the eruption. The better the groundwater hydraulic flow, the longer the steam is continuing to release. The initial pressure of the eruption is an implication to the depth of eruption center, depth of groundwater level, and the type of groundwater reservoir at the time of eruption. In the case of a phreatomagmatic eruption like Kilbourne Hole, the eruption is originated at the contact zone between magma and groundwater reservoir. Therefor we can consider that the depth of eruption is roughly the paleo-groundwater level. In time duration of gas expansion at Kilbourne Hole may not be

a good representative of the entire eruption because we can only detect the velocity of volcanic blocks that dropped at the shallow depth (< 2.54 m).

Our results show that low-frequency GPR (250 MHz) has the potential to probe the shallow subsurface to depths of 2.34 to 3.58 m in arid, volcanic terrain. The setting we used to processing our GPR data helped improve the interpretability of our GPR images and can be used as a guideline to design a GPR survey on Mars Home Plate. The geological and geophysical setting of Home Plate is similar to what we observe at Kilbourne Hole, NM (e.g., cross-bedded pyroclastic flow deposit, basalt flow deposit, volcanic blocks and sags features, size of volcanic blocks and thicknesses of their ash bed). Therefore, we suggest that a similar GPR survey could be conducted on either a robotic or human exploration mission to study features such as Home Plate on Mars. The results could be used to reveal important paleohydrologic conditions of ancient Mars. It is also appears on several researches that different volcanic deposits with different characteristics can interact with the radar beam differently (e.g. Haggy et al., 2007) and further laboratory study on the electrical properties of Martian volcanic deposit may be needed in order to design GPR surveys for Mars. In conclusion we provided here a quantitative paleohydrogeological interpretation from our GPR surveys and a survey approach to perform a GPR survey on a terrestrial volcanic setting. Our research strongly supports the idea that we can use GPR surveys to study paleohydrogeologic conditions on Mars.

References

Abrams, L. J. and Sigurdsson, H., 2007, Characterization of pyroclastic fall and flow deposits from the 1815 eruption of Tambora volcano, Indonesia using ground-penetrating radar: *Journal of Volcanology and Geothermal Research*, vol. 161, no. 4, p. 352-361.

Arcone, S. E., Prentice, M. L., and Delaney, A. J., 2002, Stratigraphic profiling with ground-penetrating radar in permafrost. A review of possible analogs for Mars: *Journal of Geophysical Research*, vol. 107 (E11), p. 5108.

Barberi, F., Navarro, J. M., Rosi, M., Santacroce, R., and Sbrana, A., 1988, Explosive interaction of magma with ground water: Insights from xenoliths and geothermal drillings: *Rendiconti della Societa Itaiana di Mineralogia e Petrologia*, vol. 43, no. 4, p. 901-926.

Barone, P. M., Graziano, F., Pettinelli, E., and Corradini, R. G., 2007, Ground‐penetrating radar investigations into the construction techniques of the Concordia Temple (Agrigento, Sicily, Italy): *Archaeological Prospection*, vol. 14, no.1, p. 47-59.

Bear, J., 2013, *Dynamics of Fluids in Porous Media*: Courier Corporation (New York), 747 p.

Beres, M. and Haeni, F. P., 1991, Application of Ground‐Penetrating Radar Methods in Hydrogeologic Studies: *Groundwater*, vol. 29, no. 3, p. 375-386.

Crilley, D. M., Matherne, A. M., Thomas, N., and Falk, S. E., 2013, Seepage investigations of the Rio Grande from below Leasburg Dam, Leasburg, New

Mexico, to above American Dam, El Paso, Texas, 2006–13: *U.S. Geological Survey Open-File Report 2013–1233*, 34 p.

Chouet, B., Hamisevicz, N., and McGetchin, T. R., 1974, Photoballistics of volcanic jet activity at Stromboli, Italy: *Journal of Geophysical Research*, vol. 79, no. 32, 4,961-4,976, doi:10.1029/JB079i032p04961.

Conyers, L. B., 1995, The use of ground‐penetrating radar to map the buried structures and landscape of the Ceren site, El Salvador: *Geoarchaeology*, vol. 10, no. 4, p. 275-299.

Conyers, L. B. and Connell, S., 2007, The applicability of using ground-penetrating radar to discover and map buried archaeological sites in Hawaii: *Hawaiian Archaeology Journal*, vol. 11, p. 62-77.

Comas, X., Slater, L., and Reeve, A., 2007, In situ monitoring of free‐phase gas accumulation and release in peatlands using ground penetrating radar (GPR): *Geophysical Research Letters*, vol. 34, no. 6, p. 1-5.

Davis, J. L. and Annan, A. P., 1989, Ground Penetrating Radar For High Resolution Mapping of Soil and Rock Stratigraphy 1: *Geophysical Prospecting*, vol. 37, no. 5, p. 531-551.

Dobrin, M. B. and Savit, C. H., 1988, *Introduction to Geophysical Prospecting*: McGraw-Hill Book Co. (New York), 867 p.

Domenico, P.A. and F. W. Schwartz, 1990, *Physical and Chemical Hydrogeology*: John Wiley & Sons (New York), 824 p.

Ebinger, C. J., van Wijk, J., and Keir, D., 2013, The time scales of continental rifting: Implications for global processes, *in* Bickford, M.E. (ed.), *The Web of Geological*

Sciences: Advances, Impacts, and Interactions (Geological Society of America Special Paper vol. 500), p. 371-396.

Ennis, M. E., Schmidt, M. E., McCoy, T., Farrand, W., and Cabrol, N., 2007, Hydrovolcano on Mars? A comparison of Home Plate, Gusev Crater and Zuni Salt Lake Maar, New Mexico: *Proceedings of the 38th Lunar and Planetary Science Conference*, vol. 38, p. 1,966.

Ezell, E. C., and Ezell, L. N., 2013, *On Mars: Exploration of the Red Planet, 1958-1978--The NASA History*: Courier Corporation (New York), 415 p.

Fagents, S. A. and Wilson, L., 1993, Explosive volcanic eruptions - VII: The ranges of pyroclasts ejected in transient volcanic explosions: *Geophysical Journal International*, vol. 113, no. 2, p. 359-370.

Frenzel, P. F., 1992, Simulation of Ground-Water Flow in the Mesilla Basin, Dona Ana County, New Mexico, and El Paso County, Texas: *USGS Water Resources Investigation Report 91-4155*, 151 p.

Grant, J. A., and Schultz, P.E., 1992, Ground penetrating radar as a tool for investigating near-surface stratigraphy on Mars: *Lunar and Planetary Institute Technical Report 92-07*, p. 5-7.

Grimm, R. E., 2003, A comparison of time domain electromagnetic and surface nuclear magnetic resonance sounding for subsurface water on Mars: *Journal of Geophysical Research*, vol.108 (E4), p. 8037.

Grimm, R. E., Heggy, E., Clifford, S., Dinwiddie, C., McGinnis, R., and Farrell, D., 2006, Absorption and scattering in ground‐penetrating radar: Analysis of the Bishop Tuff: *Journal of Geophysical Research*, vol. 111 (E6), p. 1-15.

Grote, K., Hubbard, S., and Rubin, Y, 2003, Field‐scale estimation of volumetric water content using ground‐penetrating radar ground wave techniques: *Water resources research*, vol. 39 (11), p. 1,321-1,333.

Hamran, S. E., Berger, T., Brovoll, S., Damsgard, L., Helleren, O., Oyan, M. J., and Eide, J., 2015, RIMFAX: A GPR for the Mars 2020 rover mission: *Advanced Ground Penetrating Radar (IWAGPR), 2015 8th International Workshop,* vol.8, p. 1-4.

Hawley, J. W., 1975, Quaternary history of Dona Ana country region, south-central New Mexico, *in* Seager, W. R., Clemons, R. E., and Callender, J. F. (eds.), *New Mexico Geological Society 26th Annual Fall Field Conference Guidebook,* p. 139-150.

Heiken, G. and Wohletz, K., 1985, *Volcanic Ash*: University of California Press (Berkeley, CA), 246 p.

Head, J. W. and Wilson, L., 2003, Deep submarine pyroclastic eruptions: theory and predicted landforms and deposits: *Journal of Volcanology and Geothermal Research*, vol. 121, no. 3, p. 155-193.

Heggy, E., Clifford, S. M., Grimm, R. E., Dinwiddie, C. L., Wyrick, D. Y., and Hill, B. E., 2006, Ground‐penetrating radar sounding in mafic lava flows: Assessing attenuation and scattering losses in Mars‐analog volcanic terrains: *Journal of Geophysical Research: Planets (1991–2012)*, vol. 111 (E6). p.E06S04-1-E06S04-16.

Hobbs, S.W., Paull, D.J., Clarke, J.D.A. and Roach, I.C., 2015, Multi-agent gully processes: Evidence from the Monaro Volcanic Province, Australia and Noachis Terra, Mars. *Geomorphology*, In press.

Hoffer, J. M., 1971, Mineralogy and petrology of the Santo Tomas-Black Mountain basalt field, Potrillo volcanic, south-central New Mexico: *Geological Society of America Bulletin*, vol. 82, no. 3, p. 603-612.

Iguchi, M., Ishihara, K., and Kamo, K., 1983, On ejection velocity and pressure of volcanic explosion reduced from photo-trajectory of volcanic bombs: *Annual Disaster Prevention Research Institute, Kyoto Univ*ersity, vol. 26, p. 9-21.

Isac, A., Mandea, M., Purucker, M., Langlais, B., 2015 (in press), A comparative analysis of the magnetic field signals over impact structures on the Earth, Mars and the Moon: *Advances in Space Research*.

Ishihara, K., 1985, Stability of natural deposits during earthquakes: *Proceedings of the 11th International Conference on Soil Mechanics and Foundation Engineering, San Francisco*, p. 321-376.

Ishihara, K., 1990, Pressure sources and induced ground deformation associated with explosive eruptions at an andesitic volcano: Sakurajima volcano, *in* M.P. Ryan (ed.), *Magma Transport and Storage*: John Wiley (Chichester, U. K.), p.335-356. Ingersoll, R. V., 2001, Structural and stratigraphic evolution of the Rio Grande Rift, northern New Mexico and southern Colorado: *International Geology Review*, vol. 43, no. 10, p. 867-891.

Keller, G. R., Morgan, P., and Seager, W. R., 1990, Crustal structure, gravity anomalies and heat flow in the southern Rio Grande rift and their relationship to extensional tectonics: *Tectonophysics*, vol. 174, no. 1, p. 21-37.

Kobayashi, T., Lee, S. W. R., Kumamoto, A., and Ono, T., 2014, GPR observation of the Moon from orbit: Kaguya Lunar Radar Sounder: *Proceeding of the 15th International Conference on Ground Penetrating Radar (GPR)*, p. 1,037-1,041.

Koelle, H. H. (Ed.), 1961, *Handbook of astronautical engineering*: McGraw-Hill (New York), p. 28-10.

Ku, H.H., 1966. Notes on the use of propagation of error formulas. *Journal of Research of the National Bureau of Standards*, vol. 70. No. 4.

Leuschen, C., P. Kanagaratnam, K. Yoshikawa, S. Arcone, and P. Gogineni., 2003, Design and field experiments of a ground-penetrating radar for Mars exploration: Geophysical detection of surface water on Mars: *Journal of geophysical research*, vol. 108 (E4), p. GDS15-1.

Lewis, K. W., Aharonson, O., Grotzinger, J. P., Squyres, S. W., Bell, J. F., Crumpler, L. S. and Schmidt, M. E., 2008, Structure and stratigraphy of home plate from the spirit mars exploration rover: *Journal of Geophysical Research*, vol. 113 (E12), p. E12S36-1- E12S36-16.

Lipman, P. W., Steven, T. A., and Mehnert, H. H., 1970, Volcanic history of the San Juan Mountains, Colorado, as indicated by potassium–argon dating: *Geological Society of America Bulletin*, vol. 81, no. 8, p. 2,329-2,352.

Maeno, F., Nakada, S., Nagai, M., and Kozono, T., 2013, Ballistic ejecta and eruption condition of the vulcanian explosion of Shinmoedake volcano, Kyushu, Japan on 1 February 2011: *Earth Planets Space*, vol. 65, no. 6, p. 609-621.

Manga, M., Patel, A., Dufek, J. and Kite, E.S., 2012. Wet surface and dense atmosphere on early Mars suggested by the bomb sag at Home Plate, Mars: *Geophysical Research Letters*, vol. 39, no. 1, p. 7,005.

Marra, W.A., 2015, Martian groundwater outflow processes and morphology: reconstruction of paleohydrology using landscape evolution experiments [Ph.D. thesis]: *Utrecht Studies in Earth Sciences*, 81 p.

Milsom, J., 2007, *Field Geophysics*: John Wiley and Sons (University College London), 249 p.

Morrissey, M. M., and Mastin, M.J., 2000, Vulcanian eruptions, *in* H. Sigurdsson (ed.), *Encyclopedia of Volcanoes*: Academic Press (San Diego, CA), p. 463-475.

Mouginis-Mark, P. J., 1985, Volcano/ground ice interactions in Elysium Planitia, Mars: *Icarus*, vol. 64, no. 2, p. 265-284.

Neal, A., 2004, Ground-penetrating radar and its use in sedimentology: Principles, problems and progress: *Earth Science Reviews*, vol. 66, no. 3, p. 261-330.

Nieto, C. E., and Stewart, R. R., 2003, Geophysical investigations at a Mars analog site: Devon Island, Nunavut: *Mars Polar Science Conference*, vol. 3, p. 8,115.

Olhoeft, G.R., 2003, Subsurface Exploration for Water on Mars: *Proceeding of the 6th International Conference on Mars*, p. 3,213.

Picardi, G., Biccari, D., Seu, R., Marinangeli, L., Johnson, W. T. K., Jordan, R. L., and Zampolini, E., 2004, Performance and surface scattering models for the Mars Advanced Radar for Subsurface and Ionosphere Sounding (MARSIS): *Planetary Space Science*, vol. 52, p.149.

Parfitt, L. and Wilson, L., 2009, *Fundamentals of Physical Volcanology*: John Wiley & Sons (Oxford, UK), 252 p.

Reiche, P., 1940, The origin of Kilbourne Hole, New Mexico: *American Journal of Science*, vol. 238, no. 3, p. 212-225.

Rhodes, N. and Hurtado, J. M. (Jr.), 2012, A Magnetic Survey of Kilbourne Hole, Southern New Mexico: Implications for Near Surface Geophysical Exploration of Mars and the Moon: *Proceedings of the 43rd Lunar and Planetary Science Conference*, vol. 43, p. 2914.

Russell, P. S., Grant, J. A., Williams, K. K., Carter, L. M., Garry, W. B., and Daubar, I. J., 2013, Ground penetrating radar geologic field studies of the ejecta of Barringer Meteorite Crater, Arizona, as a planetary analog: *Journal of Geophysical Research*, vol. 118, no. 9, p. 1,915-1,933.

Russell, J.K. and Stasiuk, M.V., 1997, Characterization of volcanic deposits with ground-penetrating radar: *Bulletin of Volcanology*, vol. *58*, no. 7, p. 515-527.

Self, S., Wilson, L., and Nairn, I. A., 1979, Vulcanian eruption mechanisms: *Nature*, vol. 277, no. 5696, p. 440-443.

Seager, W. R., 1987, Caldera-like collapse at Kilbourne Hole maar, New Mexico: *New Mexico Geology Science and Service*, vol. 9, no. 4, p. 69-73.

Sparks, R. S. J., 1997, Causes and consequences of pressurization in lava dome eruptions: *Earth and Planetary Science Letters*, vol. 150, no. 3, p. 177-189.

Squyres, S. W., Aharonson, O., Clark, B. C., Cohen, B. A., Crumpler, L., De Souza, P. A., Farrand, W.H., Gellert, R., Grant, J., Grotzinger, J.P., Haldemann, A. F. C., Johnson, J. R., Klingelhofer, G., Lewis, K. W., Li., R., McCoy, T., McEwen, A.

S., McSween, H. Y., Ming, D. W., Moore, J. M., Morris, R. V., Parker, T. J., Rice Jr., J. W., Ruff., S., Schmidht, M., Schroder, C., Soderblom, L. A., and Yen, A., 2007, Pyroclastic activity at home plate in Gusev Crater, Mars: *Science*, vol. 316, no. 5,825, p. 738-742.

Steinberg, G. S. and Babenko, J. I., 1978, Experimental velocity and density determination of volcanic gases during eruption: *Journal of Volcanology and Geothermal Research*, vol. 3, no. 1, 89-98.

Stillman, D., and Olhoeft, G., 2008, Frequency and temperature dependence in electromagnetic properties of Martian analog minerals: *Journal of Geophysical Research: Planets (1991–2012)*, vol. 113(E9). P. E09005-1-E09005-14.

Seu, R., Phillips, R. J., Biccari, D., Orosei, R., Masdea, A., Picardi, G., and Nunes, D. C., 2007, SHARAD sounding radar on the Mars Reconnaissance Orbiter: *Journal of Geophysical Research*,vol. 112 (E5), p. E05S05-1–E05S05-18.

Taylor, J.R., 1997, Introduction to error analysis, the study of uncertainties in physical measurements (Volume 1), *2nd Ed.*: University Science Books (New York**),** 327 p.

Tatum, D. and Francke, J., 2012, Radar suitability in aeolian sand dunes: A global review: *Proceedings of the 14th* Ground *Penetrating Radar (GPR) International Conference,* p. 695-700.

Thomson, L. I., Osinski, G. R., and Pollard, W. H., 2012, The dielectric permittivity of terrestrial ground ice formations: Considerations for planetary exploration using ground‐penetrating radar: *Journal of Geophysical Research*, vol. 117 (E9), p. 1-10.

Ulaby, F. T., Dubois, P. C., and van Zyl, J., 1996, Radar mapping of surface soil moisture: *Journal of Hydrology*, vol. 184, no. 1, p. 57-84.

Walker, G. P. L. and Croasdale, R., 1971, Characteristics of some basaltic pyroclastics: *Bulletin Volcanologique*, vol. 35, no. 2, p.303-317.

Walker, G.P.L., 1973, Explosive Volcanic Eruptions: A new classification scheme: *Geologische Rundschau*, v. 62, p. 431-446.

Wilson, L., 1972, Explosive volcanic eruptions-II the atmospheric trajectories of pyroclasts: *Geophysical Journal International*, vol. 30, no. 4, p. 381-392.

Wilson, L., 1980, Relationships between pressure, volatile content and ejecta velocity in three types of volcanic explosion: *Journal of Volcanology and Geothermal Research*, vol. 8, no. 2, p. 297-313.

Williams, D. R., 2015, *Earth Fact Sheet*. Retrieved March 1, 2015 from http://nssdc.gsfc.nasa.gov/planetary/factsheet/earthfact.html.

Walker, G. P. L., Wilson, L., and Bowell, E. L. G., 1971, Explosive Volcanic Eruptions-I The Rate of Fall of Pyroclasts: *Geophysical Journal International*, vol. 22, no.4, p. 377-383.

Wilson, L. and Head, J. W., 2004, Evidence for a massive phreatomagmatic eruption in the initial stages of formation of the Mangala Valles outflow channel, Mars: *Geophysical Research Letters*, vol. 31, no. 15, p. 1-4.

White, J. D. L. and Ross, P. S., 2011, Maar-diatreme volcanoes: A review: *Journal of Volcanology and Geothermal Research*, vol. 201, no.1, p. 1-29.

Wright, J.V., Smith, A.L., and Self, S., 1980, A Working Terminology of Pyroclastic Deposits: *Journal Volcanology and Geothermal Research*, v. 8, p. 315-336.

Wohletz, K. and Heiken, G., 1992, *Volcanology and Geothermal Energy*: University of California Press (Berkeley, CA), 432 p.

Wohletz, K. H. and Sheridan M. F., 1981, Rampart crater ejecta: experiments and analysis of melt-water interactions: *Reports of the Planetary Geology Program 1980-1981 (NASA Technical Memo 82385)*, p. 134-135.

Wohletz K.H and Sheridan M.F., 1982, Melt-water interactions: Series II experimental design: *Reports of the Planetary Geology Program 1981-1982 (NASA Technical Memo 84211)*, p. 169-171.

Wohletz, K. H. and Sheridan, M. F., 1983, Hydrovolcanic explosions; II, Evolution of basaltic tuff rings and tuff cones: *American Journal of Science*, vol. 283, no. 5, p. 385-413.

Wohletz, K. H., Sheridan, M. F., and Brown, W. K., 1989, Particle Size Distributions and the Sequential Fragmentation/Transport Theory Applied to Volcanic Ash: *Journal of Geophysical Research*, vol. 94 (B11), p. 15,703-15,721.

Wright, J. V., Smith, A. L., and Self, S., 1980, A working terminology of pyroclastic deposits: *Journal of Volcanology and Geothermal Research*, vol. 8, no. 2, p. 315-336.

Yilmaz, Ö., 1989, Velocity-stack processing: *Geophysical Prospecting*, vol. 37, no. 4, p. 357-382.

York, D., 1968, Least squares fitting of a straight line with correlated errors: *Earth and Planetary Science Letters*, vol. 5, p. 320-324.

York, D., Evensen, N. M., Martınez, M. L., and Delgado, J. D. B., 2004, Unified equations for the slope, intercept, and standard errors of the best straight line: *American Journal of Physics*, vol. 72, no. 3, p. 367-375.

Yokoo, A., Taniguchi, H., Goto, A., and Oshima, H., 2002, Energy and depth of Usu 2000 phreatic explosions: *Geophysical Research Letters*, vol. 29, no. 24, p. 48-51.

Zimanowski, B., Wohletz, K., Dellino, P., and Büttner, R., 2003, The volcanic ash problem: *Journal of Volcanology and Geothermal Research*, vol. 122, no. 1, p. 1-5.

Zimanowski, B., Fröhlich, G., and Lorenz, V., 1995, Experiments on steam explosion by interaction of water with silicate melts: *Nuclear Engineering and Design*, vol. 155, no. 1, p. 335-343.

Table 1. List of physical parameters.

Variables	Units	Descriptions
E_k	J	Kinetic energy of the eruption
M_f	kg	Mass of volcanic fragments including melt and pyroclastic deposit
M_w	kg	Mass of meteoric water in a phreatomagmatic eruption
M_m	kg	Mass of magma or melt in a phreatomagmatic eruption
M_w / M_m	-	Water to magma mass ratio or gas to magma ratio
V_o	m/s	Initial gas expansion velocity
τ	s	Time constant of gas expansion phase
V_e	m/s	Velocity at impact of volcanic blocks or gas expansion velocity
t	s	Travel time of the volconic block to its dropping location
n	-	Gas to rock fragments mass ratio
ε	F/m	Electrical permittivity
σ	S/m	Electrical conductivity
$ß$	dB/m	Attenuation rate
v	m/ns	Velocity of radar waves
z	m	Depth of radar reflector beneath the surface
Tv	ns	Arrival time or the time radar wave returned to the receiver
R	m	Radial distance from center of the eruption
R_0	m	Radial distance from crater rim where gas reached its maximum velocity
R_d	m	Radius of volcanic dike
d	m	Depth of the dike
R_c	m	Radius of the crater rim
x	m	Lateral distance from the crater rim (in Cartesian coordinates)
θ	radian	Open angle of the orifice to the center of the eruption
ρ_i	kg/m^3	Density of volcanic blocks (3100 kg/m^3)
ρ_g	kg/m^3	Atmospheric density or density of the gas cloud (4.7 kg/m^3)
g	m/s^2	Earth's gravitational acceleration (9.81 m/s^2)
φ	m	Volcanic block size
C_d	-	An empirical atmosphearic friction factor
$\varphi_{sag,\ GPR}$	m	Volcanic sag size measured from radargram
$\varphi_{sag,\ field}$	m	Volcanic sag size measured from the field
$\varphi_{blocks,}\ \varphi$	m	Volcanic block size derived from an empirical relationship

Table 2. Radial distance, GPR-determined volcanic sag size, volcanic block size, and terminal velocity for GPR line 6.

Radial Distance from Crater Rim (m)	GPR Sag Size (Y) (cm)	Volcanic Block Size (φ_i) $\varphi = (0.147Y) + 23.215$ (cm) *	Calculated Terminal Velocity $Ve=[(4\ \varphi_i\ \rho_i\ g)/(3C_d\ \rho_g)]^{1/2}$ (m/s) **
1411.7± 243.9	142.77± 0.37	44.20± 0.38	73.77± 9.42
1423.6± 244.4	103.07± 0.32	38.37± 0.33	68.73± 8.78
1445.2± 245.4	180.39± 0.43	49.73± 0.44	78.25± 10.00
1452.5± 245.7	135.74± 0.36	43.17± 0.37	72.90± 9.31
1460.7± 246.0	134.75± 0.36	43.02± 0.37	72.78± 9.30
1489.5± 247.3	128.81± 0.35	42.15± 0.36	72.04± 9.20
1535.9± 249.4	164.85± 0.41	47.45± 0.42	76.43± 9.76
1543.8± 249.8	123.96± 0.35	41.44± 0.35	71.43± 9.12
1551.7± 250.2	213.85± 0.49	54.65± 0.50	82.03± 10.48
1557.8± 250.5	115.84± 0.34	40.24± 0.34	70.39± 8.99
1568.6± 251.0	119.80± 0.34	40.83± 0.35	70.90± 9.06
1573.8± 251.2	160.39± 0.40	46.80± 0.41	75.90± 9.70
1585.5± 251.7	150.49± 0.39	45.34± 0.40	74.71± 9.54
1595.5± 252.2	114.85± 0.33	40.10± 0.34	70.26± 8.98
1610.4± 252.9	130.69± 0.36	42.43± 0.36	72.28± 9.23
1619.3± 253.3	92.08± 0.31	36.75± 0.31	67.27± 8.59
1622.9± 253.5	140.59± 0.37	43.88± 0.38	73.50± 9.39
1630.5± 253.9	99.01± 0.31	37.77± 0.32	68.19± 8.71
1632.9± 254.0	126.73± 0.35	41.85± 0.36	71.77± 9.17
1636.8± 254.2	115.84± 0.34	40.24± 0.34	70.39± 8.99
1647.4± 254.7	137.62± 0.37	43.45± 0.37	73.14± 9.34
1665.9± 255.6	119.80± 0.34	40.83± 0.35	70.90± 9.06
1671.7± 255.9	128.71± 0.35	42.14± 0.36	72.03± 9.20
1679.1± 256.2	147.52± 0.38	44.90± 0.39	74.35± 9.50
1687.7± 256.7	139.60± 0.37	43.74± 0.38	73.38± 9.37
1702.0± 257.4	160.39± 0.40	46.79± 0.41	75.90± 9.70
1706.8± 257.6	77.23± 0.29	34.57± 0.29	65.24± 8.33

* Equation after Rhodes and Hurtado (2014)
**Equation after Walker (1971)

Table 3. Maximum gas expansion velocity (V_o) and the time constant of gas expansion phase (τ).

Survey Line	Maximum Gas Expansion Velocity V_o (m/s)	Time Constant of Gas Expansion Phase τ (s)
line 2	178.26 ± 43.47	46.72 ± 13.00
line3	94.92 ± 9.87	137.54 ± 42.3
line4	106.01 ± 12.45	109.63 ± 32.60
line5	141.89 ± 27.05	56.50 ± 16.64
line6	102.85 ± 9.29	111.36 ± 26.26
line7	113.08 ± 14.27	92.02 ± 24.47
Average	122.83 ± 9.38	92.30 ± 11.29
Range	113.46-132.21	81.01-103.58

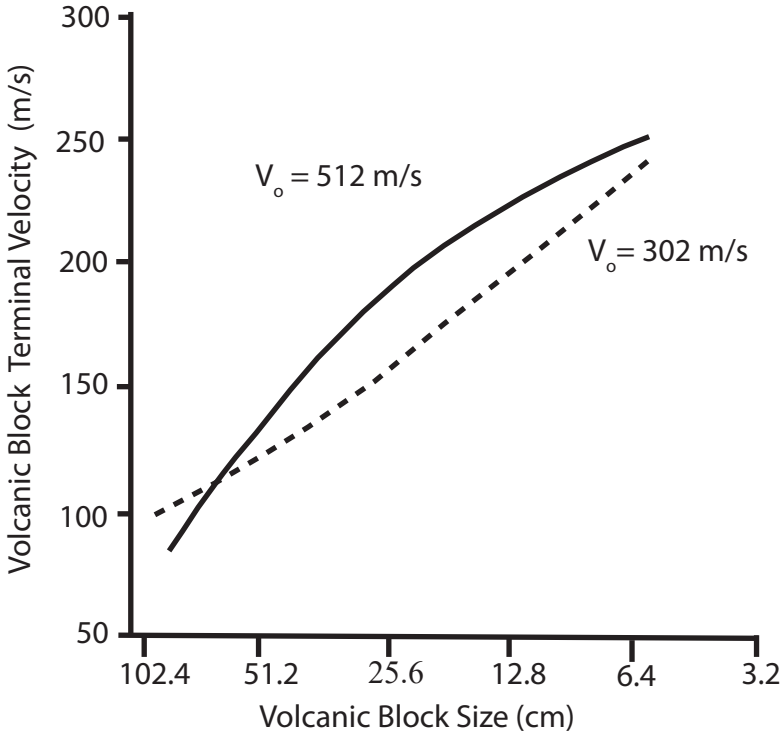

Figure 1. Relationship between the volcanic block terminal velocity and the sizes of volcanic blocks for two different initial gas velocities. Solid line represents the relationship if the initial gas velocity is 512 m/s and dotted line represents the relationship if the initial gas velocity is 302 m/s. Modified from Wilson (1999).

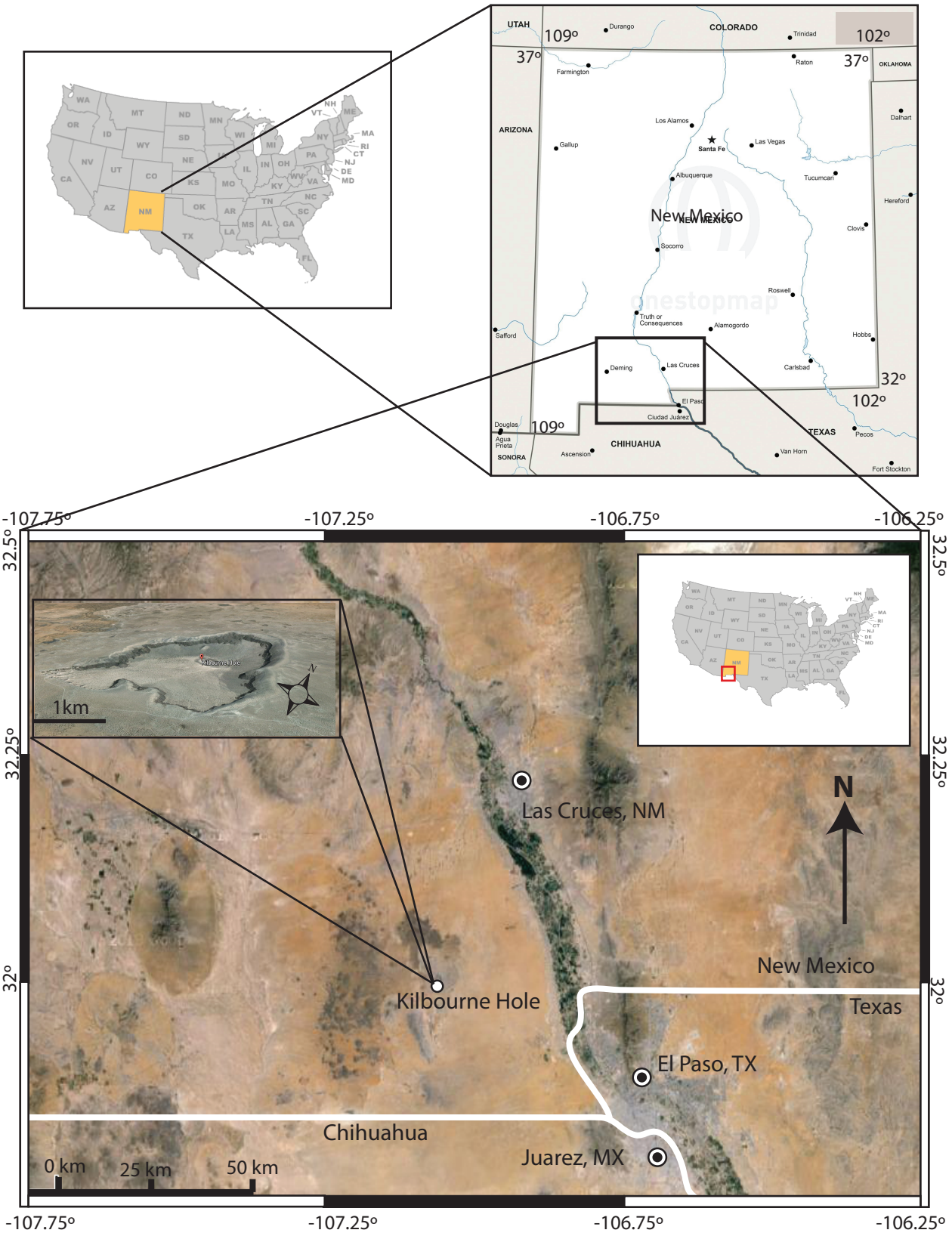

Figure 2. Location of Kilbourne Hole in southern Doña Ana County, New Mexico (imagery from Google Earth, 2008).

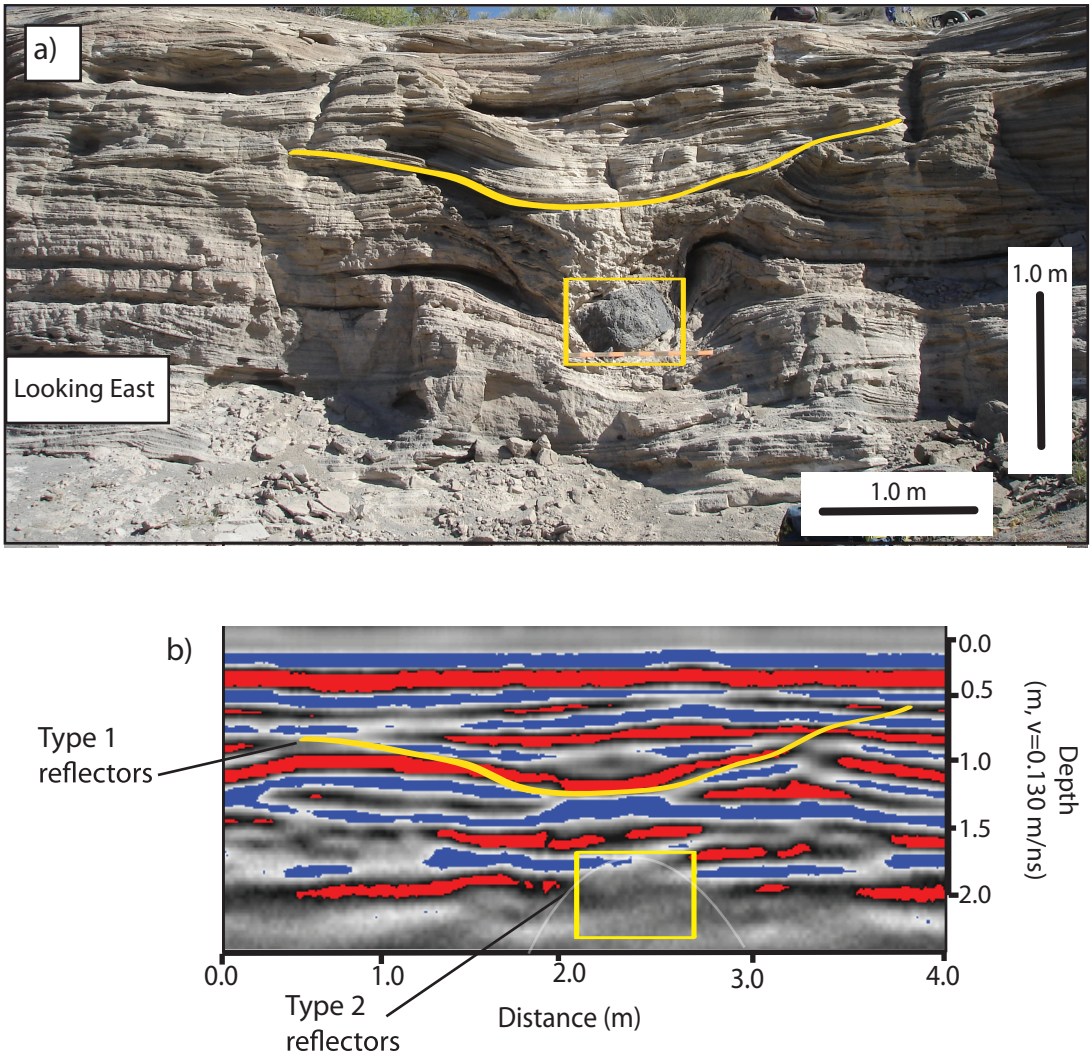

Figure 3. (a) Outcrop of a volcanic block and sag at Kilbourne Hole. Yellow box enclose a basaltic volcanic block feature. Yellow line marks the volcanic sag. (b) GPR image of the outcrop shown in (a), illustrating two types of reflectors. Type 1 reflectors are strong, continuous, smooth, undulating reflectors and correspond to features of pyroclastic deposits called volcanic sags (yellow line). Type 2 reflectors are dim and chaotic and correspond to basaltic volcanic blocks (yellow box). On some occasions, a hyperbolic reflector can be seen at the location of the volcanic block (white line was added as a demonstration).

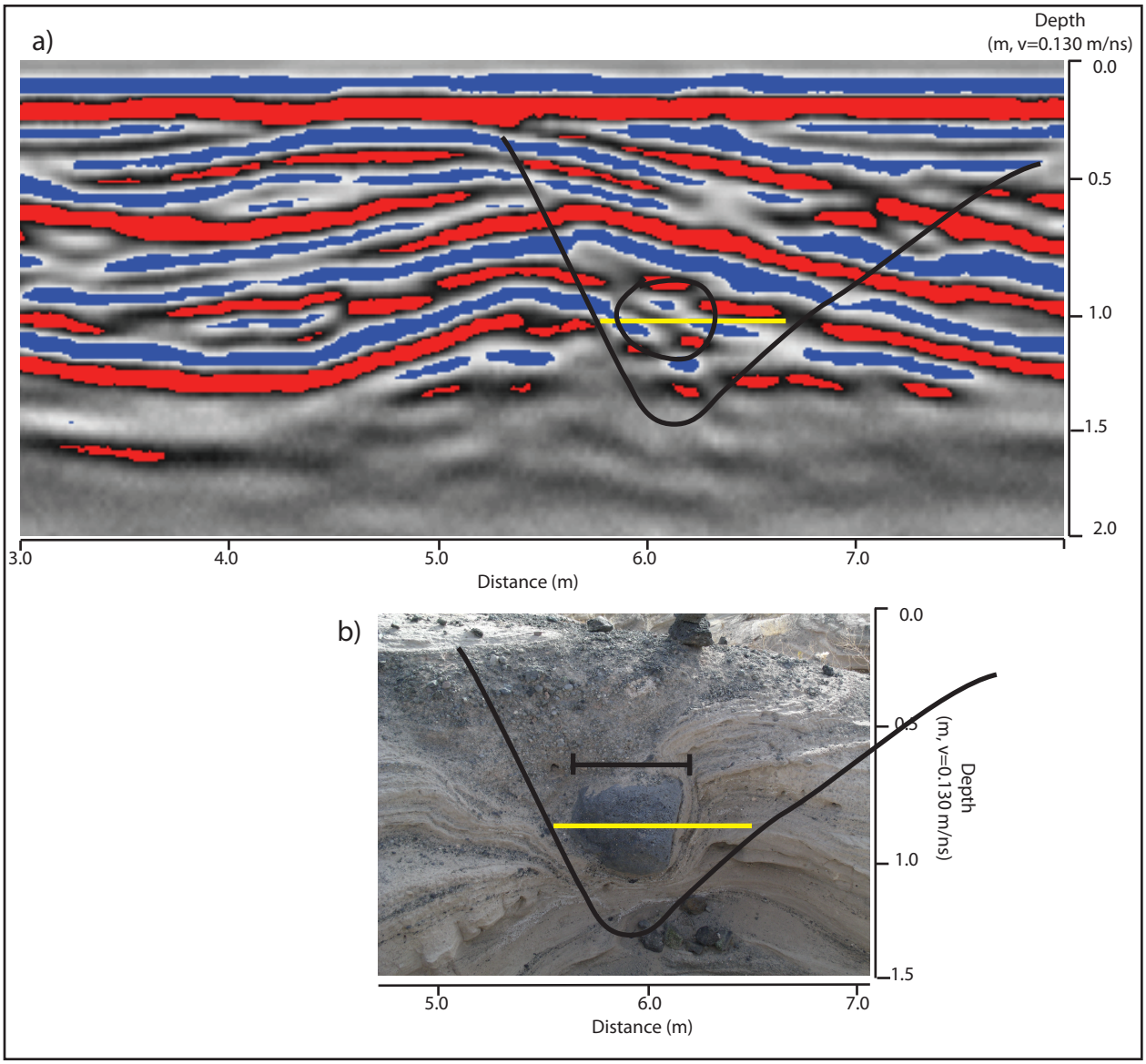

Figure 4. (a) Width measurement of a volcanic sag on GPR image. The widths of volcanic blocks cannot be measured on our GPR images because their reflections are dull and ambiguous. (b) Measurement of volcanic sags and blocks in the field. The yellow line marks the width measurement of the sag. The bracket represents the widest part of the volcanic block where the width of the block was measured.

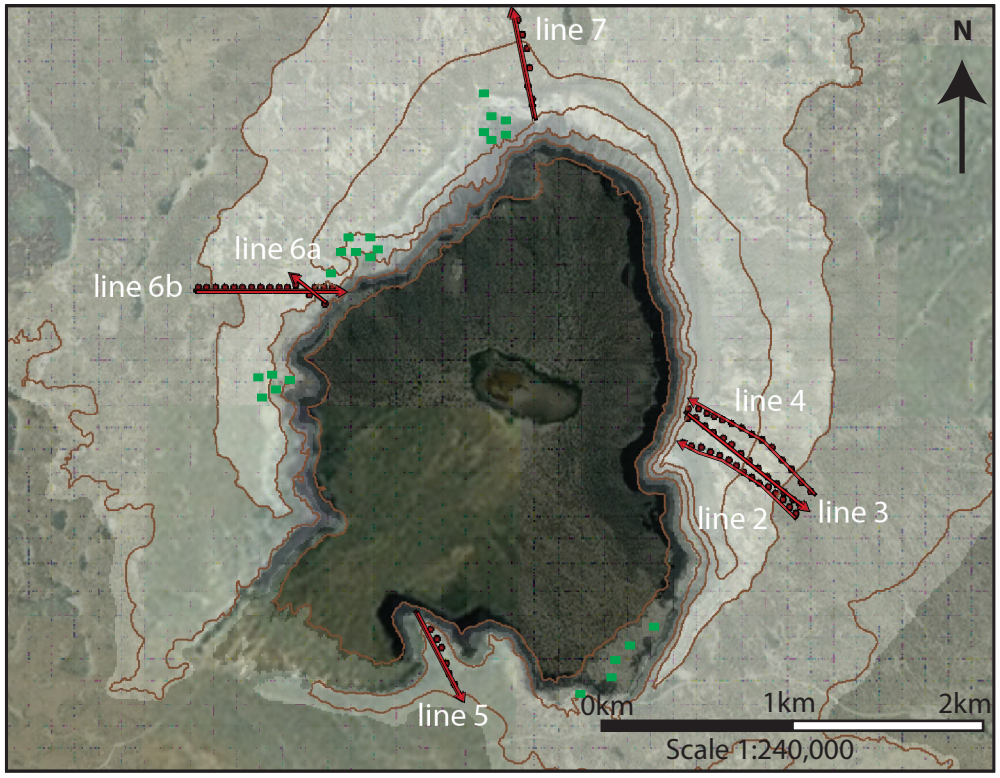

Figure 5. Location of GPR lines. Red arrows indicate direction of the GPR survey (away or toward the crater rim). Red dots indicate the location of long GPR surveys lines. Green rectangles indicate the location of twenty-nine short GPR survey lines that was performed to calibrate the volcanic sag size measurements. Base map is the 1:24,000 scale topographic map of Kilbourne Hole (U.S Geological survey, 2010).

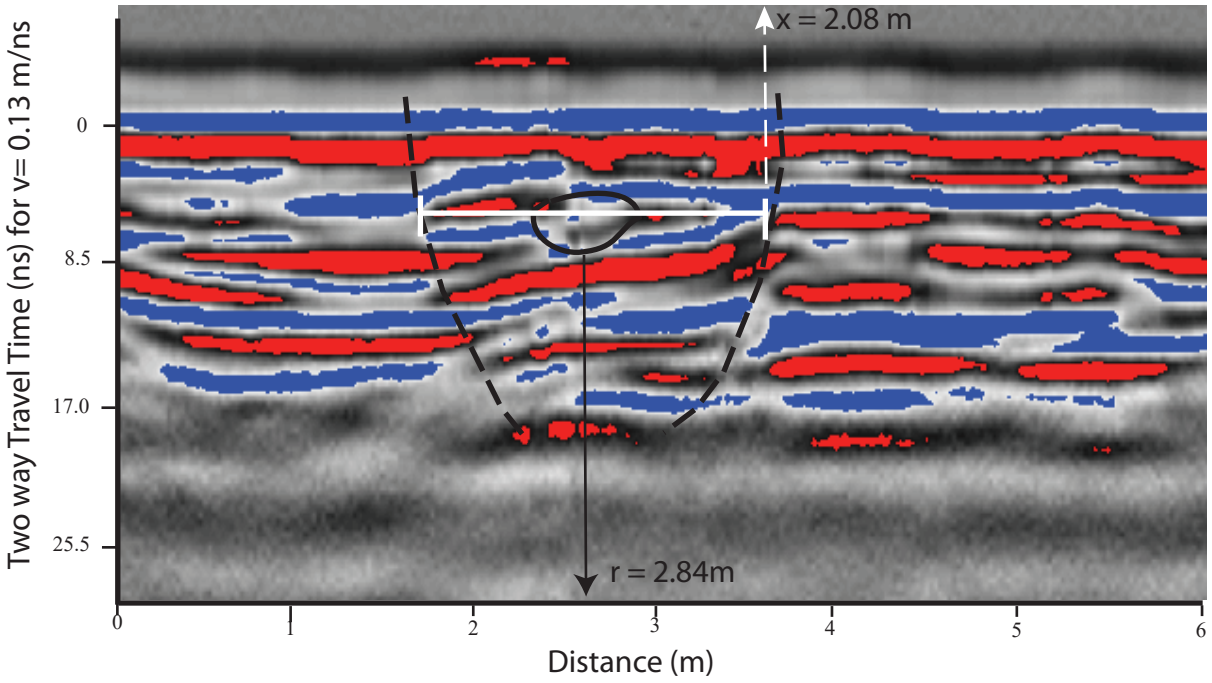

Figure 6. An example of a volcanic sag and associated block on a small section of GPR survey line 4. Plotted on the x-axis is the horizontal distance from the crater rim (in m) and plotted on the y-axis is the two-way travel time (in ns) of the GPR reflectors. Dashed lines highlight a reflection from a volcanic sag (Type 1 reflector). The oval marks a reflection from a volcanic block (Type 2 reflector). The size of the volcanic sag is represented by a white line. The horizontal distance of the sag from the crater rim (r) is 2.84 m.

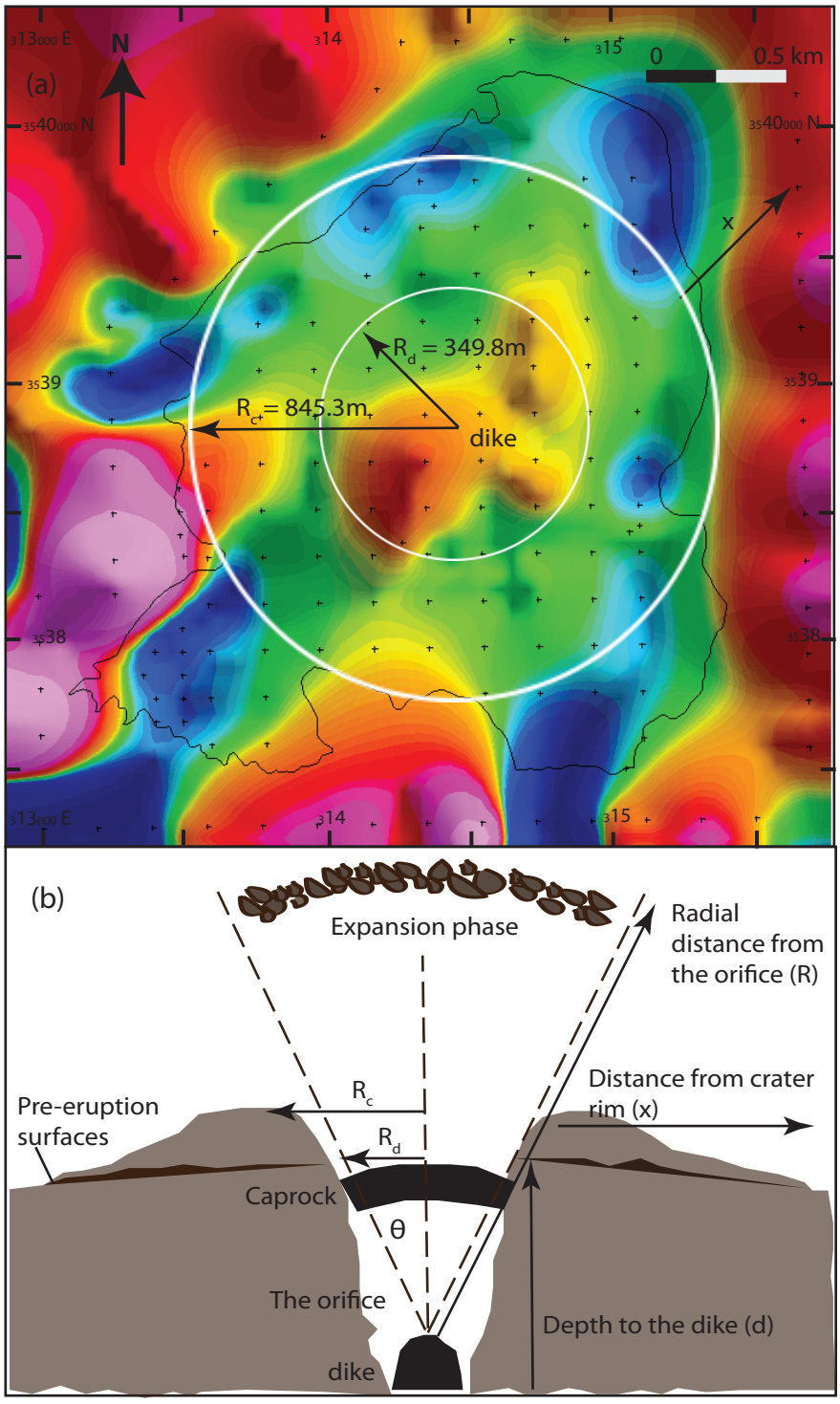

Figure 7. Structure and physical dimensions of Kilbourne Hole. (a) A magnetic anomaly map (Rhodes and Hurtado, 2012) of Kilbourne Hole showing the location of high magnetic anomalies in the center of the crater (interpreted to be dikes) and high magnetic anomalies around the crater rim that correspond to basalt flows). We consider the orifice of the explosion to be the area (of radius R_d) above the dikes, and we use a best-fit circle to the modern crater rim to estimate the crater radius (R_c). (b) A cross-sectional view of Kilbourne Hole illustrating the relationship between radial distance and horizontal distance from the orifice. The radial distance (R) is a cosine function of the horizontal distance (r). Modified from Rhodes and Hurtado (2012) and Fagents and Wilson (1995).

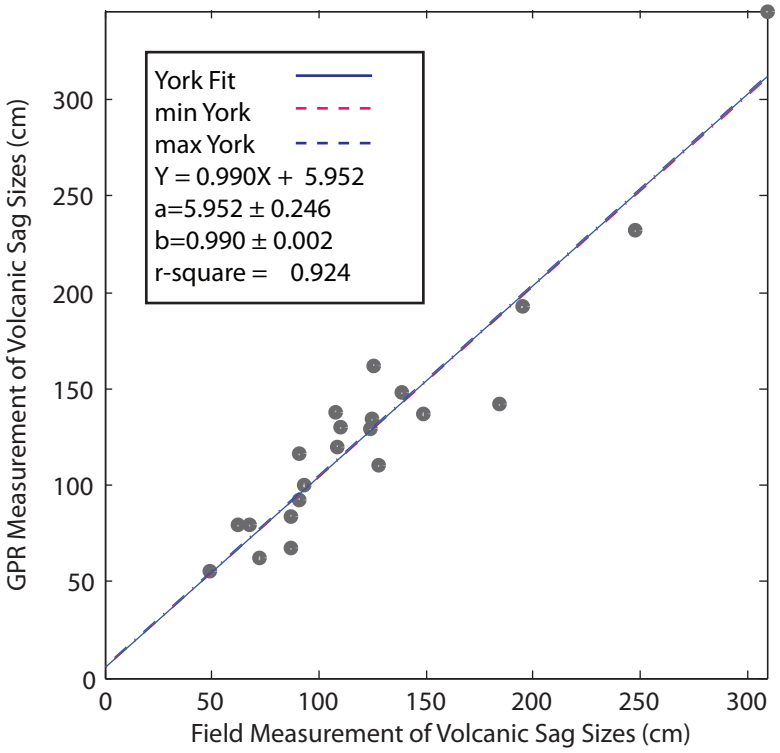

Figure 8. The relationship between volcanic sag sizes measured from the field and volcanic sag sizes measured from GPR profiles at Kilbourne Hole. This relationship is used to relate the width of a volcanic sag on the GPR profile to the actual width of the volcanic sag in the field. Uncertainties are shown by the light grey ovals and are smaller than the symbol size.

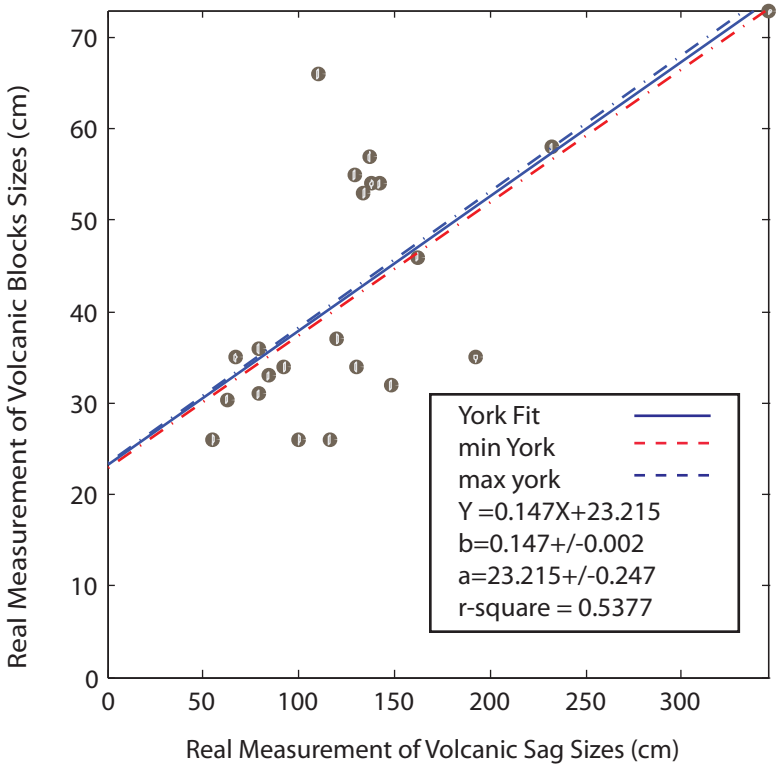

Figure 9. The relationship between actual volcanic block sizes and volcanic sag sizes at Kilbourne Hole measured in outcrop. This relationship is used to relate the actual width of a volcanic sag to the actual width of its associated volcanic block. Data uncertainties are shown by the light grey ovals and are smaller than the symbol size.

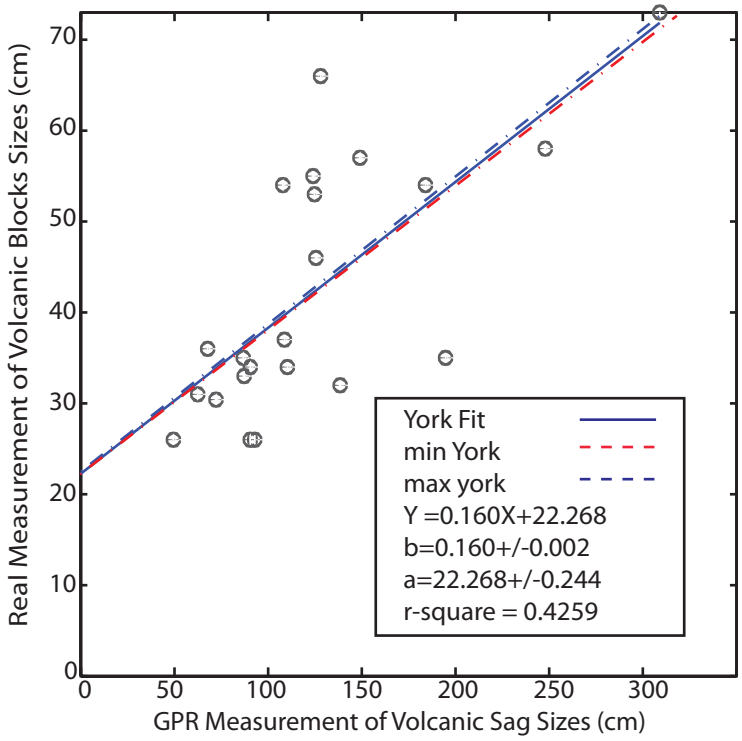

Figure 10. The relationship between the actual volcanic block sizes and volcanic sag sizes measured on GPR profiles at Kilbourne Hole. This relationship is used to relate the width of a volcanic sag on the GPR profiles to the actual width of its associated volcanic block. Data uncertainties are shown by the light grey ovals and are smaller than the symbol size.

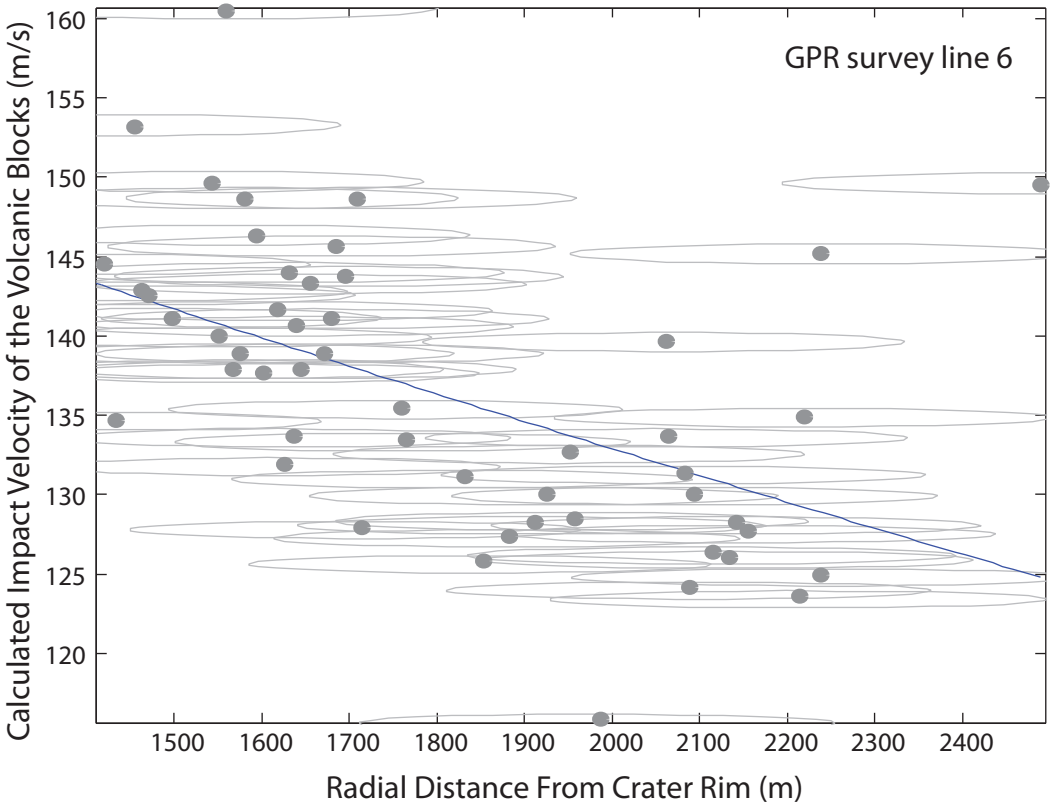

Figure 11. Impact velocity of volcanic blocks versus the radial distance from the vent of the volcanic blocks along GPR line 6. Grey ovals represent uncertainties of these two sets of data. Blue line represents an exponential relationship between the data sets.

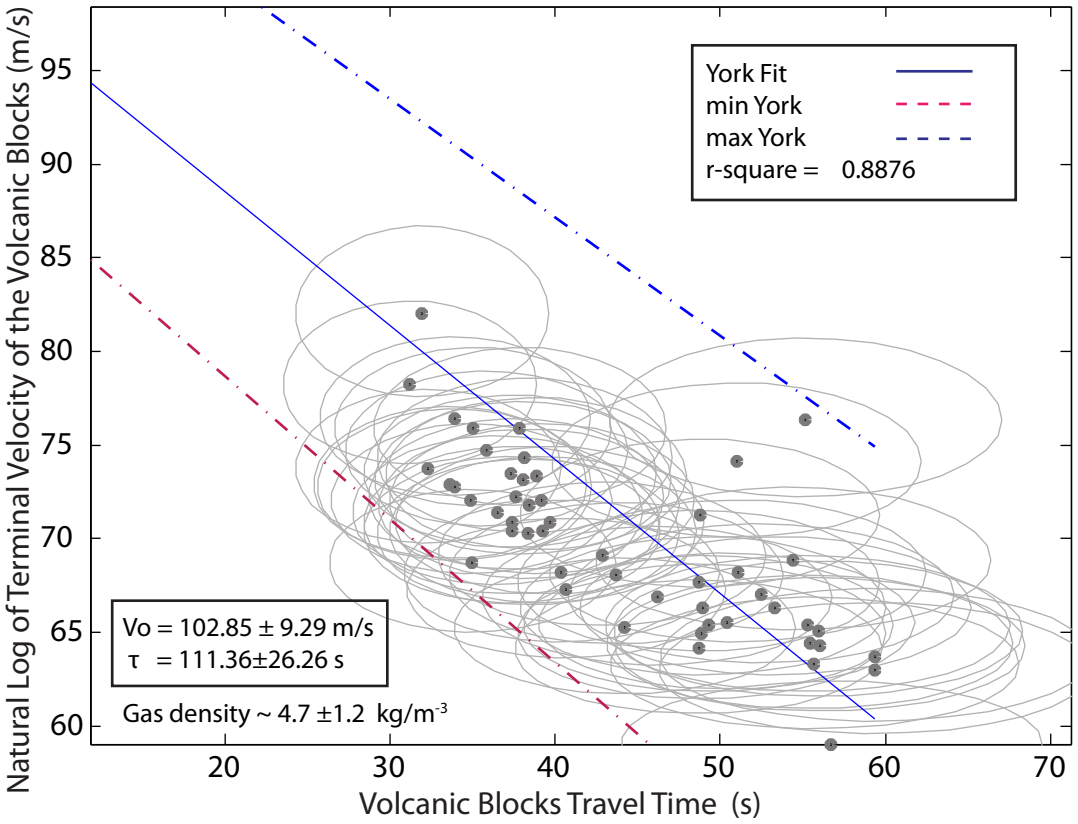

Figure 12. Linear relationship between the natural logarithm of terminal velocity of the volcanic blocks ($log_e V_e$) versus travel time to terminal location (t). The data shown here were retrieved from volcanic sags and blocks found along GPR survey line 6. The results of other survey lines are included in Table 3. Uncertainties in the data are shown by the light grey ovals. The solid blue line represents the York best fit. The dashed blue lines represent the maximum margin of York best fit. The dashed red lines represent the minimum margin of York best fit.

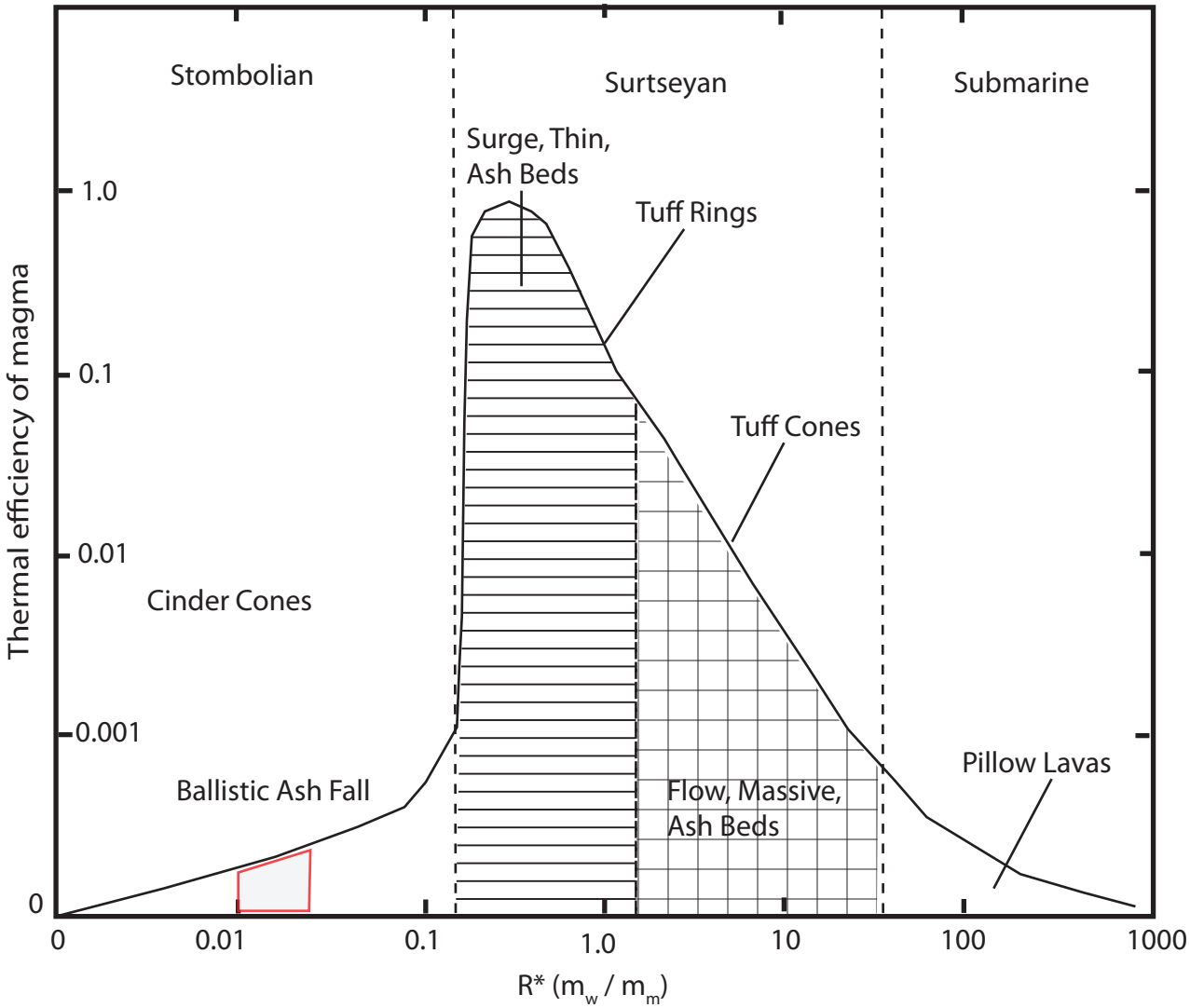

Figure 13. Ranges of thermal efficiency of phreatomagmatic eruption is shown as a function of water to magma mass ratio. Ranges are indicated types of eruptions (Strombolian, Surtseyan, and submarine) as well as the corresponding landforms and depositional facies (adapted from Wohletz and McQueen, 1984). Shaded red box indicates ranges of water to magma mass ratio (0.01- 0.02) predicted for Kiblourne Hole eruption.

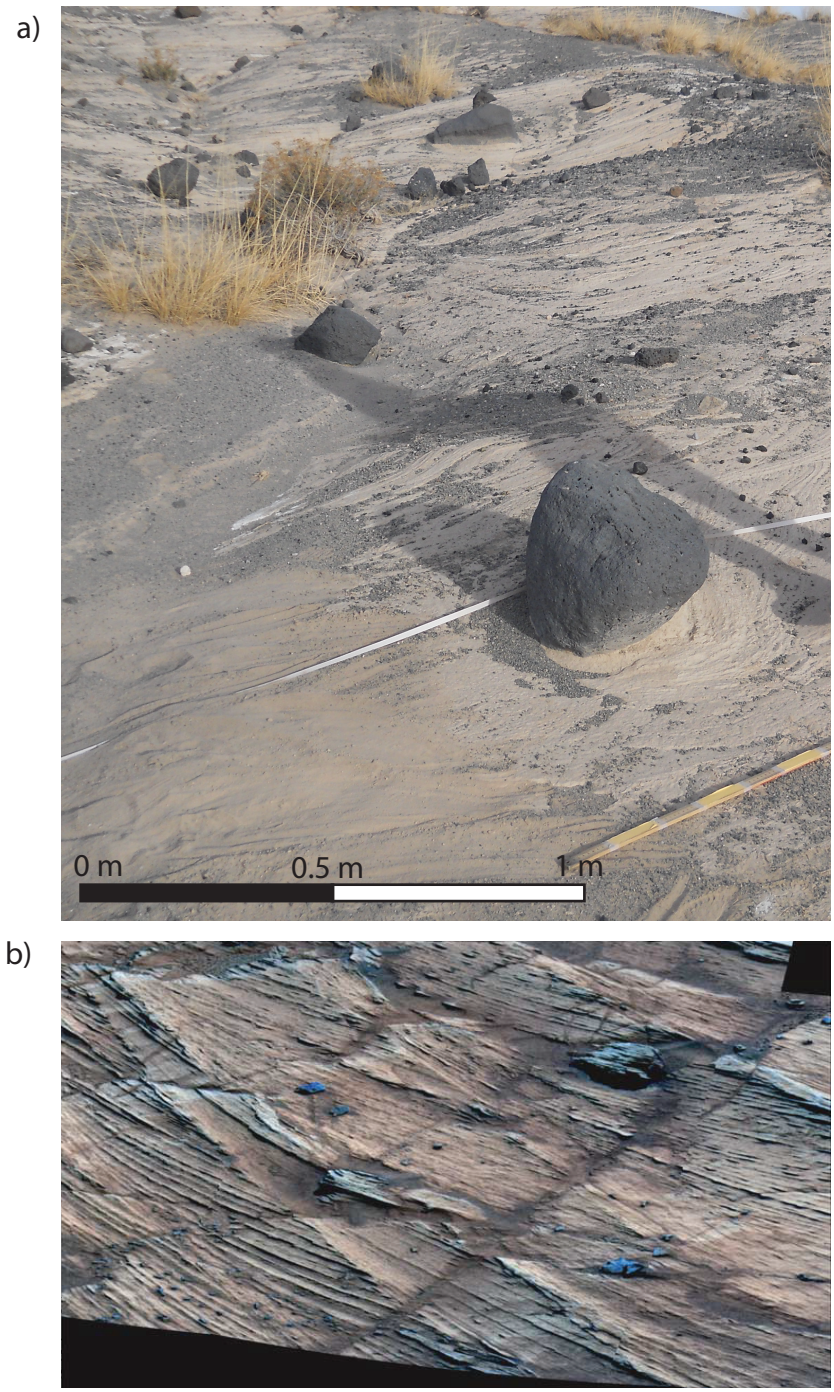

Figure 14. a) Cross bedded tuff ring, volcanic blocks, and volcanic sags found on the west rim of Kilbourne Hole. The image is a true color photograph taken by the authors in November 2014. b) High-angle cross bedding, volcanic blocks, and volcanic sags found on Home Plate, Mars. The mosaic image is a false color stretch photograph. The horizontal distance across the lower part of both images is approximately 1.5 m. (Squyres et al., 2007).

Appendix A: Maximum Gas Expansion Velocity Analysis

The routine of this code is based on the procedure suggested by Rhodes and Hurtado (2014). This code is design to determine the maximum gas velocity that ejected volcanic block from Kilbourne Hole eruption. The code was written on MATLAB 2012b. I adapted York's regression method (York, 2004) and implement it in this code to solve for the least square best fit of my data. The data input is an excel file format of 6 column. Column 1 of the excel file must be the size of the volcanic sag (in cm). Column 2 of the excel file must be the uncertainty of size of the volcanic sag (in cm). Column 3 and 4 are the size of the volcanic block (in cm) and the uncertainty of the volcanic block (in cm) Column 5 is radial distance of the volcanic block from the orifice of ejection in meter. Column 6 is the uncertainty of the radial distance. The output result of this code are: a velocity curve plot of the volcanic blocks (Terminal velocity vs, radial distance), York fit of the velocity curve with propagate uncertainty and r-square value of the regression, and result vector contain value of the maximum velocity of the gas expansion and the time constant of gas expansion phase.

References

York, D., Evensen, N. M., Martınez, M. L., & Delgado, J. D. B., 2004, Unified equations for the slope, intercept, and standard errors of the best straight line. *American Journal of Physics*, vol. 72, no. 3, p. 367-375.

```
% bomb velocity curve
%-----------------------------------------------------------------------

% Based on Wilson, 1999
% Ve = ( Vo(Ro/R)^2 )* e^(-t/T)
% Also Ve can be derived by size of volcanic clast

% linearlize the eaquation
% log10 Ve*R^2 = log10(Vo*Ro^2) -0.43*(t/T)
% now put the data in matrix system
% y = Ap^
% p^= H (At*w)wY
% p^ = [a,b]
% a = log Vo*(Ro/R)^2
% b = -(0.43/T)
% Y = log10 Ve*R^2
% A = [1, t]
% t = R/Ve
% A = [ 1, R/Ve]

clc
clear all

load line2;

%phi = line6_1(:,3); % volcanic bomb size from model (cm)
%Ve = line6_1( : , 5 ) ;% volcanic Bomb Terminal Velocity (m/s)

%% propagate error from GPR-sagsize to Real sag size

GPR_sagsize = line2(:, 2);% load data of GPR sag size
n = length (GPR_sagsize);
% All GPR sag size measuremeant contain 0.05 cm uncertainty cause by
the
% rulers
sigma_GPR_sagsize = repmat(0.05,1,n);
% We convert GPR-sagize to Real_sagsize using this York regression
between
% GPR_sagsize (X1) and real sag size( Y1)
% Y1 = b1X1 +a1
%york: a=5.952+/-0.246 b=0.990+/-0.002
a1 = 5.952;
sigma_a1 = -0.246;
b1 = 0.990;
sigma_b1 = 0.002;
Real_sagsize = (b1.*GPR_sagsize)+a1;

%then error of the GPR sag size measurement isas follow
% sigma_z1 = sigma of b1.X1
% z1 = product of b1.X1
```

```
sigma_z1_1 =  (((sigma_b1./b1).^2) + ((sigma_GPR_sagsize./
GPR_sagsize').^2)).^0.5;
sigma_z1 = (b1.*GPR_sagsize).*sigma_z1_1';

% calculate uncertainy in Y or the obtained blocksize in this model
% Y = Z1+a1
sigma_real_sagsize = ((sigma_z1.^2)+(sigma_a1.^2)).^0.5 % in cm


%% propagate error from Real sag size to the obtained blck size (phi)
% we obtained block size from relationship between blocksize and sag
size
% We convert Real_sagsize to block size using this York regression
between
% Y2 (phi) = b2X2 +a2
% where york: a=22.268+/-0.244 b=0.160+/-0.002
% where this time X2 is real sagsize

a2 = 23.215;
sigma_a2 = 0.247;
b2 = 0.147;
sigma_b2 = 0.002;

Real_blocksize = (b2.*Real_sagsize)+a2;
phi = Real_blocksize;
%then error of the GPR block size measurement is as follow
% sigma_z2 = sigma of b2.X2
% z2 = product of b2.X2
sigma_z2_1 =  (((sigma_b2./b2).^2) + ((sigma_real_sagsize'./
Real_sagsize').^2)).^0.5;
sigma_z2 = (b2.*Real_sagsize)'.*sigma_z2_1;

% calculate uncertainy in Y or the obtained blocksize in this model
% Y = Z1+a1
sigma_phi = ((sigma_z2.^2)+(sigma_a2.^2)).^0.5; % in cm
sigma_phi = sigma_phi'% in cm

%% Propropagate error from the obtained blck size (phi)to its terminal
velocity

% Terminal Velocity = SQRT((4*(phi/100)*3100*9.8)/(3*0.7*1.225))
% where phi = block size from the previous model
% density of the block = 3100 kg/m3
% density of the atmosphere = 1.225 kg/m3
% density of the plinian plume = 3.5 kg/m3 (* Patrick 2007)
% density of phreatomagmatic plume = 4.7 kg/m3 (* Steinberg and
Barbenko)
% assume 4.7-+1.2 kg/m3
% the Earth's gravity acceleration = 9.8 kg.m/s2
% given the error of Terminal Velocity is sigma_Ve
```

```
% Ve =  SQRT(constant x phi)
% Ve =  SQRT (constant) *SQRT (phi)
% c  = SQRT (constant)
rho_g = 4.7;
c = (4/100*3100*9.8)/(3*0.7);
z3 = c.*(1./rho_g).* phi;
w = 0.5; % for squareroot
Ve = (z3).^w;
Ve = Ve';

% calculate error propagation from gas density error (sigma_rho_g)and
error
% from volcanic block size ( sigma_phi)
sigma_rho_g = 1.2;
rho_phi = (1./rho_g) .* phi;
sigma_rho_phi = rho_phi.*(((sigma_rho_g./rho_g).^2+(sigma_phi./
phi).^2).^0.5);

% by error propagation rules
% sigma z3-of constant c
sigma_z3 = c*sigma_rho_phi;
% then for Ve = z3^n
w = 0.5; % for squareroot
sigma_Ve = w.*(sigma_z3./z3);
sigma_Ve = Ve.*sigma_Ve';
sigma_Ve = sigma_Ve'% unit is in m/s

% calculate error propagation from gas density error




%% Now we will have to convert distance of the blocks into radial
distance from the orifice
% including error from the measurement

r_prime = line2( : , 1 ) ;% Horizontal distance from crater rim (m)
sigma_r_prime = repmat(0.05,1,n);% because of ruler measurement on GPR
profile (0.05m error)
Rc_prime = 845.3 ; % crater rim radius (best-fit circle) (m)
sigma_Rc_prime = 126.8 % in m crater rim radius error from erosion and
collapse or original crater estimate 15%
Rd_prime = 349.8 ; % radial of the diatreme (m) derived from the
magnetic model
sigma_Rd_prime = 40.0 % this value is the best estimation from our
magnetic moddel
d = 920.0 ; % depth to the dikes (m) ( depth tot the top of the dike
are varied from 920.0, 1330.0, to 3270.0 to 3390.0 m)
sigma_d = 120.0 % this value is the best estimation from our joint
magnetic moddel (0.12 km)
```

```
theta = atand( Rd_prime ./ d ) ; % ejection angle ( degree)
% find uncertainty of theta
sigma_theta_1 = ((sigma_Rd_prime/ Rd_prime).^2+(sigma_d./d).^2).^0.5;%
first propagate uncertainty of the dividen
sigma_theta_2 = (Rd_prime./d).*sigma_theta_1;
% function of arctan
% derivative of d (arctan x) =    1 / 1 + x2
sigma_theta = (1./ (1+((Rd_prime ./ d).^2))).*sigma_theta_2

R = ( r_prime + Rc_prime )./ sind( theta ) ; % Radial distance from
the orifice (m)

% error of R that is propagated from r_prime is
% error of r_prime + Rc_prime
sigma_R1 = ((sigma_r_prime.^2) +(sigma_Rc_prime.^2)).^0.5;
% error of sind( theta )
sigma_R2 = cosd(theta).*sigma_theta;
% final error for R-radial distance
%sigma_R= (sigma_R1./sigma_R2)
sigma_R3 = (((sigma_R1./ (r_prime+Rc_prime)').^2)+(sigma_R2./
sind(theta)).^2).^0.5;
sigma_R = R'.*sigma_R3;
sigma_R = sigma_R';




%% Using Inversion technique
% Based on Wilson, 1999
% Ve = ( Vo(Ro/R)^2 )* e^(-t/T)
% Also Ve can be derived by size of volcanic clast

% linearlize the eaquation
% ln Ve*R^2 = ln(Vo*Ro^2) -(t/T)
% now put the data in matrix system
% y = Ap^
% p^= H (At*w)wY
% p^ = [a,b]
% a = log Vo*(Ro/R)^2
% given that Ro/R =1
% a = log Vo
% b = -(1/T)
% Y = log10 Ve
% A = [1, t]
% t = R/Ve
% A = [ 1, R/Ve]
% A = [ N, M]
t = R ./ Ve'; % time (sec) when the block is dropped at the radial
distance R
```

```
sigma_t = t.*(((sigma_R./R).^2 +(sigma_Ve./Ve').^2).^0.5)
Wp  = diag(sigma_t.^2); % variance identity matrix from uncertainty in
data set (t)



Y = log( Ve )' ;
% Ve comes with error see sigma_Ve
% to propagate sigma_Ve to sigma_Y using error propagation rules 4.
sigma_Y = (repmat(1,1,n)./ (Ve.*log(10))).*sigma_Ve';
sigma_Y = sigma_Y'
Wd  = diag(sigma_Y.^2);% variance identity matrix from uncertainty in
data set (Y) or Terminal Velocity

% weighting metrix W = wd/Wp
W = Wp/Wd;

G = ones( 1 , length( t ) ) ;
G = G' ;

A = [ G , t ] ;

% now perform matrix operation
%y = AP^
% a=log(VoRo^2);
% b= -0.43/T;
% P^ = [a,b]
% (Y) = AP^
% A-1.Y = A-1.A.P^

At= A' ;

% (Wd/Wp)Y = (Wd/Wp)AP^
%H = inv( At * A) * At ; % generalize inversion metrix
H = (inv(At*(W.^2)*A))*(At*(W.^2));% generalize inversion metrix
P_hat = H * Y

% P^ = [a,b]
v = P_hat( 1 ) ;
V0_inverse = exp( v )

u = P_hat( 2 ) ;
T_inverse = -1 ./ u
% Now we will try to calculate the covarience of this result
% y_theo can be obtained from A*calculated

y_theo = A * P_hat;
p = H * y_theo;
```

```
% cov_p_hat = (p^-p)(p^-p)t
cov_P_hat = ( P_hat - p ) * ( ( P_hat - p )' )

% %cor(X,Y)=cov(X,Y)/sd(X)sd(Y)
% cov2_P = n.*cov_P_hat (2,1);
% %cov2P = (1/lenght(t)).*cov2_p
% R_P = cov2_P./ ((sum((P_hat-mean(P_hat)).^2).*sum((p-
mean(p)).^2))^0.5)
% % r-square
%
% r_square_P= R_P.^2


%% Using York technique

% Based on Wilson, 1999
% Ve = ( Vo(Ro/R)^2 )* e^(-t/T)
% Also Ve can be derived by size of volcanic clast
% linearlize the eaquation
% ln Ve = lnVo -(t/T)
% Y = bX+a
 Y = log(Ve);
% a = ln Vo
 X = t';
% b = -1/T
sigma_X = sigma_t';
sigma_Y = sigma_Y';

%r is a row vector or singal value for the correlation coefficeients
%between the errors.

N = length(X);%number of points
r=0*ones(1,N);%correlation coefficient between errors in X and Y

X_range=[0 max(X)];%range of X values
a=randn;%"True Value" of a (Y=a+b*X)
b=randn;%"True Value" of b

[a_york, b_york, sigma_ayork, sigma_byork] =
york_fit(X,Y,sigma_X,sigma_Y, r);
%C2 = [X; ones(1,N)];
tmp=Y/[X; ones(1,N)];%find least squares line fit
b_lse=tmp(1);
a_lse=tmp(2);

N_plot=2;
X_plot=linspace(X_range(1),X_range(2),N_plot);
Y_plotlse = a_lse+b_lse*X_plot;
Y_plotnf =a+b*X_plot;
Y_plotyork =a_york+b_york*X_plot;
```

```
fprintf('a=%0.3f b=%0.3f\n\n',a,b);
fprintf('lse: a=%0.3f b=%0.3f\n',a_lse,b_lse);
fprintf('a-a_lse=%0.3f b-b_lse=%0.3f\n\n',a-a_lse,b-b_lse);

fprintf('york: a=%0.3f+/-%0.3f b=%0.3f+/-%0.3f
\n',a_york,sigma_ayork,b_york,sigma_byork);
fprintf('a-a_york=%0.3f b-b_york=%0.3f\n',a-a_york,b-b_york);

%%
figure(1)
h=zeros(2,1);
plot(X,exp(Y),'k.')
hold on
%plot error ellipse for each point
for i=1:N
    [Xe Ye] = ellipse(X(i),Y(i),sigma_X(i),sigma_Y(i),32);
    plot(Xe,exp(Ye),'color',[0.7 0.7 0.7])
end
%h(1)=plot(X_plot,exp(Y_plotnf),'b','linewidth',1);
h(1)=plot(X_plot,exp(Y_plotlse), 'g', 'linewidth',1);
h(2)=plot(X_plot,exp(Y_plotyork), 'linewidth',1);
hold off
xlim([0 max(X)]);
ylim([0 max(exp(Y))]);
legend(h,'lse','york')
xlabel('Time(sec)')
ylabel('Ejection Velocity (m/s)')

%% plot york error

Y_max_york = (a_york+sigma_ayork)+(b_york+sigma_byork).*X_plot;
Y_min_york = (a_york-sigma_ayork)+(b_york-sigma_byork).*X_plot;

figure (2)
h2=zeros(4,1);
plot(X,exp(Y),'k.')
hold on
%plot error ellipse for each point
for i=1:N
    [Xe Ye] = ellipse(X(i),Y(i),sigma_X(i),sigma_Y(i),32);
    plot(Xe,exp(Ye),'color',[0.7 0.7 0.7])
end
h2(1)=plot(X_plot,exp(Y_max_york),'-.');
h2(2)=plot(X_plot,exp(Y_min_york), '-.');
h2(3)=plot(X_plot,exp(Y_plotyork), '-');
h2(4)= plot(X_plot,exp(Y_plotlse), 'g', 'linewidth',1);
hold off
xlim([max(X)./1.5 max(X)]);
ylim([ min(exp(Y))./1.5 max(exp(Y))]);
```

```
legend(h2,'max-york','min-york','york','lse')
xlabel('Time (sec)')
ylabel('Ejection Velocity (m/s)')

%% solve for result
% a = ln Vo
%  Vo = e^a
V0_york = exp(a_york )

sigma_V0 = V0_york.*sigma_ayork
% b = -1/T
% T = -1/b
T_york = -1 ./ b_york
sigma_T = T_york.*(sigma_byork./b_york)


%% Compute R-square of each fit
% Covariance of x to y
%A2_york = cov(X_plot, Y_plotyork) % covaraince of york plot (x,y data
included error)
cov1 =cov(X,Y) % covaraince of original x and y data
mean_xyork = mean (X_plot);
mean_yyork = mean (Y_plotyork);
cov2_york = sum ((X-mean_xyork).*(Y-mean_yyork));
cov2 = (1/N).*cov2_york
% correlation coefficient of x and y
R1 = corrcoef(X,Y)
%R2_york = corrcoef(X_plot,Y_max_york)
R2_york = cov2_york./ ((sum((X-mean_xyork).^2).*sum((Y-
mean_yyork).^2))^0.5)
% r-square
r_square_1= R1.^2
r_square_2_york= R2_york.^2
```

Appendix B: Volcanic Clast Size Distribution at Kilbourne Hole

This appendix is in an excel format. It stored both field and laboratory measurement of Rhodes and Hurtado, 2014 GPR surveys at Kilbourne Hole. Rhodes and Hurtado (2014) performed a total of 6 long GPR surveys at Kilbourne Hole to identified buried volcanic blocks and sags. They measured the size of volcanic sags and the distance of the volcanic sags from the orifice of Kilbourne Hole. From the measured volcanic sag, we calculated the size of each volcanic block and its terminal velocity. The measurements and calculations of each GPR surveys line are in separate sheets of the excel file. These data sheet can be arranged to be compatible with the MATLAB code in Appendix A. Appendix B is also served as an input for Appendix-A.

References

Rhodes, N., & Hurtado, J. M., 2014, A GPR Survey of Kilbourne Hole, Southern New Mexico: Implications for Near Surface Geophysical Exploration of Mars and the Moon. In *Lunar and Planetary Institute Science Conference Abstracts*. vol. 45, p. 2912.

Radial distance, GPR-determined volcanic sag size, volcanic block size, and terminal velocity for GPR line 2

Distrance from crater rim (m)	Median sag size(cm)	Calculated bomb size (cm)	Calculated Terminal Velocity (m/s)
661.44	89	37.9922	68.39313723
643.24	98	34.9446	65.59267473
649.74	79	35.4258	66.04274824
631.34	82	28.8494	59.59827595
630.24	41	39.7566	69.96324141
627.74	109	37.1902	67.6674111
622.09	93	36.2278	66.78613098
613.93	87	36.5486	67.08117746
590.98	89	39.115	69.39640475
581.94	105	53.3906	81.07700639
555.49	194	44.5686	74.07638841
530.24	139	39.2754	69.53854709
506.24	106	48.0974	76.95309726
476.37	161	50.6638	78.97946443
467.51	177	39.115	69.39640475
444.29	105	53.3906	81.07700639
399.61	194	47.937	76.82467467
345.29	160	46.333	75.52844
372.39	150	45.531	74.87190764
339.09	145	52.749	80.58837887
340.49	190	45.8518	75.135209
331.19	147	41.2002	71.22213139
328.79	118	39.7566	69.96324141
314.29	109	42.323	72.18609127
316.89	125	49.7014	78.2257283
312.29	171	41.521	71.49887466
303.79	120	39.7566	69.96324141
296.48	109	43.7666	73.40687041
291.69	134	53.7114	81.32021915
283.86	196	36.709	67.22821512
281.99	90	49.541	78.09939839
276.69	170	45.0498	74.47521021
269.69	142	64.4582	89.08496032
267.19	263	52.749	80.58837887
248.99	190	39.5962	69.82196366
241.75	108	75.5258	96.43017861
227.59	332	47.6162	76.56718331
181.16	158	65.0998	89.52722665
168.46	267	70.393	93.09578991
184.94	300	65.982	90.13179947
173.92	272.5	69.19	92.29686916
157.44	292.5	48.2578	77.08130588
144.02	162	45.8518	75.135209
114.7	147	37.0298	67.52132986
116.53	92	42.323	72.18609127
112.86	125	44.0874	73.67540772
109.21	136	40.2378	70.38537324
108.17	112	39.2754	69.53854709
87.74	106	37.1902	67.6674111
91.74	93	40.0774	70.24494449
106.74	111	37.6714	68.1037748
80.46	96	39.4358	69.68039947
82.28	107	38.6338	68.96822004
78.4	102	46.8142	75.91963425
75.37	153	36.3882	66.93381679
72.37	88	53.8718	81.44155316
63.32	197	39.2754	69.53854709
67.76	106	38.1526	68.53736031
57.39	99	38.9546	69.25397067
42.59	104	42.8042	72.59529868
40.83	128	42.9646	72.73118952
15.41	129	32.3782	63.13812125
18.59	63	36.3882	66.93381679
19.73	88	41.0398	71.08335572
21.96	117	36.0674	66.63811786
2.59	86	22.273	52.36663439

Radial distance, GPR-determined volcanic sag size, volcanic block size, and terminal velocity for GPR line 3

Distrance from crater rim (m)	Median sag size(cm)	Calculated bomb size (cm)	Calculated Terminal Velocity (m/s)
9.28	142	45.0498	74.47521021
18.47	171	49.7014	78.2257283
36.11	118	41.2002	71.22213139
63.8	90	36.709	67.22821512
87.91	125	42.323	72.18609127
109.92	85	35.907	66.48977525
119.76	93	37.1902	67.6674111
122.5	81	35.2654	65.89306532
125.08	63	32.3782	63.13812125
131.2	69	33.3406	64.06959957
149.36	80	35.105	65.74304159
169.6	70	33.501	64.22353251
176.5	74	34.1426	64.83560969
177.6	75	34.303	64.98772825
182.75	90	36.709	67.22821512
188.37	100	38.313	68.68128055
209.54	52	30.6138	61.3937165
257.45	112	40.2378	70.38537324
275.34	87	36.2278	66.78613098
283.29	106	39.2754	69.53854709
307.81	47	29.8118	60.58420364
315.73	105	39.115	69.39640475
317.57	70	33.501	64.22353251
321.14	77	34.6238	65.29090213
342.54	74	34.1426	64.83560969
360.52	62	32.2178	62.98153551
366.69	124	42.1626	72.04917233
376.77	142	45.0498	74.47521021
390.31	85	35.907	66.48977525
422.32	127	42.6438	72.45915298
559.65	61	32.0574	62.8245595
561.97	74	34.1426	64.83560969
599.67	49	30.1326	60.90929985
671.29	94	37.3506	67.81317766
670.09	96	37.6714	68.1037748
668.6	50	30.293	61.071199
675.82	102	38.6338	68.96822004
683.46	69	33.3406	64.06959957

Radial distance, GPR-determined volcanic sag size, volcanic block size, and terminal velocity for GPR line 4

Distrance from crater rim (m)	Median sag size(cm)	Calculated bomb size (cm)	Calculated Terminal Velocity (m/s)
661.8	176	35.2654	65.89306532
660.43	81	42.1626	72.04917233
652	124	43.927	73.54126164
606.4	135	29.9722	60.74696922
585.85	48	38.4734	68.82489983
576.27	101	42.0022	71.91199271
556.99	123	46.6538	75.78946052
552.4	152	42.323	72.18609127
518.34	125	37.1902	67.6674111
509.29	93	40.3982	70.52552237
488.93	113	34.6238	65.29090213
468.79	77	39.115	69.39640475
463.4	105	42.0022	71.91199271
460.61	123	44.8894	74.34250734
457.4	141	33.8218	64.5302968
438.54	72	35.2654	65.89306532
430.46	81	39.5962	69.82196366
403.4	108	46.4934	75.65906282
330.09	151	36.5486	67.08117746
335.09	89	32.699	63.45013343
354.57	65	38.313	68.68128055
278.04	100	48.0974	76.95309726
227.14	161	50.343	78.72902085
219.65	175	40.719	70.8049884
203.69	115	40.0774	70.24494449
177.88	111	58.8442	85.11716214
161.96	228	50.0222	78.47777804
157.98	173	50.9846	79.22911636
148.25	179	37.9922	68.39313723
120.15	98	42.323	72.18609127
97.95	125	44.4082	73.94296978
99.15	138	34.303	64.98772825
95.35	75	35.5862	66.19209269
59.75	83	39.115	69.39640475
57.05	105	37.511	67.95863156
35.25	95	40.3982	70.52552237
41.75	113	42.323	72.18609127
47.75	125	40.0774	70.24494449
14.95	111	44.5686	74.07638841
5.95	139	41.6814	71.63684539
7.65	121	42.1626	72.04917233
3.45	124	36.5486	67.08117746
2.25	89	22.273	52.36663439

Radial distance, GPR-determined volcanic sag size, volcanic block size, and terminal velocity for GPR line 5

Distrance from crater rim (m)	Median sag size(cm)	Calculated bomb	Calculated Terminal Velocity (m/s)
3.831	145.5	45.6112	74.93781971
7.291	168.4	49.28436	77.89684439
11.33	154.9	47.11896	76.16635142
12.603	124.7	42.27488	72.14504287
17.603	112.2	40.26988	70.41342538
18.582	87.3	36.27592	66.83047099
22	98.7	38.10448	68.49412527
28.468	297.2	69.94388	92.79833075
30.603	112.2	40.26988	70.41342538
42.5	138.2	44.44028	73.96967276
44.4	142.4	45.11396	74.5282252
45.4	125.8	42.45132	72.29543972
46.67	95.6	37.60724	68.04575465
49.4	294.1	69.44664	92.4678848
53.16	103.9	38.93856	69.23971115
52.27	155.9	47.27936	76.29588212
56.27	159	47.7766	76.69603705
61.91	98.7	38.10448	68.49412527
64.12	143.4	45.27436	74.66059798
65.83	118.5	41.2804	71.29141792
71.12	163.2	48.45028	77.2348753
73.56	136.1	44.10344	73.68880889
83.8	238.3	60.49632	86.30377305
85.03	97.1	37.84784	68.26307593
86.72	136.2	44.11948	73.70220763
91.04	125.1	42.33904	72.19976888
93.58	127.1	42.65984	72.47277906
96.95	218.2	57.27228	83.97258844
96.35	145.2	45.56308	74.89827943
109.6	174.2	50.21468	78.62862006
112.85	107.1	39.45184	69.69456883
116.05	204.2	55.02668	82.30987828
124.18	126.1	42.49944	72.33640277
129.28	149.2	46.20468	75.42377886
162.35	221.2	57.75348	84.32461815
160.25	212.2	56.30988	83.26406412
166.45	128.1	42.82024	72.60889921
172.42	150.1	46.34904	75.54151244
178.57	152.2	46.68588	75.81551315
223.2	167.2	49.09188	77.74458257
228.5	120.1	41.53704	71.51268371
258.8	75.1	34.31904	65.00292052
249.2	86.1	36.08344	66.65293396
382.4	81.1	35.28144	65.90804891
388.95	84.1	35.76264	66.35598336
411.65	94.21	37.384284	67.84374884
411.45	70.1	33.51704	64.23890551
417.45	102	38.6338	68.96822004
426.85	75.1	34.31904	65.00292052
435.45	121.1	41.69744	71.65062785

Radial distance, GPR-determined volcanic sag size, volcanic block size, and terminal velocity for GPR line 6

Distrance from crater rim (m)	Median sag size(cm)	Calculated bomb size (cm)	Calculated Terminal Velocity (m/s)
2.2	138.2	44.44028	73.96967276
9.3	98.1	38.00824	68.40757322
22.3	176.2	50.53548	78.87938242
26.7	131.1	43.30144	73.01573708
31.6	130.1	43.14104	72.8803768
48.9	124.1	42.17864	72.06287593
76.77	160.5	48.0172	76.88891278
81.5	119.2	41.39268	71.38830609
86.23	210	55.957	83.00275651
89.9	111	40.0774	70.24494449
96.39	115	40.719	70.8049884
99.5	156	47.2954	76.3088231
106.5	146	45.6914	75.00367386
112.5	110	39.917	70.10423445
121.5	126	42.4834	72.322751
126.82	87	36.2278	66.78613098
128.96	136	44.0874	73.67540772
133.51	94	37.3506	67.81317766
134.99	122	41.8418	71.77455089
137.3	111	40.0774	70.24494449
143.66	133	43.6062	73.2722327
154.8	115	40.719	70.8049884
158.3	124	42.1626	72.04917233
162.7	143	45.2102	74.60767705
167.9	135	43.927	73.54126164
176.45	156	47.2954	76.3088231
179.34	72	33.8218	64.5302968
206.85	101	38.4734	68.82489983
211.65	93	37.1902	67.6674111
251.95	84	35.7466	66.34110094
264.24	64	32.5386	63.2943196
282.95	70	33.501	64.22353251
299.95	73	33.9822	64.68313339
307.95	80	35.105	65.74304159
344.95	29	26.9246	57.57579377
327.75	74	34.1426	64.83560969
325.25	90	36.709	67.22821512
390.4	118	41.2002	71.22213139
392.09	94	37.3506	67.81317766
403.9	85	35.907	66.48977525
407.4	58	31.5762	62.35126029
411.4	80	35.105	65.74304159
423.2	66	32.8594	63.60556557
434.85	65	32.699	63.45013343
439.65	73	33.9822	64.68313339
448.75	71	33.6614	64.37709738
483.35	56	31.2554	62.03372133
486.25	99	38.1526	68.53736031
651.85	160	47.937	76.82467467
497.85	141	44.8894	74.34250734
498.45	61	32.0574	62.8245595

Radial distance, GPR-determined volcanic sag size, volcanic block size, and terminal velocity for GPR line 7

Distrance from crater rim (m)	Median sag size(cm)	Calculated bomb size (cm)	Calculated Terminal Velocity (m/s)
4.29	118	38.7942	69.11124304
5.47	103	34.9446	65.59267473
6.7	79	37.1902	67.6674111
10	93	41.8418	71.77455089
14	122	39.115	69.39640475
23.32	105	41.2002	71.22213139
21.3	118	43.927	73.54126164
25.53	135	35.907	66.48977525
28.95	85	46.9746	76.04958517
42.67	154	37.3506	67.81317766
51.7	94	23.3958	53.67032858
54.79	7	40.2378	70.38537324
57.76	112	42.4834	72.322751
78.95	126	36.8694	67.37493189
75.55	91	48.2578	77.08130588
68.15	162	40.0774	70.24494449
114.9	111	45.0498	74.47521021
120.2	142	50.6638	78.97946443
142.2	177	42.323	72.18609127
144.4	125	33.9822	64.68313339
154.7	73	40.2378	70.38537324
188.35	112	37.3506	67.81317766
209.52	94	37.8318	68.24860937
218.95	97	47.2954	76.3088231
222.25	156	39.7566	69.96324141
231.55	109	47.2954	76.3088231
234.55	156	41.8418	71.77455089
260.17	122	42.323	72.18609127
262.75	125	41.2002	71.22213139
266.25	118	33.9822	64.68313339
263.35	73	47.6162	76.56718331
266.75	158	43.7666	73.40687041
293.99	134	51.947	79.97339629
348.4	185	37.1902	67.6674111
344.9	93	46.4934	75.65906282
341.8	151	44.729	74.20956716
354.9	140	39.5962	69.82196366
352.4	108	36.8694	67.37493189
308.4	91	43.7666	73.40687041
361.1	134	42.4834	72.322751
364	126	38.1526	68.53736031
371.3	99	39.7566	69.96324141
372.7	109	38.7942	69.11124304
377.6	103	43.2854	73.00221234
388.9	131	36.8694	67.37493189
392.1	91	37.3506	67.81317766
402.9	94	37.0298	67.52132986
423.54	92	37.511	67.95863156
434.74	95	37.6714	68.1037748
437.6	96	37.3506	67.81317766
439.6	94	52.4282	80.34295072
445.6	188	33.8218	64.5302968
458.83	72	47.2954	76.3088231
463.6	156	41.8418	71.77455089
468.6	122	36.2278	66.78613098
473.6	87	37.3506	67.81317766
476.3	94	35.5862	66.19209269
477.4	83	37.511	67.95863156
478.6	95	37.9922	68.39313723
482.6	98	35.7466	66.34110094
484	84	32.8594	63.60556557
490.6	66	32.0574	62.8245595
504.6	61	29.9722	60.74696922
514.05	48	31.5762	62.35126029
521.8	58	33.501	64.22353251
537.2	70	22.273	52.36663439

Appendix C: Plots of Maximum Gas Expansion Velocity Analysis

We applied the code routine from Appendix A to the volcanic blocks data from the total of six survey transects (Appendix B) and produced the plot results showing here in Appendix C. The plots in Appendix C are the display of York's regression and least square best-fit including the r-square values of the York's regression and least square best fit. The plot shows data points and area of the uncertainties of the input data. Each plot yield three linear equations, which are minimum York's best fit, maximum York's best fit, and York's best fit. The code routine from Appendix A then further calculated the final result values, which are the maximum velocity of the gas expansion and the time constant of gas expansion phase from the slope and constant of those linear equations. The final results contain uncertainties and propagated uncertainties. We used Taylor (1997)'s method to propagate the uncertainties from the input data into our calculated results. The plots show in this appendix C are from survey transect 7, 5, 4, 3, and 2. The plot from survey transect 6 is showed in Figure 12 as an example of our results and methodology for Chapter 3.

References

York, D., Evensen, N. M., Martınez, M. L., & Delgado, J. D. B., 2004, Unified equations for the slope, intercept, and standard errors of the best straight line. *American Journal of Physics*, vol. 72, no. 3, p. 367-375.

Taylor, J.R., 1997, Introduction to error analysis, the study of uncertainties in physical measurements (Volume 1), *2nd Ed.*: University Science Books (New York**),** 327 p.

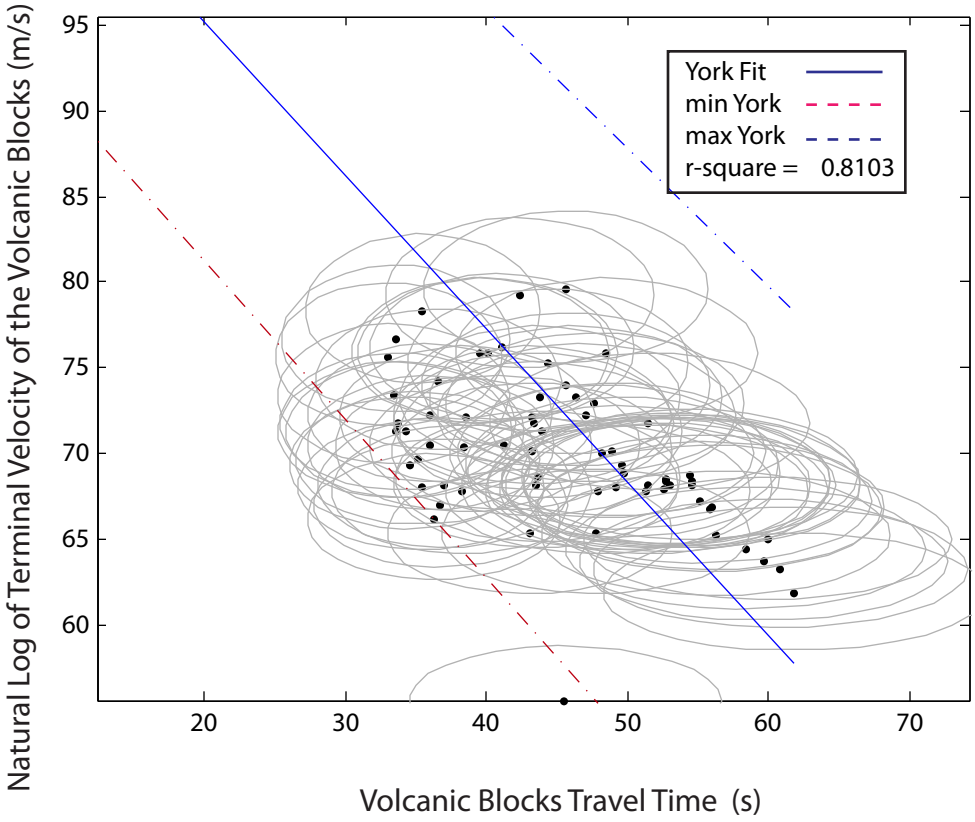

Figure C-1. Linear relationship between the natural logarithm of terminal velocity of the volcanic blocks ($log_e V_e$) versus travel time to terminal location (t). The data shown here were retrieved from volcanic sags and blocks found along GPR survey line 7 . The result of other survey lines are included in Table 3. Uncertainties in the data are shown by the light grey ovals. The solid blue line represents the York best fit. The dashed blue lines represent the maximum margin of York best fit. The dashed red lines represent the minimum margin of York best fit.

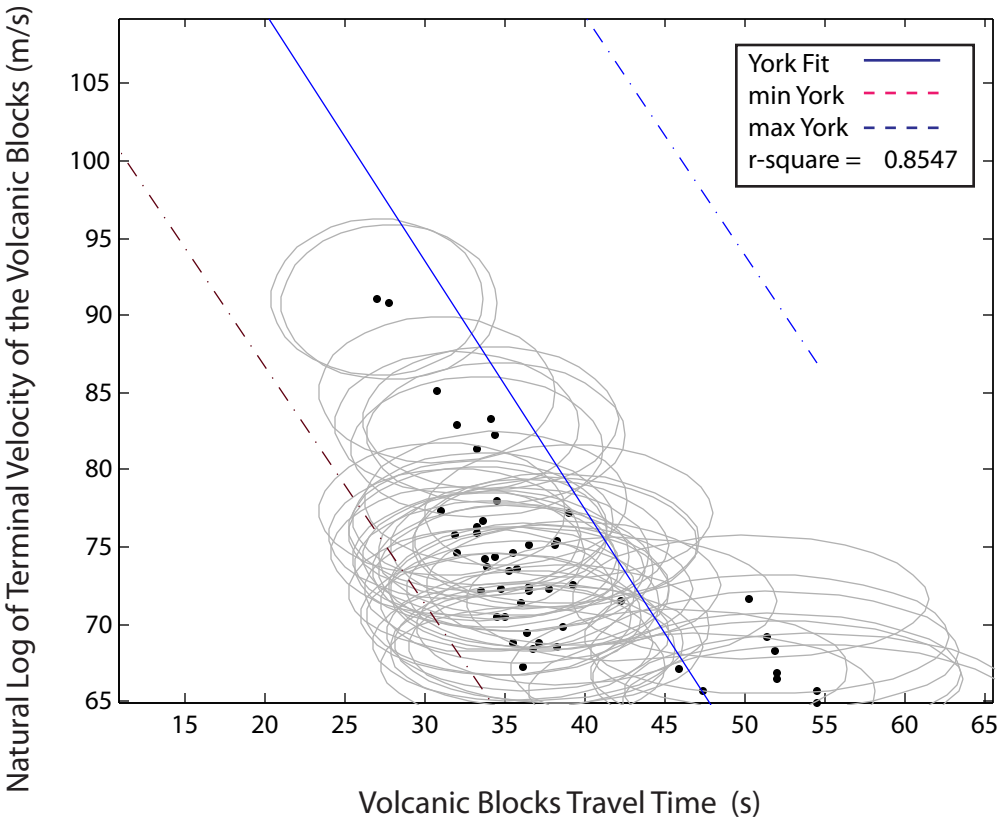

Figure C-2. Linear relationship between the natural logarithm of terminal velocity of the volcanic blocks ($log_e V_e$) versus travel time to terminal location (t). The data shown here were retrieved from volcanic sags and blocks found along GPR survey line 5 . The result of other survey lines are included in Table 3. Uncertainties in the data are shown by the light grey ovals. The solid blue line represents the York best fit. The dashed blue lines represent the maximum margin of York best fit. The dashed red lines represent the minimum margin of York best fit.

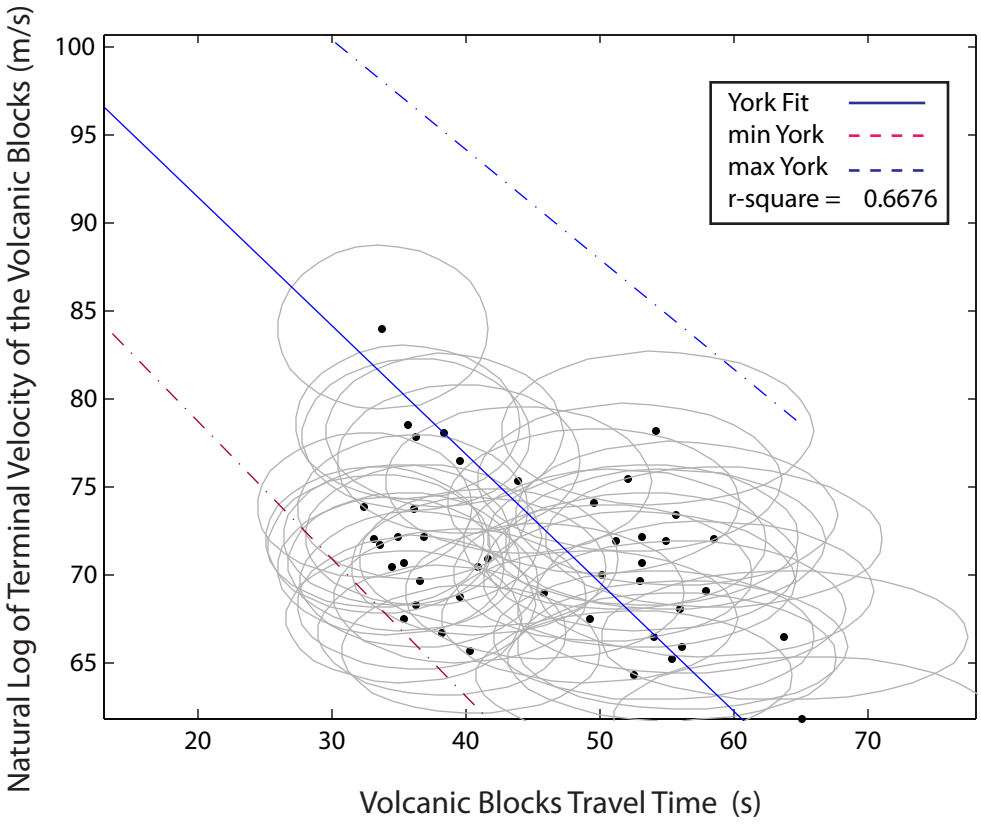

Figure C-3. Linear relationship between the natural logarithm of terminal velocity of the volcanic blocks ($log_e V_e$) versus travel time to terminal location (t). The data shown here were retrieved from volcanic sags and blocks found along GPR survey line 4. The result of other survey lines are included in Table 3. Uncertainties in the data are shown by the light grey ovals. The solid blue line represents the York best fit. The dashed blue lines represent the maximum margin of York best fit. The dashed red lines represent the minimum margin of York best fit.

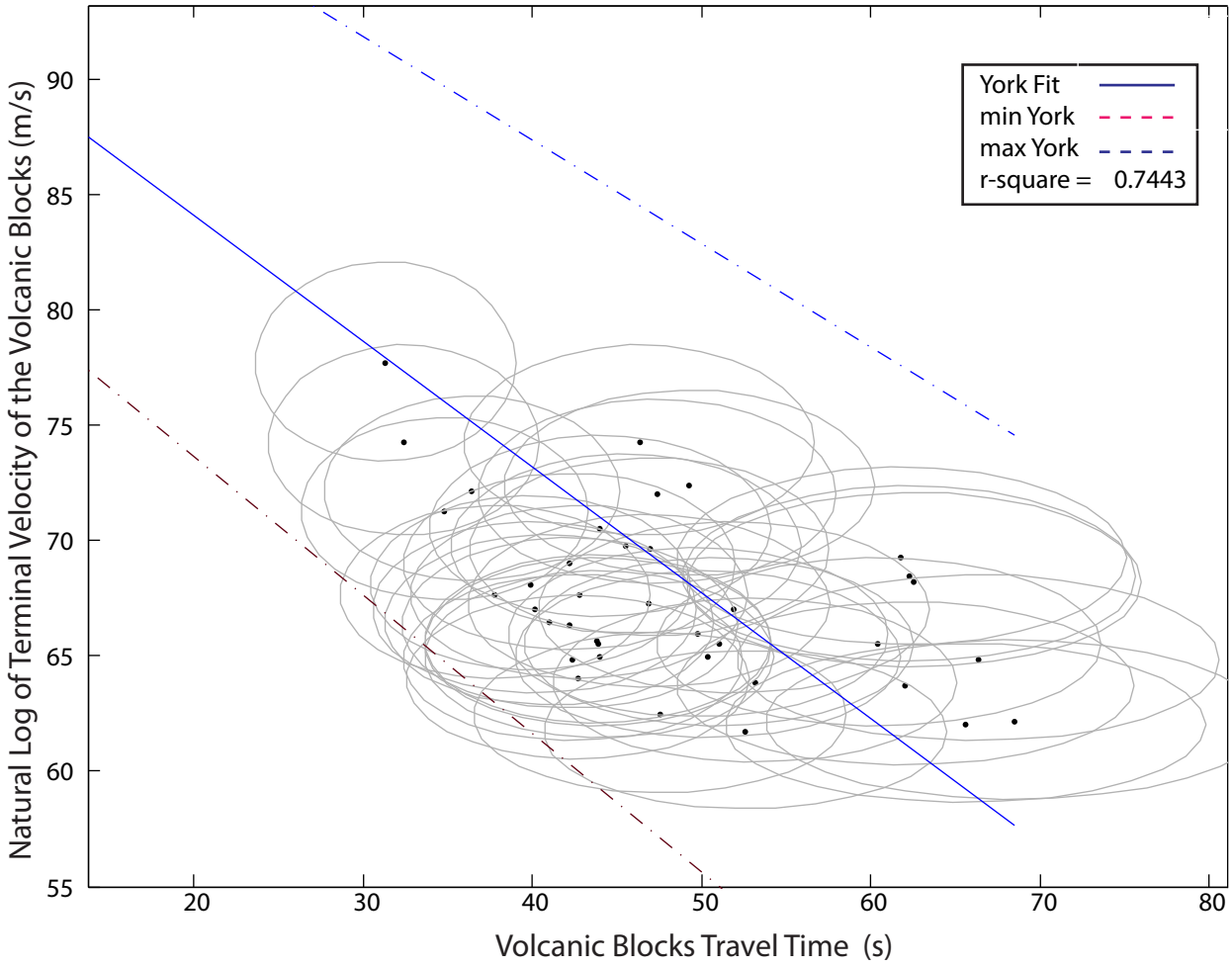

Figure C-4. Linear relationship between the natural logarithm of terminal velocity of the volcanic blocks ($log_e V_e$) versus travel time to terminal location (t). The data shown here were retrieved from volcanic sags and blocks found along GPR survey line 3. The result of other survey lines are included in Table 3. Uncertainties in the data are shown by the light grey ovals. The solid blue line represents the York best fit. The dashed blue lines represent the maximum margin of York best fit. The dashed red lines represent the minimum margin of York best fit.

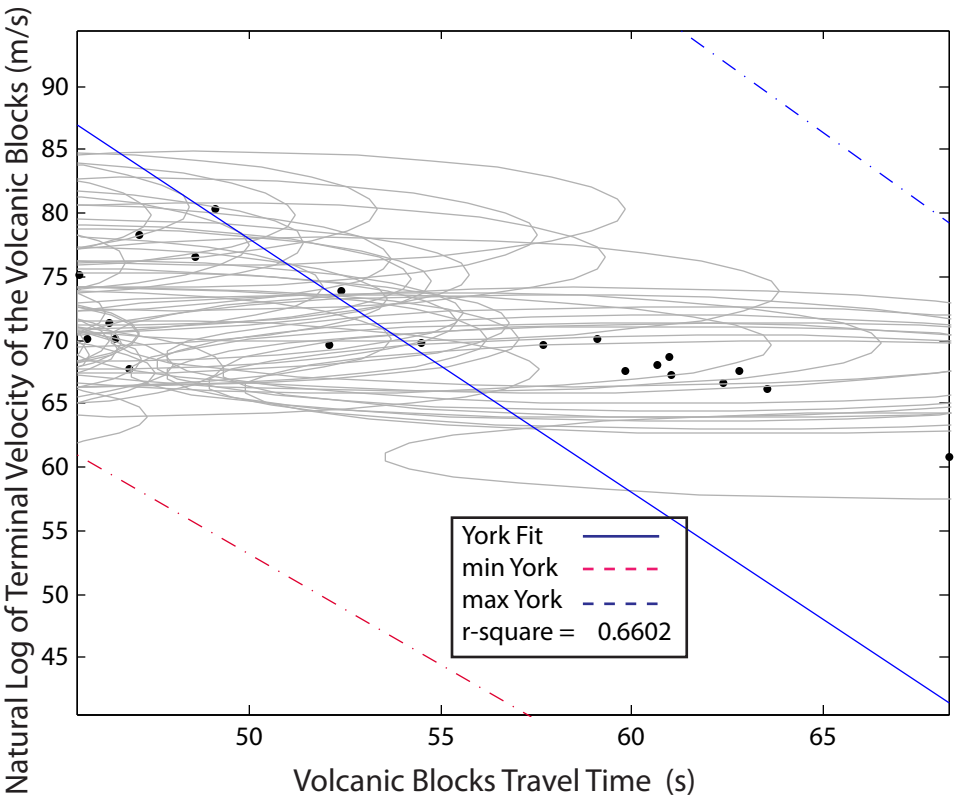

Figure C-5. Linear relationship between the natural logarithm of terminal velocity of the volcanic blocks ($log_e V_e$) versus travel time to terminal location (t). The data shown here were retrieved from volcanic sags and blocks found along GPR survey line 2. The result of other survey lines are included in Table 3. Uncertainties in the data are shown by the light grey ovals. The solid blue line represents the York best fit. The dashed blue lines represent the maximum margin of York best fit. The dashed red lines represent the minimum margin of York best fit.

Chapter 4: Preferential Filtering and Gravity Anomaly Separation using Gravity Recovery and Interior Laboratory (GRAIL) Data: Implications for 2-D Gravity Modeling of Lunar Mascon Basins

[1] Nisa Maksim, [2] Jose M. Hurtado, Jr., and [3] Diane I. Doser

The University of Texas at El Paso, 500 West University Avenue, El Paso, TX 79662

[1] nrhodes@miners.utep.edu, [2] jhurtado@utep.edu, [3]doser@miner.utep.edu

Abstract

A mass concentration (mascon) is a region that contains a large positive gravitational anomaly. Mascons on the Moon are associated with some (but not all) impact basins, but the geologic processes that form them are not yet fully understood. We hypothesize that a combination of uplifted lunar Moho, impact melt sheets, and brecciated crust creates the gravity signature of lunar mascon basins. To test this hypothesis, we utilize the lunar gravity field measured by the Gravity Recovery and Interior Laboratory (GRAIL) mission to reconstruct the history of lunar mascon basin formation and associated magmatic activity. We perform preferential filtering on the free-air anomaly map derived from the GRAIL lunar gravity model GL0660A. Using the preferential filtering method, we isolate the gravity anomalies associated with structures at 16.2 km and 30.0 km depth. We construct four 2D inversion models from the filtered gravity data to visualize the internal structure of lunar mascon basins. We conclude from our 2D inversion models that the parameters that determine the gravity signatures of mascon basins are: (1) the extent of the impact-melt sheet; (2) the depth to the mantle; and (3) the thickness and the density of the surrounding crust.

Keywords: lunar geophysics, GRAIL, mascon basins, inverse modeling, preferential filtering, gravity anomaly separation, mantle rebound, impact melt sheets

1. Introduction

The geology of the Moon is dominated by the impact process, and large impact structures can be found across the lunar surface. Impact features that are larger than 300 km in diameter are called impact basins. The geology of impact basins is very complex and includes impact melts and breccia, faults and fractures, and induced volcanic activity (Bratt et al., 1985; Neuman et al., 1996). Throughout lunar geologic history, there have been more than forty large impact basin-forming events. Among these forty impact basins are some that possess abnormally high positive gravity anomalies (Figure 1). These gravity anomalies, called mascons ("mass concentrations"), are the most striking and prominent features of the lunar gravity field (Muller and Sjogren, 1968). The origin of lunar mascon basins and their unique gravity signal is not yet fully understood. One paradox is that not all large impact basins are mascon basins, so there must be processes other than impacts that are involved in mascon formation. Another paradox is that large impact events excavate and remove mass, so, therefore, they should yield negative gravity anomalies instead of positive gravity anomalies. Models of the lunar crust (Sjogren and Smith, 1976; Zuber et al., 1994; Weiczorek and Phillips, 2000) show that mascon basins do indeed have very thin crustal thicknesses as expected. In light of this, what contributes to the positive gravity anomalies of mascon basins is not yet known.

In this research, we demonstrate the use of lunar geophysics as a tool to resolve the internal structure of mascon basins and shed light on the processes responsible for their formation. We utilize the lunar gravity field measured by the Gravity Recovery and Interior Laboratory (GRAIL) mission to reconstruct the history of lunar mascon basin formation and associated magmatic activity. Utilizing lunar gravity data for this purpose is not straightforward because the lunar crust has been highly affected by impacts that have changed the topography

and have produced impact melts that have altered subsurface densities and porosities (Zuber et al., 2013). Previous analyses of the high-resolution GRAIL gravity maps have shown that over 98% of the gravity anomalies are associated with topography, and only 2% represent subsurface structures (Zuber et al., 2013). In order to retrieve gravity anomalies that represent interior structure rather than these surficial characteristics, we perform low pass filtering and preferential filtering (Spector and Grant, 1970; Guo et al., 2013) of the free-air anomaly map derived from GRAIL lunar free-air gravity model GL0660A to filter out the high frequency gravity signal and selectively filter the gravity signal from the depth of 16 km and 30 km.

In this paper we describe: (1) the low pass filtering method used to isolate the contributions to the lunar gravity anomaly associated with lunar interior structure; (2) the power spectrum depth analysis method (Spector and Grant, 1970) and the preferential filtering method (Guo et al., 2013) used to isolate lunar gravity anomalies associated with specific depths; and (3) 2D inversion modeling of the filtered gravity anomaly data used to reconstruct the internal structure of mascon basins. We hypothesize that the anomalous positive gravity anomalies associated with mascon basins may be the result of a combination of: (1) shallow high-density mantle; (2) moderate density impact melt sheets; (3) low-density, brecciated crust; and/or (4) high density igneous intrusions.

2. Background

2.1 Mascon Basins

Lunar mascons are found associated with some (but not all) impact basins. The major mascons are shown in Figure 1 (Wilhelms et al., 1985; Spudis, 1996; Cook et al., 2000): Serenitatis, Humorum, Imbrium, Orientale, Crisium, Nectaris, Smythii, and Grimaldi. Konopliv et al. (2001) proposed that there are six additional mascons on the lunar farside (Figures 1 and 2): Hertzsprung, Moscoviense, Korolev, Freundlich-Sharonov, Coulomb-Sarton, and Dirichlet-Jackson. Six out of the eight mascon basins on the lunar nearside are on or around the area called Oceanus Procellarum (Figure 1). Oceanus Procellarum itself is not considered a mascon basin, but it is one of the most geologically complex regions on the Moon (Andrews-Hanna, 2013).

On a free-air gravity anomaly map (Figure 2), mascon basins have a bull's-eye pattern comprising a central positive anomaly surrounded by an annular negative anomaly and an outermost annular positive anomaly. As observed by Namiki et al. (2009) (Figure 1), there are differences in the character of the mascon basins on the lunar nearside (Type I mascons) compared to those on the lunar farside (Type II mascons). Type I mascons have central positive anomalies that are extensive and wide, and they are surrounded by weak and subtle negative gravity anomalies (Figure 2). In contrast, Type II mascons are characterized by more distinct rings of positive and negative gravity anomalies, yielding a more pronounced bull's-eye pattern (Figure 2). In addition, the amplitude of the positive gravity anomalies associated with Type I mascons is ~250-500 mGal, whereas the amplitude of the positive gravity anomalies associated with Type II mascons is ~400-900 mGal. In the GRAIL GL0600A free-air gravity model (Figure 2), Orientale, Mendel-Rydberg, Lorentz, and Humboldtianum show more affinity to the

farside mascons than to the nearside mascons. These basins show more pronounced bull's-eye patterns and have positive gravity anomalies with amplitudes consistent with Type II mascons (~600 mGal). Therefore, we group them as Type II mascons.

Namiki et al. (2009) suggest that the difference in the positive gravity anomaly amplitude between Type I and Type II mascons is likely due to differences in super-isostatic, dynamic uplift of the mantle during the thermal evolution of the Moon. Namiki et al. (2009) also speculate that the central positive gravity anomaly peak and the negative gravity anomaly annulus of Type II mascons are associated with: (1) brittle deformation of the lithosphere; and (2) mare volcanism. Brittle deformation induces a negative gravity signal because porous and brecciated rocks have lower density than the surrounding crust. Mare basalt and associated intrusions induce a positive gravity signal because they have a greater density than the surrounding crust.

Muller and Sjogren (1968) suggested that the positive gravity anomalies in Type I mascon basins are not associated with mare basalts. They argue this based on the observation that the magnitude of the anomaly exceeds what mare basalt could produce. Similarly, Andrews-Hanna et al. (2013) showed that mare basalts in Oceanus Procellarum are too thin to explain the mascons within Oceanus Procellarum. Using a hydrocode model that simulates the isostatic rise of the lunar mantle following an impact, Melosh et al. (2013) demonstrated that the bull's-eye gravity anomaly of lunar mascon basins can, instead, be explained by mantle rebound, flexure of the crust, and the cooling and contraction of a body of impact melt. Jozwiak et al. (2014) further speculated on the contribution of mare basalts to the gravity anomalies associated with lunar mascons. They proposed that the density contrast between high-density intrusions along

fractures and the low density, highly brecciated lunar crust on the impact basin floor should produce the observed high positive gravity anomalies.

Head and Wilson (1992) suggested that mare basalt alone could be responsible for the origin of the gravity anomalies in mascon basins. Mare basalts are fined grained basalts with olivine microphenocrysts and generally high density (3270 ± 10 to 3460 ± 50 kg/m^3). They are confined to the topographic depressions formed by lunar impact basins (Baldwin, 1971), predominantly on the lunar nearside. Head and Wilson (1992) estimated the total volume of mare basalt (~1 × 10^7 km^3) as a function of basin size and amount of basin subsidence. They suggested that the mass of mare basalt is large enough to cause impact basins to subside, resulting in the subsequent accumulation of thickened sequences of mare basalt and a positive gravity anomaly (Head and Wilson, 1992). However, this hypothesis does not explain the gravity signature of mascon basins that do not contain extensive mare basalt such as Mare Orientale. The majority of mare basalt is found in Mare Imbrium, with lesser amounts in Serenitatis, Crisium, Imbrium, and Humorum, and the least in mare Orientale. The mare Orientale basalts formed in early lunar history (3.8-3.6 Ga) whereas those in Mare Imbrium, Serenitatis, Crisium, Imbrium, and Humorum erupted later in lunar history (3.6-3.2 Ga; Head and Wilson, 1992).

2.2 Oceanus Procellarum

Oceanus Procellarum covers a 3,000-km wide area on the lunar nearside (Wieczorek and Phillip, 2000) and is considered to be one of the most geologically complex regions on the Moon (Warren and Wasson, 1979; Lawrence et al., 1999; Jolliff et al., 2000). Oceanus Procellarum is

thought to be the remnant of an ancient giant impact, although the impact origin of Oceanus Procellarum is still under debate (Wieczorek and Phillips, 1998). While Oceanus Procellarum contains local positive gravity anomalies associated with mascons (e.g. Mare Imbrium, Mare Sarenitatis, Mare Crisium), Procellarum itself is not considered a mascon basin (Sjogren and Wimberly, 1974; Wieczorek and Phillips, 1998; Joliff et al., 2000).

Oceanus Procellarum is the location of the youngest Mare basalts on the lunar nearside, particularly in Mare Imbrium and Mare Serenitatis (~1.5-1.6 b.y) (Hiesinger et al., 2000; Hiesinger et al., 2003). Hiesinger et al. (2003) estimated that the mare basalts in Oceanus Procellarum cover an area >4,000,000 km^2 and are several hundred meters deep. The composition of this basalt is dominated by potassium, rare-earth elements, and phosphorous (KREEP) and the area in which these KREEP basalts are found is called the Procellarum KREEP Terrane (PKT; Joliff et al., 2000). KREEP itself is a geochemical component found in only some lunar impact breccia and basaltic rocks and which contains significant amounts of elements that are usually concentrated in the magma during fractional crystallization. KREEP also contains significant amounts of the heat-producing elements uranium, thorium, and potassium (Warren and Wassan, 1979; Warren, 1985). It is estimated that the KREEP contains 300 times more uranium and thorium than chondrites (Joliff et al., 2000). Because of the large quantity of radiogenic heat producing elements KREEP contains, previous workers (Spudis et al., 1991; Ryder, 1997; Haskins, 1998) have hypothesized that KREEP may have been the heat source that contributed to the high volume of mare volcanic activity on the lunar nearside. Wieczorek and Phillips (2000) focused on the role of sub-crustal heating for PKT in the thermal evolution of the Moon. Wieczorek and Phillips (2000) suggested in their model that there was a 10 km thick KREEP-rich layer with radiogenic heat producing elements emplaced beneath the PKT crust at

60 km depth. Wieczorek and Phillips (2000) suggested that the KREEP-rich layer should have been in a molten to partially molten state for most of the Moon's history, and persists long after the solidification of the Moon magma ocean. In their model, the PKT was represented as a spherical cap, axisymmetrically located above the conduction zone of this KREEP-rich layer. This model is also marginally consistent with elevated heat flow observed at the Apollo 15 site.

This long-lived molten KREEP-rich layer was speculated to have been produced by global differentiation during the cooling of lunar magma ocean. Wieczorek and Phillips (2000) stated that during the crystallization of the lunar magma ocean, KREEP-rich later were molten and trapped between the solid upper crust and the Moho. The composition of KREEP-rich layer is deriving from the residual the final crystallization product (urKREEP) from the early Moon's magma Ocean itself (Wieczorek and Phillips, 2000). Both Oceanus Procellarum and the KREEP-rich layer below it were subsequently modified by impact cratering process (Wieczorek and Phillips, 2000). Large impact events, such as that which formed Mare Imbrium, may have penetrated the entire lunar upper crust, exhuming KREEP from the lower crust and olivine rich rocks from the mantle (Wieczorek and Phillips, 2000). Grimm (2013) agreed with Wieczorek and Phillips, 2000 but also suggested that the possible model of the KREEP-rich layer below the PKT in Oceanus Procellarum was instead an ancient impact that resulted in the uplift of the lunar Moho (Grimm, 2013).

We speculate that, since not all impact basins are mascon basins, mascon formation is not dependent on the impact process alone but also requires other processes. We suggest that the existence of the molten KREEP-rich layer beneath the Oceanus Procellarum may play a major part of mascon formation. We postulate that the impact event done on the molten or partially molten KREEP basalt layer may disrupt and excavate the still molten KREEP basalt magma

chamber. Pre-impact crustal structure can control the amplitude of mantle relaxation and subsequent crustal deformation (Namiki et al., 2009). For example, ductile deformation after an impact can increase the density contrast between the impact basin and the surroundings due to extension of the impact melt pool (Namiki et al., 2009). Brittle deformation can instead decrease the density contrast between the impact basin and the surroundings due to brecciation or intrusions facilitated by deep fracture zones caused by the impact (Namiki et al., 2009). Wieczorek and Phillips (2000) suggested that impact into a molten KREEP basalt magma chamber was also the reason why the materials from an ancient lunar magma ocean (urKREEP) were able to mix and melt into KREEP material.

2.3 Lunar Crustal Models

In this research, we utilize an inversion modeling method to gain insight into the formation lunar mascon basins. *A priori* geologic information (e.g., lithologies, densities, sizes and thicknesses of subsurface structures, etc.) is needed to constrain and to reduce the uncertainties of these inverse models. We refer to several crustal models by previous researchers (e.g. Wieczorek and Phillips, 1998; Yamamoto et al., 2010; Yamamoto et al., 2012; Wieczorek et al., 2013; Zuber et al., 2015; Andrews-Hanna et al., 2014) to constrain our models.

Based on surface reflectance data collected by the spectral profiler on the Kaguya spacecraft, the lunar crust is olivine-dominated with small quantities of admixed plagioclase (Yamamoto et al., 2010; Yamamoto et al., 2012). GRAIL crustal thickness models imply an average lunar crustal thickness of 34-43 km (Wieczorek et al., 2013), which is substantially thinner than previously thought (~60 km; Wieczorek and Phillips, 1998). The recent GRAIL crustal thickness models predict that the crust is nearly absent (<5-km thick) beneath nearside

impact basins such as Crisium and also beneath the farside Moscoviense basin (Wieczorek et al., 2013). The GRAIL crustal models also indicate that the average density of the lunar upper crust is markedly low (2580 ± 170 kg m^{-3}) due to impact fracturing (Wieczorek et al., 2013). The average lunar crustal (upper and lower crust) density is 2,900 kg m^{-3} and the average lunar mantle (upper and lower mantle) density is 3,400 kg/m^3 (Wiezorek and Phillips, 1998). Huang and Wieczorek (2012) estimate the lunar crustal density to be 2,590-2,870 kg m^{-3}. Kiefer et al. (2014) measured the bulk density of lunar rock samples and suggested a crustal density of 2,550 kg m^{-3} and a mantle density of 3,220 kg m^{-3}.

Spudis et al. (2014) showed that impact basins on the Moon are only partly flooded by mare basalt. A major portion of material exposed on the floor of lunar impact basins is the impact melt sheet. Zuber et al. (2015) demonstrated the thickness of the impact melt sheet in Mare Orientale is ~10 km thick. The bulk density of impact breccia and impact melt is 2,450-2,850 kg m^{-3} (Kiefer et al., 2014), however, the grain density of impact breccia and impact melt is as high as 2,990-3,100 kg m^{-3}. This high grain density implies that impact melt is primarily composed of mantle material, a result supported by hydrocode simulations of large impacts that eject most crustal material from the resulting basin (Potter et al., 2013; Melosh et al., 2013; Vaughan et al., 2013).

3. Methodology

3.1 GRAIL

The Gravity Recovery and Interior Laboratory (GRAIL) mission (Zuber et al., 2014) was designed to remotely map the lunar gravity field to address fundamental questions about lunar evolution. Understanding the lunar gravity field can provide insights into lunar internal structure, bulk composition, heat flow, and the duration of volcanism and tectonism. For this study we used the Radio Science Digital Map Product (RSDMAP) data products available from the Planetary Data System (PDS) LGRS RDR archive. These are derived from the GL0660A GRAIL lunar gravity model (Zuber et al., 2013). GL0660A is a degree and order 660 spherical harmonic model (truncated to degree and order 320) (Zuber et al., 2013). Because a single crustal density of 2,560 kg m^{-3} was assumed to create the available GL0660A Bouguer gravity anomaly map (Zuber et al., 2013), it may not be completely free of all topographic and terrain effects. We therefore choose to instead use the GL0660A free-air gravity anomaly map (Figure 2) for the purposes of this study. The free-air gravity anomaly map has a resolution of 4 pixels per degree, or ~7.6 km per pixel on a reference sphere with semi-major-axis radius of 1,738 km (Zuber et al., 2013). Each pixel gives the free-air gravity anomaly in milligals (mGal).

3.2 High-Pass Filtering and Low-Pass Filtering

We considered several kinds of filters (high pass, low pass filter and preferential filter) to understand the lunar free-air gravity signal spectrum and to isolate and suppress interfering signal from lunar shallow subsurface. We perform both low pass and high pass filtering on the GL0660A free-air gravity anomaly data. To perform a low pass filtering and remove the gravitational potential of short-wavelength, high-frequency anomalies arising from near surface

geology, we applied a low-pass filter operator to the free-air gravity anomaly map in the frequency domain. We developed a Gaussian low pass filter operator at the cutoff wavelength 10-degree. We then imported the GL0660A free-air gravity anomaly data into MATLAB and converted the free-air anomaly map from spatial domain to frequency domain. In frequency domain we convolve the free-air gravity signal with the low pass filter operator. The resulting low pass filtered signal is transformed back to the spatial domain, to obtain the low pass filtered free-air gravity anomaly map (Figure 3). With this low pass filter, only the gravity signals that are larger than 10-degree are isolated and the gravity signal produced from the geological features that are smaller than the 10-degree are suppressed. To perform high pass filtering, we created a high-pass filter operator by subtracting the low-pass filter operator from 1. By applying this high-pass filter operator to the unfiltered GL0660A free-air gravity anomaly signal in the frequency domain, we removed the long wavelength signal from the free-air gravity signal. We then converted the high pass filtered gravity signal back to the special domain to obtain a high-pass filtered gravity map that reveals short-wavelength, high-frequency anomalies belonging to near surface geology (Figure 4).

3.3 Power Spectrum of the Gravity Signal

The gravity signal is an ensemble of the gravitational effects of geologic features of varying depths, widths, thicknesses, and densities. To understand the various contributions to the gravity signal, we employ a power spectrum analysis approach. In the spatial domain, the total free-air gravity anomaly, $g_{fa}(x,y)$, is the sum of gravitational anomalies originating from the deep subsurface, $g_d(x,y)$, and gravitational anomalies originating from the shallow subsurface, $g_s(x,y)$ (Nettleton, 1957; Powlowski., 1994):

$$g_{fa}(x,y) = g_d(x,y) + g_s(x,y) \qquad (1).$$

Similarly, in the frequency domain, the Fourier power spectrum (P) of the total free-air gravity signal is the sum of the radially averaged power spectra of deep subsurface (P_{i+1}) and shallow subsurface (P_i) components (Naidu, 1968):

$$P = P_1 + P_2 + \cdots + P_i + P_{i+1} \qquad (2).$$

The power spectrum of the gravity signal due to a subsurface component i is an exponential function (Dampney et al, 1969; Guo et al., 2013):

$$P_i = s_i e^{-2k_i h_i} \qquad (3),$$

where h_i is the depth to subsurface layer I; k_i is the angular, or radial, frequency of its power spectrum; and the constant s_i is the strength, or intensity, of the gravitational signal associated with that layer (Dampney et al, 1969; Guo et al., 2013). Combining Equations (2) and (3) yields (Guo et al., 2013):

$$P = s_1 e^{-2k_1 h_1} + s_2 e^{-2k_2 h_2} + \cdots + s_i e^{-2k_i h_i} \qquad (4).$$

To analyze the power spectrum of the unfiltered lunar free air gravity signal, we imported the non-filtered GL0660A free-air gravity anomaly data into MATLAB (see Appendix A). We transformed the data into the frequency domain and calculated the radially averaged power spectrum (P) using the raPsd2d command (Figure 5). Similarly, to analyze the power spectrum of the low pass filtered and high pass filtered lunar gravity signal, we imported the low pass filtered and high pass filtered GL0660A free-air gravity anomaly data into MATLAB (see Appendix A), respectively, then transformed the data into the frequency domain and calculated

the radially-averaged power spectrum (P) using the raPsd2d command on both sets of data (Figure 6 and 7).

3.4 Power Spectrum Depth Analysis

To understand the geological process that contributes to lunar free air gravity signal, we apply average radial power spectrum analysis (Guo et al., 2013) to the unfiltered free-air gravity anomaly map, the high-pass filtered free-air gravity anomaly map, and the low-pass free-air gravity anomaly map. By this analysis, we can estimate the depth of the gravity signal and also gain *a priori* information about lunar crustal structure (e.g. thickness of the crust, depth to mantle, and depth of gravitational anomalies). Knowing the depth of gravity signal allows us to decide whether the gravity signal is appropriate to model with the given data. With the known depth of gravity signal we also are able to constrain the model. Upon the justification that the depth analysis results from all three types of lunar gravity anomaly maps are in agreements and the confirmation that the gravity signal from the shallow subsurface were completely removed from the low pass filtered gravity anomaly map, we then continued to the next step of preferentially filtering on the low pass free air gravity map only.

We used a method modified from Guo et al. (2013) and Spector and Grant (1970) to define the depth of gravity signal. This method relates average depths to source to rate of decay of the gravity power spectra. Under the presumption that: 1) the gravity signal from the same source depth with uniform distribution should also yield similar range of power spectrum and similar power decay rate (Spector and Grant, 1970); 2) the gravity signal from each source depth are independent from once another (Spector and Grant, 1970). We calculated the depths of the

gravity signal from the slope of power spectrum analysis plots (Figures 5-7). The shifting in decay rate of the power spectrum marks depth variation of the gravitational source. Our depth calculation method modified from Spector and Grant (1970) was implemented in MATLAB (see Appendix A). Using MATLAB, in the frequency domain, we plotted radially averaged power spectra (P) as a function of radial frequency, k, of all three lunar gravitation anomaly maps on a logarithmic scale (Figures 5-7). The MATLAB user must select the component of the radially averaged power spectrum (P) if the gravity signal profiles can be divided into sub-profiles following Spector and Grant's theory. P can be divided into several components (P_1, P_2,…, P_i) each representing the power of an individual subsurface layer (i.e. Equations (2) and (4)). Each component P_i contains several sub-profiles within it. To make sure that the assumed depth values from our calculations are in the closest agreement to the field condition as possible, we generated depths values from a synthetic component of P_i, called $P_{i,cal}$. Then by using least square method we can significantly reduce the variation of the mean and standard deviations between the sub-profiles (P_i) in comparison with the whole profile ($P_{i,cal}$). In MATLAB, we apply a piece-wise linearization (using the lsq_lut command in MATLAB) to fit straight-line segments to each power spectrum component (P_i). These fits provide the best fit synthetic power spectrum of $P_{i,cal}$ for each layer (P_i) . Each segment of the power spectrum is from a different depth inside lunar crust, and we can estimate the depth from the piece-wise best-fit segments. Depth (h_i) for each subsurface component can be calculated (Guo et al., 2013) using (Wiener et al., 1949; Guo et al., 2013):

$$h_i = \frac{P_i(k_i) - P_{i+1}(k_{i+1})}{4\pi(k_i - k_{i+1})} \qquad (5),$$

where k_i and k_{i+1} are the starting and ending radial frequencies of a given spectral segment and $P(k_i)$ and $P(k_{i+1})$ are the values of the radially averaged power spectra (in cycles per km) at the

start and end of a given spectral segment (Spector and Grant, 1970; Guo et al., 2013) (Figures 5-7).

Because picking spectral segments on the power spectrum plot can be very subjective, in additional to the radially averaged power spectra plot, we also plot the first- and second-derivatives of the power spectrum (Figure 5-7). The first- and second-derivative plots reveal the continuum of the Moon's gravitational signal in term of power spectrum and radial frequency. Where the changes in the power spectrum decay rate are significant (from minimum rate to maximum rate or vice versa), there is a prominent spike (positive spike or negative spike) on the first- and second-derivative plots. We can use those spikes to define the locations where the power spectrum trend had shifted. The first- and second-derivative plots allow the selection of spectrum segments to be done more precisely, less subjectively, and more consistently.

Now that user can identify the variation of source depth on the radially averaged power spectra more accurately and precisely, following Wiener's filtering theory (Wiener 1980; Guo et al., 2013), the user can selectively filter the desired gravity signal spectra from a source depth of interest. This preferentially filtering method is described in Section 3.5. We further studied the selected signal using gravity 2D inversion method (see Section 3.6).

3.5 Preferential Filtering and Gravity Anomaly Separation

The preferential filtering method is similar to frequency-domain Wiener filtering (Spector and Grant, 1970; Wiener, 1949). We use this method to filter the low-pass filtered free-air gravity anomaly data at a specific bandwidth in order to selectively retrieve the gravity signal associated with a specific depth (Spector and Grant, 1970; Wiener, 1949; Guo et al., 2013). The

Wiener preferential filtering operator we use is in this form (Spector and Grant, 1970; Wiener, 1949):

$$W_{pfi} = \frac{P_{i,cal}}{P_i} \qquad (6),$$

where P_i is the power spectrum of the gravity signal of subsurface component i and $P_{i,cal}$ is the calculated synthetic power spectrum of subsurface component i.

To perform the preferential filtering, we imported the low pass filtered GL0660A free-air gravity anomaly data into MATLAB. We used Equation (6) to generate the Wiener preferential filtering operator (W_{pfi}) to separate gravity signal from geological layer i at the depth of h_i apart from other gravity signal assembly. By replacing the obtained radially-averaged power spectrum component (P_i) and the calculated synthetic power spectrum ($P_{i,cal}$) from the previous Section 3.4) into equation (6), we retrieve the Wiener preferential filtering operator (W_{pfi}). In MATLAB, using matrix multiplication command, we apply the W_{pfi} filtering operator of the target layer to our low pass filtered gravity data in the frequency domain to filter the gravity signal from target layer i (Guo et al., 2013; Weiner, 1949). We then apply an inverse Fourier transformation to the result to yield the filtered free-air gravity anomaly associated with target layer i in the spatial domain (Figure 8 and 9; see Appendix A). With the preferential filtering method we make the assumption that gravity anomalies isolated with a given depth are independent of gravity anomalies at other depths, specifically with no amplification and downward continuity between each other.

3.6 Two-Dimensional Inversion Modeling

To resolve the internal structure of the lunar crust, we built inverse models from the low-pass and preferentially filtered free-air gravity anomaly data using *Geosoft Oasis Montage v. 6.2*. Because *a priori* geologic information (e.g. seismic data, boreholes, magnetic data, etc.) for the Moon is limited, our models were mainly constrained using surface geological features such as the distribution of mare and highlands lithologies (Weiczorek et al., 2006; Kiefer et al., 2012). The results of the gravity models are particularly dependent on the densities we choose for these lithologies.

The models include the following density values: for mafic intrusions, we use the density of mare basalt (3,150 $kg.m^{-3}$) (Zuber et al., 2014; Weiczorek et al., 2006; Kiefer et al., 2012); for the lunar crust we use an average density of 2,560 $kg.m^{-3}$ (Zuber et al., 2014; Weiczorek et al., 2013; Keifer et al., 2012); and, for impact melt, we use a density of 2,770 $kg.m^{-3}$ (Kiefer et al., 2015; Zuber et al., 2015). The lunar crustal thickness, also used as a constraint in our models, is approximately 10-30 km in the PKT and 35-55 km in the lunar highlands (Miljkovic et al., 2015; Vaughan et al., 2013;). When modeling depths greater than 30 km, we use a density of 3,000 $kg.m^{-3}$ for the lower crust (Vaughan et al., 2013) and 3,300 $kg.m^{-3}$ for the upper mantle (Vaughan et al., 2013).

The results of our power spectrum depth analysis, (see Results), are also used as an additional depth constraint. We also adjusted our model based on *a priori* knowledge of the impact basin-forming processes. For example, *a priori* information previously indicated the thickness of impact melt sheet are speculated to vary from 1s-10s km thick (Zuber et al., 2015; Andrews-Hanna, 2014), so we adjusted and varied the thicknes of our model accordingly to see which thickness makes the most sense for our model. Most impacts that form craters >300 km in

diameter produce enormous volumes (>105 km^3) of impact melt (Abramov et al., 2012). Abramov et al. (2012) suggest, based on models of impact melt production and topographic data, that the impact melt produced by the Orientale-forming impact formed a 15.5 km thick impact melt sheet. Accordingly, the thickness of the impact melt sheets in our models is adjusted proportionally for impact basins that are larger or smaller than Mare Orientale.

We constructed a total of four 2D inversion models from the low-pass and preferentially filtered free-air gravity anomaly map. To begin model construction, we assigned a simple, two-layer crustal structure to each model in areas outside of mascon basins. The upper layer is the lunar crust and lower layer is lunar mantle. For mascon basins, we assigned a three layer crustal: (1) an uppermost impact melt sheet; (2) underlying brecciated crust; and (3) uplifted mantle at the bottom. Each component layer in the model was assigned an appropriate density, depth, and cross-sectional width. We then used Euler deconvolution (Phillips, 2007), as implemented in *Geosoft Oasis Montage v. 6.2*, to calculate the predicted gravity anomaly based on the thickness, size, and density each model component. The dimensions and densities of the modeled geologic bodies were iteratively adjusted to minimize the RMS misfit between the calculated gravity anomaly and the observed gravity anomaly. Models were considered reliable if the RMS misfit was less than 10%.

4. Results

4.1 Radially-Averaged Power Spectrum of the Lunar Gravity Signal

Figures 3 and 4 show the low-pass and high-pass filtered free-air gravity maps, respectively. The low-pass filtered gravity signal contains mostly long-wavelength, low-amplitude (3 to 96 mGal), and high-degree power spectrum. The high-pass filtered gravity signal contains mostly short-wavelength, high-amplitude (-77 to 156 mGal), and low-degree power spectrum.

Using the method of Spector and Grant (1970) to analyze the radially averaged power spectra of the unfiltered and filtered free-air gravity maps, we estimate the depths corresponding to the dominant gravity signals. We find that the unfiltered, lunar free-air gravity signal includes components at depths of 4.0 km, 8.8 km, 15.6 km, and 53.7 km (Figure 5). The power spectrum depth analysis of the high-pass filtered free-air gravity data shows short wavelength, high amplitude, and low degree power components at depths of 8.4 km, 8.9 km and 12.9 km (Figure 6). The power spectrum analysis of the low-pass filtered free-air gravity data suggests that long-wavelength, low frequency gravity anomaly sources are located at depths of 11.9 km, 16.2 km, and 30 km (Figure 7).

The unfiltered and high-pass filtered free-air gravity data is not appropriate for 2D inversion modeling because: (1) the depths obtained are all smaller than the Nyquist wavelength (~15.2 km, or twice the resolution) of the GL0660A free-air gravity data; and (2) the gravity signal of short-wavelength anomalies contains high amplitude noise (Figures 4 and 6) due to surface excavation produced by impacts and due to mare basalt that filled in the basins (Zuber et al., 2015). The most effective method to eliminate these high frequency signals from our

analysis is to only consider the low-pass filtered free-air gravity data. We believe the low-pass filtered free-air gravity data is more appropriate for 2D inversion modeling because: (1) the 16.2 km and 30 km depths obtained are larger than the ~15.2 km Nyquist wavelength; and (2) the 30 km depth is consistent with the average crustal thickness of the Moon (~34 km; Wieczorek et al., 2012). The 2D inversion model of the gravity signal from 30 km depth should, therefore, reveal the structure of the lunar Moho. The 16.2 km signal may be related to important crustal features such as the thickness of the crust under the PKT (Wieczorek et al., 2012), mare basalt (Zuber et al., 2015), intrusions (Zuber et al., 2015), and the uplifted Moho underneath large impact basins (Zuber et al., 2015). Because it is smaller than the Nyquist wavelength, we do not consider the 11.9 km depth in our modeling.

4.2 Low-Pass and Preferentially Filtered Free-air Gravity Anomaly Maps

Prior to modeling, we used the preferential filtering method (Section 3.2) to isolate the gravity anomalies associated with 16 km and 30 km depths from the low-pass filtered free-air gravity map. The results are shown in Figures 8 and 9. Figure 8 shows that the low-pass and preferentially filtered gravity anomaly map for 16 km depth has magnitudes between -10 and 102 mGal. Figure 9 shows that the low-pass and preferentially filtered gravity anomaly map for 30 km depth has magnitudes between -3 and 17 mGal. Dashed and solid white ovals in Figure 8 and 9 show the locations of Type I and Type II mascon basins. We found that all mascon basin features remain on both filtered maps. Both low pass filtering and preferentially filtering process does not remove the mascon basin features from the filtered maps. At 16 km depth, Type I mascons, which do not exhibit bull's-eye features, exhibit positive gravity anomalies with amplitudes from +50 to +102 mGal (Figure 8). At 30 km depth, Type I mascons, which also do

not exhibit bull's-eye features, exhibit positive gravity anomalies with amplitudes from +11 to +18.5 mGal (Figure 8). All Type II mascons have positive gravity anomalies with amplitudes between +30 and +50 mGal at a depth of 16 km and have amplitudes between +5 and +10 mGal at a depth of 30 km (Figure 9). Most of the Type II mascons do not exhibit bull's-eye features at 16 km depth, except for Mare Orientale and Mendel Rydburg, which do (Figure 8). To begin the modeling process, we select transects where the greatest positive magnitude of anomaly are found. Because positive gravity anomalies are normally associated with large density contrasts in the subsurface (Milsom, 2007), hence mascon basin should be allocated to the area of high positive gravity anomalies. At depths of 16 and 30 km, the largest positive anomalies (>100 mGal) are found along latitude 37°N in Mare Imbrium, a Type I mascon basin (Figure 8). At depths of 16 and 30 km, the largest positive anomalies associated with Type II mascon basins (~60 mGal) are found in Mare Orientale along latitude 20°S (Figure 9). Because of this, we choose transects along those latitudes for our 2D inversion modeling.

4.3 Two-Dimensional Inversion Model of the Low-Pass Filtered and Preferentially Filtered Free-air Gravity Anomaly

We constructed four 2D inversion models (Figures 10 and 11): (1) for 16 km depth along transect A-A'; (2) for 16 km depth along transect B-B'; (3) for 30 km depth along transect A-A'; and (4) for 30 km depth along transect B-B'. We are able to resolve the structure of major mascon basins in Oceanus Procellarum, the lunar near side, and the lunar far side. The RMS misfit between the inversion models and the filtered free-air gravity data is small. All misfits are less than 10 percent (4.0-9.7 %).

The 16-km model for transect A-A' suggests two 42-76 km diameter mafic intrusions beneath Oceanus Procellarum along latitude 37°N (Figure 10). The model also suggests bodies of impact melt with densities of 2,770 kg m^{-3} located within Mare Imbrium, Mare Serenitatis, Mare Crisium, Humboldtianum, and Moscoviense. The impact melt sheets do not appear to be symmetrical and their diameters vary. The diameters of the impact melt sheets beneath Mare Imbrium, Mare Serenitatis, Mare Crisium, Humboldtianum, and Moscoviense are 800-1000 km, 608-630 km, 364-486 km, 445-798 km, and 224-427 km, respectively (Figures 10). The thicknesses of the impact melt sheets in these basins also vary. The 16-km model for transect A-A' indicates the thickest impact melt sheet (extends to 25.14 km depth) is in Mare Imbrium. It also appears that there is no crustal material left below the impact melt sheet in Mare Imbrium. This is shown by the sharp transition from impact melt sheet to lunar Moho underneath Mare Imbrium and it suggests that the impact may have excavated the entire crust. The 16-km model for transect A-A' shows 3-6 km thick crust remains underneath Mare Serenitatis, Mare Crisium, Humboldtianium, and Moscoviense (Figure 10).

The 16-km model for transect B-B' indicates there are impact melt sheets in Mare Orientale, Mare Humorum, and Mare Nectaris (Figure 11). The diameters of the impact melt sheets within Mare Orientale, Mare Humorum, and Mare Nectaris are 170-308 km, 716-974 km, and 440-917 km, respectively (Figures 11). The thicknesses of the impact melt sheets in Mare Orientale, Mare Humorum, and Mare Nectaris are 18.4 km, 17.3 km, and 19.8 km, respectively. The 16-km model for transect B-B' suggests that the crust below Mare Orientale was not completely removed and that 8.9 km of crust remains (Figure 11). The model also shows that the crustal thicknesses underneath Mare Humorum and Mare Nectaris are 6.2-10.8 km (Figure 11). With no evidence of crustal removal due to mascon forming events, it also appears that the

thicker the impact melt sheet, the thinner the crust below the impact basin, as is the case in Mare Nectaris (Figure 11). Thicker impact melt sheets are likely due to larger impact events, which, as a result, also may remove more crust. The 16-km model for transect B-B' also suggests a 19-22 km diameter mafic intrusion beneath Oceanus Procellarum along latitude 20°S (Figure 11).

The 30-km models for transect A-A' and B-B' show that the lunar Moho has been uplifted to an approximate depth of ~30 km (Figure 10) beneath the northern latitude of Oceanus Procellrarum and to an approximate depth of ~22 km (Figure 11) beneath the southern latitude of Oceanus Procellrarum and to an approximate depth of 24 km underneath Mare Orientale (Figure 11).

All four models indicate the crustal thicknesses within the mascon basins on the lunar farside are ~10 km thicker than those on the nearside. The impact melt sheet within Mare Imbrium is the thickest (25.1 km). The second thickest impact melt sheet is found within Mare Nectaris (19.8 km). Although we constrained our models with the known densities of lunar lithologies (Keifer et al., 2015), in order to minimize the RMS misfits of the models we found that we must use a lower density than expected (2,460 $kg.m^{-3}$) for the crust underneath mascon basins. Kiefer et al. (2015) suggest that impact breccia can have a density as low as 2,450 $kg.m^{-3}$, similar to the density we use for the crust beneath mascons. This suggests that the crust beneath mascons could be highly fractured and its porosity increased substantially. This interpretation is also supported by other studies that show how large impacts can completely shatter the upper crust (Scott and Wilson, 2005; Milbury et al., 2015). Soderblom et al. (2015) studied the residual Bouguer gravity anomaly of the GRAIL data and concluded that the positive gravity anomaly values associated with mascon basins also correlate with high porosity in the surrounding crust. With these considerations in mind, we consider the low-density crust beneath

the mascons in our models to be brecciated crust underneath impact melt sheets. All four models indicate crust with a density of 2,460 kg m^{-3} below the impact melt sheets of most impact basins with the exception of Humboldtianum and Moscoviense, where the crust may not be brecciated as extensively, and Mare Imbrium where the crust was completely removed (Figures 10-11).

5. Discussion

Miljković et al. (2015) speculated during basin-forming events complete crustal excavation might have occurred in several of the largest impact basins on the nearside as well as the Moscoviense basin on the farside. Our results suggest that total crustal removal and mantle excavation are not as common as previously thought (Zuber et al., 2015; Wieczorek and Phillips, 1998; Miljkovic et al., 2015). Among the seven mascon basins included in our model transects, only Mare Imbrium may have completely lost its crust. Our results are compatible with those of Andrews-Hanna et al. (2014) who present an inversion model of Oceanus Procellarum using the GRAIL GL0420A Bouguer anomaly data. Their results suggest that Oceanus Procellarum is a mare filled depression and that the underlying feldspathic crust extends to a depth of 34 km. Below the feldspathic crust is uplifted lunar Moho (Andrews-Hanna et al., 2014). In some places underneath the Oceanus Procellarum, the uplifted lunar Moho can be as shallow as ~8 km from the lunar surface (Andrews-Hanna et al., 2014).

Our models suggest that the feldspathic crustal materials within Oceanus Procellarum are very porous and brecciated and that the thickness of this feldspathic crust in Oceanus Procellarum varies from 0 km to 22 km. The thickness of the feldspathic crust within major mascon basins such as Mare Serenitatis, and Mare Crisium is very thin (<5km) and, according to our model results, there is no crustal material left in Mare Imbrium. Our model also suggests that the maximum uplift of the lunar Moho (up to 22 km) occurred toward the south side of Oceanus Procellarum. This pattern in lunar Moho depths is compatible with the most recent GRAIL-derived lunar crustal thickness models (Wieczorek et al., 2013) that also predict the absence of the crust (<5 km) beneath some of the nearside impact basins.

Both of the 16-km models suggest several areas of large positive anomalies (>50 mGal) are associated with Type I mascon basins (Mare Imbrium, Mare Serenitatis, Mare Crisium, Humboldtianum, and Mare Nectaris) and smaller positive gravity anomalies (<25 mGal) are associated with Type II mason basins (Mare Orientale, Humboldtianum, and Moscoviense). Both 2D-inverse models from 16-km depth suggest that the positive gravity anomalies of large impact basins are the result of extensive crustal fracturing. The density of the crust below the impact basins in our model is lower than the average feldspathic crust, which may be because of impact-related brecciation and fracturing. We note that the highest positive anomaly of any mascon basin (Mare Imbrium) is caused by a body of moderate-density impact melt overlying a body of low-density fractured crust. Together, these bodies yield a high-density contrast, which causes a positive gravity anomaly signal.

Both 16-km models suggest two, 19-70 km diameter mafic intrusions underneath Oceanus Procellarum. Along the 20°S model transect, the model indicates one intrusion zone located approximately at 45°W. Along the 37°N transect, the model indicates two intrusion zones located approximately at 50°W and 100°E. The mafic intrusions revealed in our models are not associated with any mascon basin in particular (Figures 10 and 11), but, instead, they may be associated with previously identified cryptomaria that have been interpreted by previous workers to be the frozen remnants of lava-filled rifts and underlying feeder dikes (Miljkovic et al., 2015; Whitten and Head, 2015). We are not certain of the origin of the mafic intrusions, but our 30-km inversion models show that the roots of the mafic intrusions are connected to the zone of uplifted upper mantle beneath Oceanus Procellarum.

All four inversion models reveal important differences between Type I and Type II mascon basins. We found that Type I mascon basins show larger positive anomalies (>100

mGal) than Type II mascon basins (~60 mGal). We found that all Type I mascon basins share the following characteristics: (1) they contain larger and thicker impact melt sheet bodies than Type II mascon basins; (2) the crust below their impact melt sheets tends to be very thin (<6 km) compared to the crust below impact melt sheets in Type II mascon basins (~6-10 km); (3) they are associated with uplifted Moho at shallow depths (30-22 km); and (4) all Type I mascon basins are located within the boundary of Oceanus Procellarum. For Type II mascon basins, we found these common characteristics: (1) they have 25% thinner impact melt sheets than Type I mascon basins; (2) the crust below the impact melt sheet is thick (~6-10 km); (3) they do not always have an uplifted Moho at shallow depths (22-30 km); and (4) all Type II mascon basins are located outside Oceanus Procellarum.

We conclude that only very large impact events such as that which formed Mare Imbrium could trigger total crustal removal. For the Mascon basins that are smaller than Mare Imbrium, our model indicated that the bodies of lightly lower density than the average lunar crustal density still remain below the bodies of impact melt sheet. We speculated that large, mascon-forming impact events would have excavated the majority of the crust but not all of the crustal material and formed extensive impact melt sheets. Our modeling shows a maximum depth of melting of 16-25 km (depending on impact angle and impact velocity). Below the impact melt zone, we find a crustal density of 2,460 kg m^{-3}, which is lower density than the average feldspathic crust. This low-density crust indicates that the crust is highly porous and fractured, most likely due to impact brecciation. Underneath the crater floor is uplifted Moho. Our models suggest high-density zones of uplifted lunar Moho are also located at the thinnest part of mascon basins.

To validate the internal structure of Lunar Mascon basins obtained from our models, we compared our results to the well-known terrestrial impact basin, the Sudbury impact structure in

Ontario, Canada. We found that our model of lunar crustal structure and the structure of mascon basins is similar to the results of numerical modeling of the Sudbury impact structure in Ontario, Canada (i.e. Milkereit et al., 2010). The Sudbury impact structure differs from other known terrestrial impacts on Earth for its enormous size and features that more assimilate to impacts from other planetary system. The Sudbury impact structure including Chicxulub and Vredefort is one of the largest impact structures (> 250 km) on Earth. Only the Sudbury structure is hosting the remnant of solidified impact melt that overlays impact breccia and erosional relic of deformed multi ring impact basin (Riller, 2005; Pope et al., 2004). Another distinctive feature of the Sudbury impact structure is the fractured crater floor and associated dikes that are well preserved and can be seen in high-resolution topographic data (Milkereit et al., 2010). Because of the great thickness and mineralogic layering of the impact melt sheet, impact breccia, fractures crater floor similar to mineralogic layering of Lunar impact basin, the Sudbury impact structure can be used to identify with our lunar impact basin model. Our impact basin model suggests a different interpretation of lunar crustal structure and the structure of mascon basins than the model of Zuber et al. (2015). Comparing to the Sudbury impact structure, we found that our model provides mascon impact basin structure that resemble the structure of the Sudbury impact. We instead suggest that at least 8.9 km of brecciated crust remains between above the Moho beneath Mare Orientale similar to the Sudbury impact structure.

Previous gravity models of lunar impact basins suggested that most large impact basins completely excavated through the crust. For example, the gravity model of the Orientale basin at 3-5 km depth by Zuber et al. (2015) suggests a sharp transition between the basin floor and the uplifted Moho and implies that the basin-forming impact completely excavated the crust beneath Mare Orientale.

Based on our interpretations of Type I and Type 2 mascons, we conclude that variable styles of deformation occur as a result of large impact events, resulting in variable gravity anomaly signatures among major mascon basins. Both pre- and post-impact crustal structure and type greatly affect impact-induced deformation mechanisms of the mascon basins. In the early history of the Moon, the lunar farside crust may have been supported by a rigid lithosphere, whereas the lunar nearside crust (especially in Oceanus Procellarum and the PKT) may have been underlain by a molten KREEP-rich layer (Wieczorek and Phillips, 2000). The exponential rate of magma ocean crystallization indicates the KREEP-rich layer may have continued solidification and remained molten for an extra 200–400 million years or longer than the rest of the magma ocean (Wieczorek and Phillips, 1998; Wieczorek and Phillips, 2000; Nemchin et al., 2009). The age of KREEP-rich layer solidification were between 3.8 and 4.6 Gyr (Borg et al., 2004). Our suggestion is also supported by Mare Imbrium's weighted average age of impact at 3938 ± 4 Ma (Merle et al., 2014) that was older than the age of the KREEP-rich layer solidification. The coherence timing between the age of the KREEP-rich layer solidification and the timing of Mare Imbrium's impact indicates that Mare Imbrium's impactor may have hit the still molten KREEP rich layer and resulted in a complete removal of the brecciated crust as shown in our model.

The brittle deformation of the crust on lunar farside left behind a vast area of brecciated crust below impact melt sheets. The impact into the brittle target instead of the ductile flow regime could release more ejecta (Comerford, 1967). The negative density contrast between thick, brecciated crust, thick layer of loose ejecta, and the impact melt sheets can be seen as a negative ring in the bull's eyes gravity signatures typical of Type II mascons. In contrast, the impact onto the possibly ductile target on lunar near side, left behind only little to no brecciated

crust. The positive density contrast between thin brecciated crust, thin layer of loose ejecta, and thick impact melt sheets, and uplifted Moho can be seen as an extensive positive anomaly in the center of the bull's eyes gravity signatures typical of Type I mascons.

6. Conclusions

We performed power spectrum analysis on the GRAIL GL0660A lunar free-air gravity dataset and, for the major mascon basins on the Moon, we were able to quantify the size and thicknesses of impact melt sheets, the thickness and the density of crust below crater floors, and the elevation of uplifted lunar upper mantle. Our power spectrum analysis provides an understanding of lunar crustal structure, including the depth of prominent gravity signals and depth constraints for 2D gravity inversion models. Our power spectrum analysis results appear to be compatible with other lunar gravity studies (Zuber et al., 2015; Wieczorek and Phillips, 1998; Miljkovic et al., 2015; Andrews-Hanna et al., 2014). The low pass and preferential filtering approaches we use allow us to eliminate the high frequency gravity signal due to highly impacted subsurface from the total lunar free-air gravity anomaly. As a result, we are able to selectively perform inverse modeling on the gravity signal arising from features at a known depth and are also able to constrain the model with *a priori* knowledge from that depth.

Aside from the regional crustal structure that we are able to resolve, we are also able to model the detailed structure of several Type I (Mare Imbrium, Mare Serenitatis, Mare Crisium, Mare Nectaris, Humboldtianum) and Type II (Mare Orientale, and Moscoviense) mascon basins. Based on our model results, we suggest that the sources of the high gravity anomalies associated with mascon basins are: (1) impact melt sheets; (2) impact breccia; and (3) uplifted, shallow Moho. We conclude that the outer negative rings of the bull's-eye gravity signature of Type I mascons are due to low-density contrasts in the upper lithosphere. The upper lithosphere mainly consists of loose material ejected during the excavation stage of crater formation (Comerford, 1967). The high amplitude positive gravity anomaly (>60 mGal) of Type I mascon basins is directly influenced by the high density contrasts between shallow lunar mantle (3,220 kg m^{-3}),

very thin brecciated crust (2,460 kg m^{-3}), and moderate density impact melt sheets (2,770 kg m^{-3}), for example in Mare Imbrium and Mare Serenitatis (Figures 10 and 11, transect A-A'). The lower amplitude positive gravity anomaly (<50 mGal) of Type II mascon basins is directly influenced by thicker brecciated crust (2,460 kg m^{-3}) and a deeper Moho, both of which result in a reduced density contrast as seen in Mare Orientale and Moscoviense (Figures 10-11, transect A-A' and B-B').

References

Abramov, O., Wong, S. M., and Kring, D. A., 2012, Differential melt scaling for oblique impacts on terrestrial planets: *Icarus*, vol. 218, no. 2, p. 906-916.

Andrews-Hanna, J. C., Besserer, J., Head III, J. W., Howett, C. J., Kiefer, W. S., Lucey, P. J., McGovern, P.J., Melosh, H.J., Neumann, G.A., Phillips, R.J., Schenk, P.M., Smith, P.M., Solomon, S.C., and Zuber, M. T., 2014, Structure and evolution of the lunar Procellarum region as revealed by GRAIL gravity data: *Nature*, vol. 514, p. 68-71.

Baldwin, R. B., 1971, On the history of lunar impact cratering: The absolute time scale and the origin of planetesimals: *Icarus*, vol. 14, no. 1, p. 36-52.

Bratt, S. R., Solomon, S. C., and Head, J. W., 1985, The evolution of impact basins: Cooling, subsidence, and thermal stress: *Journal of Geophysical Research*, vol. 90 (B14), p. 12,415-12,433.

Borg, L. E., Shearer, C. K., Asmerom, Y., and Papike, J. J., 2004, Prolonged KREEP magmatism on the Moon indicated by the youngest dated lunar igneous rock. *Nature*, vol. 432(7014), p. 209-211.

Cook, A. C., Watters, T. R., Robinson, M. S., Spudis, P. D., and Bussey, D. B. J., 2000, Lunar polar topography derived from Clementine stereoimages: *Journal of Geophysical Research*, vol. 105 (E5), p. 12,023-12,033.

Comerford, M. F., 1967, Comparative erosion rates of stone and iron meteorites under small-particle bombardment. *Geochimica et Cosmochimica Acta*, vol. 31, p. 1457–1471.

Dampney, C. N. G., 1969, The equivalent source technique: *Geophysics,* vol. 34, no. 1, p. 39-53.

Grimm, R. E. and Mcsween, H. Y., 1989, Water and the thermal evolution of carbonaceous chondrite parent bodies: *Icarus*, vol. 82, no. 2, p. 244-280.

Grieve, R. A. F. and Cintala, M. J., 1992, An analysis of differential impact melt-crater scaling and implications for the terrestrial impact record: *Meteoritics*, vol. 27, no. 5, p. 526-538.

Guo, L., Meng, X., Chen, Z., Li, S., and Zheng, Y., 2013, Preferential filtering for gravity anomaly separation: *Computers & Geosciences*, vol. 51, p. 247-254.

Haskin, L. A., 1998, The Imbrium impact event and the thorium distribution at the lunar highlands surface: *Journal of Geophysical Research*, vol. 103 (E1), p. 1,679-1,689.

Hiesinger, H., Head, J. W., Wolf, U., Jaumann, R., and Neukum, G., 2003, Ages and stratigraphy of mare basalts in Oceanus Procellarum, Mare Nubium, Mare Cognitum, and Mare Insularum: *Journal of Geophysical Research*, vol. 108 (E7), p. 1-27.

Head, J. W. and Wilson, L., 1992, Lunar mare volcanism: Stratigraphy, eruption conditions, and the evolution of secondary crusts: *Geochimica et Cosmochimica Acta*, vol. 56, no. 6, p. 2,155-2,175.

Jolliff, B. L., Gillis, J. J., Haskin, L. A., Korotev, R. L., and Wieczorek, M. A., 2000, Major lunar crustal terranes: Surface expressions and crust-mantle origins: *Journal of Geophysical Research*, vol. 105 (E2), p. 4,197-4,216.

Jozwiak, L. M., Head, J. W., and Wilson, L., 2015, Lunar floor-fractured craters as magmatic intrusions: Geometry, modes of emplacement, associated tectonic and volcanic features, and implications for gravity anomalies: *Icarus*, vol. 248, p. 424-447.

Kiefer, W. S., Macke, R. J., Britt, D. T., Irving, A. J., and Consolmagno, G. J., 2014, The Density and Porosity of Lunar Impact Breccias and Impact Melt Rocks and Implications for GRAIL Gravity Modeling of the Orientale Impact Basin Structure: *Geophysical Research Letters,* vol. 41, p. 5,771-5,777.

Konopliv, A. S., Asmar, S. W., Carranza, E., Sjogren, W. L., and Yuan, D. N., 2001, Recent gravity models as a result of the Lunar Prospector mission: *Icarus*, vol. 150, no. 1, p. 1-18.

Merle, R. E., Nemchin, A. A., Grange, M. L., Whitehouse, M. J., and Pidgeon, R. T., 2014, High resolution U-Pb ages of Ca-phosphates in Apollo 14 breccias: Implications for the age of the Imbrium impact. *Meteoritics & Planetary Science*, vol. 49(12), p.2241-2251.

Melosh, H. J., Freed, A. M., Johnson, B. C., Blair, D. M., Andrews-Hanna, J. C., Neumann, G. A., and Zuber, M. T., 2013, The origin of lunar mascon basins: *Science*, vol. 340, no. 6,140, p. 1,552-1,555.

Miljković, K., Wieczorek, M. A., Collins, G. S., Solomon, S. C., Smith, D. E., and Zuber, M. T., 2015, Excavation of the lunar mantle by basin-forming events on the Moon: *Earth and Planetary Science Letters*, vol. 409, p. 243-251.

Milkereit, B., Artemieva, N., and Ugalde, H., 2010, Fracturing, thermal evolution and geophysical signature of the crater floor of a large impact structure: The case of the Sudbury Structure, Canada, *in* Gibson, R.L. (ed.), *Large Meteorite Impacts and Planetary Evolution IV* (Geological Society of America Special Paper vol. 465), p. 103-113.

Milsom, J., 2007, *Field Geophysics (Vol. 25)*: John Wiley and Sons (University College London), 244 p.

Muller, P. M. and Sjogren, W. L., 1968, Mascons: Lunar mass concentrations: *Science*, vol. 161, no. 3,842, p. 680-684.

Naidu, P., 1968, Spectrum of the potential field due to randomly distributed sources: *Geophysics*, vol. 33, no. 2, p. 337-345.

Namiki, N., Iwata, T., Matsumoto, K., Hanada, H., Noda, H., Goossens, S., Ogawa, M., Kawano, N., Asari, K., Tsuruta., S., Ishihara, S., Lui, Q., Kikuchi, F., Ishikawa, T., Sasaki, S., Aoshima, C., Kurosawa, K., Sugita, S., and Takano, T., 2009, Farside gravity field of the Moon from four-way Doppler measurements of SELENE (Kaguya): *Science*, vol. 323, no. 5,916, p. 900-905.

Nemchin, A., Timms, N., Pidgeon, R., Geisler, T., Reddy, S., and Meyer, C., 2009, Timing of crystallization of the lunar magma ocean constrained by the oldest zircon. *Nature Geoscience*, vol. 2 (2), p.133-136.

Neumann, G. A., Zuber, M. T., Smith, D. E., and Lemoine, F. G., 1996, The lunar crust: Global structure and signature of major basins: *Journal of Geophysical Research*, vol. 101 (E7), p. 16,841-16,863.

Nettleton, L. L., 1942, Gravity and magnetic calculations: *Geophysics*, vol. 7, no. 3, p. 293-310.

Potter, R. W., Kring, D. A., Collins, G. S., Kiefer, W. S., and McGovern, P. J., 2013, Numerical modeling of the formation and structure of the Orientale impact basin: *Journal of Geophysical Research*, vol. 118, no. 5, p. 963-979.

Pawlowski, R. S., 1995, Preferential continuation for potential-field anomaly enhancement: *Geophysics*, vol. 60, no. 2, p. 390-398.

Ryder, G. and Taylor, G. J., 1976. Did mare-type volcanism commence early in lunar history: *Proceedings of the 7th Lunar and Planetary Science Conference*, v. 7, p. 1,741-1,755.

Ryder, G., Norman, M. D., and Taylor, G. J., 1997, The complex stratigraphy of the highland crust in the Serenitatis region of the Moon inferred from mineral fragment chemistry: *Geochimica et Cosmochimica Acta*, vol. 61, no. 5, p. 1,083-1,105.

Sjogren, W. L., Wimberly, R. N., and Wollenhaupt, W. R., 1974, Lunar gravity via the Apollo 15 and 16 subsatellites: *The Moon*, vol. 9, no. 1-2, p.115-128.

Sjogren, W. L. and Smith, J. C., 1976, Quantitative mass distribution models for Mare Orientale: *Proceedings of the 7th Lunar and Planetary Science Conference*, v. 7, p. 2,639-2,648.

Soderblom, J. M., Evans, A. J., Johnson, B. C., Melosh, H. J., Miljković, K., Phillips, R. J., and Zuber, M. T., 2015, The fractured Moon: Production and saturation of porosity in the lunar highlands from impact cratering: *Geophysical Research Letters*, vol. 42, no. 17, p. 6,939-6,944.

Spector, A. and Grant, F. S., 1970, Statistical models for interpreting aeromagnetic data: *Geophysics*, vol. 35, no .2, p. 293-302.

Spudis, P. D., Hawke, B. R., Lucey, P. G., Taylor, G. J., and Stockstill, K. R., 1996, Composition of the ejecta deposits of selected lunar basins from Clementine elemental maps: *Proceedings of the 27th Lunar and Planetary Science Conference*, v. 27, p. 1,255.

Vaughan, W. M., Head, J. W., Wilson, L., and Hess, P. C., 2013, Geology and petrology of enormous volumes of impact melt on the Moon: A case study of the Orientale basin impact melt sea: *Icarus*, vol. 223, no. 2, p. 749-765.

Whitten, J. L. and Head, J. W., 2015, Lunar cryptomaria: Physical characteristics, distribution, and implications for ancient volcanism. *Icarus*, vol. 247, p.150-171.

Wieczorek, M. A. and Phillips, R. J., 1998, Potential anomalies on a sphere: Applications to the thickness of the lunar crust: *Journal of Geophysical Research*, vol. 103 (E1), p. 1,715-1,724.

Wieczorek, M. A. and Phillips, R. J., 2000, The "Procellarum KREEP Terrane": Implications for mare volcanism and lunar evolution: *Journal of Geophysical Research*, vol. 105 (E8), p. 20,417-20,430.

Wieczorek, M. A., Neumann, G. A., Nimmo, F., Kiefer, W. S., Taylor, G. J., Melosh, H. J., and Zuber, M. T., 2013, The crust of the Moon as seen by GRAIL: *Science*, vol. 339, no. 6,120, p. 671-675.

Wiener, N., 1949, *Extrapolation, Interpolation and Smoothing of Stationary Time Series*: John Wiley & Sons (New York), 321 p.

Wilhelms, D. E., 1985, Unmanned spaceflights needed as scientific preparation for a manned lunar base: *Lunar Bases and Space Activities of the 21st Century*, v. 1, p. 245-251.

Wiseman, S. M., Donaldson Hanna, K. L., Mustard, J. F., Isaacson, P. J., Pieters, C. M., and Jolliff, B. L., 2012, Aristarchus olivine in context with circum-Imbrium olivine deposits: *Proceedings of the 2nd Conference on the Lunar Highlands Crust*, vol. 2, p. 61-62.

Yamamoto, S., Nakamura, R., Matsunaga, T., Ogawa, Y., Ishihara, Y., Morota, T., and Haruyama, J., 2010, Possible mantle origin of olivine around lunar impact basins detected by SELENE: *Nature Geoscience*, vol. 3, no. 8, p. 533-536.

Yamamoto, S., Nakamura, R., Matsunaga, T., Ogawa, Y., Ishihara, Y., Morota, T., and Haruyama, J., 2012, Massive layer of pure anorthosite on the Moon: *Geophysical Research Letters*, vol. 39, no. 13, p. 1-6.

Zuber, M. T., Smith, D. E., Lemoine, F. G., and Neumann, G. A., 1994, The shape and internal structure of the Moon from the Clementine mission: *Science*, vol. 266, no. 5,192, p. 1,839-1,843.

Zuber, M. T., Smith, D. E., Watkins, M. M., Asmar, S. W., Konopliv, A. S., Lemoine, F. G., Melosh, H. J., Neumann, G. A., Phillips, R. J., Solomon, S. C., Wieczorek, M. A., Williams, J. G., Goossens S. J., Kruizinga, G., Mazarico, E., Park, R. S., and Yuan, D. N., 2013, Gravity field of the Moon from the Gravity Recovery and Interior Laboratory (GRAIL) mission: *Science*, vol. 339, no. 6,120, p. 668-671.

Zuber, M. T., Smith, D. E., Goossens, S. J., Asmar, S. W., Konopliv, A. S., Lemoine, F. G., Melosh, H. J., Neumann, G. A., Nimmo, F., Phillips, R. J., Solomon, S. C., Watkins, M. M., Wieczorek, M. A., Andrews-Hanna, J. C., Head, J. W., Keifer, W. S., McGover, P. J., Nimmo, F., Taylor J. G., Besserer, J., Johnson, B. D., Miljkovic, K., Park, R. S., Soderblom, J. M., Blair, D. M., Mazarico, E., and Yuan, D. N., 2014, A high-resolution view of the Orientale basin and surroundings from the Gravity Recovery and Interior Laboratory (GRAIL): *Proceedings of the 45th Lunar and Planetary Science Conference*, v. 45, p. 2,061.

Zuber, M. T., Smith, D. E., Goossens, S. J., Andrews-Hanna, J. C., Head, J. W., Kiefer, W. S., Asmar., S. W., Konopliv, A. S., Lemoine, F. G., Matsuyama, I., McGovern, P. J., Melosh, H. J., Neumann, G. A., Nimmo, F., Phillips, R. J., Solomon, S. C., Taylor, G. J., Watkins, M. M., Wieczorek, M. A., Johnson B. C., Kean, J., Miljkovic, K., Park, R. S., Soderblom, J. M., Blair, D. M., Mazarico, E., and Yuan, D. N., 2015,. Gravity Field of the Orientale Basin from the Gravity Recovery and Interior Laboratory (GRAIL) Mission: *Proceedings of the 46th Lunar and Planetary Science Conference*, v. 46, p. 1,447.

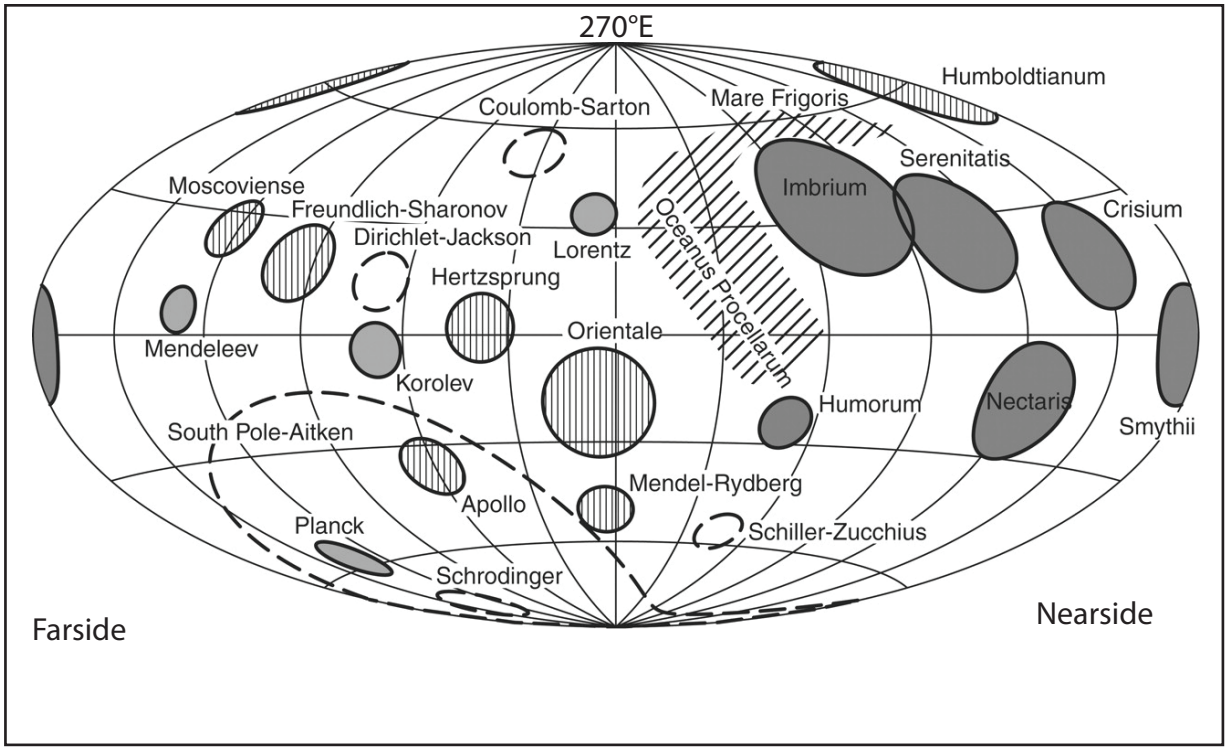

Figure 1. Locations of major lunar basins showed on the western side of the Moon viewed from Earth. The lunar nearside is to the right and the farside is to the left in this view. Dark shaded circles are Type I mascon basins which are Imbrium, Serenitatis, Crisium, Nectaris, Smythii, and Humorum. Hatched circles are Type II mascon basins which are Orientale, Hertzsprung, Moscoviense, Freundlich-Sharonov, Apollo, and Mendel-Rydberg. Circles with dashed lines are unclassified basins. Modified from Namiki et al. (2009).

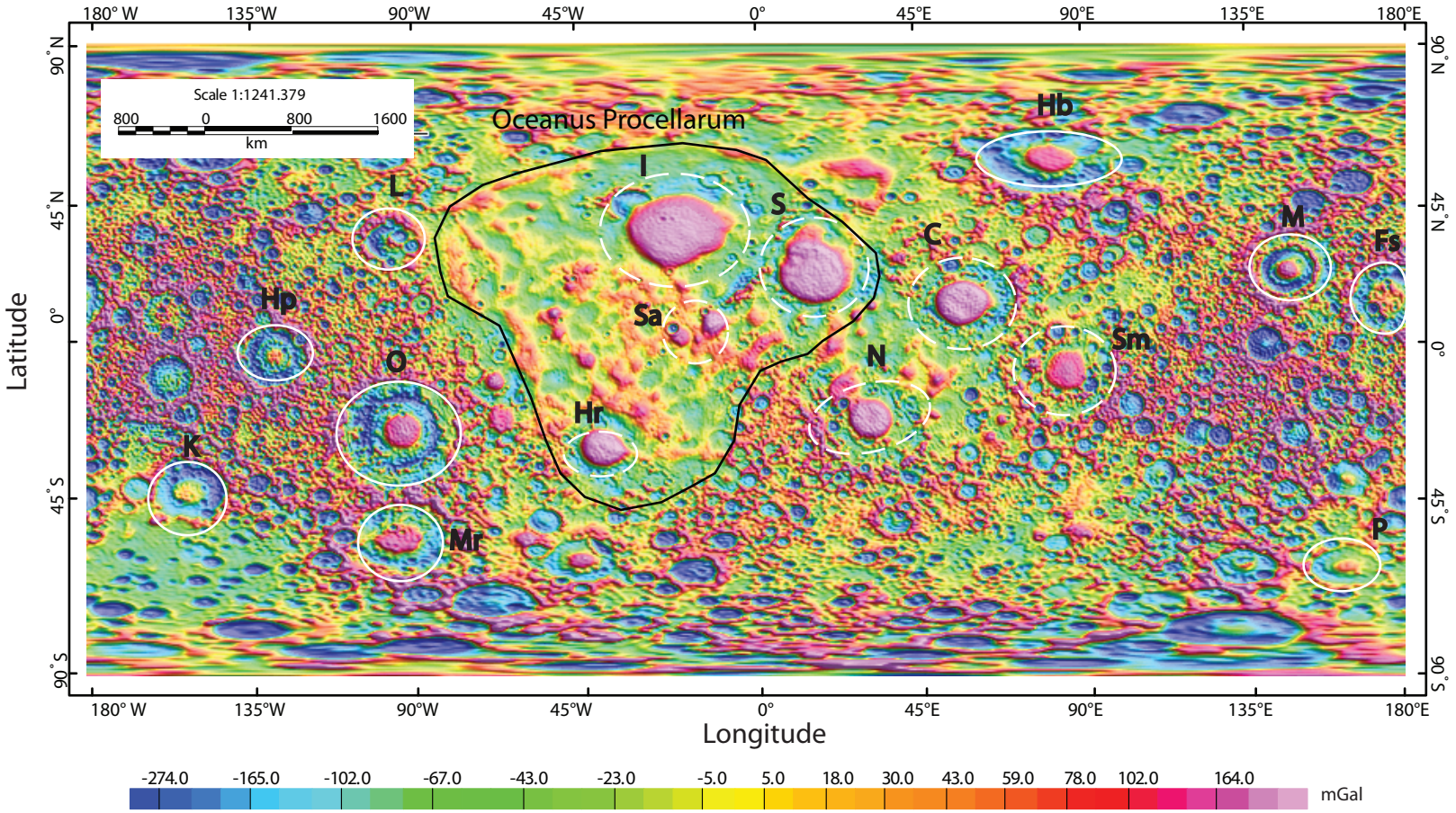

Figure 2. A GL0660A free-air gravity anomaly map. Dashed white circles are Type I mascons. Type I mascons show less prominent bull's eyes pattern and are located on Oceanus Procellarum (enclosed by black line) on the lunar nearside. Solid white circles are Type II mascons. Type II mascons show more prominent bull's eye surrounded with an annulus ring of negative anomaly. Type II mascons are located outside the Oceanus Procellarum (enclosed by black line) or on the lunar farside. I = Mare Imbrium, S = Mare Serenitatis, C = Mare Crisium, Hb = Humboldtianum, M = Moscoviense, O = Mare Orientale, Hr = Mare Humorum, N = Mare Nectaris, Mr = Mendel-Rydburg, Sm = Smythii, Fs = Freundlich-Sharonov, Hp = Hertzsprung, Sa = Sinus Aestuum, L = Lorentz, K = Korolev.

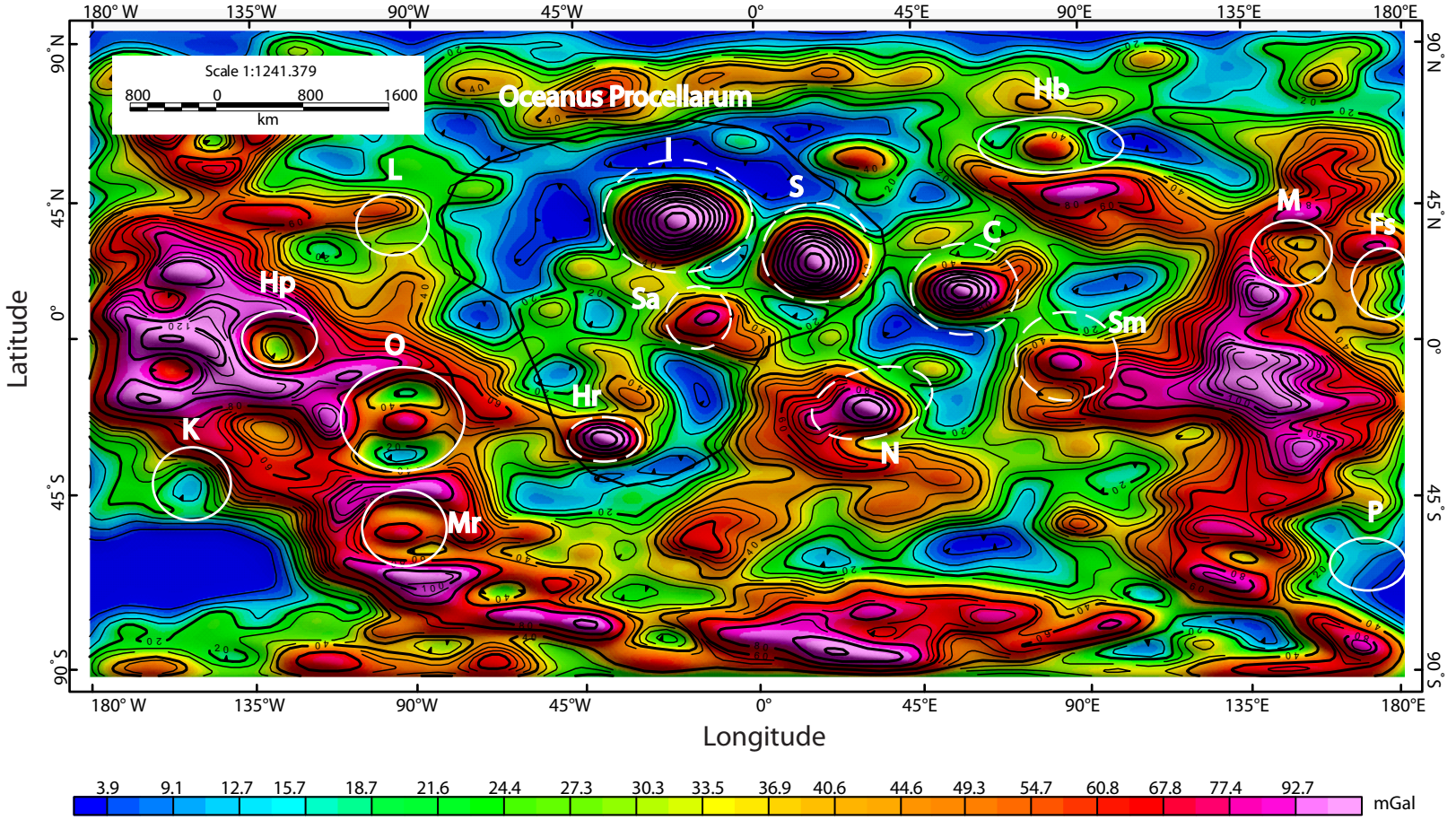

Figure 3. A low pass filtered GL0660A free-air gravity anomaly map. See Figure 2 for explanation of symbols and lettering.

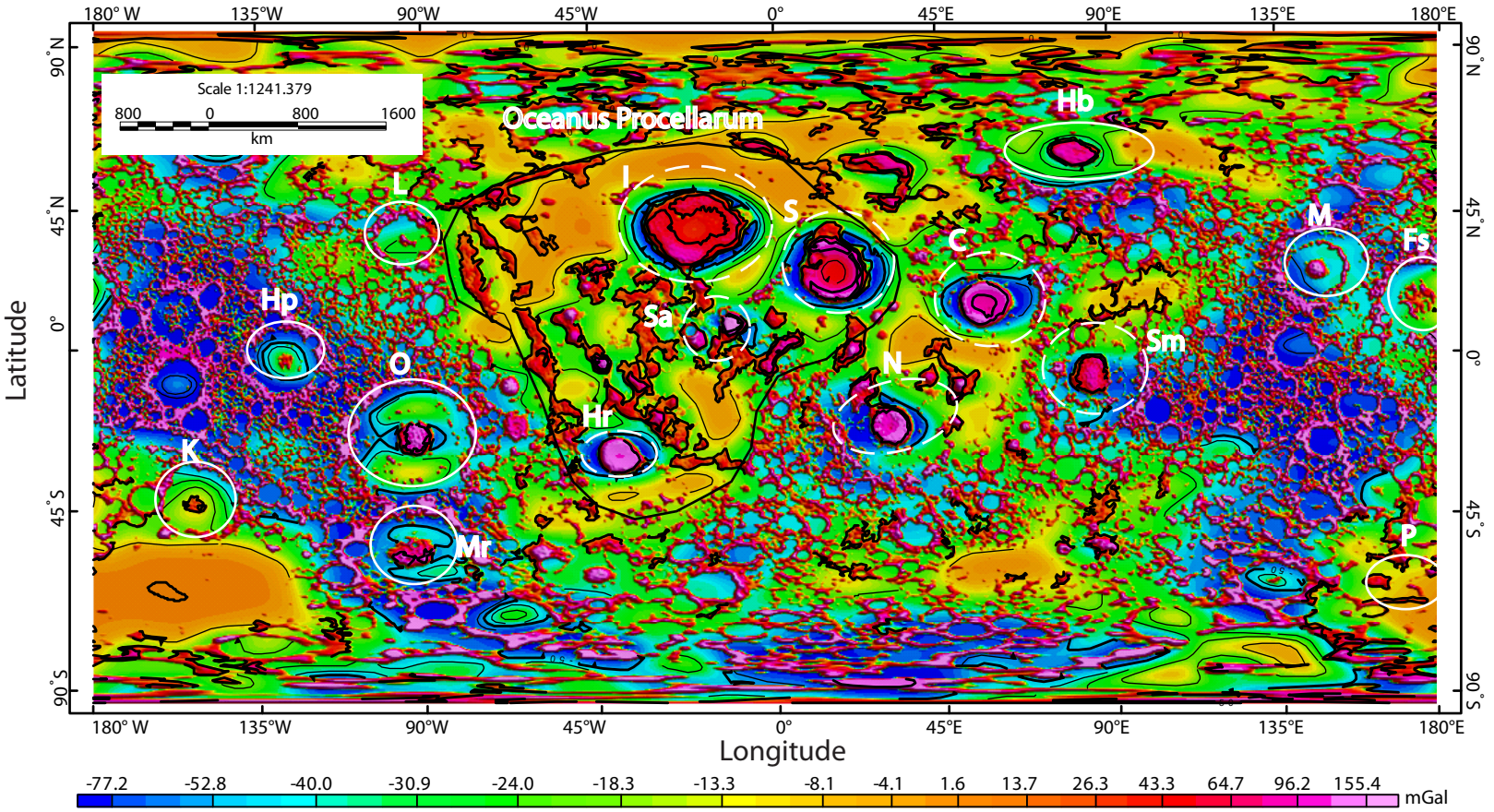

Figure 4. A high pass filtered GL0660A free-air gravity anomaly map. See Figure 2 for explanation of symbols and lettering.

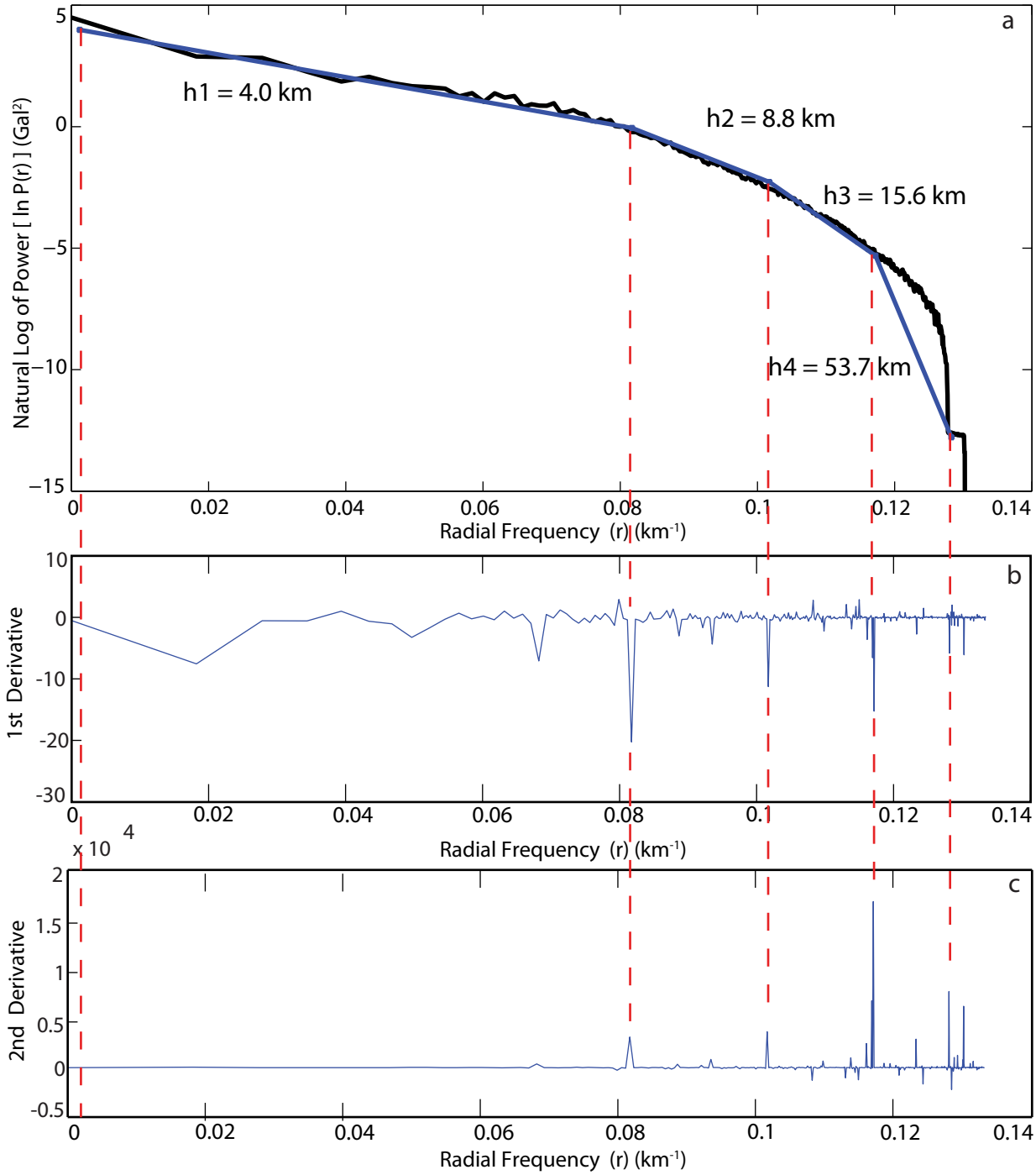

Figure 5. a) Power spectrum of the GL0660A free-air gravity anomaly map of the Moon. The x-axis is radial frequency of the gravity signal in the frequency domain. The y-axis is the natural logarithm of the power spectrum of the gravity signal. The black line is the spectrum of the gravity signal. Blue line segments represent ideal spectra fit to the lunar free-air gravity signal from different depths within the lunar crust. b) An alternate plot of the first derivative of the power spectrum show in a) and its radial frequency is used to define equivalence depths of the gravity signal. c) A plot of the second derivative of the power spectrum show in a). Red lines indicate the beginning and ending locations of each line segment.

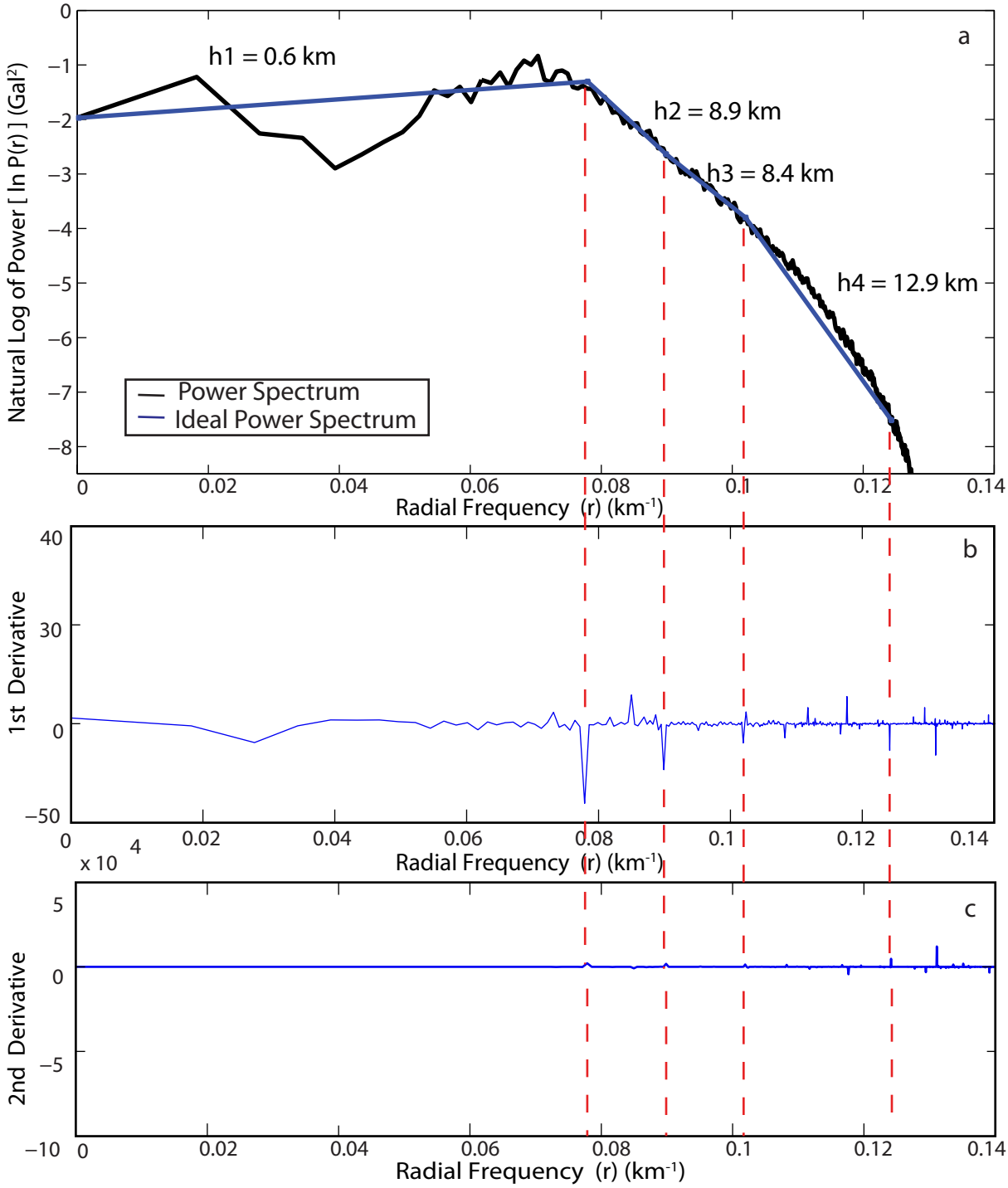

Figure 6. a) Power spectrum of the high-pass filtered GL0660A free-air gravity anomaly map of the Moon. The x-axis is radial frequency of the gravity signal in the frequency domain. The y-axis is the natural logarithm of the power spectrum of the gravity signal. The black line is the spectrum of the gravity signal. Blue line segments represent ideal spectra fit to the lunar free-air gravity signal from different depths within the lunar crust. b) An alternate plot of the first derivative of the power spectrum show in a) and its radial frequency is used to define equivalence depths of the gravity signal. c) A plot of the second derivative of the power spectrum show in a). Red lines indicate the beginning and ending locations of each line segment.

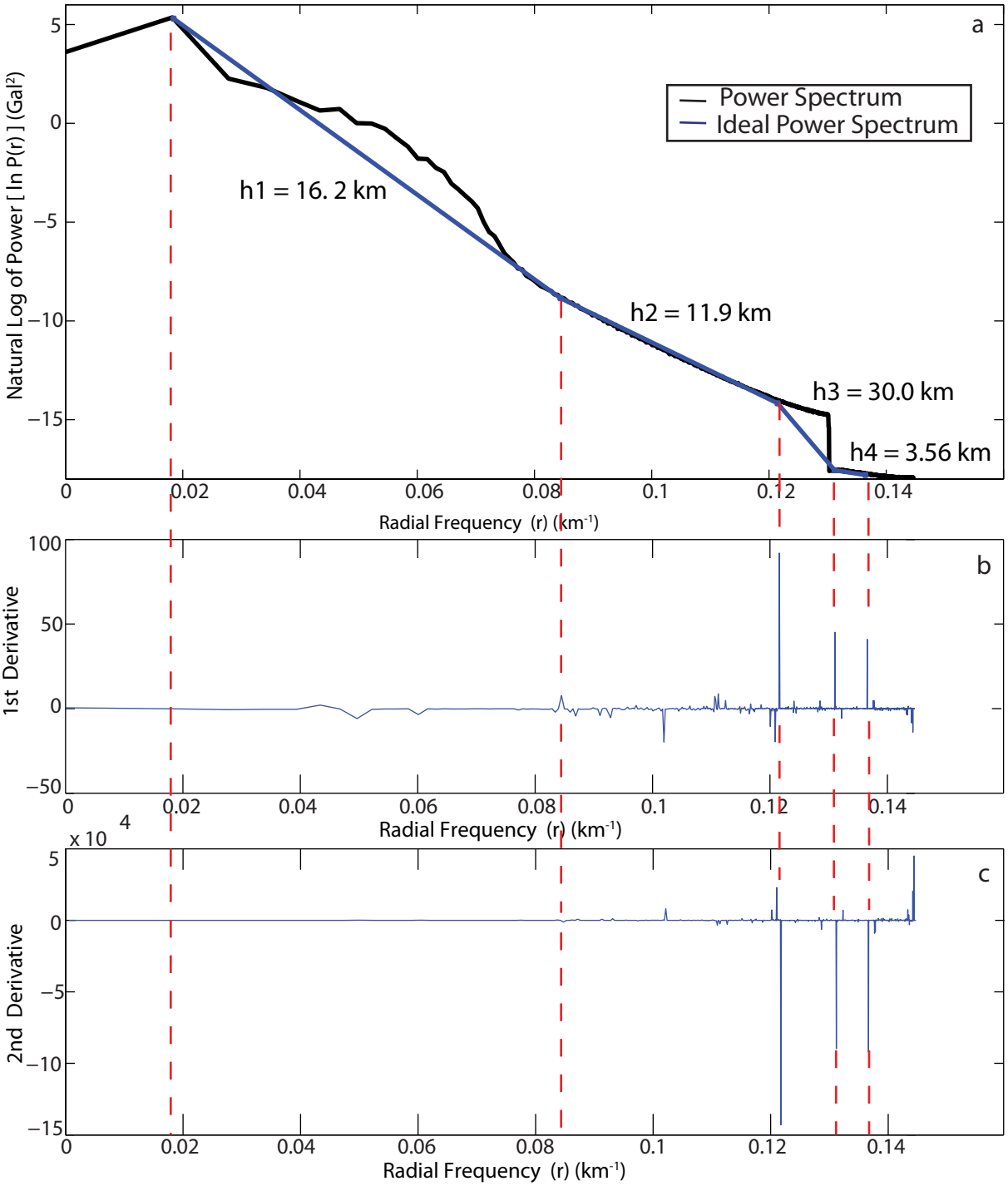

Figure 7. a) Power spectrum of the low-pass filtered GL0660A free-air gravity anomaly map of the Moon. The x-axis is radial frequency of the gravity signal in the frequency domain. The y-axis is the natural logarithm of the power spectrum of the gravity signal. The black line is the spectrum of the gravity signal. Blue line segments represent ideal spectra fit to the lunar free-air gravity signal from different depths within the lunar crust. b) An alternate plot of the first derivative of the power spectrum show in a) and its radial frequency is used to define equivalence depths of the gravity signal. c) A plot of the second derivative of the power spectrum show in a). Red lines indicate the beginning and ending locations of each line segment.

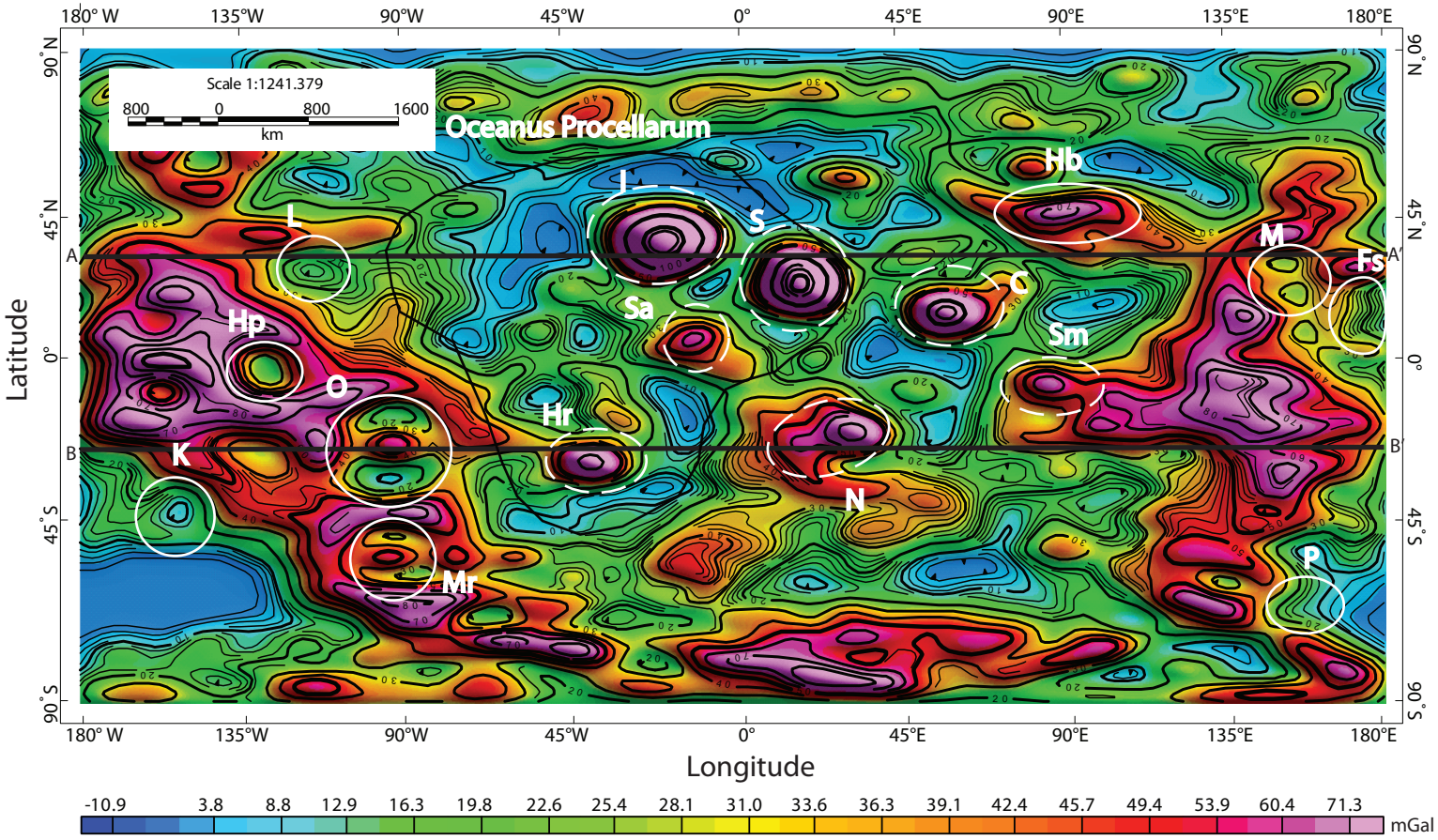

Figure 8. Contoured map of preferentially-filtered (16 km depth) and low pass filtered free air gravity anomaly GL0660A. See Figure 2 for explanation of symbols and lettering.

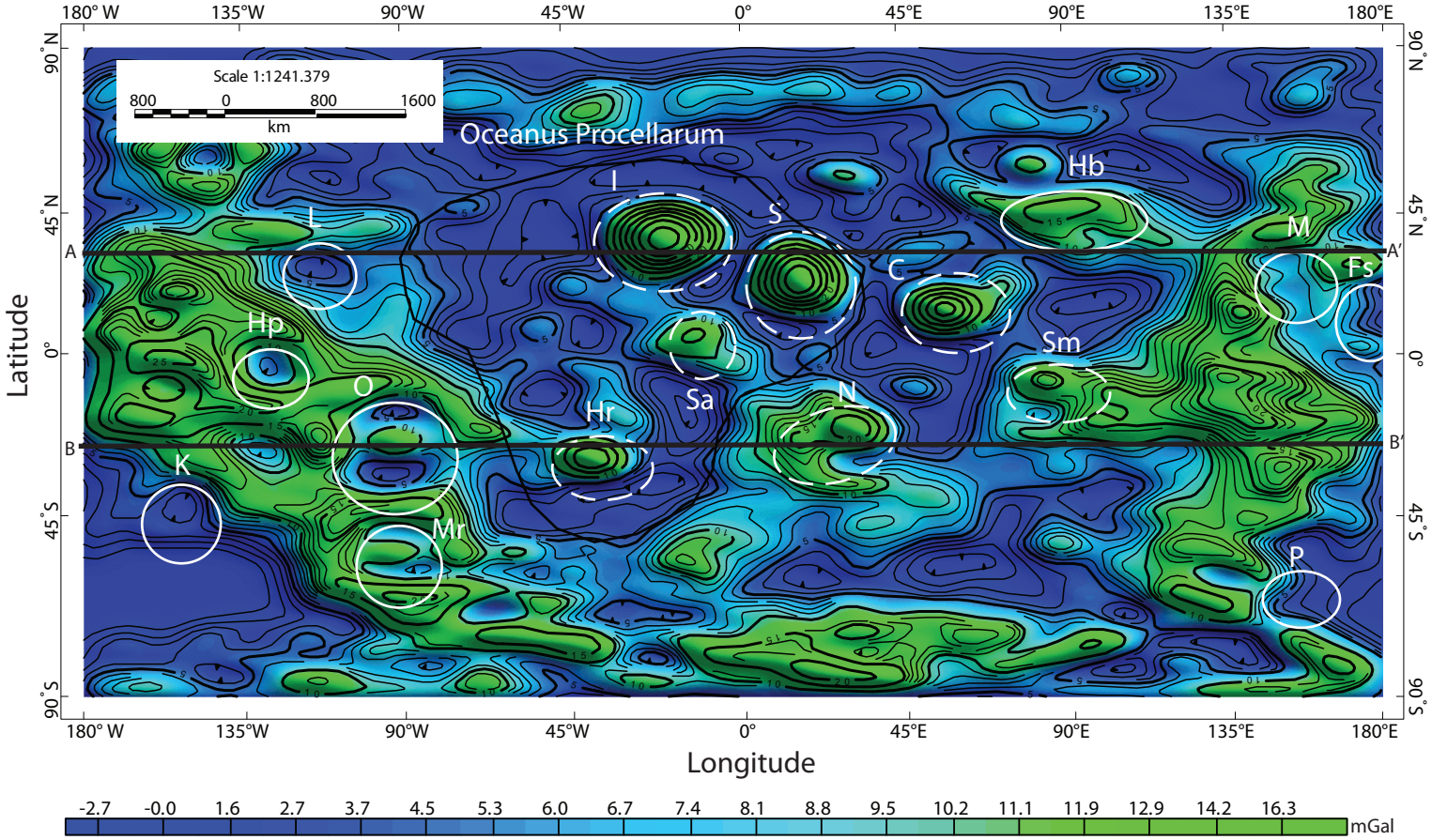

Figure 9. Contoured map of preferentially-filtered (30 km depth) and low pass filtered free air gravity anomaly GL0660A. See Figure 2 for explanation of symbols and lettering.

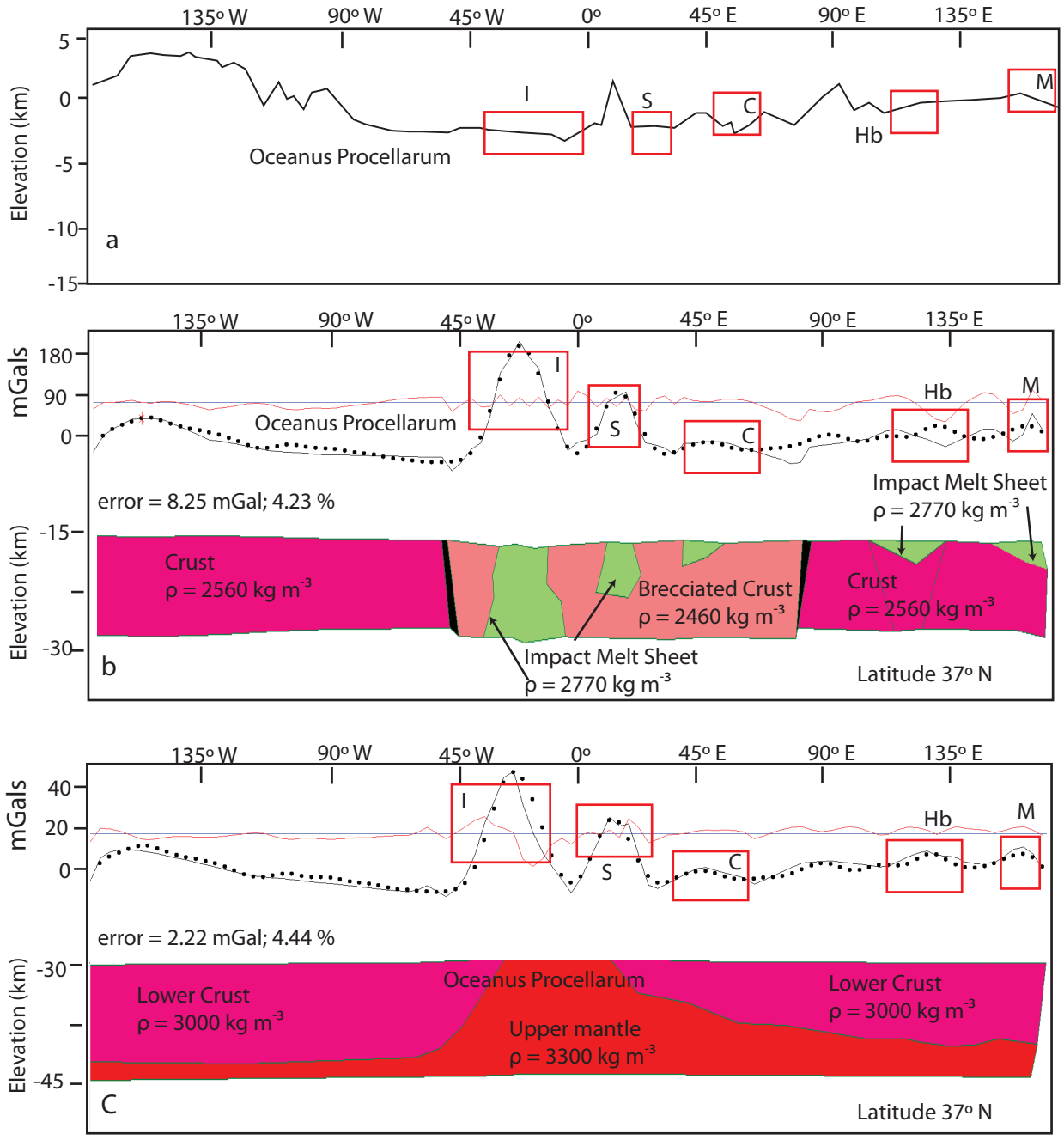

Figure 10. a) Black solid line is the topographic profile from Google Moon (2008). b) 2D inversion model of lunar crustal structure of a preferentially filtered and low passed filtered lunar free air gravity anomaly map GL0660A at a depth of 16 km at latitude 37°N [transect A-A' in Figure 8 and 9]. c) 2D inversion model of lunar crustal structure at a depth of 30 km at latitude 37°N [transect A-A' in Figure 8 and 9]. Dots are the observed, preferentially filtered gravity anomaly values. Dashed black line is the calculated gravity anomaly. Topography and crustal model are shown with 230x vertical exaggeration. Red line represents the misfit value between the observed and calculated gravity data. Red boxes are mascons; I = Mare Imbrium, S = Mare Serenitatis, C = Mare Crisium, Hb = Humboldtianum, M = Moscoviense.

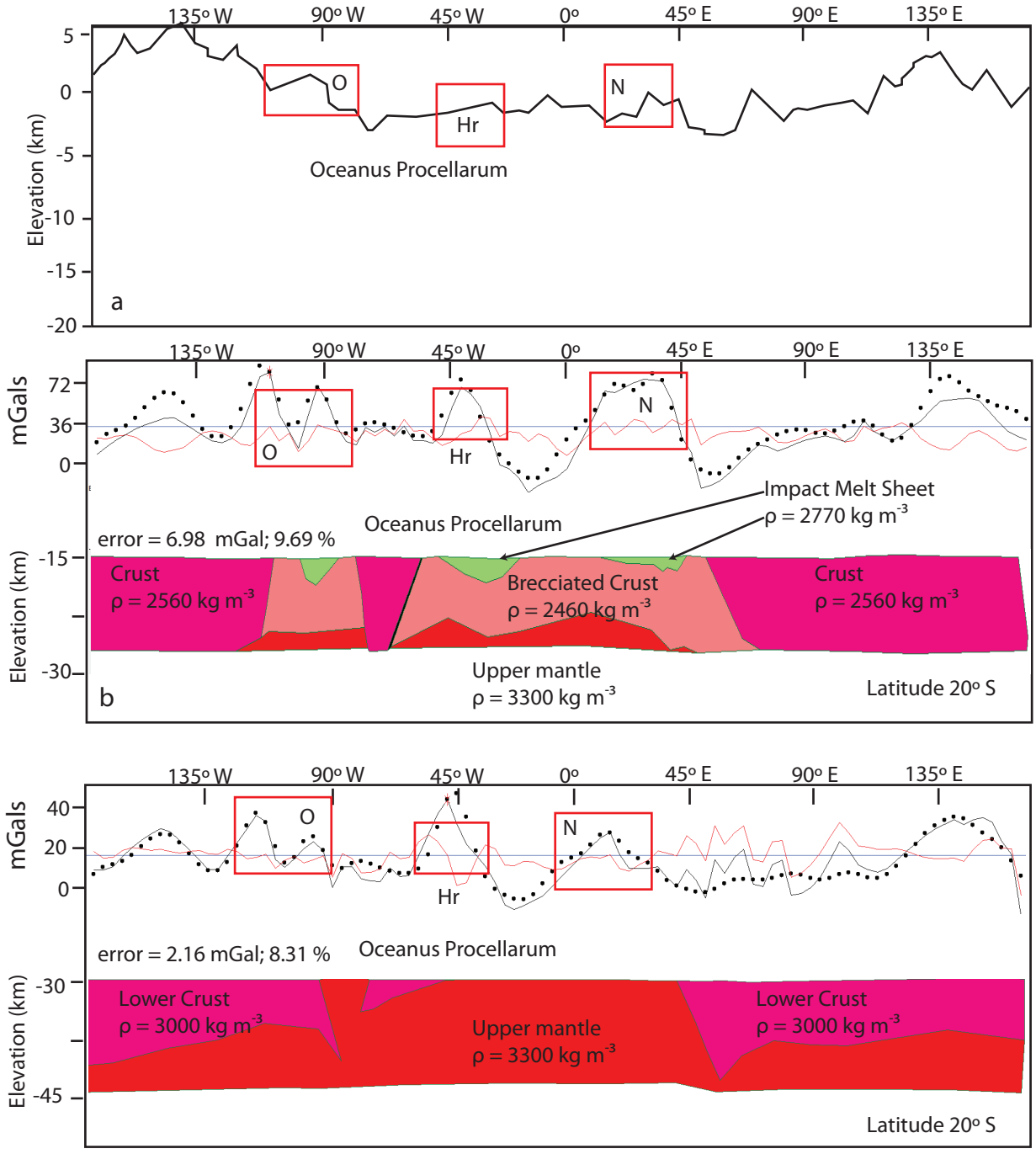

Figure 11. a) Black solid line is the topographic profile from Google Moon (2008). b) 2D inversion model of lunar crustal structure of a preferentially filtered and low passed filtered lunar free air gravity anomaly map GL0660A at a depth of 16 km along latitude 20°S [transect B-B' in Figure 8 and 9]. c) 2D inversion model of lunar crustal structure at a depth of 30 km at latitude 20°S [transect B-B' in Figure 8 and 9]. Dots are the observed, preferentially filtered gravity anomaly values. Dashed black line is the calculated gravity anomaly. Red line represents the misfit value between the observed and calculated gravity data. Red boxes are mascons; O = Mare Orientale, Hr = Mare Humorum, N = Mare Nectaris. Topography and crustal model are shown with 230x vertical exaggeration.

Appendix A: The Preferentially Filtering Routine for Gravity Signal

The routine of this code is based on the procedure suggested by Guo et al., 2013. This code is an adaptation of Guo et al., 2013 to separate the gravity anomaly of the Moon free air gravity signal-GL0600A. A detail explanation of this code can be found in Maksim et al., 2015. The input of this code must be a gravity or magnetic map in .csv (ASCII format). The output of the code routine will be 1) an interpolated plot of the original map, 2) a high pass filtered of the original map, 3) a low pass filtered of the original map, 4) am average radial power spectrum plot of selected map (unfiltered, low pass, or high pass), 5) option to make (x, y) selection on the power spectrum plot, 6) spectrum depths results from user's selection, 7) Five preferentially filtered maps from the selected depths, 8) an option to export all the maps product in .csv format to be further used for modeling. The code convert the input gravity or magnetic map from spatial domain to frequency domain. In frequency domain the code performs low pass and high pas s filtering then computes power spectrum of the low-pass signal and plots the average value of power spectral density to radial frequency or wave number. The code then generate an ideal power spectrum that will be used as a filtering operator to separate the interested band of spectrum from the rest of the data (Guo et al, 2013).

References

Guo, L., Meng, X., Chen, Z., Li, S., & Zheng, Y., 2013, Preferential filtering for gravity anomaly separation. *Computers & Geosciences*, vol. 51, p. 247-254.

Maksim, N. R., Biddle, J., & Hurtado, J. M., 2015, Preferential Filtering and Gravity Anomaly Separation Using Gravity Recovery and Interior Laboratory (GRAIL) Data. In *Lunar and Planetary Science Conference*, vol. 46, p. 3023.

```
clc
clear
% read GRAIL data
F_M_I = imread('gggrx_0660.tif');
%F_M_I = imread('JL0900_fa.tif');
F_M = uint8(F_M_I);
B = imresize(F_M_I, [180 360]);
 %F_M_I = flipdim(F_M_I ,2); %# horizontal flip
 %F_M_I = flipdim(F_M_I ,1); %# vertical flip
 %F_M_I = flipdim(F_M_I ,2);

% Create a colored plot of the Moon's original map
figure (1)
imagesc(B);
colorbar
hold off
title('The Moon free air gravity anomaly map from GRAIL database
GL0660 (resize to fit spherical coordinates)')
xlabel('Longtitude')
ylabel('Latitude')

 %
%-------------------------------------------------------------------------
------------------------

 % To eliminate the effect of top sediment (high frequency?), I did a
low pass filter
 % first I would try with convert the
   % gravity data into frequency domain first and pad the image

   padx = paddedsize (size (F_M)); % pad GRAIL image
   FTx  = fft2 (F_M, padx(1), padx (2)); % perform Fourier transform
with extra padding

% now apply lowpass filter function, I got this code publish on matlab
   sig = 10; % we use 10 degree as the size of our filter
   Lp = lpfilter ('gaussian',padx(1),padx(2), 2*sig); % now double the
size of the filter to match the size of the pad.
   Gp = Lp.*FTx;
   Lo_grav = real (ifft2(Gp)); % now convert back to spatial domain
   lograv_size = Lo_grav (1:size (F_M, 1), 1: size (F_M,2));


% now also apply high pass filter, just to see what did we got rid off

   Hp = 1- Lp;
   Gp2 = Hp.*FTx;

   Hi_grav = real (ifft2(Gp2)); % now convert back to spatial domain
```

```
   higrav_size = Hi_grav (1:size (F_M, 1), 1: size (F_M,2));



 % now plot to see image after lowpass filtered in spatial domain
   figure (2)
   subplot (4,1,1)
   imagesc (1:360, 1:180, lograv_size);
   colorbar
  % now try plot in 3D

  subplot (4,1,2)
  t1 = del2(lograv_size);
  mesh(lograv_size, t1);
  colorbar
  hold off

% now plot to see image after hipass filtered in spatial domain

   subplot (4,1,3)
   imagesc (1:360,1:180,higrav_size);
   colorbar
  % now try plot in 3D
subplot (4,1,4)
t2 = del2(higrav_size);
mesh(higrav_size, t2);
colorbar
hold off



%%
% now try Guo et al., 2013 method

% Process image size information

img =  lograv_size;
res = 7.6 ;

[N M] = size(img);

%% Compute power spectrum
imgf = fftshift(fft2(img));
imgfp = (abs(imgf)/(N*M)).^2;
% Normalize

%% Adjust PSD size
dimDiff = abs(N-M);
dimMax = max(N,M);
```

```
% Make square
if N > M
% More rows than columns
    if ~mod(dimDiff,2)
% Even difference
        imgfp = [NaN(N,dimDiff/2) imgfp NaN(N,dimDiff/2)];
% Pad columns to match dimensions
    else
% Odd difference
        imgfp = [NaN(N,floor(dimDiff/2)) imgfp NaN(N,floor(dimDiff/
2)+1)];
    end
elseif N < M
% More columns than rows
    if ~mod(dimDiff,2)
% Even difference
        imgfp = [NaN(dimDiff/2,M); imgfp; NaN(dimDiff/2,M)];
% Pad rows to match dimensions
    else
        imgfp = [NaN(floor(dimDiff/2),M); imgfp; NaN(floor(dimDiff/
2)+1,M)];% Pad rows to match dimensions
    end
end

halfDim = floor(dimMax/2) + 1;
% Only consider one half of spectrum (due to symmetry)

%% Compute radially average power spectrum
[X Y] = meshgrid(-dimMax/2:dimMax/2-1, -dimMax/2:dimMax/2-1);
% Make Cartesian grid
[theta rho] = cart2pol(X, Y);
% Convert to polar coordinate axes
rho = round(rho);
i = cell(floor(dimMax/2) + 1, 1);
for r = 0:floor(dimMax/2)
    i{r + 1} = find(rho == r);
end
Pf = zeros(1, floor(dimMax/2)+1);
for r = 0:floor(dimMax/2)
    Pf(1, r + 1) = nanmean( imgfp( i{r+1} ) );
end

%% Setup plot
fontSize = 12;
maxX = 10^(ceil(log10(halfDim)));
f1 = linspace(1,maxX,length(Pf));
% Set abscissa

% Find axes boundaries
xMin = 0;
```

```
% No negative image dimension
xMax = ceil(log10(halfDim));
xRange = (xMin:xMax);
yMin = floor(log10(min(Pf)));
yMax = ceil(log10(max(Pf)));
yRange = (yMin:yMax);




%% differential method
% in order to define the location where slope of spectrum has changed

% first derivatives

 for i=1:(length(f1)-2)
 %m(i)= (f1(i+1) -f1(i))/(Pf(i+1)-Pf(i));
 m(i)= (log(f1(i+1)) - log (f1(i)))/(log (Pf(i+1))-log(Pf(i)));
 end

 m(numel(f1)) = 0;

 % second derivatives
for i=1:(length(f1)-2)
 %dm(i) = (m(i+1) -m(i))/(Pf(i+1)-Pf(i));
 dm(i) = (log (m(i+1)) -log (m(i)))/(log(Pf(i+1))-log(Pf(i)));
end

dm(numel(f1)) = 0;




%%-------------------------------------------------------------


%% trying
Pf =  log (Pf);
f1 = log (f1);


% wave frequency was in cycle /pixel convert it to cycle / km
% 1 pixel = 7.6 km (res)
f1 = f1./res ;

% convert frequency to frequency 1/km by dividing radial frequency
with 2pi
f1 = f1./(2.*pi) ;
```

```
%%

figure (4)
subplot (3,1,1)
%semilogx (f1,Pf,'k-','LineWidth',2.0)
plot (f1,Pf,'k-','LineWidth',2.0)
set(gcf,'color','white')
set(gca,'FontSize',fontSize,'FontWeight','bold','YMinorTick','off',...
    'XGrid','on','YAxisLocation','right','XDir','normal');
%xlim([min(log(f1)) max(log (f1))]);
xlim([min(f1) max(f1)]);
ylim ([min(Pf) max(Pf)]);
xlabel('frequency (1/km)','FontSize',fontSize,'FontWeight','Bold');
ylabel('Power','FontSize',fontSize,'FontWeight','Bold');
title('Radially averaged power
spectrum','FontSize',fontSize,'FontWeight','Bold')

% plot first derivative
subplot (3,1,2)
set(gca,'FontSize',fontSize,'FontWeight','bold','YMinorTick','off',...
    'XGrid','on','YAxisLocation','right','XDir','normal');
% semilogx (f1,m)
plot(f1,m)
%plot (log (f1), m)
%xlim([min(log(f1)) max(log (f1))]);
xlim([min(f1) max(f1)]);
% plot second derivative
subplot (3,1,3)
set(gca,'FontSize',fontSize,'FontWeight','bold','YMinorTick','off',...
    'XGrid','on','YAxisLocation','right','XDir','normal');

%semilogx (f1,dm)
plot (f1, dm)
%plot (log(f1), dm)
%xlim([min(log(f1)) max(log (f1))]);
xlim([min(f1) max(f1)]);

 %%
 % obtain vector of 1-D look-up table "y" points
 % this will be location index i
[x1,y1] = ginput

% plot lines and fitting line
figure(5)
%loglog(f1,Pf,'k-','LineWidth',2.0)
plot(f1,Pf,'k-','LineWidth',2.0)
hold on
plot(x1,y1,'+-', 'LineWidth',2.0);
hold off
```

```
% now we will need to find location index of value x and y on Pf (i)
and f1 (1)
%Then, supposing you create your plot using:
% plot lines and fitting line

P =zeros (1,length (y1) ); % pre-allocation
for j =1 : length (y1)

[q1 index1] = min(abs(Pf-y1(j)));
 closestValues1 = Pf(index1);
 % Finds first one only!

P (j) = closestValues1;

end

r = zeros (1,length (x1) ); % pre-allocation

for w =1 : length (x1)

[q2 index2] = min(abs(f1-x1(w)));
 closestValues2 = f1(index2);
 % Finds first one only!;
r (w) = closestValues2 ;

end

h1 = zeros(1,length (P)-1);
for k= 1:1:length(P)-1;
    h1(k) = (P(k)-P(k+1))/(4*pi*(r(k+1)-r(k)));
end


h2 = zeros(1,length (x1)-1);
for k= 1:1:length(x1)-1;
    h2(k) = (y1(k)-y1(k+1))/(4*pi*(x1(k+1)-x1(k)));
end

% show depth result
h1
h2
h = h2.*4.*pi % Li's method do not divide the result with 4pi.
% probably the different betweeen radial distance (radian.km-1) versus
frequency (km-1)

% plot depth calculated
figure (6)
stem(h2);
xlabel('Layer','FontSize',fontSize,'FontWeight','Bold');
```

```
ylabel('Depth (km)','FontSize',fontSize,'FontWeight','Bold');
title('Depth to each geologic
layer','FontSize',fontSize,'FontWeight','Bold')




%%

 % step 4- Use the depth to calculate density of each layer.
 % using Naidu, 1968 and Dampney (1969)the power spectral density
function
 % P = se^(-2kh) % of the observe data
 % P in matrix format
 % P  = AS +E
 % P is the power spectrum density of source i anomaly
 % A (i) = e^(-2kh)
 % k is angular wave vector
 % k = 2*pi/lamda
 % E = The error in fitting the spectral model in step 3
 % where Pi is the power spectrum density of source i anomaly
 %       h is the depth to equivalent payer in km
 % S(u, v, W) is the three-dimensional spectrum of random density
rho(x, y, z).
 % to solve for S in matrix format
 % S = [AtA]-1 AtP


 h2 (length(x1))= 0;
 A = exp((-2*2*pi).*(x1)).*(h2');
 % [y1] = [A][S] which is P = SA from our observe plot
 % t0 solve for S we multiple both side with inverse matrix of A
 % to get inverse matrix we must create a square matrix of A using
 % transpose matrix of A
 % [AtA]^-1 * At * [y1] = [AtA]*[AtA]^-1 *[S]

 At = A';
 H = At*A; % [AtA]
 Hw = inv(H); % [AtA]^-1
 S = (Hw.*At)'.*y1  % [AtA]^-1 * At * [y1]

 % now calculated ideal P (power spectrum density of source I) without
 % anomaly ( clear and clean filtered signal) at the ith radial sample
(P

 PR = A.*S

 % now calculate Weiner preferenial filter operator
```

```
 %Weiner preferenial filter operator
 Wpf = PR./y1
 %Wpf = isfinite(Wpf)
%-----------------------------------------------------------------

%% Now we can impliment weiner filter

 pad = paddedsize (size ( lograv_size)); % pad GRAIL image
   FT  = fft2 ( lograv_size, pad(1), pad (2)); % perform Fourier
transform with extra padding

% for layer 1 at from the depth h1

   Wpf1= Wpf (1);
   Gp3 = (Wpf1.*FT);

   Wpf_grav_1 = real (ifft2(Gp3)); % now convert back to spatial
domain
   Wpf_grav_1_size = Wpf_grav_1 (1:size (F_M_I, 1), 1: size (F_M_I,
2));


% for layer 2 at from the depth h2

 Wpf2= Wpf (2);
   Gp4 = (Wpf2.*FT);

   Wpf_grav_2 = real (ifft2(Gp4)); % now convert back to spatial
domain
   Wpf_grav_2_size = Wpf_grav_2 (1:size (F_M_I, 1), 1: size (F_M_I,
2));

% for layer 3 at from the depth h3

 Wpf3= Wpf (3);
   Gp5 = (Wpf3.*FT);

   Wpf_grav_3 = real (ifft2(Gp5)); % now convert back to spatial
domain
   Wpf_grav_3_size = Wpf_grav_3 (1:size (F_M_I, 1), 1: size (F_M_I,
2));

% for layer 4 at from the depth h4

 Wpf4= Wpf (4);
   Gp6 = (Wpf4.*FT);

   Wpf_grav_4 = real (ifft2(Gp6)); % now convert back to spatial
domain
   Wpf_grav_4_size = Wpf_grav_4 (1:size (F_M_I, 1), 1: size (F_M_I,
```

```
2));

   % for layer 5 at from the depth h5

 Wpf5= Wpf (5);
   Gp7 = (Wpf5.*FT);

   Wpf_grav_5 = real (ifft2(Gp7)); % now convert back to spatial
domain
   Wpf_grav_5_size = Wpf_grav_5 (1:size (F_M_I, 1), 1: size (F_M_I,
2));


%%
 figure (7)

%  % define colorbar plot
   maxValue = round (max(Wpf_grav_1_size(:)))
   minValue = round (min(Wpf_grav_1_size(:)))

 % pre-filtered anomaly
 subplot (3,2,1)
 z0= imagesc ( F_M_I);
  colormap(jet(256))
%caxis([minValue, maxValue]) % change caxis
  title('Gravity Anomaly low-pass filtered');
  colorbar
 hold on
contourf (lograv_size);

% D0 = get(z0,'CData'); %image data
%  [~,idx0] = histc(D0,linspace(min(min(D0)),max(max(D0)),5)); %bin it
%  [C0,z0] = contour(idx0,'color','k'); %contour of the bins
%  clabel(C0,z0)


 % layer 1 plot
 subplot (3,2,2)
z1 = imagesc( Wpf_grav_1_size);
colormap(jet(256))
%caxis([minValue, maxValue])
colorbar
title('Gravity Anomaly after filtered geologic layer 1');
 xlabel('Longtitude');
 ylabel('Latitude')
 hold on
contourf (Wpf_grav_1_size);


% D1 = get(z1,'CData'); %image data
```

```
%  [~,idx1] = histc(D1,linspace(min(min(D1)),max(max(D1)),5)); %bin it
%  [C1,z1] = contour(idx1,'color','k'); %contour of the bins
%  clabel(C1,z1)


 % layer 2 plot
 subplot (3,2,3)
z2=imagesc( Wpf_grav_2_size);
%caxis([minValue, maxValue])
colormap(jet(256))
colorbar
title('Gravity Anomaly after filtered geologic layer 2');
 xlabel('Longtitude');
 ylabel('Latitude')

 hold on
contourf (Wpf_grav_2_size);

% D2 = get(z2,'CData'); %image data
%  [~,idx2] = histc(D2,linspace(min(min(D2)),max(max(D2)),5)); %bin it
%  [C2,z2] = contour(idx1,'color','k'); %contour of the bins
%  clabel(C2,z2)



 % layer 3 plot
 subplot (3,2,4)
z3 = imagesc( Wpf_grav_3_size);
caxis([minValue, maxValue])
colormap(jet(256))
colorbar
title('Gravity Anomaly after filtered geologic layer 3');
 xlabel('Longtitude');
 ylabel('Latitude')
 hold on
contourf (Wpf_grav_3_size);
% D3 = get(z3,'CData'); %image data
%  [~,idx3] = histc(D3,linspace(min(min(D3)),max(max(D3)),5)); %bin it
%  [C3,z3] = contour(idx3,'color','k'); %contour of the bins
%  clabel(C3,z3)


 % layer 4 plot
 subplot (3,2,5)
z4 = imagesc(Wpf_grav_4_size);
%caxis([minValue, maxValue])
 colormap(jet(256))
colorbar
title('Gravity Anomaly after filtered geologic layer 4');
 xlabel('Longtitude');
```

```
 ylabel('Latitude')

 hold on
 contourf (Wpf_grav_4_size);
%  D4 = get(z4,'CData'); %image data
%  [~,idx4] = histc(D4,linspace(min(min(D4)),max(max(D4)),5)); %bin it
%  [C4,z4] = contour(idx4,'color','k'); %contour of the bins
%  clabel(C4,z4)

  % layer 5 plot
 subplot (3,2,6)
z5 = imagesc(Wpf_grav_5_size);
colormap(jet(256))
%caxis([minValue, maxValue])
colorbar
title('Gravity Anomaly after filtered geologic layer 5');
 xlabel('Longtitude');
 ylabel('Latitude')
 hold on
contourf (Wpf_grav_5_size);
%   D5 = get(z5,'CData'); %image data
%  [~,idx3] = histc(D5,linspace(min(min(D5)),max(max(D5)),5)); %bin it
%  [C5,z5] = contour(idx3,'color','k'); %contour of the bins
%  clabel(C5,z5)




%  %
%  %now write the result in .cvs file
%  %ready to be exported for inversion model.
%
%  %for layer 1
%
%  csvwrite('layer1_grav_16km_1015.csv',Wpf_grav_1_size);
% % for later 2

 %  csvwrite('layer2_grav_12km_1015.csv',Wpf_grav_2_size);
%
%   %for layer 3
%
%  csvwrite('layer3_grav_30km_1015.csv',Wpf_grav_3_size);
%
%  % for low pass filter of the moon
%
%  csvwrite('lowpass_grav_1015.csv',lograv_size);
% for hi pass filter of the moon
%
%  csvwrite('hipass_grav_1015.csv',lograv_size);
%
```

```
 %-----------------------------%
 %%

  pad3 = paddedsize (size (Wpf_grav_3)); % pad GRAIL image
   FT3  = fft2 (Wpf_grav_3, pad3(1), pad3 (2)); % perform Fourier
transform with extra padding

   % Now try to filter the low frequency gravity anomaly  with
gaussain low path filter.
   %Passes low wavenumber components; attenuates high wavenumber or
short wavelength components

   sig = 10; % we use 10 degree as the size of our filter
   Lp3 = lpfilter ('gaussian',pad3(1),pad3(2), 2*sig); % now double
the size of the filter to match the size of the pad.
   L3= Lp3.*FT3;
   L3 = real (ifft2(L3)); % now convert back to spatial domain
   L3_size = L3 (1:size (F_M_I, 1), 1: size (F_M_I,2));

 figure (12)

z3_try = imagesc( L3_size);
caxis([minValue, maxValue])
colormap(jet(256))
colorbar
title('Gravity Anomaly after filtered geologic layer 3');
 xlabel('Longtitude');
 ylabel('Latitude')
 hold on
contourf (Wpf_grav_3_size);
% D3 = get(z3,'CData'); %image data
%  [~,idx3] = histc(D3,linspace(min(min(D3)),max(max(D3)),5)); %bin it
%  [C3,z3] = contour(idx3,'color','k'); %contour of the bins
%  clabel(C3,z3)
```

Chapter 5: Synthesis

I achieved the primary objective of this research, which is to design an integrated geophysical method for paleohydrogeological study with an implication in planetary exploration. The obtained product of the primary objective was the estimated quantity of the groundwater reservoir that fed the Kilbourne Hole eruption. I also achieved the second objective of this research, which is to develop a procedure to utilize the high-resolution lunar gravity data (GRAIL). The obtained product of the secondary objectives was two detailed crustal models of the Moon that reveal the internal structure of type I and type II mascons.

For the primary objectives, I performed my developed survey design on an analogous Earth site at Kilbourne Hole in New Mexico. As described in Chapters 2 and 3, I was able to successfully design ground-based surveys using GPR, gravity, and magnetics at Kilbourne Hole to map the internal structure of Kilbourne Hole. I am also able to further use the mapping result to quantitatively understanding paleohydrological conditions of Kilbourne at the time of eruption. The results show that these methods could be performed on Mars or the Moon. By integrating the result of my joint gravity and magnetic model and the GPR surveys at Kilbourne Hole, I yield quantitative constraints for the mass and volume of groundwater reservoir at the time of the eruption. In Chapter 2 I described in detail the method and results of gravity and magnetic survey and 2D gravity-magnetic joint inverse model. In chapter 3 I described in detail the method and results of my GPR surveys and volcanic blocks velocity analysis. However it must be noted that the gravity and magnetic surveys in Chapter 2 and the GPR surveys are not stand-alone results. To obtain the final product of this research which is the amount of groundwater in the reservoir at the time of Kilbourne Hole eruption, we must know the initial velocity of the gas expansion at the time of eruption which can only be retrieved from our GPR

results (Chapter 3) and we must know the mass of material that was excavated from the eruption, and the mass of magma which can only be retrieved from our gravity and magnetic result.

From the magnetic and gravity survey of Kilbourne Hole, NM described in Chapter 2, I mapped the extent and amount of erupted pyroclastic material. Inverse modeling of the gravity and magnetic data reveals three main basaltic dikes underneath Kilbourne Hole. The depth below the pre-eruption ground surface to the top of the dikes varies: dike 1, on the eastern rim of the crater, is between 1.75 to 2.25 km deep; dike 2, underneath the center of the crater, is between 0.91 to 3.58 km deep; and dike 3, underneath the western rim of the crater, is between 0.14 to 2.50 km deep. The three 2D magnetic and gravity jointed inverse models are also able to delineate several complex areas of slump and rotated blocks associated with crater collapse, the diatreme, and post-eruption fill units within the crater. The tuff ring deposit around the crater extends 600 m to 1 km away from the crater rim and my inverse models show that the tuff ring deposit varies in thickness and measures between 50 and 150 m. Based on the geophysical models I have developed for Kilbourne Hole, I estimate the mass of the magma (m_m) related to the Kilbourne Hole eruption to be $(1.38 \pm 0.15) \times 10^{13}$ kg and the mass of water (m_w) to be $(1.09 \pm 0.31) \times 10^{13}$ kg, for a water-to-magma mass ratio of 0.79 ± 0.23.

In Chapter 3, I show that a 250 MHz GPR can be performed on pyroclastic deposit in an arid, volcanic terrain at Kilbourne Hole to map the size distribution of volcanic blocks as a function of distance from the crater rim up to the depth of 2.54 m. Low-frequency (250 MHz) GPR surveys have the potential to probe the shallow subsurface to depths of 2.54 m in arid, volcanic terranes. Using the volcanic block size distribution, I estimate that the volcanic blocks were ejected during the Kilbourne Hole eruption at a velocity between 113-132 m s^{-1} and that the time duration of the gas expansion phase was as long as 81-103. s. The ejection velocity

suggests that the eruption occurred with an initial pressure of 163 ± 9 bar. Kilbourne Hole's maximum gas expansion and ejection velocity falls within the same ranges as other modern phretomagmatic eruption. Other workers observed recent phreatomagmatic eruptions to have the maximum gas expansion velocity to be between 100-400 m s^{-1}. The duration of the gas expansion phase is a good indicator about the groundwater reservoir that fed the eruption. The better the groundwater hydraulic flow, the longer the steam would continue to release. The initial pressure of the eruption is an implication to the depth of eruption center, depth of groundwater level, and the type of groundwater reservoir at the time of eruption. In the case of a phreatomagmatic eruption like Kilbourne Hole, the eruption originated at the contact zone between magma and groundwater reservoir. Therefor we can consider that the depth of eruption is roughly the paleo-groundwater level.

For the second objective of this research, I developed an additional method to the traditional gravity modeling to interpret the GRAIL data because even with the highest resolution (~7.6 km per pixel), it is still insufficient for studying the lunar subsurface as we do not presently have enough detail of lunar subsurface geology to constrain gravity models of the lunar subsurface. We performed power spectrum analysis on the GRAIL GL0660A lunar free-air gravity dataset and for the major mascon basins on the Moon. I show the detail on how to apply power spectra analysis, low-pass and preferential filtering, and 2D inverse modeling to interpret the Moon's complex crustal structure and to map the internal structure of Mascon basins in Chapter 4. We were able to quantify the size and thicknesses of impact melt sheets, the thickness and the density of crust below crater floors, and the elevation of uplifted lunar upper mantle. Our power spectrum analysis provides an understanding of lunar crustal structure, including the depth of prominent gravity signals and depth constraints for 2D gravity inversion

models. Our power spectrum analysis results appear to be compatible with other lunar gravity studies (Zuber et al., 2015; Wieczorek and Phillips, 1998; Miljkovic et al., 2015; Andrews-Hanna et al., 2014). The low pass and preferential filtering approaches we use allow us to eliminate the high frequency gravity signal due to highly impacted subsurface from the total lunar free-air gravity anomaly. As a result, we are able to selectively perform inverse modeling on the gravity signal arising from features at a known depth and are also able to constrain the model with *a priori* knowledge from that depth.

Chapter 4 provided a quantitative interpretation of the GRAIL data. Using the lunar free air gravity anomaly, we developed three filtered gravity anomaly maps and four 2-D inversion models that reveal the internal geologic structure of lunar mascon basins. Aside from the regional crustal structure that we are able to resolve, we are also able to model the detailed structure of several Type I (Mare Imbrium, Mare Serenitatis, Mare Crisium, Mare Nectaris, Humboldtianum) and Type II (Mare Orientale, and Moscoviense) mascon basins. We conclude that source of the high gravity anomalies associated with mascon basins are: (1) impact melt sheets; (2) impact breccia; and (3) uplifted, shallow Moho. We conclude that the outer negative rings of the bull's-eye gravity signature of Type I mascons are due to low-density contrasts in the upper lithosphere. The upper lithosphere mainly consists of loose material ejected during the excavation stage of crater formation (Comerford, 1967). The high amplitude positive gravity anomaly (>60 mGal) of Type I mascon basins is directly influenced by the high density contrasts between shallow lunar mantle (3,220 kg m^{-3}), very thin brecciated crust (2,460 kg m^{-3}), and moderate density impact melt sheets (2,770 kg m^{-3}). The lower amplitude positive gravity anomaly (<50 mGal) of Type II mascon basins is directly influenced by thicker brecciated crust

(2,460 kg m^{-3}) and a deeper Moho, which both result in a reduced density contrast as seen in Mare Orientale and Moscoviense.

To summarize the accomplishment of my research for this dissertation, the results from my study at Kilbourne Hole not only validate the ability of my method in planetary exploration, but it also reveals important information about the internal structure of Kilbourne Hole, its eruption history, and the paleo-hydrologic conditions of the Rio Grande rift basin in much more detail than any surface geological study could. We had demonstrated that our research from Chapter 2 and 3 could serve as a pilot study as an implication for planetary geophysical surveys to understand hydrogeological history of a planet such as Mars. The results of a GPR survey similar to the one performed at Kilbourne Hole could be used to map the size distribution of volcanic blocks at a phreatomagmatic volcano on Mars from which an estimate for the amount of groundwater involved in the eruption could be made. I also introduce in this research an application of low pass filtering, radial power spectrum depth analysis (Spector and Grant, 1970), and preferential (Guo et al., 2003). These additional techniques helped us find a way to constrained and increase reliability of the obtained gravity models that reflect the internal structure of the Moon, even with minimal *a priori* knowledge of the Moon's complex geology. My models successfully provided quantitative interpretation of mascon basins and crustal structure of the Moon. The application of our integrated geophysical method also provided us geophysical model of Kilbourne Hole that are more reliable than solely using the geophysical modeling method with limited *a priori* data.

In conclusion, GPR, gravity, and magnetic surveys are low cost, provide data that are easy to process, and the fieldwork can be quickly conducted. Data collection and interpretation can be done within days or weeks, and can provide preliminary information instantly at the time

of data collection. With appropriate data processing (dependant on geological setting and field conditions: see detail in chapter 2 and 3), we can later derive quantitative interpretation from the data. To design surveys and data processing on Mars, we need to base the survey design on the electrical properties of Martian volcanic material, possibly on the analog material or from other context. As of now there are several studies on a dry regolith unit and two volcanic ash units in Elysium Planitia that yield high electrical permittivity (6 F/m) and low attenuation constant (~30-50 dB) (Picardi et al., 2004; Heggy et al., 2006: Vaucher et al., 2009). These preliminary conditions of Martian volcanic material is somewhat compatible with the volcanic material at Kilbourne Hole and may allow low frequency radar signals to propagate to greater depths.

The future recommendations to improve and to carry on our research in addition to other workers' numerous research (Picardi et al., 2004; Seu et al., 2007; Hamran et al., Kobayashi et al., 2014; 2015) involving the design and test of geophysical instruments for Mars and the Moon are: 1) utilize several types of GPR, gravimetry, and magnetometry equipment that have been deployed at Mars and the Moon (Seu et al., 2007; Hamran et al., 2015) to conduct a ground based GPR, gravity and magnetic survey similar to what I am doing at Kilbourne Hole, 2) to practical adaptations of our method for Martian ground based surveys as well as a number of other key observations must also be made to retrieve better quality *a priori* information of Mars and Moon rock. In addition to present exploration of Mars that is focused on evaluating the habitability of surface environments, we argue that we may also need to look back further in time as the Martian surface had become extremely cold, oxidized and arid long before. With further observations, great information can be learned about the climate history of the terrestrial planets through this type of research. For a lunar and Mars mission, my gravity and magnetic surveys would provide us with a richer data set than the current high-resolution free air gravity anomaly

map from GRAIL. I am excited for the next decades and for the possibility that I may soon be able to apply my methods to exploring the surfaces of Mars and the Moon.

References

Comerford, M. F., 1967, Comparative erosion rates of stone and iron meteorites under small-particle bombardment. *Geochimica et Cosmochimica Acta*, vol. 31, p. 1457–1471.

Hamran, S. E., Berger, T., Brovoll, S., Damsgard, L., Helleren, O., Oyan, M. J., and Eide, J., 2015, RIMFAX: A GPR for the Mars 2020 rover mission: Advanced Ground Penetrating Radar (IWAGPR), 2015 8th International Workshop, vol.8, p. 1-4.

Heggy, E., Clifford, S. M., Grimm, R. E., Dinwiddie, C. L., Wyrick, D. Y., and Hill, B. E., 2006, Ground-penetrating radar sounding in mafic lava flows: Assessing attenuation and scattering losses in Mars-analog volcanic terrains: *Jmynal of Geophysical Research: Planets (1991–2012)*, vol. 111 (E6). p. E06S04-1- E06S04-16.

Guo, L., Meng, X., Chen, Z., Li, S., and Zheng, Y., 2013, Preferential filtering for gravity anomaly separation: *Computers & Geosciences*, vol. 51, p. 247-254.

Kobayashi, T., Lee, S. W. R., Kumamoto, A., and Ono, T., 2014, GPR observation of the Moon from orbit: Kaguya Lunar Radar Sounder: Proceeding of the 15th International Conference on Ground Penetrating Radar (GPR), p. 1,037-1,041.

Milsom, J., 2007, Field Geophysics: John Wiley and Sons (University College London), 249 p.

Picardi, G., Biccari, D., Seu, R., Marinangeli, L., Johnson, W. T. K., Jordan, R. L., and Zampolini, E., 2004, Performance and surface scattering models for the Mars Advanced Radar for Subsurface and Ionosphere Sounding (MARSIS): *Planetary Space Science*, vol. 52, p.149.

Spector, A. and Grant, F. S., 1970, Statistical models for interpreting aeromagnetic data: *Geophysics*, vol. 35, no .2, p. 293-302.

Seu, R., Phillips, R. J., Biccari, D., Orosei, R., Masdea, A., Picardi, G., and Nunes, D. C., 2007, SHARAD sounding radar on the Mars Reconnaissance Orbiter: Jmynal of Geophysical Research,vol. 112 (E5), p. E05S05-1–E05S05-18.

Vaucher, J., Baratoux, D., Mangold, N., Pinet, P., Kurita, K., and Grégoire, M., 2009, The volcanic history of central Elysium Planitia: Implications for martian magmatism: *Icarus*, vol. 204(2), p. 418-442.

Zuber, M. T., Smith, D. E., Watkins, M. M., Asmar, S. W., Konopliv, A. S., Lemoine, F. G., Melosh, H. J., Neumann, G. A., Phillips, R. J., Solomon, S. C., Wieczorek, M. A., Williams, J. G., Goossens S. J., Kruizinga, G., Mazarico, E., Park, R. S., and Yuan, D. N., 2013, Gravity field of the Moon from the Gravity Recovery and Interior Laboratory (GRAIL) mission: *Science*, vol. 339, no. 6,120, p. 668-671.

Curriculum Vitae

Nisa Maksim is a granddaughter of a corn farmer. She was born and raised in the rain forest of rural Thailand. She received her Bachelor of Science in Physics from Kasetsart University in 2004 and a Master of Science in Geophysics/Hydrogeology in 2006 from Chiang Mai University. She had spent some years working and digging as a paleontologist in Southern California. She later decided to go back to school and pursue her doctorate education and got accepted to the doctoral program with the Department of Geological Science at the University of Texas at El Paso in 2011. Her dissertation title is an Integrated Geophysical Surveys at Kilbourne Hole, Southern New Mexico: Implications for Near Surface Geophysical Exploration of Mars and the Moon. Dr. Jose M. Hurtado Jr. is her supervisor. Nisa Maksim was the recipient of several scholarships and awards including a UTEP-NSF GK12 fellowship, UTEP-LEAP grants, Chevron's Students Leaderships Symposium Award and Dodson's Research Award. Nisa Maksim dedicated her times at UTEP to both inside and outside curriculum activities. She had served as the 26th UTEP Geology Colloquium co-chair and had served as a vice president and a president to the Society of Exploration Geophysicists (SEG)-UTEP student chapter in 2012-2014. She had been travelling the world to participate in numerous international meetings and to climb several mountains from India to the middle of nowhere in Mexico and Mount McKinley. Nisa Maksim received her doctoral degree in the summer of 2016. After graduation Dr. Maksim will follow her military husband to Wiesbaden, Germany and hopes to receive a post-doctoral fellowship to continue doing her research over there. If not, as a geologist and an army wife, she will probably find some other dirt/rock related jobs to do.

This dissertation was typed by Nisa Maksim